LEOPOLD-FRANZENS UNIVERSITY OF INNSBRUCK
INSTITUTE FOR EXPERIMENTAL PHYSICS

Dissertation: Experiments with single photons emitted by single atoms

Thesis submitted to the
Faculty of Mathematics, Computer Science and Physics
of the Leopold-Franzens University of Innsbruck
in partial fulfillment of the requirements for the degree of
Doctor of Philosophy
(Physics)

Carried out under the supervision of Prof. Rainer Blatt at the
Quantum Optics and Spectroscopy Group

GABRIEL ANDRÉS ARANEDA MACHUCA
INNSBRUCK - AUSTRIA
2019

Abstract

Ions confined in Paul traps present unique features that allows us to study well-controlled single (or few) quantum objects isolated from the environment, enabling one of the most prominent platforms for quantum information processing. These features, combined with high collection efficiencies of the emission in a single optical mode permit the study of the properties of the emission at the single quantum level -a photon- and its correlations with the internal and external states of the emitter.

In this thesis, we perform several experiments where the detected optical field is a single photon emitted by a single or two trapped ions. These photons are highly correlated with the internal state of the ions, allowing the creation and characterization of entanglement between different ions. In a first experiment, we show that the presence of entanglement in a pair of ions can lead to enhancement and inhibition of the emission of single photons in a common emission mode. The rate of emission on this mode can be tuned by changing the relative distance of the ions in the common emission mode and the contrast of the observed signal maps directly the amount of entanglement in the ion pair.

In a second experiment, we study how angular momentum of the atoms and the spin and orbital angular momentum of the emitted photons are correlated. We show how the change on the internal angular momentum of an atom during the emission of a single photons determines the distribution of spin and orbital angular momenta of the emitted field. This relation is mapped into the spatial properties of field, and the presence of angular momentum can be detected as displacement in the position of the atom's images with respect to its actual position.

Finally, we consider the design and construction of a new experimental apparatus in which a single ion is trapped in the center of a hemispherical mirror. Such a setup would enable the study of quantum electrodynamics effects such as perfect inhibition and enhancement of the spontaneous emission, but also increase the collection of single emitted photons up to 38%.

Zusammenfassung

Gespeicherte Ionen in Paulfallen erlauben es aufgrund ihrer besonderen Eigenschaften, mit sehr guter Kontrolle einzelne (oder mehrere) Quantenobjekte in insolierter Umgebung zu untersuchen und ermöglichen so eine der bedeutendsten Plattformen für Quanteninformationsverarbeitung. Diese Eigenschaften machen es möglich, in Kombination mit hoher Sammeleffizienz der von den Ionen in den freien Raum abgestrahlten optischen Felder, die Eigenschaften der Abstrahlung und deren Korrelation mit den inneren und äußeren Zuständen des Emitters auf dem Niveau einzelner Quanten (Photonen) zu studieren.

In der vorliegenden Arbeit führen wir mehrere Experimente durch, in denen das detektierte optische Feld ein einzelnes Photon ist, das von einem oder zwei Ionen emittiert wird. Diese Photonen sind stark korreliert mit dem inneren Zustand des Ions/der Ionen, was die Erzeugung und Charakterisierung von Verschränkung zwischen verschiedenen Ionen erlaubt. In einem ersten Experiment zeigen wir, dass das Vorhandensein von Verschränkung eines Ionenpaars zu verstärkter oder unterdrückter Emission von einzelnen Photonen in eine gemeinsame Emissionsmode führt. Die Emissionsrate in diese Mode kann variiert werden, indem der relative Abstand der Ionen in der Emissionsmode geändert wird. Zudem bildet der Kontrast des gemessenen Signals direkt die Menge an Verschränkung des Ionenpaars ab.

In einem zweiten Experiment untersuchen wir, wie der Drehimpuls des Atoms und der Bahndrehimpuls der emittierten Photonen korreliert sind. Wir zeigen, wie die Änderung des inneren Drehimpulses des Atoms während der Emission eines Photons die Verteilung von Spin und Bahndrehimpuls des emittierten Feldes bestimmt. Dieser Zusammenhang übersetzt sich in die räumlichen Eigenschaften des Feldes und das Vorhandensein von Bahndrehimpuls kann als Verschiebung der Position der Abbildung des Atoms relativ zu seiner tatsächlichen Position gemessen werden.

Schließlich betrachten wir Design und Konstruktion eines neuen experimentellen Aufbaus, in dem ein einzelnes Ion im Zentrum eines halbkugelförmigen Spiegels gefangen ist. In solch einem Aufbau können quantenelektrodynamische Effekte wie die vollständige Unterdrückung und die Verstärkung der Spontanemission untersucht werden. Außerdem kann die Sammeleffizienz der emittierten einzelnen Photonen auf bis zu 38% erhöht werden.

Publications

This thesis is based on the work realized in the Barium laboratory of the Quantum Optics and Spectroscopy group, between September 2013 and December 2017. Original results presented in this thesis have been published in the following articles:

- "Interference of single photons emitted by entangled atoms in free space", G. Araneda, D. B. Higginbottom, L. Slodička, Y. Colombe and R. Blatt, *Physical Review Letters* **120**, 193603 (2018), arXiv:1712.02105v3.

- "Wavelength-scale errors in optical precision localization due to spin-orbit coupling of light", G. Araneda, S. Walser, Y. Colombe, D. B. Higginbottom, J. Volz, R. Blatt and A. Rauschenbeutel, *Nature Physics* **15**, 1, 17 (2018).

During my PhD, I also contributed to experimental and theoretical projects that led to the following publications:

- "Scalable interference from trapped ion chains", D. P.Obšil, A. Lešundák, T. Pham, G. Araneda, O. Číp, R. Filip and L. Slodička, arXiv:1804.01518.

- "Fabrication of precision hemispherical mirrors for quantum optics applications", D. B. Higginbottom, G. Campbell, G. Araneda, F. Fang, Y. Colombe, B. C. Buchler and P. K. Lam, *Scientific Reports* **8**, 221 (2018), arXiv:1706.07858

- "Pure single photons from a trapped atom source" D. B. Higginbottom, L. Slodička, G. Araneda, L. Lachman, R. Filip , M. Hennrich and R. Blatt, *New Journal of Physics* **18**, 093038 (2016), arXiv:1605.03774

- "Telecloning of qudits via partially entangled states", G. Araneda, N. Cisternas and A. Delgado, *Quantum Information Processing* **15**, 3443 (2016), arXiv:1712.00624.

Contents

List of Figures

List of Tables

List of Acronyms

APD Avalanche photo diode

AOM Acousto-optical modulator

COC Computer numerical control

COC Center of curvature

COM Centre of mass

DDS Direct digital synthesizer

EIT Electromagnetically-induced transparency

EOM Electro-optical modulator

HALO High-aperture laser objective

NA Numerical aperture

NEG Non evaporable getter

OAM Orbital angular momentum

PCB Printed circuit board

PDH Pound-Drever-Hall locking scheme

QED Quantum electrodynamics

RF Radio frequency

SAM Spin angular momentum

UHV Ultra-high vacuum

1 Introduction: Single atoms and single photons

The study of the interaction between light and matter is of interest in a wide variety of fields, covering topics such as photosynthesis in biology [1], efficient generation of electrical energy in engineering [2], spectroscopy of antimatter in fundamental physics [3] and quantum networking in applied physics [4]. For a full comprehension of many macroscopic and microscopic phenomena, it is necessary to study the interaction between light and matter at the most basic level: when it is reduced to the interaction of their fundamental constituents, i.e., atoms and photons. At this scale, the laws of classical physics do not properly describe their behaviour, and it becomes necessary to use the tools provided by quantum mechanics to properly explain the diverse phenomena associated with their interaction.

Quantum mechanics is one of the most successful physical theories. It has been able to predict and explain a large variety of phenomena related with the interaction of matter and light, such as spontaneous emission or the functioning of a laser. One of the most intriguing predictions of quantum mechanics is the existence of entanglement, whose consequences were deemed by A. Einstein as "Spooky action at distance" and considered unreasonable when first suggested [5, 6]. Entanglement is a phenomenon in which the state of multiple quantum objects cannot be described independently of each other, even though they could be spatially separated. This implies that the change in the quantum state of one object can instantaneously influence the state of a spatially separated object. Entanglement has been found crucial for the speed-up of computation using quantum mechanical phenomena to process information; a problem that is studied in the field of *Quantum Computation* [7]. Furthermore, entanglement has proved to be useful in the field of communication, where cryptographic schemes can be improved by the use of entangled states, allowing secure communication [8].

Recent technological developments have allowed the observation of many phenomena that initially were considered only idealized physical situations, such as performing experiments with a single atom or a single photon. The development of techniques for isolation of single quantum objects and control of their properties has dramatically evolved in the last decades. Today it is possible to isolate single atoms and precisely control their internal and external features, and thus engineer their interactions with other isolated quantum systems, or extract single energy quanta

from them. In the same way, a single photon can be isolated and transmitted, and properties such its polarization or the shape of its temporal wavepacket can be manipulated.

One of the fundamental quantum processes involving atoms and photons is spontaneous emission. Spontaneous emission happens when an atom, initially in an excited electronic state decays to an energetically lower state, releasing a quantum of energy, i.e., a photon. The energy, the linear momentum and the angular momenta of the emitted photon correspond to the difference of those of the initial and final state of the atom. In this way, detection and analysis of the emitted single photons can give us information about the initial and final states of the atoms.

In this thesis, we study phenomena related to spontaneous emission from single atoms in the regime of single photons. To do so, we use the experimental toolbox available with trapped ions, where ionized single atoms can be confined and isolated. We use laser beams and radio frequency waves to control external and internal degrees of freedom of the atom, such as its center-of-mass motion and electronic state. To collect the emitted photons, we use high-numerical-aperture low-aberrations lenses located close to the atom, which in contrast with other approaches such as using optical cavities, preserve the spatial properties of the emission. In this thesis we study two fundamental optical phenomena related with the emission of single photons from one or two ions. The first is the fundamental difference in the emission of single photons from atoms either in separable states or entangled states. And the second is the coupling of spin and orbital angular momentum in the single photons emitted by a single atom.

This thesis is divided into four main parts:

- In the first part, the main experimental tools and techniques used in this thesis are reviewed, as well as their theoretical basis. These tools and techniques include ion trapping using Paul traps, cooling and coherent control of its internal and external degrees of freedom using lasers and radio frequencies (Chapter 2). In Chapter 3, the experimental setup for trapping and manipulation of singly ionized Barium atoms used in the thesis is presented, along with the control and detection systems and spectroscopy of the different ion transitions.

- In the second part (Chapter 4), the experiment titled “Interference of single photons emitted by a pair of entangled atoms” is presented. In this experiment, we study the emission properties of a pair of entangled atoms. We optically entangle two atoms by detecting a single photon emitted by of the atom pair [9]. Then, we observe the emission of photons by the entangled atom pair in a free-space optical mode. The rate of this emission is modulated by the length of the optical path connecting the atoms, and the difference between the maximum and minimum rates is determined by the degree of entanglement shared between the atoms, i.e., their concurrence. The probability of detection of single photons can be used directly to characterize the amount of entanglement of the atoms. Furthermore, large sensitivity of the interference phase evolution points to applications of the presented scheme in high precision gradient sensing, which we demonstrate by measuring spatial magnetic field differences at the positions of the atoms.

- In the third part (Chapter 5), we study the angular momentum properties of the light emitted by a single atom. The conservation of angular momentum during spontaneous emission implies that the emitted photon carries the angular momentum lost (or acquired) by the atom during the transition. We specifically study dipole transitions in the case in which the angular momentum carried by the photon is purely orbital angular momentum (OAM). In this case, the angular momentum of the photon is mapped to an apparent displacement of the position of the emitting atom. We measured this displacement for two dipole transitions with opposite angular momentum change. Additionally, we analyse the imaging process of the emitted photons for different dipole orientations and apertures of the optical system used for detection, and give analytical results in certain regimes and its relation with weak measurements. We present extended experimental results obtained using a nanoscopic dipole emitter (a nanosphere) as part of a collaborative project.

- Finally, in the fourth part (Chapter 6), we present the design and construction of a new setup for quantum optics experiments. The main feature of this setup is the use of a hemispherical mirror, and the ability to trap an atom in its center of curvature using a high optical access Paul trap. Such a setup benefits from an improvement in the collection of the emitted light, with a gain of more than three times the best collection in our old linear trap setup. This improvement will be beneficial for applications where the detection of single photons is needed, specially for those experiments involving the creation of entanglement between distant emitters. Furthermore, it will allow the realization of paradigmatic quantum electrodynamics (QED) experiments. The light modes emitted in the half space covered by the hemispherical mirror can be totally reflected towards the emitting atom, and depending on the curvature radius of the mirror, total inhibition and enhancement of the spontaneous emission can be achieved in the full space.

  The realization of the considered apparatus presents several technical challenges, such as the construction of a hemispherical mirror with sub-wavelength surface smoothness and tunable radius, the design and construction of a Paul trap which permits the confinement of the atom with optical clearance compatible with optical setup, and the inclusion of a high numerical aperture aspheric lens with low wavefronts distortion. All of these challenges are presented, studied and overcome in this thesis.

2 Trapping and manipulation of single atomic ions

2.1 Introduction: Single quantum objects

The study of single quantum objects is in general a difficult task, since many of these properties become unclear when these objects interact with the rest of the universe. This process is called decoherence, and it can be defined as the "loss of information of a system to the environment" [10]. Decoherence can ultimately cause the loss of quantum behaviour of the observed system. In the latest 20 years, many technological developments have enabled several experimental platforms to drastically reduce the decoherence of the observed system. This is achieved by isolating the objects from the influence of external perturbations by, e.g., placing them in ultra-high vacuum (UHV) environments or at very low temperatures. For experimental purposes, it is also desirable to have the quantum objects spatially well localized, facilitating the control of their quantum properties using lasers or other field sources and their interaction with other objects (quantum or not). Experimental platforms enabling the study of spatially confined single quantum objects include:

- Atomic ions in Paul traps [11] or in Penning Traps [12],
- Neutral atoms in magneto-optical traps [13], dipole traps [14] or optical lattices [15],
- Crystallographic defects in diamond, e.g., Nitrogen-vacancy centres [16],
- Polar molecules in electrical traps [17],
- Semiconductor nanostructures, i.e, quantum dots [18],
- Josephson junctions in superconducting circuits [19],
- Donor spins qubits in Silicon [20],
- Rare-earth ions in crystals [21],
- Photons confined in resonators, i.e., cavity electrodynamics [22],

Each of these platforms has its advantages and disadvantages concerning features such as the degree of control of internal (e.g., electronic state) and external degree of freedom (e.g. center-of-mass motion), coherence times of these degrees of freedom, controlled interactions with other similar quantum objects, state read-out fidelity, photon extraction efficiency, scalability of the number of well-controlled objects and the possibility to interface them with quantum objects of different nature.

The control and measurement of the quantum properties of most quantum objects listed above are achieved through their interaction with electromagnetic radiation, typically in the optical and radio-frequency (RF) regimes. The detection of quantum features is then done by observing their emission or absorption, or through their interaction with other quantum objects. The properties of the emitted photons can be highly correlated with the state of the emitting quantum object so that we can obtain information about the emitter through them. A high probability of capturing single emitted photons makes the acquisition of information about the emitter more efficient and improves the success probability of quantum information protocols, such as information transfer to other remote quantum objects.

From the systems listed above, atomic ions stand out for having most of the mentioned desired features. Single atomic ions can be confined into small spatial volumes by taking advantage of their charge and using electromagnetic traps, so-called Paul traps [23], which provides extremely long trapping times, with record times of up to years. Paul traps can generate deep harmonic potentials in which the different motional modes of the trapped particle are quantized. Laser cooling techniques such Doppler cooling or sideband cooling are then used to lower the motion of the trapped particles down to its ground state, reducing drastically the motion-related decoherence. Laser and RF pulses can be used to control both the motional and the internal states of the trapped particles, allowing the creation of quantum superpositions with coherence times that exceed by far any other characteristic time in the system, with record times of up to 10 minutes [24]. The relative large distances between between the trapped ions, on the order of several micrometers, it is possible to address them individually using lasers.

The readout of the internal state of ions is generally done by measuring their fluorescence emission. This emission, depending on the used species, is in the visible or near-visible regime, and naturally occurs in all spatial directions. In order to maximize the detected emission, collimating lenses are placed close to the trap, redirecting the photons to the detection device. Alternatively, it is possible to build a resonator around the ion which modifies the mode density around it, increasing the emission probability along the resonator axis. This and other methods are discussed in Chapter 3.

Paul traps can be constructed in such a way that trapping several ions separated by few micrometers is possible. These ions, by equilibrium of the mutual Coulomb repulsion and the trapping forces, distribute themselves in crystal-like structures. Alternatively, it is possible to build miniaturized Paul traps which provide individual trapping potentials for each ion [25]. Different tools permit the creation of arbitrary quantum states along the whole crystal, including complex entangled states [26]. Whereas it is possible to trap up to tens of ions keeping individual control of each particle [27], scaling up to larger numbers of ions remains a technological challenge.

In this chapter, we review the background necessary to understand how trapping and manipulations of single atomic ions is realized.

2.2 Principles of ion trapping

2.2.1 The Paul trap

To confine a particle with charge e in a point in space using a static electric potential, we would need to have a potential with a local minimum in each spatial direction. Such a potential could be, for example, the 3D quadratic potential

$$\Phi(x, y, z) = \alpha_x x^2 + \alpha_y y^2 + \alpha_z z^2, \tag{2.1}$$

with α_x, α_y and α_z real numbers. As every electrical potential in free space with no charges, Φ must satisfy the Laplace equation $\nabla^2\Phi = 0$, which implies

$$\alpha_x + \alpha_y + \alpha_z = 0. \tag{2.2}$$

Therefore, if $\alpha_x, \alpha_y > 0$, then $\alpha_z < 0$. Thus, the Laplace equation prevents the existence of an electric potential with a minimum in each three spatial directions simultaneously. This is true not only for harmonic potentials but for any potential: every 2D minimum is a 3D saddle point, meaning that it is not possible to spatially confine a charged particle using a static electric potential. This fundamental limitation can be circumvented by using a time-varying electric potential, which is commonly known as Paul trap in honor of Wolfgang Paul, one of its inventors [28][1].

The basic idea of a Paul trap is using a time-varying potential in such a way that when, at a given time, the particle is pushed towards the 2D minimum and expelled in the third direction, the potential is rapidly inverted. In this way, the direction that previously had a maximum close-by, now has a minimum, and the particle is pulled towards it (see Fig. 2.1). Every time that the particle starts to fall out of the trap, it is pushed back to the center instants later.

Following the proposition of Paul, such a potential can be decomposed into the sum of a static part with voltage U, plus a time-dependent part, with amplitude U_{RF}, oscillating harmonically at the angular frequency Ω_{RF},

$$\begin{aligned}\Phi(x, y, z, t) &= \frac{U}{2}(\alpha_x x^2 + \alpha_y y^2 + \alpha_z z^2) \\ &\quad + \frac{U_{\mathrm{RF}}}{2}\cos(\Omega_{\mathrm{RF}} t)(\alpha'_x x^2 + \alpha'_y y^2 + \alpha'_z z^2).\end{aligned} \tag{2.3}$$

By correctly choosing the parameters in this equation is possible to observe a net confinement in three dimension, which corresponds to the average force excerted by the potential $\Phi(x, y, z, t)$ on the particle over one oscilation period $2\pi/\Omega_{\mathrm{RF}}$. The resulting trapping potential is referred to as a *pseudopotential* and can be calculated

[1] Another way is superimposing a static magnetic field, creating a so-called Penning Trap [12]

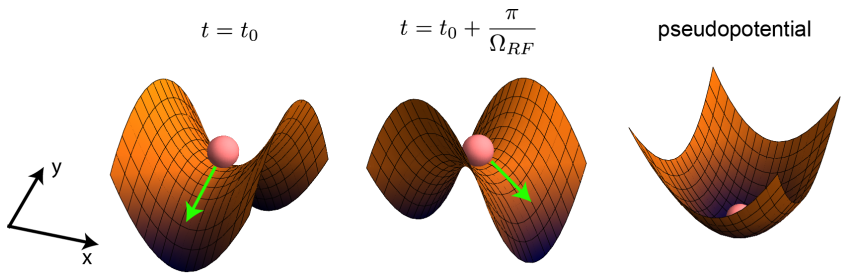

Figure 2.1: Working principle of a Paul trap. By using a time-varying electric potential it is possible to confine a particle in three dimension. The figure shows a 2D analogy, where an electric potential is harmonically varied. At $t = t_0$ the particle is confined in the x direction, but not in the y direction. Half a period later the situation is the opposite. Since the potential varies faster than the timed by the particle to scate, the particle "sees" a trapping pseudopotential.

as [29]

$$\Psi = \frac{e^2}{4M\Omega_{\mathrm{RF}}^2} \left|\nabla\Phi(x,y,z,t)\right|^2, \tag{2.4}$$

where M is the mass of the particle.

2.2.2 Equations of motion and stability

The conditions for stable trapping can be found by solving the equations of motion of the particle

$$\frac{d^2 r_i}{dt^2} = -\frac{e}{M}(\nabla\Phi)_i, \tag{2.5}$$

where r_i $(i = x, y, z)$ are the three spatial directions. Using the potential of Eq. (2.3) and defining the variables

$$\xi = \frac{\Omega_{\mathrm{RF}} t}{2}, \qquad a_i = \frac{4|e|U\alpha_i}{m\Omega_{\mathrm{RF}}^2}, \qquad q_i = \frac{2|e|U_{\mathrm{RF}}\alpha_i'}{m\Omega_{\mathrm{RF}}^2} \tag{2.6}$$

the equations of motion can be written as

$$\frac{d^2 r_i}{d\xi^2} + \left[a_i - 2q_i\cos(2\xi)\right] r_i = 0. \tag{2.7}$$

Eq. (2.7) is the homogeneous *Mathieu equation*, which has two kinds of solutions: stable solutions oscillating with frequency Ω_{RF} around a mean position, and unstable solutions with exponentially growing amplitude. a_i and q_i are the parameters which define the regions in the parameter's space (a_i, q_i) in which the solutions $r_i(t)$ of Eq. (2.7) are stable trajectories in the three spatial directions [30].

For small values $|a_i|, q_i^2 \ll 1$ the stable trajectories, in lowest-order approxima-

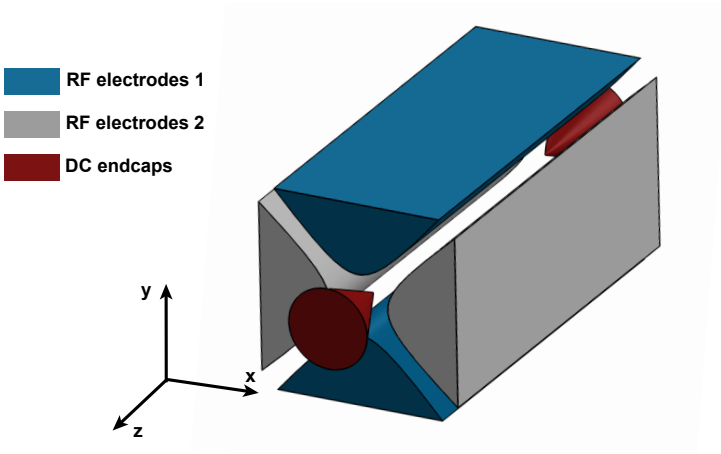

Figure 2.2: Linear Paul trap with hyperbolic electrodes. A time-varying voltage is applied to the RF electrode 1 (blue), and a dephased similar voltage to the RF electrodes 2 (blue), which provides confinement in the $x-y$ plane, whereas a DC voltage is applied to the endcaps to produce confinement along the z axis.

tion, can be described by

$$r_i(t) \approx r_i^{(0)} \underbrace{\cos(\omega_i t)}_{\text{secular motion}} \underbrace{\left(1 - \frac{q_i}{2}\cos(\Omega_{\text{RF}} t)\right)}_{\text{micromotion}}, \tag{2.8}$$

where

$$\omega_i = \beta_i \frac{\Omega_{\text{RF}}}{2}, \qquad \beta_i = \sqrt{a_i + \frac{q_i^2}{2}}. \tag{2.9}$$

The stable trajectories described in Eq. (2.8) are composed of two oscillatory parts. The first part oscillates with angular frequency $\omega_i \ll \Omega_{\text{RF}}$, for $\beta_i \ll 1$, and is referred to as *secular motion* or *macromotion*. The second part oscillates with the same frequency as the driving field, Ω_{RF}, with a reduced amplitude in comparison with the first part (by a factor $q_i/2$). This fast-oscillating part is referred to as *micromotion*.

The amplitude of the macromotion can be experimentally reduced by means of, e.g., laser cooling. If the amplitude of the micromotion is much smaller than the amplitude of the secular motion, the fast oscillating part of the trajectories can be neglected. This corresponds to a particle oscillating in the 3D harmonic pseudopotential

$$e\Psi_{seq} = \frac{1}{2} M \sum_i \omega_i^2 r_i^2. \tag{2.10}$$

2.2.3 Basic implementation

One way of creating a harmonic pseudopotential is using a set of electrodes with a hyperbolic cross section, as shown in Fig. 2.2. In this case, an RF voltage $V_1(t) = [U_{\mathrm{RF}}\cos(\Omega_{\mathrm{RF}}t) - U]/2$ is applied to the hyperbolic electrodes 1 (blue in the figure), and a π-dephased RF voltage $V_2(t) = [U - U_{\mathrm{RF}}\cos(\Omega_{\mathrm{RF}}t)]/2$ is applied to the other hyperbolic electrodes (electrodes 2, grey). The use of hyperbolic electrodes creates a quadratic electrical potential over the whole internal volume, given by

$$\phi(x,y,t) = (U - U_{\mathrm{RF}}\cos(\Omega_{\mathrm{RF}}t))\left(\frac{x^2-y^2}{2r_0^2}\right), \tag{2.11}$$

where r_0 is the semi distance between hyperbolic electrodes. The parameters a and q in the Mathieu equation take the value

$$a_x = -a_y = \frac{4eU}{mr_0^2\Omega_{\mathrm{RF}}^2}, \qquad q_x = -q_y = \frac{2eU_{\mathrm{RF}}}{mr_0^2\Omega_{\mathrm{RF}}^2}. \tag{2.12}$$

By additionally applying DC voltages to both endcaps, it is possible to create a harmonic 3D potential, as the one in Eq. (2.10). The voltage amplitudes and driving frequency Ω_{RF} which lead to stable trapping depend on the mass M and charge e of the particle. The trap's depth in the radial direction of such a trap is

$$D_i = \frac{1}{2}M\omega_i^2 r_0^2. \tag{2.13}$$

Hyperbolic electrodes provide a pseudopotential that is harmonic over the whole internal volume of the construction, but are in general difficult to fabricate and do not provide enough optical access to the trapped particle, a feature that we will show to be crucial in the following chapters. Another problem with this implementation is the difficulty of keeping the desired phase relation between different electrodes. Even small phase jitters and offsets can significantly displace the electrical center of the trap, increasing the amplitude of the micromotion of the particle. Since having a harmonic pseudopotential that covers all the volume is in most cases not necessary, but only necesarry in the region covered by the particle trajectory, these problems can be solved by using other electrode geometries. In Chapter 3 we will present the electrode configuration currently used in our experiments: a linear *Innsbruck-style* trap. In Chapter 6 we will present a new approach for the realization of a monolithic high numerical aperture ion trap, which is needed for planned quantum-electrodynamics experiments. There are many other approaches, some of which are described in Refs. [31, 32].

2.2.4 Ion crystals

It is possible to trap more than one particle in a Paul trap. The particles can achieve an equilibrium state between the confinement force due the trapping potential and their mutually repulsive Coulomb forces. This equilibrium leads to the formation of crystal-like structures. The simplest case is a linear chain of particles along the

N	$z_1^{(0)}$	$z_2^{(0)}$	$z_3^{(0)}$	$z_4^{(0)}$
1	0	–	–	–
2	$-\left(\frac{1}{2}\right)^{2/3} l$	$+\left(\frac{1}{2}\right)^{2/3} l$	–	–
3	$-\left(\frac{5}{4}\right)^{1/3} l$	0	$+\left(\frac{5}{4}\right)^{1/3} l$	–
4	$-1.44l$	$-0.45l$	$+0.45l$	$+1.44l$

Table 2.1: Equilibrium positions for a chain of up to 4 equally charged particles. The equilibrium positions shown are calculated assuming N identical particles and as a function of the characteristic length l, defined in Eq. 2.16.

axis where the weakest confinement is applied, e.g., along the $z-$axis. This occurs for trapping potentials satisfying the inequality [33, 34]

$$\frac{\omega_{x,y}}{\omega_z} > 0.77 \frac{N}{\sqrt{\ln N}}, \tag{2.14}$$

where N is the number of particles, and it is assumed that $\omega_x = \omega_y$. Such a trap can be realized, for example, using the electrode configuration of Fig. 2.2.

The charged particles "see" a potential composed by the trapping pseudopotential plus the Coulomb potential generated by each particle. Using the harmonic pseudopotential approximation of Eq. (2.10), and assuming that all the particles have the same mass (M) and charge (e), the total potential is

$$\Psi' = \frac{M}{2} \sum_{m=1}^{N} \omega_z z_m^2 + \sum_{\substack{n,m=1 \\ n \neq m}}^{N} \frac{e^2}{8\pi\epsilon_0} \frac{1}{|z_m - z_n|}, \tag{2.15}$$

where z_n is the position of the n^{th} particle and ϵ_0 is the vacuum permittivity. The equilibrium positions of each particle are the positions where the potential has its minimum. Table 2.1 shows the equilibrium positions along the $z-$axis for a trap with secular frequency ω_z and minimum at $z = 0$. The equilibrium positions are calculated as a function of the *characteristic length*, defined as [35]

$$l = \left(\frac{e^2}{4\pi\epsilon_0 M \omega_z^2} \right)^{\frac{1}{3}}. \tag{2.16}$$

It is noteworthy that for four or more trapped particles in harmonic pseudopotentials the spacing is not uniform, whereas by using anharmonic pseudopotentials it is possible to achieve uniformly spaced chains. In general, if the condition of Eq. 2.14 is not satisfied, more complicated 2D and 3D structures can be formed [36].

N	$\omega_{z,1}$	$\omega_{z,1}$	$\omega_{z,1}$	$\omega_{z,1}$
1	ω_z			
2	ω_z	$\sqrt{3}\omega_z$		
3	ω_z	$\sqrt{3}\omega_z$	$\sqrt{\frac{29}{5}}\omega_z$	
4	ω_z	$\sqrt{3}\omega_z$	$\sqrt{\frac{29}{5}}\omega_z$	$\sqrt{9.308}\omega_z$

Table 2.2: Motional modes frequencies. Frequencies of the different motional modes of a chain of N identical particles in a Harmonic potential.

2.2.5 Normal modes of oscillation

The motion of each particle in a chain of N particles can be described by $3N$ normal oscillatory modes, with N modes for each spatial direction. In this section we calculate the frequency of these modes along the chain axis z for N identical particles, but the same treatment can be applied in the other directions. Following the calculation presented in Ref. [35], the position of the n^{th} particle can be approximated as a small oscillatory motion $q_n(t)$ around its equilibrium position $z_n^{(0)}$,

$$z_n(t) = z_n^{(0)} + q_n(t). \tag{2.17}$$

The motion of the system is described by the Lagrangian

$$L = \frac{M}{2}\sum_{n=1}^{N}(\dot{q}_m)^2 - \frac{1}{2}\sum_{n,m=1}^{N} q_n q_m \left[\frac{\partial^2\psi}{\partial z_n \partial z_m}\right]_{z=z^{(0)}}, \tag{2.18}$$

where terms of order $\mathcal{O}[q_n^3]$ have been neglected. The frequencies of the normal modes can be calculated by finding the eigenvalues of the real, symmetric, positive semi-definite matrix

$$A_{nm} = \left[\frac{\partial^2\psi}{\partial z_n \partial z_m}\right]_{z=z^{(0)}}. \tag{2.19}$$

The eigenvalues μ_n are non-negative, and together with the p^{th} eigenvector $\vec{b}_m^{(p)}$ $(p = 1, 2, ..., N)$, satisfy the eigenvalue equation

$$\sum_{n=1}^{N} A_{nm}\vec{b}_n^{(p)} = \mu_p \vec{b}_m^{(p)} \quad (p = 1, 2, ..., N). \tag{2.20}$$

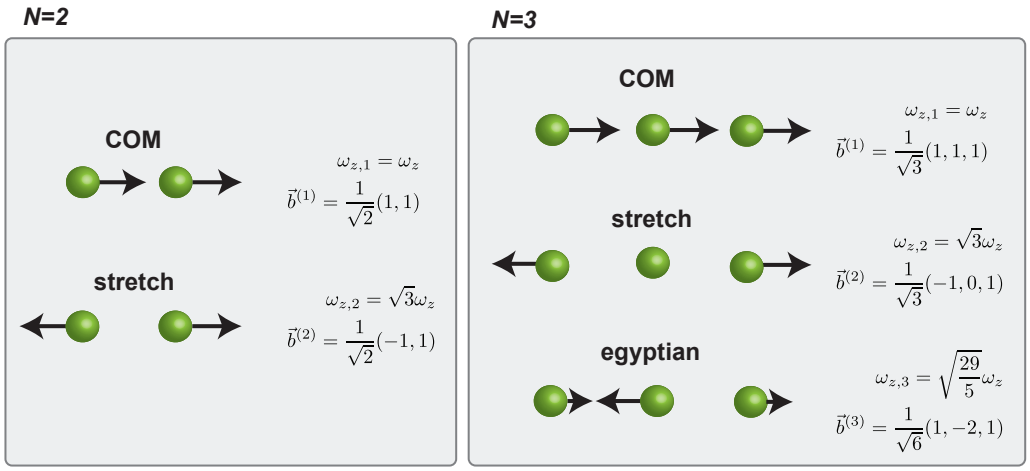

Figure 2.3: Motional eigenmodes along the chain axis. The different motional eigenmodes of a chain of $N = 2$ and 3 identical particles along the chain axis, with frequency $\omega_{z,p}$ and eigenvector $\vec{b}^{(p)}$. In the case of $N = 2$ there are two normal modes: the center of mass mode (COM) and stretch mode, whereas for $N = 3$ there are three normal modes: COM, stretch and the so-called *egyptian* or *zig-zag* mode.

Therefore, it is possible to rewrite a decoupled Lagrangian in terms of the normal modes Q_p of the system,

$$L = \frac{M}{2}\sum_{p=1}^{N}\left[\dot{Q}_p^2 - \omega_{z,p}^2 Q_p^2\right], \tag{2.21}$$

where the angular frequency of the p^{th} mode is given by

$$\omega_{z,p} = \sqrt{\mu_p}\omega_z. \tag{2.22}$$

For $N = 1, 2, 3$, the values of μ_p can be calculated analytically. Table 2.2 shows the frequencies of the normal modes up to $N = 4$ particles. Fig. 2.3 depicts the different motional modes along the $z-$axis for two and three particles.

2.2.6 Quantization of the motion

From the decoupled Lagrangian of Eq. (2.21) and using the canonical conjugate momentum of each mode $P_p = M\dot{Q}$ the Hamiltonian of the total motion in one direction can be written as

$$H = \frac{1}{2M}\sum_{p=1}^{N} P_p^2 + \frac{M}{2}\sum_{p=1}^{N}\omega_p^2 Q_p^2. \tag{2.23}$$

We have dropped the subindex z, since the expression is valid in each normal direction. From now on, the subindex represents the secular motion mode, therefore $p = 1, ..., 3N$. The quantum motion of the particles can then be described by intro-

ducing the quantum operators of motion and momentum

$$Q_p \to \hat{Q}_p = \sqrt{\frac{\hbar}{2M\omega_p}}(\hat{a}_p + \hat{a}_p^\dagger), \tag{2.24}$$

$$P_p \to \hat{P}_p = -i\sqrt{\frac{M\omega_p\hbar}{2}}(\hat{a}_p - \hat{a}_p^\dagger), \tag{2.25}$$

where the *annihilation* and *creation* operators of motional excitations are defined as

$$\hat{a}_p = \frac{1}{\sqrt{2M\omega_p\hbar}}\left(M\omega_p\hat{Q}_p + i\hat{P}_p\right), \tag{2.26}$$

$$\hat{a}_p^\dagger = \frac{1}{\sqrt{2M\omega_p\hbar}}\left(M\omega_p\hat{Q}_p - i\hat{P}_p\right), \tag{2.27}$$

respectively, and satisfy the commutation relations

$$\left[\hat{Q}_p, \hat{P}_q\right] = i\hbar\delta_p q, \qquad \left[\hat{a}_p, \hat{a}_q^\dagger\right] = \delta_{pq}. \tag{2.28}$$

Thus, it is possible to write the Hamiltonian operator as

$$\hat{H}_p = \hbar\omega_p(\hat{a}^\dagger\hat{a} + \frac{1}{2}), \tag{2.29}$$

and the Schrödinger equation

$$\hat{H}_p|\psi\rangle = E_p|\psi\rangle, \tag{2.30}$$

where E_p is the motional energy in the p^{th} mode, and $|\psi\rangle$ its motional state. This Schrödinger equation can be written as an eigenvalue equation for the operator $\hat{N}_p := \hat{a}_p^\dagger\hat{a}_p$,

$$\hat{N}_p|\psi\rangle = \left(\frac{E_p}{\hbar\omega_p} - \frac{1}{2}\right)|\psi\rangle. \tag{2.31}$$

It is easy to see that the eigenvalue of $\hat{N}_p$ is the number of motional quanta n_p, each quantum with energy $\hbar\omega_p$, in the mode p, such that $E_p/(\hbar\omega_p) - 1/2 = n_p$. The operator $\hat{N}$ is called *number operator*, since its eigenvalues correspond to the number of motional excitations (*phonons*) in a given motional mode. The eigenstates of the operator $\hat{N}_p$ are called *number* or *Fock* states, which correspond to motional states with a fixed number of excitations.

The energy of the p^{th} motional mode of a particle with n_p excitation quanta in that mode is then given by

$$E_p(n_p) = \hbar\omega_p(n_p + \frac{1}{2}). \tag{2.32}$$

From this equation it is possible to identify the so-called *vacuum energy* $\hbar\omega_p/2$. Even for a particle in its ground state ($n_p = 0$) the energy is not zero, with implications such as the existence of Casimir-Polder forces [37].

2.2.7 Extent of the motional wavepacket

Now we will derive an expression for the spatial extent of the oscillations of particles trapped in an harmonic potential. From the normalization condition of state vectors and the eigenvalues equation for the number operator,

$$\hat{N}_p|n_p\rangle = n_p|n_p\rangle, \tag{2.33}$$

where $|n_p\rangle$ are the eigenstates of the number operator, the action of the creation and annihilation operator over the states $|n_p\rangle$ is calculated to be:

$$\hat{a}_p^\dagger|n_p\rangle = \sqrt{n_p+1}|n_p+1\rangle, \tag{2.34}$$
$$\hat{a}_p|n_p\rangle = \sqrt{n_p}|n_p-1\rangle. \tag{2.35}$$

From theses equations it is clear that the action of the annihilation operator on the ground state is $\hat{a}_p|0\rangle = 0$. Replacing the definition of the annihilation operator of Eq. (2.27),

$$\hat{a}_p|0\rangle = \frac{1}{\sqrt{2M\omega_p\hbar}}\left(M\omega_p\hat{Q}_p - i\hat{P}_p\right)|0\rangle = 0; \tag{2.36}$$

which, by using the canonical definition of the momentum operator in the position representation

$$\hat{P}_p = -i\hbar\frac{\partial}{\partial Q_p} \tag{2.37}$$

leads to the differential equation

$$\left(\frac{M\omega_p}{\hbar}Q_p + \frac{\partial}{\partial Q_p}\right)\psi_0(Q_p) = 0, \tag{2.38}$$

where $\psi_0(Q_p)$ is the spatial wavepacket of the ground state of the p^{th} motional mode. The solution of this equation is a Gaussian function,

$$\psi_0(Q_p) = \mathcal{N}\exp\left(-\frac{M\omega_p}{2\hbar}Q_p\right), \tag{2.39}$$

with $\mathcal{N}$ the normalization of the Gaussian distribution,

$$\mathcal{N} = \left(\frac{M\omega_p}{\pi\hbar}\right)^{\frac{1}{4}}. \tag{2.40}$$

It is important to notice here that this spatial distribution is written as a function of the mode displacement Q_p, so the actual spatial coordinate for each particle has to be weighted with the corresponding element of the eigenvector associated with the mode. So, for example, for three particles in the ground state of the egyptian mode, the extent of the spatial distribution of the position of the particle in the center is twice the extent of the outer two (see Fig. 2.3).

From the Gaussian distribution of Eq. 2.39, we can extract its standard deviation. This standard deviation defines a characteristic length for the extent of the motional wavepacket. It also corresponds to the position uncertainty at zero energy, and is given by

$$(\Delta Q_p)_0 = \sqrt{\frac{\hbar}{2M\omega_p}}. \tag{2.41}$$

For excited motional states, the extent of the wave packet can be calculated from the variance of the position operator,

$$(\Delta Q_p)^2_{n_p} = \langle n_p|\hat{Q}_p^2|n_p\rangle - \langle n_p|\hat{Q}_p|n_p\rangle^2, \tag{2.42}$$

which yields the expression

$$(\Delta Q_p)_{n_p} = (\Delta Q_p)_0\sqrt{n_p + \frac{1}{2}} \tag{2.43}$$

$$= \sqrt{\frac{\hbar}{M\omega_p}}\sqrt{n_p + \frac{1}{2}} \tag{2.44}$$

for the characteristic length or *size* of the motional wavapacket. For one particle, this length corresponds to the amplitude of the oscillation of its center of mass, as soon as the particle is in a state with a well defined number of phonons, i.e., a Fock state of motion. This is in general not true, since the particles can be in superposition states or statistical mixed states of motion, such as a thermal state. The case of a thermal state is studied later in this thesis.

In this thesis the trapped particles considered are single atomic ions, specifically $^{138}\mathbf{Ba}^{+}$. With typical driving parameters is it possible to achieve trapping frequencies around ~ 1 MHz in each direction. By using laser cooling techniques it is possible to reduce the number of motional excitations to few phonons, or even to the ground state. In the following we describe the basics of light-matter interaction necessary to control the motional and internal state of the atoms.

2.3 Light-matter interaction

As described in the previous section, it is possible to spatially confine charged particles, and in particular, single atomic ions using Paul traps. In this section we study how light interacts with a single atom and how this interaction is used to control its internal and external quantum state.

First, we will examine the simplest case: a two-level atom interacting with a quantized field, as well as in the semi-classical limit, where we will consider the driving field to be a classical one. This model is useful to understand the basic features of the interaction, but it is just an idealization and does not give a good description for the trapped ions used in this thesis. The simplest realistic model for electronic dipole transitions of the atomic species used in this experiment ($^{138}\mathrm{Ba}^{+}$,

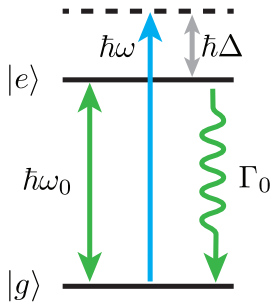

Figure 2.4: Two-level atoms. A two-level atom, with ground state $|g\rangle$ and excited state $|e\rangle$, with an energy difference between the two levels equal to $\hbar\omega_0$ and which is driven by an oscillatory field with energy per photon equal to $\hbar\omega$. The energy difference between the driving field and the atom is $\hbar\Delta = \hbar(\omega - \omega_0)$. The excited state decays spontaneously at a rate Γ_0.

as we detail in Chapter 3) is a three-level system in Λ configuration, as we present in Section 2.3.2

Furthermore, the presence of a Zeeman splitting due to external magnetic fields makes it necessary to describe the atom as an eight-level system, as we will review in Chapter 3. The three and eight-level descriptions make use of the tools presented for the two-level case, such as the optical Bloch equations, but consider every possible transition. On the other hand, in some regimes it will be possible to neglect the coupling with the rest of the atomic levels and treat the interaction between the field and atom as an effective two-level system. This happens when we drive a dipole forbidden transition with a narrow laser, where we broadly satisfy the condition $\Omega \gg \Gamma$, so that, up to a certain time scale, we can neglect the spontaneous emission. Such a narrow band laser allows us to spectroscopically resolve motional sidebands and to control the motional excitation. To study this, at the end of this chapter, we discuss the Hamiltonian which describes how motional and electronic states of the atom are coupled [38].

2.3.1 The two-level atom

The simplest model to describe the interaction between light and matter considers a single atom with two internal energy levels: ground $|g\rangle$ and excited $|e\rangle$ states, with energies E_g and E_e, respectively. The energy difference of these two levels can be written in terms of the resonant frequency of the transition ω_0, $E_e - E_g = \hbar\omega_0$. Since in this idealization there is no other state to decay to, the excited state decays only to the ground state with natural decay rate Γ_0 (see Fig. 2.4). The free Hamiltonian of the atom can be written as

$$\hat{H}_{\mathrm{A}} = \hbar\omega_0 \left(|e\rangle\langle e| - |g\rangle\langle g| \right). \tag{2.45}$$

It is convenient to define the atomic lowering and raising operators,

$$\hat{\sigma}_+ = |e\rangle\langle g|, \qquad \hat{\sigma}_- = |g\rangle\langle e| \tag{2.46}$$

and the Pauli operators

$$\hat{\sigma}_x = \frac{1}{2}\left(|e\rangle\langle g| + |g\rangle\langle e|\right), \quad \hat{\sigma}_y = i\frac{1}{2}\left(|e\rangle\langle g| - |g\rangle\langle e|\right), \quad \hat{\sigma}_z = \frac{1}{2}\left(|e\rangle\langle e| - |g\rangle\langle g|\right) \tag{2.47}$$

so that the free Hamiltonian of the two-level atoms can be rewritten as

$$\hat{H}_{\mathrm{A}} = \hbar\omega_0\hat{\sigma}_z. \tag{2.48}$$

Initially, we will consider that the electromagnetic field interacting with the atom is quantized. In this case the electric field operator can be written as [39]

$$\hat{\vec{E}}(\vec{r}) = i\sum_{\vec{k},\vec{\varepsilon}_k}\sqrt{\frac{\hbar\omega_k}{2\epsilon_0}}\left[\hat{a}_{\vec{k},\vec{\varepsilon}_k}\vec{u}_{\vec{k},\vec{\varepsilon}_k} - \hat{a}^{\dagger}_{\vec{k},\vec{\varepsilon}_k}\vec{u}^{*}_{\vec{k},\vec{\varepsilon}_k}\right], \tag{2.49}$$

where $\hat{a}_{\vec{k},\vec{\varepsilon}_k}$ and its Hermitian conjugate are annihilation and creation operators of photons in the mode with wave vector $\vec{k}$ and polarization $\vec{\varepsilon}_k$, and $\vec{u}_{\vec{k},\vec{\varepsilon}_k}(\vec{r})$ is a plane wave mode function for the corresponding mode,

$$\vec{u}_{\vec{k},\vec{\varepsilon}_k}(\vec{r}) = \frac{1}{V}\vec{\varepsilon}_k e^{i\vec{k}\cdot\vec{r}}, \tag{2.50}$$

with V the quantization volume.

If we consider the radiation interacting with the atom to be a single-mode quantized field, with frequency ω, then it can be described by the Hamiltonian

$$\hat{H}_{\mathrm{L}} = \hbar\omega\left(\hat{a}^{\dagger}\hat{a} + \frac{1}{2}\right), \tag{2.51}$$

where $\hat{a}^{\dagger}$ and $\hat{a}$ are the creation of annihilation operators of photons in the considered mode.

The simplest case to study the interaction between a two-level atom and the field is described by the so-called dipole approximation. In this approximation, as the size of the atom is much smaller that the wavelength of the field, the electric field is considered constant over the spatial extent of the atom. The action of the oscillatory field on the atom corresponds to the induction of an electric dipole due to the superposition of the different levels. The atomic dipole moment operator is then defined as

$$\hat{\vec{d}} = e\hat{\vec{r}}, \tag{2.52}$$

where e is the charge of the electron and $\hat{\vec{r}}$ is the position operator. The Coulomb potential generated by the atom's nucleus is spherically symmetrical, so that eigenstates $|e\rangle$ and $|g\rangle$ do not have a net dipole moment. The dipole moment operator can be therefore written as

$$\hat{\vec{d}} = \vec{d}_{eg}|e\rangle\langle g| + \vec{d}_{ge}|g\rangle\langle e| = \vec{d}_{eg}\hat{\sigma}_+ + \vec{d}_{ge}\hat{\sigma}_-, \tag{2.53}$$

where $\vec{d}_{eg} = \langle e|\hat{\vec{d}}|g\rangle = e\langle e|\hat{\vec{r}}|g\rangle$ (and $\vec{d}_{ge} = \vec{d}^*_{ge}$) is the off-diagonal dipole matrix element. The expectation value of the dipole operator is

$$\langle\hat{\vec{d}}\rangle = \mathrm{Tr}(\rho\hat{\vec{d}}) = \vec{d}_{eg}\rho_{eg} + \vec{d}_{ge}\rho_{ge}, \tag{2.54}$$

where ρ is the density matrix characterizing the electronic state of the atom. This expectation value depends solely on the coherence ρ_{eg} of the atom and not on the populations ρ_{ee} and ρ_{gg}.

The Hamiltonian describing the interaction between the atomic dipole and the electric field in the dipole approximation is given by

$$\hat{H}_{\mathrm{int}} = -\hat{\vec{d}}\cdot\hat{\vec{E}}(\vec{r}_0), \tag{2.55}$$

where $\vec{r}_0$ is the atom position. Replacing the $\hat{\vec{E}}$ with the expression for a single mode electric field with frequency ω, wave vector $\vec{k}$ and plane mode function $\vec{u}$, the interaction Hamiltonian is

$$\hat{H}_{\mathrm{int}} = -i\hbar\left(\hat{\sigma}_- + \hat{\sigma}_+\right)\left(\kappa\hat{a}e^{i\vec{k}\cdot\vec{r}_0} - \tilde{\kappa}\hat{a}^\dagger e^{-i\vec{k}\cdot\vec{r}_0}\right), \tag{2.56}$$

where the coupling constants κ and $\tilde{\kappa}$ are defined as

$$\kappa := \sqrt{\frac{\omega}{2\hbar\epsilon_0}}\vec{d}_{eg}\cdot\vec{u}(r_0), \qquad \tilde{\kappa} := \sqrt{\frac{\omega}{2\hbar\epsilon_0}}\vec{d}_{eg}\cdot\vec{u}^*(r_0). \tag{2.57}$$

It is convenient to write the evolution of the system in the interaction picture[2] instead of the Schrödinger picture. In the interaction picture the operators carry the time dependence instead of the state vectors. In both pictures the operators are related by a unitary transformation defined by the free Hamiltonian of the system,

$$\hat{U}(t) \;=\; \exp\left[-\frac{i}{\hbar}\left(\hat{H}_{\mathrm{A}} + \hat{H}_{\mathrm{L}}\right)t\right]. \tag{2.58}$$

Using this transformation, the atom-field interaction Hamiltonian $\hat{H}_{\mathrm{int}}$ in the interaction picture is then

$$\begin{aligned}\hat{H}_{\mathrm{I,int}} \;=\;& i\hbar\hat{\sigma}_-\left(\hat{a}^\dagger\kappa^* e^{i(\omega-\omega_0)t-i\vec{k}\cdot\vec{r}_0} - \hat{a}\tilde{\kappa}^* e^{-i(\omega+\omega_0)+i\vec{k}\cdot\vec{r}_0}\right)\\ & -i\hbar\hat{\sigma}_+\left(\hat{a}\kappa e^{-i(\omega-\omega_0)t+i\vec{k}\cdot\vec{r}_0} - \hat{a}^\dagger\tilde{\kappa}e^{i(\omega+\omega_0)-i\vec{k}\cdot\vec{r}_0}\right).\end{aligned} \tag{2.59}$$

We are here interested mostly in phenomena in the near-resonant driving regime, i.e, when the difference between the frequency of the field and the transition frequency of the atom $\Delta = \omega - \omega_0$ is small ($\Delta \ll \omega_0$). This regime sets a time scale for

[2] In the interaction picture the operators evolve following the Heisenberg equation. The equation for the evolution of quantum operators was introduced by Paul A. M. Dirac (who was known for his modesty) in 1925 [40].

the evolution of the system, given by $2\pi/\Delta$. The interaction Hamiltonian contains two kind of terms, the first, oscillating with frequency $\omega - \omega_0$, are energy conserving, i.e, terms corresponding to the creation of an atomic excitation and annihilation of a field photon ($\hat{\sigma}_+\hat{a}$) and the opposite atomic process, i.e., atomic relaxation and the creation of field photon ($\hat{\sigma}_-\hat{a}^\dagger$). The second kind of terms contains processes involving simultaneous excitation of the atom and the field ($\hat{\sigma}_+\hat{a}^\dagger$) or simultaneous annihilation ($\hat{\sigma}_-\hat{a}$). This second kind of terms oscillates much faster, with frequencies $\omega + \omega_0$, at time scales much shorter than those observed in typical atomic experiments. For example, for an optical transition with wavelength ~ 500 nm driven by a laser with detunings on the order of tens of MHz, the typical time scale for the slowly oscillating terms is on the nanoseconds scale, while for the fast oscillating terms it is on the orders of femtoseconds. So in practical terms, we can neglect the fast oscillating terms, in what is called the *rotating wave approximation*. In this approximation, the interaction Hamiltonian can be written as

$$\hat{H}_{\text{I,int}} \approx i\hbar \left(\hat{\sigma}_-\hat{a}^\dagger \kappa^* e^{i(\omega-\omega_0)t - i\vec{k}\cdot\vec{r}_0} - \hat{\sigma}_+\hat{a}\kappa e^{-i(\omega-\omega_0)t + i\vec{k}\cdot\vec{r}_0} \right). \tag{2.60}$$

By assuming that the atom is at the origin of the coordinate system, it is possible to further simplify this expression, so that the total Hamiltonian of the system back in the Schrödinger picture can by written as

$$\hat{H}_{\text{J-C}} = \frac{1}{2}\hbar\omega_0\hat{\sigma}_z + \hbar\omega(\hat{a}^\dagger\hat{a} + \frac{1}{2}) + \hbar\kappa \left(\hat{\sigma}_-\hat{a}^\dagger - \hat{\sigma}_+\hat{a} \right), \tag{2.61}$$

which is called *Jaynes-Cummings Hamiltonian* in honor of Edwin Jaynes and Fred Cummings, who proposed it in 1963. This Hamiltonian contains three terms: the free evolution of the atom, the free evolution of a single mode the field and the exchange of energy between the atom and the single mode field through the creation and annihilation of atomic excitations and photons.

Eigenstates of the interacting system

Let us consider first the free Hamiltonian $\hat{H}_{\text{free}}$ of the non-interacting field and atom, i.e.,

$$\hat{H}_{\text{free}} = \hat{H}_{\text{L}} + \hat{H}_{\text{A}}, \tag{2.62}$$

where H_{L} and H_{A} correspond to the free Hamiltonian of the light and the atom, respectively. The other part of the Jaynes-Cummings Hamiltonian is what from now on we refer to as $\hat{H}_{\text{int}}$. The states $|g\rangle|n\rangle$ and $|e\rangle|n\rangle$ are eigenstates of $\hat{H}_{\text{free}}$, $|n\rangle$ being a Fock state for the field, i.e, a field with a well-defined number of photons. Let us first discuss the case in which the atom and field are in resonance. In this case the eigenstates $|e\rangle|n\rangle$ and $|g\rangle|n+1\rangle$ are degenerate, i.e., they have the same energy $\hbar\omega_0((n+1)+1/2)$. Therefore, any superposition of this two eigenstates, i.e.,

$$\alpha|e\rangle|n\rangle + \beta|g\rangle|n+1\rangle, \qquad \text{with} \quad |\alpha|^2 + |\beta|^2 = 1, \tag{2.63}$$

is also an energy eigenstate with energy $\hbar\omega_0((n+1)+1/2)$. The eigenstates of the full Hamiltonian can be calculated from the fact that it commutes with $\hat{H}_{\text{free}}$, and

are given by the so-called *dressed states*,

$$|\Psi_n^{\pm}\rangle = \frac{1}{\sqrt{2}}\left(|e\rangle\langle n| \pm |g\rangle|n+1\rangle\right), \tag{2.64}$$

satisfying the eigenstate equation

$$\hat{H}_{\text{J-C}}|\Psi_n^{\pm}\rangle = \left(\hbar\omega_0((n+1)+1/2) \pm \hbar\kappa\sqrt{n+1}\right)|\Psi_n^{\pm}\rangle, \tag{2.65}$$

whose eigenenergies are non-degenerate.

Rabi Oscillations

The time evolution due to the atom-field interaction can be calculated as

$$\begin{aligned} |\Psi_n^{\pm}(t)\rangle &= e^{-\frac{i}{\hbar}\hat{H}_{\text{int}}t}|\Psi_n^{\pm}\rangle & (2.66)\\ &= e^{\mp i\kappa\sqrt{n+1}t}|\Psi_n^{\pm}\rangle. & (2.67)\end{aligned}$$

If we consider the initial state of the atom to be $|e\rangle$, and the initial state of the field to be $|n\rangle$, and write using the basis formed by the dressed states,

$$|\psi(t=0)\rangle = \frac{1}{\sqrt{2}}\left(|\Psi_n^{+}\rangle + |\Psi_n^{-}\rangle\right), \tag{2.68}$$

then at a time t, the state of the atom-field system is

$$|\psi(t)\rangle = \cos(\kappa\sqrt{n+1})|e\rangle|n\rangle - i\sin(\kappa\sqrt{n+1})|g\rangle|n+1\rangle. \tag{2.69}$$

The probabilities $P_e(t)$ and $P_h(t)$ of finding the atom in the excited state or in the ground state are given by

$$\begin{aligned} P_e(t) &= \cos^2(\kappa\sqrt{n+1}t) = \frac{1}{2}\left[1+\cos(\Omega_n t)\right], & (2.70)\\ P_g(t) &= \sin^2(\kappa\sqrt{n+1}t) = \frac{1}{2}\left[1+\cos(\Omega_n t)\right]. & (2.71)\end{aligned}$$

This behaviour is called Rabi oscillation or Rabi cycle, after Isidor Isaac Rabi, and corresponds to a periodic exchange of energy between the atom and the field. The frequency of the oscillation

$$\Omega_n = 2\sqrt{n+1}\kappa \tag{2.72}$$

depends on the number of photons n in the field, and it is called *quantized Rabi Frequency*.

For a small detuning $\Delta \ll \omega_0$, Rabi oscillations with the same amplitude as in the resonant case are obtained, but with a modified Rabi frequency, given by

$$\tilde{\Omega}_n = \sqrt{4(n+1)\kappa^2 + \Delta^2}. \tag{2.73}$$

Off-resonant interaction

In the case of large detuning between the driving field and the atom satisfing $\omega_0 \ll \Delta \ll \kappa$, the calculations yield the atom-field Hamiltonian [41]

$$\hat{H}_{\text{detuned}} = \frac{1}{2}(\omega_0 + \Delta) + \omega \hat{a}^\dagger \hat{a} + \frac{\kappa^2}{\Delta}\left(\hat{\sigma}_z \hat{a}^\dagger \hat{a} + |e\rangle\langle e|\right). \tag{2.74}$$

Under this Hamiltonian and applying the same treatment as in the resonant case, we get that if the initial state of the system is the atomic superposition $|\psi(t=0)\rangle = a_e|e\rangle|n\rangle + a_g|g\rangle|n\rangle$, at time t the state is given by

$$|\psi(t)\rangle = e^{-i\frac{\kappa^2}{\Delta}(n+1)t} a_e|e\rangle|n\rangle + e^{+i\frac{\kappa^2}{\Delta}(n+1)t} a_e|e\rangle|n\rangle. \tag{2.75}$$

In this case, there is no oscillation of the atomic and the field populations, but instead a linear dephasing between the excited and ground states. Other regimes of non-resonant interaction and related effects such AC-Stark shift and Autler–Townes effect are discussed in Chapter 5 of Ref. [42].

Semiclassical limit

The results described above are calculated for the case in which both the field and the atom are quantized, in particular we have assumed that the field is initially in a Fock state. This is a useful treatment when the number of photons in the field is small or in a well characterized quantum state, as in the case of an atom interacting with a single or few mode field of a cavity. In this thesis, the atom is excited with a narrow-linewidth laser beam, with continuous power on the order of 10^{-6} - 10^{-3} W, which corresponds to a field with an average of 10^{15} - 10^{16} photons per second. In the case in which the linewidth of the laser used for exciting the transition is narrower than the atomic transition linewidth, the electric field laser field is well described by the classical wave

$$\begin{aligned} \vec{E} &= \frac{1}{2}\vec{\varepsilon} E_0 \left(e^{-i\omega t} + e^{i\omega t}\right), && (2.76)\\ &= \vec{E}_0 e^{-i\omega t} + \vec{E}_0 e^{+i\omega t} && (2.77)\\ &= \vec{E}^+(t) + \vec{E}^-(t) && (2.78) \end{aligned}$$

with polarization $\vec{\varepsilon}$ and propagating along $\vec{k}$ (the spatial phase has been omitted). Note that the spatial dependence of the field has been ignored by only considering the field at the position of the atom. This is a reasonable assumption in the frame of the dipole approximation, where the wavelength of the field is considered to be much longer than the size of the atom.

From the quantum equations presented above it is possible to get the semiclassical expressions, i.e., considering a quantized atom and a classical field, by means of the substitution

$$\kappa \hat{a} \to \Omega, \tag{2.79}$$

where

$$\Omega := -\frac{2\vec{d}_{eg} \cdot \vec{E}_0^+}{\hbar} \tag{2.80}$$

is the Rabi frequency in the semiclassical limit, quantifying the coupling strength between the classical field and the atom. The atom-field Hamiltonian is then written as

$$\hat{H}_{\mathrm{SC}} = \frac{1}{2}\hbar\omega_0\hat{\sigma}_z + \hbar\left(\Omega^*\hat{\sigma}_- - \Omega\hat{\sigma}_+\right). \tag{2.81}$$

By solving the Schrödinger equation using this Hamiltonian Rabi oscillations are again found. The same results of Eq. (2.71) can be obtained using the substitution of Eq. (2.79), in which case the frequency of the Rabi cycle turns to be

$$2\sqrt{n+1}\kappa = \Omega_n \underbrace{\longrightarrow}_{\kappa\hat{a}\to\Omega} \Omega. \tag{2.82}$$

In the near-resonant limit, the Rabi frequency is given by

$$\tilde{\Omega} = \sqrt{\Omega^2 + \Delta^2}, \tag{2.83}$$

also in correspondence with the modified quantized Rabi frequency of Eq. (2.73).

From a broader point of view, a Rabi frequency quantifies the coupling between a field and a transition, independent of the nature of the transition. Up to now we have considered only transitions mediated by the induced dipole moment of the electron, but later in this thesis we will also study electric quadrupole transitions. In general any multipole-allowed transition, electric or magnetic, can be described using a Rabi frequency, the detuning between the transition and the field, and the propagation and polarization of the field.

Spontaneous emission and damping

Since spontaneous decay of the atom and emission of a photon is a stochastic, incoherent effect, it cannot be described by a Hermitian Hamiltonian as we have done here so far. However, the inclusion of this effect in the dynamics of the system can be calculated using the Lindblad master equation[3] [42]. In this approach, an additional heuristic super operator term is added to the Heisenberg equation for the evolution of the atomic density matrix, which accounts for the non-Hermitian evolution of the system, i.e, the spontaneous decay and damping due to the finite linewidth of the driving field. This equation reads

$$\frac{d\hat{\rho}}{dt} = \frac{-i}{\hbar}\left[\hat{H}, \hat{\rho}\right] + \mathcal{L}(\hat{\rho}), \tag{2.84}$$

[3]The Lindblad master equations is also known as Gorini–Kossakowski–Sudarshan–Lindblad equation

where the super operator $\mathcal{L}$ action over $\hat{\rho}$ is defined as

$$\mathcal{L}(\hat{\rho}) = -\frac{1}{2}\sum_m \left[\hat{C}_m^\dagger \hat{C}_m \hat{\rho} + \hat{\rho}\hat{C}_m^\dagger \hat{C}_m - 2\hat{C}_m \hat{\rho} \hat{C}_m^\dagger\right], \tag{2.85}$$

and the index m denotes each damping mechanism. In the case of a two-level atom, these are: the spontaneous decay to the state $|g\rangle$ from the excited state $|e\rangle$ with a decay rate Γ, which is represented by

$$\hat{C}_g = \sqrt{\Gamma}\hat{\sigma}_- = \sqrt{\Gamma}|g\rangle\langle e|; \tag{2.86}$$

and the operator describing the free evolution due to the finite linewidth δ_l of the driving field,

$$\hat{C}_l = \sqrt{\delta_l}\hat{\sigma}_{gg} = \sqrt{\delta_l}|g\rangle\langle g|. \tag{2.87}$$

Γ can be calculated as a function of the dipole moment operator elements using Fermi's Golden rule,

$$\Gamma = \frac{\omega_0^3}{3\pi\epsilon_0\hbar c^3}|\vec{d}_{eg}|^2. \tag{2.88}$$

As many of the quantities involved in the calculation oscillate in phase with the frequency of the driving field, it is helpful to write the atomic density matrix and the Hamiltonian in a co-rotating frame, i.e.,

$$\tilde{\hat{H}} = \hat{U}^\dagger \hat{H}\hat{U} - i\hbar\hat{U}^\dagger \frac{d}{dt}\hat{U}, \tag{2.89}$$

$$\tilde{\hat{\rho}} = \hat{U}^\dagger \hat{\rho}\hat{U}, \tag{2.90}$$

with $\hat{U} = e^{i\omega t\hat{\sigma}_z}$. It is worth noticing that under this transformation the atomic populations remain unchanged, i.e., $\tilde{\hat{\rho}}_{ee} = \hat{\rho}_{ee}$ and $\tilde{\hat{\rho}}_{gg} = \hat{\rho}_{gg}$.

The Lindblad master equation can be rewritten as a set of linear coupled equations for each component of the density matrix. This set of equations, in the case of a perfect single-frequency laser, i.e., $\delta_l = 0$, are given by

$$\frac{\partial}{\partial t}\hat{\rho}_{ee} = -i\frac{\Omega}{2}\left(\tilde{\hat{\rho}}_{eg} - \tilde{\hat{\rho}}_{ge}\right) - \Gamma\rho_{ee}, \tag{2.91}$$

$$\frac{\partial}{\partial t}\hat{\rho}_{gg} = i\frac{\Omega}{2}\left(\tilde{\hat{\rho}}_{eg} - \tilde{\hat{\rho}}_{ge}\right) + \Gamma\rho_{ee}, \tag{2.92}$$

$$\frac{\partial}{\partial t}\tilde{\hat{\rho}}_{ge} = -\left(\frac{\Gamma}{2} + i\Delta\right)\tilde{\hat{\rho}}_{ge} - i\frac{\Omega}{2}\left(\hat{\rho}_{ee} - \hat{\rho}_{gg}\right), \tag{2.93}$$

$$\frac{\partial}{\partial t}\tilde{\hat{\rho}}_{eg} = -\left(\frac{\Gamma}{2} - i\Delta\right)\tilde{\hat{\rho}}_{ge} + i\frac{\Omega}{2}\left(\hat{\rho}_{ee} - \hat{\rho}_{gg}\right). \tag{2.94}$$

This set of linear coupled equations is called the *Optical Bloch equations* in honor to Felix Bloch, because they are identical to the equations used to explain spin

precession in nuclear magnetic resonance systems developed by him [4].

This equation can be used for calculating, for example, the steady-state solutions, i.e., after an interaction time much longer than the decay rate such that the populations reach "equilibrium" and the changes in the density matrix elements become negligible ($\partial\hat{\rho}/\partial t \sim 0$). The steady-state solution for the population of the excited state is

$$\hat{\rho}_{ee}(t \to \infty) = \frac{\Omega^2/\Gamma^2}{1 + \left(\frac{2\Delta}{\Gamma}\right)^2 + 2\frac{\Omega^2}{\Gamma^2}} = \frac{s/2}{1+s}, \tag{2.95}$$

where we have defined the *saturation parameter*

$$s = \frac{2\Omega^2/\Gamma^2}{1 + (2\Delta/\Gamma)^2}. \tag{2.96}$$

Eq. (2.95) corresponds directly to the absorption line shape of the atom, which tells us the steady-state probability of atomic excitation as a function of the Rabi frequency, the natural decay rate and the detuning of the driving field. Note that the expression for ρ_{ee} does not depend on the initial atomic density matrix. The saturation parameter in this equation is positive, and the population of the excited state $\hat{\rho}_{ee}$ tends asymptotically to 1/2, known as saturation, as $s \to +\infty$. The population of the excited state can be expressed also as a function of the *saturation intensity*, defined as

$$\frac{I}{I_{\text{sat}}} = \frac{2\Omega^2}{\Gamma^2}, \tag{2.97}$$

and therefore,

$$\hat{\rho}_{ee}(t \to \infty) = \frac{1}{2}\frac{I/I_{\text{sat}}}{1 + \left(\frac{2\Delta}{\Gamma}\right)^2 + I/I_{\text{sat}}}. \tag{2.98}$$

The saturation intensity is related to the non-linear response of the atom to the field. For low intensities $I \ll I_{\text{sat}}$ the response of the atom is well described as a classical oscillating dipole, but for the opposite case, a quantum treatment is necessary. The saturation intensity also sets the intensity on which the atom absorption drops to half the on-resonance maximum. The explicit expression for the saturation intensity is

$$I_{\text{sat}} = \frac{c\epsilon_0\Gamma^2\hbar^2}{4|\langle g|\hat{\varepsilon}\cdot\hat{\vec{d}}|g\rangle|^2}. \tag{2.99}$$

We can differentiate two very distinct regimes, the strong-driving regime, when $I \gg I_{\text{sat}}$, in which the line shape is reduced to

$$\rho_{ee}(t \to \infty) = \frac{\Omega^2/4}{\Delta^2 + \Omega^2/2}, \tag{2.100}$$

[4] The equations in the way shown in this thesis were first derived by Tito Arecchi and Rodolfo Bonifacio in 1965 [43].

which is a Lorentzian with FWHM $\sqrt{2}\Omega$. For the opposite weakly driven case, $I \ll I_{\text{sat}}$, we find

$$\rho_{ee}(t \to \infty) = \frac{\Omega^2/4}{\Delta^2 + \Gamma^2/4}. \tag{2.101}$$

Orders of magnitude

Typically, we will drive the atom with a laser beam, with a Gaussian transverse mode, adn with a beam waist w_0 at the position of the atom. For a laser beam with power P, the intensity at the position of the atom is then

$$I = \frac{P}{\pi w_0^2}. \tag{2.102}$$

The Rabi frequency is then, for a z-oriented dipole and a parallel laser beam

$$\Omega = \sqrt{\frac{2\eta_0 |\langle g|d_z|e\rangle|^2 P}{\pi \hbar^2 w_0^2}}, \tag{2.103}$$

where $\eta_0 \approx 376.730313$ Ohm is the impedance of vacuum.

Using the Bohr approximation for Barium, and considering the "cooling" transition at 493 nm between two electronic states with principal quantum number $n = 6$, the distance between the electron and the nucleus is $\sim 10^{-11}$ m. The dipole moment is then $\sim 10^{-30}$ C·m. Without very specialized focusing optics, it is possible to achieve a laser beam waist of the order of tens of μm in the visible spectrum, so lets consider $w_0 \approx 50$ μm. Typical laser powers are around 100 μW, though much higher power can be achieved. In this regime, Rabi frequencies of around $\Omega/2\pi \sim 1$ MHz can be easily achieved. In this regime and considering a transition with Γ in the range of few tens of MHz, saturation parameters s of 10-30% can be reached.

2.3.2 The three-level atom

Up to here, we have considered a two-level atom, but to have a more accurate description of the atom-field interaction we need to introduce a more complex model that can account for decay of the excited state through other channels. The simplest realistic model for the $^{138}Ba^+$ electronic transitions used for cooling in our experiment (Chapter 3) is a three-level atom in Λ configuration (see Fig. 2.5).

In this case, we consider three distinct electronic states $|1\rangle$, $|2\rangle$ and $|3\rangle$. The transitions between the states $|1\rangle \leftrightarrow |2\rangle$ and $|2\rangle \leftrightarrow |3\rangle$ are dipole-allowed, with energies $\hbar\omega_{12(0)}$ and $\hbar\omega_{23(0)}$ respectively, while the transition $|1\rangle \leftrightarrow |3\rangle$ is dipole-forbidden. The excited state $|2\rangle$ decays spontaneously to the state $|1\rangle$ with rate Γ_{12} and to the state $|3\rangle$ with rate Γ_{23}. We consider two laser beams driving the dipole-allowed transitions, with frequencies ω_{12} and ω_{23}, and with Rabi frequencies Ω_{12} and Ω_{23}. Finally, each laser has a detuning from the atomic transitions $\Delta_{12} = \omega_{12} - \omega_{12(0)}$

and $\Delta_{23} = \omega_{23} - \omega_{23(0)}$.

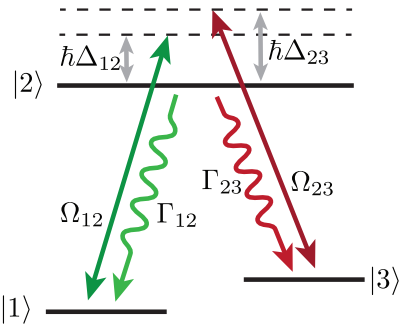

Figure 2.5: Three-level atoms in Λ configuration. A two-level atom, with two ground states $|1\rangle$ and $|3\rangle$, and one excited state $|2\rangle$, with energy difference between the ground levels and the excited state equal to $\hbar\omega_{12}$ and $\hbar\omega_{23}$ respectively. These two transitions are driven by two lasers with Rabi frequencies Ω_{12} and Ω_{23} and detunings Δ_{12} and Δ_{23}, respectively. The exited state decays with rates Γ_{12} and Γ_{23} to the ground states $|1\rangle$ and $|3\rangle$, respectively.

Following a treatment similar to the one used in the two-level atom case, and fixing the energy of the state $|1\rangle$ as the zero energy, the free Hamiltonian for the atom is given by

$$\hat{H}_{\mathrm{A}} = \hbar\left(|2\rangle\langle 2| + |3\rangle\langle 3|\right). \tag{2.104}$$

The interaction Hamiltonian in the semiclassical dipole rotating-wave approximation, is given by

$$\hat{H}_{\mathrm{int}} = \hbar\left(\Omega_{12}^{*}|1\rangle\langle 2| - \Omega_{12}|2\rangle\langle 1|\right) + \hbar\left(\Omega_{23}^{*}|3\rangle\langle 2| - \Omega_{23}|2\rangle\langle 3|\right). \tag{2.105}$$

To include damping and spontaneous decay using the Lindblad master equation, we consider the following operators,

$$\hat{C}_{21} = \sqrt{\Gamma_{12}}|1\rangle\langle 2|, \tag{2.106}$$
$$\hat{C}_{23} = \sqrt{\Gamma_{23}}|3\rangle\langle 2|, \tag{2.107}$$
$$\hat{C}_{11} = \sqrt{\delta_{11}}|1\rangle\langle 1|, \tag{2.108}$$
$$\hat{C}_{33} = \sqrt{\delta_{33}}|3\rangle\langle 3|, \tag{2.109}$$

where δ_{12} and δ_{23} are the linewidth of the respective driving lasers.

Coherent population trapping

As we vary the intensity, the detuning and the direction of the laser beams, several features appear when observing the spectroscopic signal, which are related with the steady state solution for the population of the excited state ρ_{22}. One of the most notorious features in three-level systems are the so-called *dark resonances*. In the three-level atom case, this corresponds to the situation with the detuning of both lasers is the same with respect to the state $|2\rangle$, i.e., $\Delta = \Delta_{12} - \Delta_{13} = 0$, called *Raman resonance*. Δ is called *two-photon detuning*. To study this phenomenon it is

convenient to define the state vectors

$$|g_+\rangle = \frac{1}{\sqrt{\Omega_{12}^2+\Omega_{23}^2}}\left(\Omega_{12}^2|1\rangle+\Omega_{23}^2|3\rangle\right) = \cos\theta|1\rangle+\sin\theta|3\rangle \quad (2.110)$$

$$|g_-\rangle = \frac{1}{\sqrt{\Omega_{12}^2+\Omega_{23}^2}}\left(-\Omega_{23}^2|1\rangle+\Omega_{12}^2|3\rangle\right) = -\sin\theta|1\rangle+\cos\theta|3\rangle, \quad (2.111)$$

with $\tan\theta = \Omega_{23}/\Omega_{12}$. The free atomic Hamiltonian can be rewritten as

$$\hat{H}_{\mathrm{A}} = \hbar\Delta_+|g_+\rangle\langle g_+| + \hbar\Delta_-|g_-\rangle\langle g_-| + \hbar\Omega_g\left(|g_+\rangle\langle g_-| + |g_-\rangle\langle g_+|\right), \quad (2.112)$$

with the definitions

$$\Delta_+ = \cos^2(\theta)\Delta_{12} + \sin^2(\theta)\Delta_{23}, \quad (2.113)$$

$$\Delta_- = -\sin^2(\theta)\Delta_{12} + \cos^2(\theta)\Delta_{23}, \quad (2.114)$$

$$\Omega_g = (\Delta_{23}-\Delta_{12})\sin\theta\cos\theta = (\Delta_{23}-\Delta_{12})\frac{\Omega_{12}\Omega_{23}}{\Omega_{12}^3+\Omega_{23}^2}. \quad (2.115)$$

Ω_g represents the coupling between $|g_-\rangle$ and $|g_+\rangle$. The interaction Hamiltonian can also be rewritten as

$$\hat{H}_{\mathrm{int}} = \frac{\hbar}{2}\sqrt{\Omega_{12}^2+\Omega_{23}^2}\left(\tilde{\sigma}_+ + \tilde{\sigma}_+^\dagger\right), \quad (2.116)$$

where $\tilde{\sigma}_\pm = |g_\pm\rangle\langle 2|$. Note that in this interaction Hamiltonian there is no coupling term between $|g_-\rangle$ and $|2\rangle$, and the coupling between $|g_+\rangle$ and $|2\rangle$ is $\Omega_+ = \sqrt{\Omega_{12}^2+\Omega_{23}^2}$. If we additionally set $\Delta = 0$, the coupling term in the free atomic Hamiltonian vanishes, and the state $|g_-\rangle$ is totally decoupled from the rest of the states. This phenomenon is called *coherent population trapping*: if the atom is initially in the state $|g_-\rangle$, it will remain there, without populating the excited state $|2\rangle$, so that there is no emission (or absorption) by the atom. For this reason $|g_-\rangle$ is often called *dark state*.

The written Hamiltonian represents a new effective Hamiltonian for the basis of atomic states $|g_-\rangle, |g_+\rangle$ and $|2\rangle$. If we now introduce spontaneous emission in this model through the Lindblad master equation, in this new basis, we get the same equation of motion as presented before, with effective decay rates from $|2\rangle$ to $|g_+\rangle$ and $|g_-\rangle$

$$\Gamma_+ = \cos^2\theta\Gamma_{12} + \sin^2\theta\Gamma_{23}, \quad (2.117)$$

$$\Gamma_- = \sin^2\theta\Gamma_{12} + \cos^2\theta\Gamma_{23}, \quad (2.118)$$

respectively. Also, an additional term accounting for asymmetric decay appears in the master equation, namely

$$(\Gamma_{23}-\Gamma_{12})\sin\theta\cos\theta\left(\tilde{\sigma}_-\tilde{\hat{\rho}}\tilde{\sigma}_+^\dagger + \tilde{\sigma}_+\tilde{\hat{\rho}}\tilde{\sigma}_-^\dagger\right). \quad (2.119)$$

Therefore, there is still spontaneous decay to both $|g_\pm\rangle$ states, but only pumping from $|g_+\rangle$ to $|2\rangle$. This means that after some time the population is trapped in $|g_-\rangle$, independent of the initial population distribution. This is a manifestation of

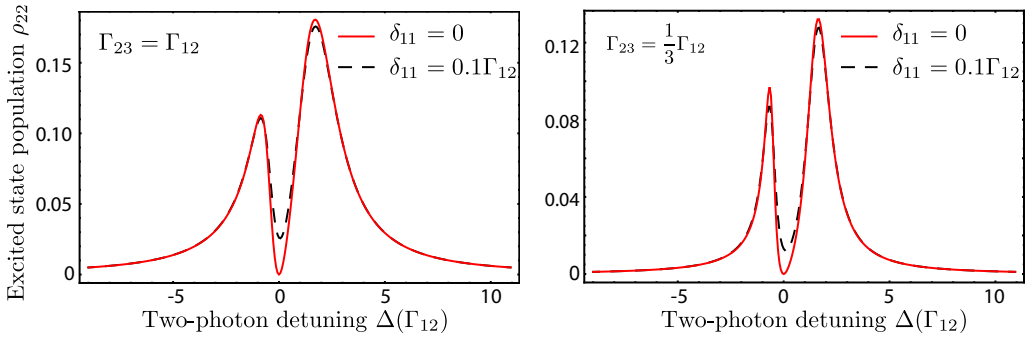

Figure 2.6: Three-level atom dark resonances. Different spectra (population of the excited state) for a three-level atom with driving Rabi frequencies $\Omega_{12} = 2\Gamma_{12}$, $\Omega_{23} = \Gamma_{12}$, detuning $\Delta_{12} = -\Gamma$. The depth of dark resonance (coherent population trapping) depends on the linewidth δ_{11} of the driving laser in the $|1\rangle \rightarrow |2\rangle$. δ_{33} is set equal to zero. The overall shape of the spectra depends also in the ratio between the spontaneous decay rates Γ_{12} and Γ_{23}.

coherence, or quantum interference, between the two ground states.

Fig. 2.6 show the numerically calculated spectrum of the fluorescence of a three-level atoms for different laser linewidths and Rabi frequencies. When the two-photon detuning Δ is zero, the population of the excited state is zero for the the case of an ideally narrow laser ($\delta_{11} = 0$) and small for the case of a laser with finite linewidth ($\delta_{11} \neq 0$). These dips are the dark resonances and correspond to the phenomenon of total or partial coherent population trapping in the state $|g_-\rangle$.

The three-level model here presented is in many cases a good approximation to describe the overall dynamics of the field-atom interaction. As we will see in the next chapter, the basic level scheme of $^{138}Ba^+$ corresponds to a three-level atom Λ configuration, but in the presence of a magnetic fields these levels split into sublevels due to *Zeeman splitting*, which makes it necessary to describe the atom as an eight-level system.

2.3.3 Coupling of motional and electronic states

The simple models for light-atom coupling presented so far neglect the fact that the atoms are moving. In the case of cold ionized atoms confined in Paul traps this motion is harmonic and quantized. To include the effect of the motion, we start by adding a term corresponding to a quantized harmonic oscillator, as in Eq. (2.29) to the free Hamiltonian of the atom. For simplicity, we consider only two atomic levels $|g\rangle$ and $|e\rangle$ and the motion to be along the $x-$axis, with a mode frequency ω_x, so that the free Hamiltonian of the atom is

$$\hat{H}_{\mathrm{A}} = \hbar\omega_0\hat{\sigma}_z + \hbar\omega_x\left(\hat{a}^\dagger\hat{a} + \frac{1}{2}\right), \tag{2.120}$$

where $\hbar\omega_0$ is the energy difference between $|e\rangle$ and $|g\rangle$, $\hat{a}^\dagger$ and $\hat{a}$ represent in this case the creation and annihilation of a phonon. The interaction between the electronic

state and the quantized motion is similar to the one with a quantized electromagnetic field described above, so that the interaction Hamiltonian can be written as

$$\hat{H}_{\text{int,motion}} = \frac{1}{2}\hbar\Omega\left(\hat{\sigma}_+\hat{\sigma}_-\right)\left(e^{i(k\hat{x}-\omega t+\phi)} + e^{-i(k\hat{x}-\omega t+\phi)}\right) \tag{2.121}$$

where k and ω are the wavenumber and the angular frequency of the driving laser field, respectively, $\hat{x}$ is the position operator of the atom within the harmonic trap, ϕ is the phase of the field at the position of the atom and Ω is the Rabi frequency quantifying the strength of the coupling, calculated below. Now we introduce the so-called *Lamb-Dicke* parameter along the x-direction, defined as

$$\eta_x = k\cos\alpha\sqrt{\frac{\hbar}{2M\omega_x}}, \tag{2.122}$$

where α is the angle between the oscillation axis and the propagation of the laser beam, M is the mass of the atom. We will consider that the laser beam is parallel to the oscillation axis ($\alpha = 0$). By using this definition and the definition of the position operator of Eq. (2.24), and by applying the rotating wave approximation (RWA) described in Section 2.3.1, the interaction Hamiltonian can be rewritten in the interaction picture as

$$\hat{H}_{\text{int,motion}} = \frac{\hbar}{2}\Omega\left(e^{i\eta(\hat{a}+\hat{a}^\dagger)}\hat{\sigma}_+e^{-i\Delta t} + e^{-i\eta(\hat{a}+\hat{a}^\dagger)}\hat{\sigma}_-e^{i\Delta t}\right), \tag{2.123}$$

with $\Delta = \omega - \omega_0$. This Hamiltonian shows coupling between the electronic states of the atomic motion. The energy for the electronic excitation of the atom can come jointly from the laser beam and a phonon, as long as this satisfies the conservation of energy. The opposite process is also possible: a transition from the excited state to the ground state releasing a quantum of energy $\hbar\omega_0$, which can be a photon with this energy, or a less energetic photon plus a phonon. This is made clear by applying the Lamb-Dicke approximation, i.e., assuming $\eta^2(2n+1) \ll 1$, where n is the average motional occupation number. In this regime the recoil energy of an emitted photon is much smaller than the energy separation between the motional levels, the extent of the motion is much smaller than the wavelength of the transition and the probability of transitions involving two photons are neglected. The accuracy of the approximation is discussed in [35].

By applying an additional rotating wave approximation, depending on the laser detuning Δ the interaction Hamiltonian is reduced to three distinct cases [38]:

- $\Delta = 0$,

$$\hat{H}_{\text{C}} = \hbar\Omega(\hat{\sigma}_+e^{i\phi} + \hat{\sigma}_-e^{-i\phi}). \tag{2.124}$$

  In this case the laser field drives the transition $|g\rangle|n\rangle \leftrightarrow |e\rangle|n\rangle$, where the motional state of the atom $|n\rangle$ is not changed. It is called the *carrier transition*. This transition has a Rabi frequency Ω (see Fig. 2.7).

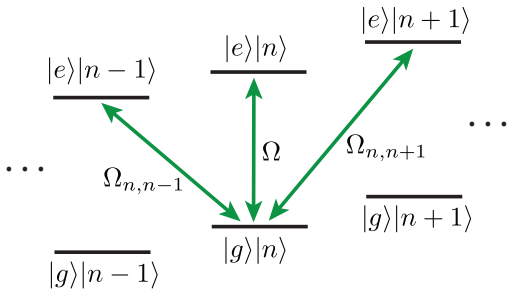

Figure 2.7: Coupling between motional states. Depending on the detuning of the driving beam, different transitions coupling electronic and motional states of the atoms are achievable: carrier transitions with Rabi frequency Ω, blue sideband transitions with Rabi frequency $\Omega_{n,n+1}$ and red sideband transitions with Rabi frequency $\Omega_{n,n-1}$

- $\Delta = \omega_x$,

$$\hat{H}_{\mathrm{BS}} = \hbar\Omega(\hat{\sigma}_+\hat{a}^\dagger e^{i\phi} - \hat{\sigma}_-\hat{a}e^{-i\phi}). \tag{2.125}$$

In this case the laser field drives the transition $|g\rangle|n\rangle \leftrightarrow |e\rangle|n+1\rangle$, exciting the atom, and increasing the number of phonons by one unit. This transition is called the *first blue sidebeand transition*, and its Rabi frequency is

$$\Omega_{n,n+1} = \Omega\sqrt{n+1}\eta \tag{2.126}$$

- $\Delta = -\omega_x$,

$$\hat{H}_{\mathrm{RS}} = \hbar\Omega(\hat{\sigma}_+\hat{a}e^{i\phi} - \hat{\sigma}_-\hat{a}^\dagger e^{-i\phi}). \tag{2.127}$$

In this case the laser field drives the transition $|g\rangle|n\rangle \leftrightarrow |e\rangle|n-1\rangle$, exciting the atom, and decreasing the number of phonons by one unit. This transition is called the *first red sideband transition*, and its Rabi frequency is

$$\Omega_{n,n-1} = \Omega\sqrt{n}\eta \tag{2.128}$$

In general, this model also predicts the existence of higher order sideband transitions, including multi-phonon creation and annihilation processes. However, the strengths of these transitions decrease in powers of η as the number of phonons exchanged increases. The value of the Rabi frequency for a transition with laser detuning $\Delta = m\omega_x$ (with m integer) is calculated, for example, in Ref. [35].

The red sideband transitions reduce the number of motional excitations while electronically exciting the atom. This gives hints about this process being useful to systematically reduce the motion of the atoms. This process is called *sideband cooling* and is used in systems of trapped ions to reduce the motion to its ground state [44, 45].

2.3.4 Laser cooling

Many decoherence effects can be drastically reduced by decreasing the motion of the atom, i.e., by *cooling* it. As the model predicts, this is possible using lasers, provided that, on average the emitted photons carry more momentum than the absorbed ones. The presented model for electronic-motional coupling still ignores the existence of other electronic states besides $|g\rangle$ and $|e\rangle$ and assumes that the linewidth of the laser is narrow enough such that it is possible to address a single transition (carrier or sideband). But it also assumes that the sidebands are spectrally separated from the carrier and from each other, i.e., that the frequency of the motion is higher than the transition linewidth, or $\omega \gg \Gamma$. Based on this assumption, to address the problem of laser cooling of atomic ions in Paul traps subject of harmonic motion we need to distinguish the treatment in two cases:

- $\omega_x \ll \Gamma$, *unresolved sidebands / weak trapping limit.* In this case the spacing between the sidebands ω_x is much smaller than the linewidth of the considered transition, so that it is not possible to resolve them in the spectrum. The absorption and emission of a photon occurs much faster than the velocity change of the trapped atom due to the harmonic confinement. Effectively, this can be described as a standing atom interacting with a laser that changes its frequency harmonically due to the Doppler shift. The cooling mechanism is termed in this case *Doppler cooling*. For atomic ions in Paul Traps, the oscillatory motion has frequencies ranging from hundreds of kHz to several MHz, Doppler cooling is achievable in dipole-allowed transitions, with Γ on the order of tens of MHz.
- $\omega_x \gg \Gamma$, *resolved sidebands / strong trapping limit.* In this case the spacing between sidebands is much larger than the absorption line of the transition, such that a narrow-linewidth laser can be tuned to specific sidebands. Therefore, sideband transitions can be systematically driven to reduce the motional amplitude of the atom. This regime is achievable using dipole-forbidden transitions, such as electric quadrupole transitions, with Γ on the order of Hz or mHz.

In the experiments presented in this thesis, Doppler cooling is performed routinely, whereas sideband cooling was not used, though it has been implemented in our setup [46]. Other schemes for cooling such as Raman cooling [47], EIT cooling [48] and polarization gradient cooling [49] have been implemented in trapped ions systems, but for the purpose of this thesis, we will just describe the principle of Doppler cooling.

Doppler Cooling

Now, we present a basic description of Doppler cooling in an ion trap in which the effect of micromotion is neglected. We consider, for simplicity, a motional mode along the $x-$axis. As the motion of an atomic ion in a Paul trap is harmonic in each mode, its velocity (in the classical approximation) is proportional to $v = v_0 \cos(\omega_x t)$,

where ω_x is the frequency of a given motional mode along the $x-$axis. As the radiative decays occurs much faster than the oscillation period, the change in velocity due to a single absorption-emission cycle in negligible, so that the cooling process can be modelled as a velocity-dependent continuous force. If we consider the laser field to be red-detuned and parallel to the motional mode, each absorption event gives a momentum kick $\Delta p = \hbar k$ to the atom, in the direction of propagation of the laser (with k the wavenumber of the laser). Consequently, the field exerts a radiation pressure to the atom, given by

$$\frac{dp}{dt} = F_a = \hbar k \Gamma \rho_{ee}, \tag{2.129}$$

where Γ is the decay rate of the excited state and ρ_{ee} is the population of the excited state, which from Eq. (2.95) is

$$\hat{\rho}_{ee} = \frac{\Omega^2/\Gamma^2}{1 + \left(\frac{2\Delta_{\text{eff}}}{\Gamma}\right)^2 + 2\frac{\Omega^2}{\Gamma^2}}. \tag{2.130}$$

The effective detuning $\Delta_{\text{eff}} = \Delta - \vec{k} \cdot \vec{v}$ corresponds to the detuning of the laser plus the Doppler shift. The cooling rate, averaged over many oscillations is $\dot{E}_c = \langle F_a v \rangle$.

As the emission is spontaneous and it has a center-symmetric distribution, it leads to a zero average momentum transfer, but causes a random walk in momentum space, proportional to p^2. Therefore, spontaneous emission contributes as a heating mechanism, with rate

$$\dot{E}_h = \frac{1}{M}\frac{d}{dt}\langle p^2 \rangle \approx \frac{1}{2M}\Gamma \hat{\rho}_{ee}(v = 0), \tag{2.131}$$

where it has been assumed that the velocity of the atoms is small and that the emission is uncorrelated. Equilibrium of both rates leads to an expression for the lowest achievable temperature [44]

$$k_{\text{B}}T = \frac{1}{16}\hbar \left[\left(1 + \frac{\Omega^2}{\Gamma^2}\right)\Gamma^2 + 4\Delta^2\right](1 + \xi) \tag{2.132}$$

where k_{B} is the Boltzmann constant, and ξ is a parameter quantifying the anisotropy of the spontaneous emission. For an isotropic emitters $\xi = 1$, whereas for a linear dipole oriented along the motion axis $\xi = 2/5$ [44]. A rough estimation of the average phononic occupation can be computed as $k_B T = n\hbar\omega_x$. In the low intensity limit ($\Omega \ll \Gamma$), for an isotropic emitter the minimum temperature is achieved for the detuning

$$\Delta_{\text{D}} = -\frac{1}{2}\Gamma, \tag{2.133}$$

corresponding to the energy

$$k_B T_{\text{D}} = \frac{1}{2}\hbar\Gamma, \tag{2.134}$$

and in general

$$k_B T_{\mathrm{D}} = \frac{1}{4}\hbar\Gamma(1+\xi). \tag{2.135}$$

The actual steady-state temperature depends on the detuning of the laser, its intensity, its orientation with respect to the axis of motion, and the orientation of the transition dipole with respect to the laser propagation direction. An advantage of using Doppler cooling is the ability to cool several motional modes simultaneously, by having a laser beam with a propagation direction that overlaps with each motional mode, though the final temperature in each mode is in general different. For most quantum optics experiments the temperatures achieved with Doppler cooling are low enough, so no additional cooling stages are necessary. This is not the case for quantum computation, where sideband cooling or other schemes are applied to reach the motional ground state in order to avoid motional decoherence.

As we will see in the next chapter, the dipole transitions used for Doppler cooling are not cyclic transitions, so that a second *repumper* laser is needed to repopulate the excited state. To estimate the actual final temperature it is necessary to introduce an effective decay rate $\Gamma_{\mathrm{eff}} = \Gamma_1 + \Gamma_2$, accounting for the two possible decay channels.

2.4 Summary

In this chapter we reviewed the principles of ion trapping using Paul traps. A general framework to study the motion of the ions trapped in harmonic potential was presented, including the effects of trapping several ions simultaneously. Additionally, we studied the theory describing the interaction of single atoms with coherent electromagnetic fields. This theoretical framework will be used to control the behaviour of the atoms and their emission fields in the performed experiments. Although some of the concepts presented in this chapter were developed by assuming electric-dipole transitions, the treatment in terms of Rabi frequencies and saturation parameters is similar for any kind of electronic transitions, including electric-quadrupole transitions and magnetic-dipole transitions, as we will apply in the next chapter.

3 The Barium Experiment

In this chapter, the experimental setup used to trap and control single $^{138}Ba^{+}$ ions is described, including the trap, the laser system and the detections schemes. The main component of the setup is a linear "Innsbruck style" Paul trap, in which several ions can be trapped simultaneously. The light emitted by the ions is collected by two high-numerical-aperture, low-aberration lenses, closely located at the sides of the trap. These lenses allow a high collection efficiency of the emitted photons, high optical resolution and small wavefront aberrations. The combination of these features is crucial for the experiments presented in Chapters 4 and 5.

Additionally, we spectroscopically characterize the different electronic transitions used in the experiments. In particular, we study the main features of the two qubit transitions used in different parts of this thesis: the electric-quadrupole optical transition and the magnetic-dipole RF transition.

3.1 Introduction: Why Barium?

Several ion species are used in quantum optics and quantum information processing experiments. The criteria for selecting the species include fundamental limitations, such as the existence of short-lived transitions, which are adequate to perform laser cooling, or technical limitations such the availability of adequate lasers sources at the required wavelengths and high-efficiency detectors at the emission wavelengths. Another important criterion is the existence of long-lived states that can be used as one of the states of a qubit. The presence of nuclear spin is in some cases desirable, since it provides hyperfine structure which is advantageous for the realization of magnetically insensitive qubits.

The mass of the selected species has a direct influence on how efficiently the atom can be laser cooled and how fast the atom heats up due to environmental conditions. The mass also has a direct impact on the time needed to perform high-fidelity quantum logic operations between different ions, since they are typically performed using their motional coupling.

Species	Cooling wavelength (nm)	Optical qubit	Nuclear spin
$^{9}Be^{+}$	313	–	3/2
$^{24}Mg^{+}$	279	–	0
$^{25}Mg^{+}$	279	–	5/2
$^{40}Ca^{+}$	397	at 729 nm	0
$^{43}Ca^{+}$	397	at 729 nm	7/2
$^{87}Sr^{+}$	422	at 674 nm	9/2
$^{88}Sr^{+}$	422	at 674 nm	0
$^{137}Ba^{+}$	493	at 1761 nm	3/2
$^{138}Ba^{+}$	493	at 1761 nm	0
$^{171}Yb^{+}$	370	–	1/2
$^{174}Yb^{+}$	370	–	0
$^{202}Hg^{+}$	194.2	at 282 nm	0

Table 3.1: Singly-ionized atomic species typically used in quantum optics experiments

Natural candidates for quantum optics experiments are stable elements in the second group of the periodic table (alkaline earth metals), although this is not a requisite (transition metals such as Hg and lanthanoids such as Yb are also used). Since the elements of the second group have two electrons in the outer shell when neutral, there is only one electron remaining after singly ionizing them. These hydrogen-like ions have simple electronic states structures, which reduces the complexity of their control.

Table 3.1 lists some of the species often used in quantum optics and quantum information processing. Ca^{+}, Ba^{+} and Sr^{+} have dipole-forbidden transitions between S and D states, with excited state lifetimes of $\approx$ 1 s, 26 s and 0.3 s, respectively [35, 50], which can be driven with commercially available lasers. These transitions are used as qubits, since decoherence due to spontaneous decay is low for typical experimental time scales. Additionally, high-fidelity read-out of the qubit state is achievable in this transitions by using the electron-shelving technic, as we explain later in this chapter. In other species without a direct optical qubit transition, such as Be^{+} or Yb^{+}, a qubit is realized by coupling different fine- or hyperfine-split ground states, and driving the transitions using microwaves or coherent Raman pulses [51, 52].

Since we deal with the detection of single photons in the experiments described in this thesis, it is important to detect them efficiently. For Ba^{+}, we typically detect the photons emitted by the fast-decaying cooling transition at 493 nm, at which the detection efficiency with commercial room-temperature detectors ($\sim$70%)is slightly higher than those for Ca^{+} ($\sim$40% at 397 nm) or Sr^{+} ($\sim$60% at 422 nm)[1].

The high detection efficiencies make Ba^{+} adequate for quantum optical experiments performed in this thesis, where the isotope $^{138}Ba^{+}$, with natural abundance of 71.7% is used due to its simple internal structure, although other isotopes such as $^{137}Ba^{+}$ (abundance 11.3 %) have been proved useful for quantum computation or fundamental quantum theory tests [53–55]. The main limitation posed by Ba^{+}

[1] as reference, see Laser Components Blue Series avalanche photodiodes

is its high mass. The coupling between motion and internal state scales with the Lamb-Dicke parameter η (see Eq. (2.122)), which is proportional to $1/\sqrt{M}$, with M the mass of the ions. Therefore, the high mass of Ba^+ makes the time needed to achieve ground state cooling and to perform motional-based logic gates much longer than for other species, such $^{40}Ca^+$. Additionally, the high mass limits the achievable trapping frequencies.

3.2 The Barium ion

3.2.1 $^{138}Ba^+$ electronic structure

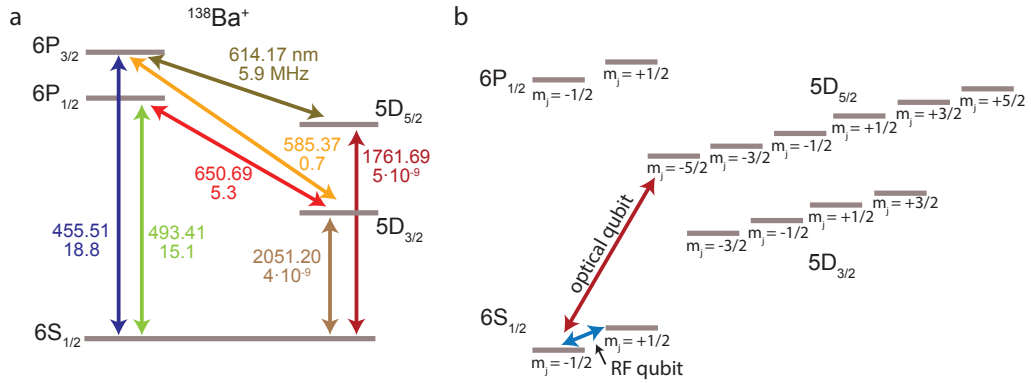

Figure 3.1: $^{138}Ba^+$ relevant electronic transitions. a. States of the outer electron relevant for this thesis. The vacuum wavelength for each transition in nm (upper number) and the decay rate $\Gamma/2\pi$ in MHz (bottom number) are shown [56–58]. **b.** Zeeman splitting of the $6S_{1/2}$, $6P_{1/2}$, $5D_{3/2}$ and $5D_{5/2}$ manifolds. The Landé factors are not taken into account in the scheme. The optical and RF qubit transitions described in Section 3.4.2 and 3.4.3 are highlighted.

The electronic configuration of $^{138}Ba^+$ is the same as for Xenon, with an additional electron. The configuration of the relevant electronic states is shown in Fig. 3.1a. All of the shown transitions can be driven with commercially available lasers. The wavelengths in the visible spectrum can be achieved with diode lasers or through second harmonic generation from infra-red diode lasers. The wavelengths 1761 nm and 2051 nm are typically achieved within doped fiber lasers, or within optical-parametric-oscillator (OPO) lasers. Recently diode lasers have become available for these wavelengths.

In our experiment, Doppler cooling and detection is performed using the 493 nm transition between the ground state $6S_{1/2}$ and the fast-decaying excited state $6P_{1/2}$ (from now on, the "cooling transition"). The excited state $6P_{1/2}$ spontaneously decays to the ground state with decay rate $\Gamma_c/2\pi = 15.1$ MHz, emitting a 493 nm photon, or to the metastable state $5D_{3/2}$ with decay rate $\Gamma_r = 5.3$ MHz, emitting a ∼650 nm photon. Thus, the probability of direct decay to the ground state is ≈ 0.74. The metastable state $5D_{3/2}$ has a lifetime of ≈ 18 s, and therefore, to achieve efficient cooling, it is necessary to pump out the population of this state

using a laser at 650 nm. Both lasers need to drive the ion simultaneously in order to achieve a closed cycle and continuously emit photons.

Electronic levels connected by both the 2051 nm and the 1762 nm transitions can be used as optical qubits. Both of them have lifetimes of tens of seconds, namely ≈ 17.5 s and ≈ 47 s, respectively [57–59]. In order to have a high fidelity qubit state read out, it is necessary to have one of the two states involved decoupled from the transitions used for detection, a technique know as electron shelving. As the state detection is done using the states connected by the 493 nm and 650 nm transitions, the 1762 nm transition is used as an optical qubit, whose excited metastable state $5D_{5/2}$ is decoupled from the detection transitions. This excited state is long lived, and therefore, a laser driving the 614 nm transition is also needed in order to repopulate the ground state in reasonable times, when necessary.

3.2.2 Zeeman spliting

In our experiments, we apply a weak magnetic field at the position of the ions to define a quantization axis. This magnetic field splits the energy levels of states with angular momenta $\vec{J} = \vec{L} + \vec{S}$, where $\vec{L}$ is the orbital angular momentum and $\vec{S}$ the electron spin, resulting in $2J + 1$ non-degenerate sublevels. This effect is known as *Zeeman-splitting*[2]. The Zeeman substates are described with the magnetic quantum number m_j, which takes the values $m_j = -J, -J+1, ..., J-1, J$. In the weak magnetic field approximation, the energy shift due to Zeeman splitting is given by

$$\Delta E_j = \mu_B m_j g_j |\vec{B}|, \tag{3.1}$$

where μ_B is the Bohr magneton and g_j is the Landé factor, that can be calculated as [42]

$$g_j = g_L \frac{j(j+1) + l(l+1) - j(j+1)}{2j(j+1)} + g_S \frac{j(j+1) - l(l+1) - s(s+1)}{2j(j+1)}, \tag{3.2}$$

with $g_L = 1$ and $g_S \approx 2$ the electron orbital and the spin gyromagnetic ratio, respectively. Fig. 3.1b shows the split states in the $6S_{1/2}$, $6S_{3/2}$ and $5S_{5/2}$ manifolds.

In our case, s corresponds to the electron spin, $s = 1/2$. The total orbital angular momentum for the S, P and D states are $l = 0$, 1 and 2 respectively, in $\hbar$ units. Therefore, the Landé factors are 2, 2/3, 4/3, 4/5 and 6/5 for the $6S_{1/2}$, $6P_{1/2}$, $6P_{3/2}$, $5D_{3/2}$ and $5D_{5/2}$ respectively.

Transitions from a state with magnetic quantum number m_i to a state with magnetic quantum number m_f implies a change of $\hbar\Delta m = \hbar(m_f - m_i)$ in the total angular momentum of the atom. Since the total angular momentum of the field-atom system is conserved, the difference in angular momentum must be present in the field. Therefore, to drive a transition with, e.g., $\Delta m = +1$ (a σ^+–transition), we use a laser beam circular-right polarized about the quantization axis (the magnetic field), which contains the necessary angular momentum in polarization. The

[2] After Pieter Zeeman, who discovered it in 1987 when studing the effects of magnetic fields in the spectra of different substances [60].

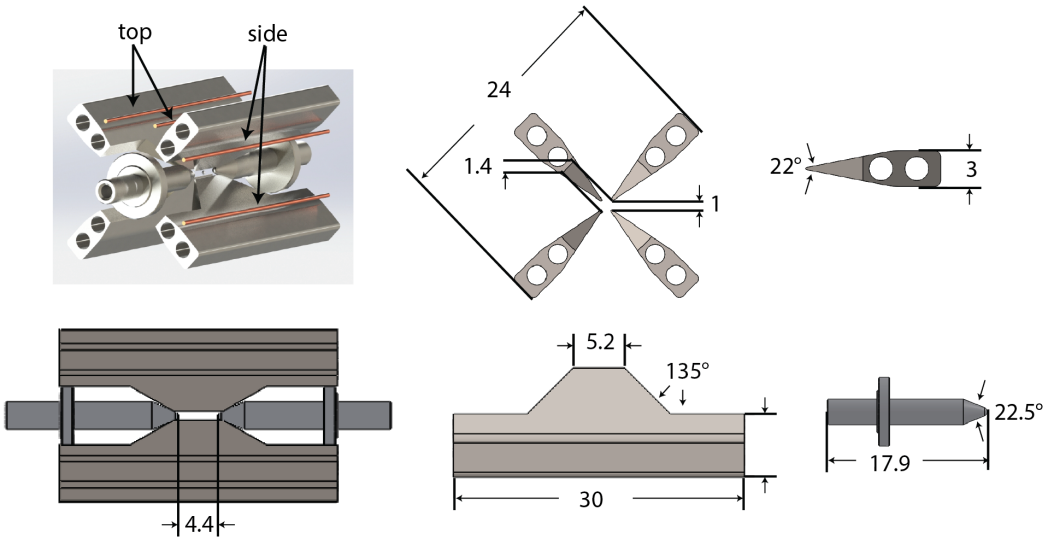

Figure 3.2: Barium's linear Paul trap. Scheme with the dimensions of the linear Paul trap used for the experiments presented in this thesis, all the distances are in mm. The location of the compensation electrodes "top" and "side" is displayed.

same occurs during spontaneous emission, the emitted photon carries the angular momentum corresponding to the change of atomic angular momentum $\hbar\Delta m$ during the transition. Transitions with $\Delta m = 0$ (a π-transition) do not change the angular momentum of the atom.

3.3 The Ba^+ trapping and control apparatus

The experiments presented in this thesis are perfomormed using an "Innsbruck style" linear Paul trap specially designed for Ba^+. This trap is composed of four blade electrodes, two opposite electrodes carry an in-phase RF voltage, while the other two are grounded, thus providing the radial pseudo-potential confinement. Axial confinement is provided by two end-caps, which are supplied with equal DC voltages. The trap geometry is shown in Fig. 3.2, including the relevant dimensions. For a more detailed description and design considerations see Chapter 4 in Ref. [61].

Ideally, in the described electrode configuration, the minimum of the pseudo-potential and the sadle point of the DC potential coincide, but in reality they can be displaced due to errors in the fabrication and assembly of the electrodes, or due the presence of stray electric fields. As a consequence, the trapped ions will not necessarily be located in the minimum of the RF pseudo-potential and the micromotion will not be at its minimum. For this reason, additional compensation electrodes are located around the main electrodes (Copper colored wires in Fig. 3.2), to which DC voltages are applied. Residual axial micromotion, if present, can be reduced by offsetting one of the end-caps with respect to the other. As the stray fields can vary over time, the DC voltages necessary for compensation of the micromotion must be adjusted from time to time. There are several methods to perform this compensation [62]. In Sec. 3.5 we show the method used in our experiment.

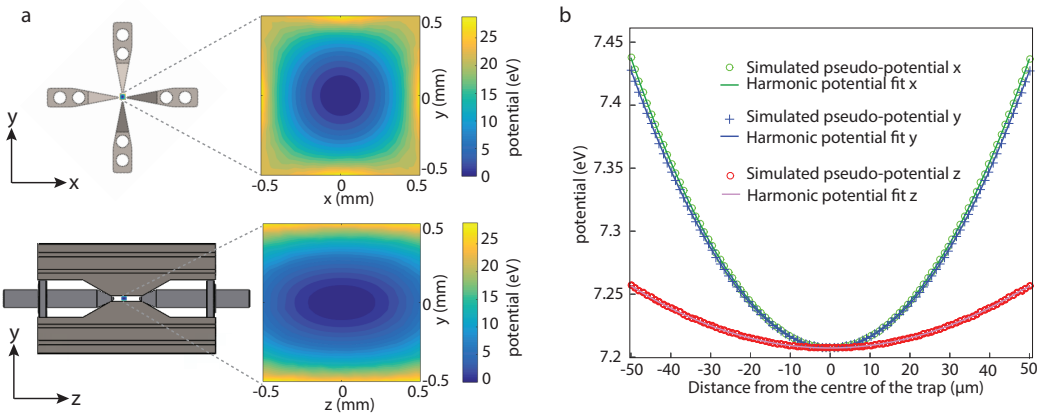

Figure 3.3: Barium's linear Paul trap potential a Cuts at $z = 0$ and $x = 0$ of the finite-elements simulated trapping potential. The simulations were done using COMSOL Multiphysics® 4.4. and with the parameters shown in Table 3.2 for one ion. The normal motional modes of the trapped ions follow the plotted axes. **b** x, y and z trapping potentials about the center of the trap. The three of them are very well fitted by quadratic potentials. Note that the coordinate reference system used here corresponds to the directions of the normal motional modes of the ions.

The trapping frequencies of a linear Paul trap can be roughly calculated using the approximations [35]

$$\omega_{x,y} \approx \frac{1}{\sqrt{2}} \frac{|e|^2 U_{\mathrm{RF}}}{M r_0 \Omega_{\mathrm{RF}}}, \tag{3.3}$$

$$\omega_z \approx \sqrt{\frac{2\kappa |e| U_{\mathrm{cap}}}{M z_0^2}} \tag{3.4}$$

where $r_0 = 0.7$ mm is the half distance between opposite blades, $z_0 = 2.2$ mm is the half distance between the end-caps, $M \approx 2.28 \cdot 10^{-25}$ kg is the mass of $^{138}Ba^+$, U_{cap} is the voltage applied to the end-caps, U_{RF} is the amplitude of the RF voltage applied to the blades, Ω_{RF} is the angular frequency of the applied RF voltage, and κ is a geometrical parameter. This geometrical parameter can be extracted from measurements or from electric field simulations. Four our trap it is estimated from measurements to be $\kappa \approx 0.112$ [61].

The simulated trapping potential achieved with typical driving configurations is shown in Fig. 3.3b, where the overlap with an harmonic potential around the center of the trap is depicted. Table 3.2 shows the voltages and frequencies used in this thesis, for experiments with one or two Ba^+ ions. The RF voltage is produced by an RF signal generator[3], then amplified[4] and stepped-up using a helical resonator [63]. The DC voltages are generated directly using a low-noise DC voltage supply[5].

[3] Rhode & Schwartz SML01
[4] 43 dB gain, Mini-Circuits LZY-1
[5] ISEG EHQ 8040p
[6] The two radial frequencies are actually slightly different, namely 1.81 and 1.78 MHz, and 1.48 and 1.52 MHz, respectively

	1 ion config.	**2 ions config.**
RF freq. $\Omega_{\mathrm{RF}}/2\pi$ (MHz)	15.1	15.1
RF amplitude U_{RF}(V)	1400	1100
End-caps voltage (V)	1000	400
"Top" electrodes voltage (V)	260	1290
"Side" electrodes voltage (V)	200	600
Radial frequency $\omega_{y,x}/2\pi$ [6](MHz)	1.8	1.5
Axial frequency $\omega_z/2\pi$ (MHz)	0.9	0.6
Trap depth (eV)	27	22
q	0.44	0.35

Table 3.2: Electrode voltages and trap frequencies. The listed trapping frequencies are measured with sideband spectroscopy (see Section 3.4.2). The trap depths are estimated via COMSOL simulations. "Top" and "side" electrodes are compensation electrodes.

3.3.1 Vacuum vessel

The trap is located at the center of an octagonal vacuum chamber (Fig. 3.4), with twelve viewports providing optical access: eight CF-63-sized on the side, one CF-160 on the base and three CF-16 on the top flange (see Fig. 3.4). All theses viewports have an anti-reflective coating for all the used light wavelengths.

The vacuum is maintained at the 10^{-11} mbar level by continuously pumping with an ion-getter pump[7]. This pump, a Titanium sublimation pump, a Bayard-Alpert vacuum gauge, and a valve, are connected to a six-way cross attached to the octagon. All the electrical connections are made through feedthroughs in the top vacuum flange (not displayed in Fig. 3.4).

Three pairs of magnetic field coils are attached on six octagon flanges in order to produce a stable and uniform magnetic field at the position of the ions. The three pairs configuration, one pair per axis (partially shown in Fig. 3.4), allows the control of the direction and intensity of the magnetic field.

3.3.2 Light collection

In the experiments presented in this thesis, it is crucial to achieve collection and detection efficiencies of the photons emitted by the trapped ions as high as possible. Furthermore, in experiments involving interference of photons emitted by one or different ions, such as the experiment presented in Chapter 4, the efficient collection of photons in a single spatial mode, e.g., defined by a single mode fiber, is required.

There are several approaches for the collection of the emitted photons. Some of them include:

- Use lenses to collimate the emission and direct it to a detector, as done in this

[7]Varian Vaclon plus 20 StarCell

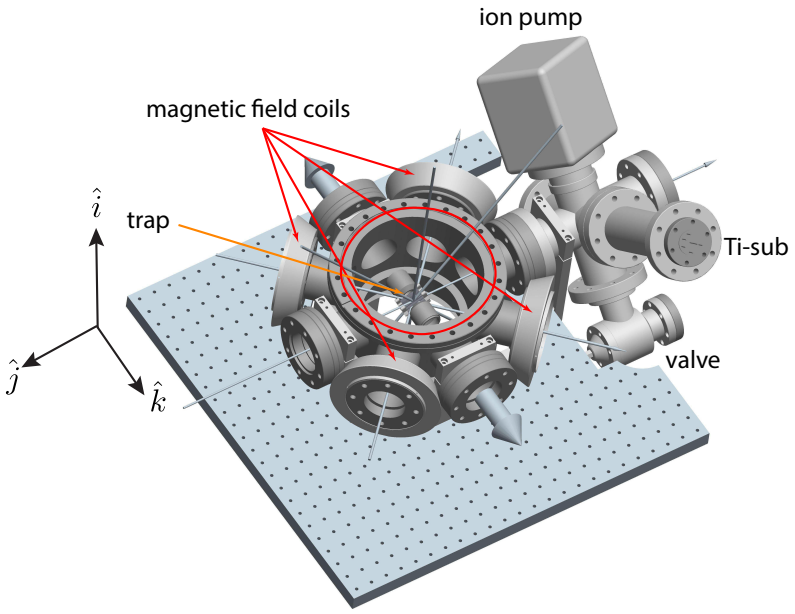

Figure 3.4: Vacuum vessel. The main chamber and the 6-ways cross are shown. The ion getter pump, the Titanium-sublimation pump (Ti-sub), a vacuum valve and a pressure gauge are located in the cross, while the main chamber contains the trap, the collection optics and the ovens. The gryy lines show all the possible axes providing optical access to the center of the trap. Magnetic field coils, pointed with red arrows and red circle, are attached to the exterior to provide a uniform magnetic field. There is an additional, not-displayed coil at the bottom side of the vacuum chamber. Rendered by D. Rotter.

thesis [64].

- Couple the emission to a resonant mode of a Fabry-Perot resonator and then couple its output mode to a detector [65].
- Collimate the emission using a parabolic mirror with focus at the position of the ion [66] and direct it to a detector.
- Collimate the emission using diffractive optical elements and couple it to a detector [67].
- Couple the emission to the guided field of an optical fiber or other waveguides and then couple it to a detector [68, 69].
- Directly locate photon-detectors close to the atom [70].
- Couple the emission to the evanescent mode of, e.g., an optical fiber [71] [8].

Approaches such as direct coupling to an optical cavity can provide high light collection, but the spatial properties of the emission are mapped into the mode of

[8] The successful coupling between the field of a charged atom and the evanescent field of an optical fiber has not been reported, although, some important advances have been made, see https://quantumoptics.at/en/research/nanofiber.html

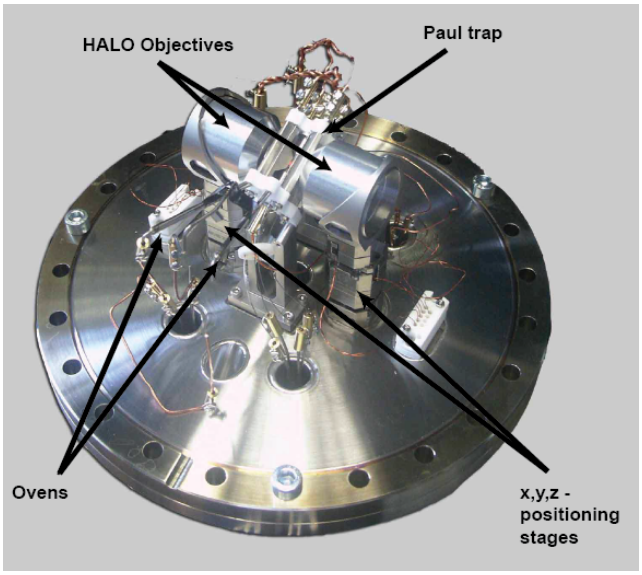

Figure 3.5: Linear Paul trap and collection setup. Two high numerical aperture objectives (HALOs) for collection of the emitted light are mounted in x, y, z-possitioning stages at the sides of the linear Paul trap. The trap axis z is tilted 22.5° with respect to the horizontal plane, and the x and y axes are rotated 45° in order to provide optical access through the front and back viewports of the vacuum chamber. A neutral-Ba oven dispenser is located close to the trap. All the necessary electrical connections are made through the electrical feedthrough in the displayed flange. The displayed flange is the top flange of the vacuum chamber, so that all the components here shown are indeed upside down. Photograph by D. Rotter.

the cavity, and are therefore lost. In our setup, the collection of the light is done by placing two high numerical aperture laser objectives (HALO) close to the ions, which has been demonstrated to be very versatile for quantum optics experiments due the multiple achievable detection configurations (see Fig. 3.6 and Ref. [64]). The crucial advantage of this approach in the context of this thesis is that the spatial properties of the spontaneous emission are preserved, and can be imaged using additional optics in, e.g., a CCD-camera, as we prove in Chapter 5. Additionally, the collection systems allows us to efficiently couple the collected light into single mode fiber (mode overlap $> 80\%$).

The HALOs[9] are located at each horizontal side of the ion trap, as shown in Fig. 3.5. Each HALO has an NA $= 0.4$, focal length 25 mm and wavefront distortion $< \lambda/10$ at $\lambda = 493$ nm [10]. Each one covers 4% of the solid angle and is mounted on xyz slip-stick piezo translation stages allowing precise positioning and alignment[11]. The viewports on the detection axis also have a low wavefront distortion $< \lambda/10$. This last feature is necessary for the interference and imaging experiments presented in Chapters 4 and 5.

[9] Linos, cutomized four non-cemented elements lens objective
[10] For a more detailed description of the custom-designed HALO objectives see Ref. [72]
[11] Attocube xyz-positioners, ANPxyz 100, which are currently inoperative.

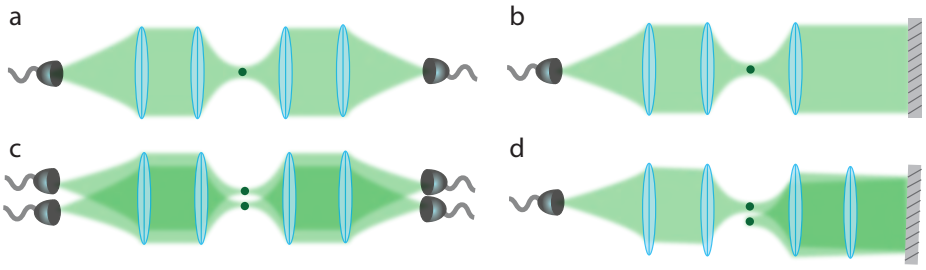

Figure 3.6: Detection configurations. The detection through a pair of high resolution lenses close to the ions allows several configurations. **a.** Each lens, plus additional out-of-vacuum focusing lenses, is used independently to collect the light emitted in opposite directions. **b.** The light emitted in the right direction is back-reflected to the atom. The fields that initially were emitted in opposite directions are superimposed, allowing for interference experiments. **c.** The field emitted by two different ions can be partially collected and directed to separate detectors, with negligible crosstalk. **d.** The emission of one ion can be superimposed with the emission of a second ion. This configuration allows interference experiments between the emission of different ions.

Collection efficiency

The light collection efficiency achievable using lenses is given by the overlap of the spatial distribution of the emission and the solid angle covered by the lens. The numerical aperture NA of axial-symmetric lens is defined as

$$\mathrm{NA} = n \sin\theta, \tag{3.5}$$

where θ is the half-aperture angle, and n is the refraction index of the surrounding medium, $n = 1$ in our case (vacuum). The corresponding solid angle collected by such a lens is given by $\Omega = 2\pi(1 - \cos\theta)$.

In this thesis we will deal with the detection of the spontaneously emitted photons by transitions where the angular momentum of the atom about the quantization axis is not changed, i.e., a π–transition ($\Delta m = 0$), or where the angular momentum of the atom is changed by one quantum, i.e., a $\sigma^{\pm}$–transition ($\Delta m = \pm 1$). The spatial intensity distribution of the emitted photons for each of these transitions corresponds, respectively, to that of a linear or a circular dipole, i.e., [73]

$$I_{\pi}(\Theta) = \frac{3}{8\pi}\sin^2\Theta, \tag{3.6}$$

$$I_{\sigma^{\pm}}(\Theta) = \frac{3}{16\pi}(1 + \cos^2\Theta), \tag{3.7}$$

where Θ is the polar angle with respect to the quantization axis defining the direction of observation. The portion of the emission collected by a lens with half-aperture θ and optical axis along the direction given by a particular angle Θ is then calculated

as [74]

$$C_{\pi}(\Theta,\theta) = \frac{1}{8}\left(4-3\cos\theta-\cos^3\theta+3\left[\cos^3\theta-\cos\theta\right]\cos^2\Theta\right), \quad (3.8)$$

$$C_{\sigma^{\pm}}(\Theta,\theta) = \frac{1}{128}\left(3\left[\cos 2\Theta-21\right]\cos\theta-\left[3\cos 2\theta+1\right]\cos 3\theta+64\right). \quad (3.9)$$

In our experiments the quantization axis is defined by the magnetic field produced by the coils outside of the vacuum chamber. The current in the coils is tuned to achieve a uniform magnetic field around the trap center, oriented horizontally as shown in Fig. 3.8. The angle between the quantization axis and the detection axis ($\hat{j}$ in Fig. 3.8) is then 90°, which together with the NA = 0.4, yields a collection of

$$C_{\pi}(\pi/2,\arcsin 0.4) \approx 6.0\%, \quad (3.10)$$

$$C_{\sigma^{\pm}}(\pi/2,\arcsin 0.4) \approx 3.5\% \quad (3.11)$$

for each lens. Therefore, combining the two HALOs, it is possible to detect up to 12% of the light emitted by a π transition and 7% of the light emitted by a $\sigma^{\pm}$ transition.

The efficiency of this approach is limited mostly by technical constraints, such as the maximum achievable NA or the optical clearance provided by the electrodes of the trap. Another difficulty is that, even though higher NA lenses and electrodes configurations with full clearance can be realized, locating dielectric materials close to the charged atoms (e.g., the surface of a lens) can dramatically distort the trapping potential. In Chapter 6 we discuss how a new light-collection approach based on a spherical mirror, a high-NA spherical lens (NA = 0.7) and a pseudo-planar electrode configuration can be used to drastically increase the collection efficiency.

Light detection

Depending on the experiment, we detect the light collected by the HALOs with single-photon detector modules (APDs) and/or CCD-cameras. The detectors used in this thesis and their main features are listed here:

- **APD Count-20B-FC, Laser Components**
  - Quantum efficiency at 493 nm ≈ 70 %
  - Dark count rate ≈ 10 counts/s
  - Dead time ≈ 60 ns
  - Connector for fiber coupling

  There are two of these single-photon detector modules available in our laboratory. Typically, the light collected by the HALOs is coupled to single-mode fibers, which are then connected to these detectors. The single-mode fibers coupling, plus additional polarization and wavelength filters, allows the detection in a single optical mode, enabling the realization of experiments that require high-visibility interference of the emitted fields. This is crucial in inteference experiments such as the one presented in Chapter 4. These detectors can be

operated in gated-mode with detection windows shorter than 100 ns and set in Hanbury Brown–Twiss configuration in order to measure short time-scale correlation functions. In this configuration, and given the low dark-counts rate, we have been able to measure the lowest coincidence rate in an atomic photon source, namely $g^2(0) = (1.9 \pm 2) \cdot 10^{-3}$, without background subtraction, nor post-selection [75].

The output electrical pulses of the detectors are counted using several devices. The main photon-counting device[12] features two identical, synchronized but independent, input channels, with time-tagging resolution of 4 ps, plus four additional channels for marking and triggering.

We also use the two detectors in a configuration similar to the one shown in Fig. 3.6c, but using only one of the HALOs. This configuration allows fast discrimination of the state of each ion, counting the number of photons detected in a given time by each ion in separate detectors.

The maximum end-to-end detection efficiency achieved using both APDs, single-mode fiber-coupled and both HALOs, is 3 %, mostly limited by the NA of the HALOs and mode-matching into the fibers.

- **Electron-multiplying CCD-camera Andor iXon DU-897: Low noise**
  - Quantum efficiency at 493 nm $\approx 95\,\%$
  - Active pixels: 512 × 512
  - Pixel size: 16 μm × 16 μm
  - Dark current: 0.001 electrons/pixel/s at -85 °C
  - Maximum read-out speed: 10 MHz/pixel
  - Linear absolute electron multiplier gain: 1-1000×
  - Minimum effective read-out noise at maximum gain: < 0.1 electron

  By focussing the light collected with the HALOs it is possible to image the trapped ions. Given the resolution of the optical system and the camera it is possible to distinguish multiple ions, typically separated by 3 to 8 μm, with negligible overlap. Fig. 3.7 shows a chain of six ions imaged while emitting fluorescence. The low-noise features of this camera allows to detect light at the single-photon level. These noise features are a consequence of the low sensor temperature. The typical CCD-sensor operating temperature, under air-cooling only, is −60 °C, but −85 °C can be achieved when low gains are set. Lower temperatures (down to 100 °C), and therefore lower noise level, can be achieved with water cooling.

- **Electron-multiplying CCD-camera Andor Luca DL-604M-OEM: Small pixels**
  - Quantum efficiency at 493 nm $\approx 52\,\%$
  - Active pixels: 1004 × 1002
  - Pixel size: 8 μm × 8 μm
  - Dark current: 0.17 electrons/pixel/s at -20 °C

[12] PicoQuant PicoHarp 300

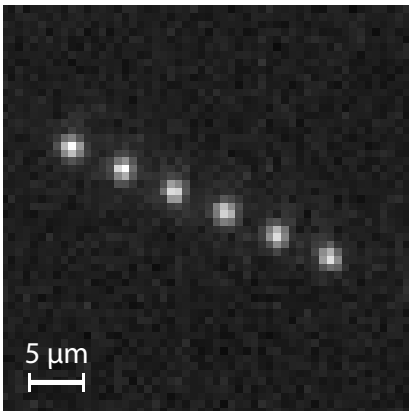

Figure 3.7: Trapped $^{138}Ba^{+}$ imaged with a CCD camera. A chain of six $^{138}Ba^{+}$ ions along the trap axis. The trap axis is tilted 22.5° with respect to the horizontal plane of the laboratory.

  - Maximum read-out speed: 13.5 MHz/pixel
  - Linear absolute electron multiplier gain: 1-1000×

The smaller pixel size of this camera, in comparison with the iXon camera, allows the acquisition of higher-resolution images. We use it mostly for the precise calibration of the magnification of the optical detection system (see Chapter 5).

- **Intensified CCD-camera Andor iStar DH334T-18U-63: Fast gating**
  - Quantum efficiency at 493 nm ≈ 50%[13]
  - Active pixels: 1024 × 1024
  - Pixel size: 13 μm × 13 μm
  - Dark current: 0.25 electrons/pixel/s at -30°C
  - Maximum relative gain: 349×
  - Maximum read-out speed: 5 MHz/pixel
  - Minimum optical gate width: 4.2 ns (rising time 0.15 ns)
  - Maximum gating repetition rate: 500 kHz
  - Resolution limit: 30 μm

The main feature of this intensified CCD-camera[14] is that the intensifier can be gated extremely fast. This becomes useful, as we will see in Chapter 5, when we need tp synchronize the opening of the intensifier with a laser pulse triggering the emission of a single photon by the ion, and keep it open only the time necessary for the arrival of the photon in the detector. This allows capturing images only with specially prepared photons. The short gating times also allow the direct tracking of the micro- and secular motion of the ion in the trap. This camera, in comparison with the others, features the worst nominal resolution (30 μm), more than twice the pixel size[15]. However, this is not a

[13] Photo-cathode Gen 3, HVS

[14] A description of the functioning principle of the camera can be found in http://www.andor.com/learning-academy/intensified-ccd-cameras-the-technology-behind-iccds

[15] The resolution is limited by the gap and the bore size of the microchannel plate

limitation for the experiments in this thesis, where we mostly use this camera to estimate the centroid of the ion images. We also note that the phosphor (type P43) used in the fluorescent screen of this camera has a decay time of 2 ms to 10% fluorescence intensity, which can limit the maximum repetition rate in some scenarios.

3.3.3 Laser system

As mentioned above, our laboratory is equipped with the lasers needed to drive the $^{138}Ba^+$ ion transitions at 493 nm, 650 nm, 1762 nm and 614 nm. Additionally, a laser at 413 nm is used to photo-ionize neutral Barium. The axes used to access the ions are shown in Section 3.3.3. The wavelenghts of all these lasers are monitored using wavemeters[16], and in the following, we describe the laser sources and locking schemes used in each case.

- **493 nm**. This laser light is generated by a Toptica TA-SHG Pro system. A master diode laser at 986 nm is amplified using a tapered-amplifier, and subsequently converted to 493 nm using a non-linear crystal in a bow-tie optical resonator. The output power at 493.4 nm is 300 mW. The master laser at 986 nm is locked to an optical cavity, with a finesse of about 1200, using the Pound-Drever-Hall (PDH) scheme [76]. A small portion (1 mW) of the 493 nm light is frequency shifted and used for Modulation-transfer-spectroscopy of Te_2 in a hot cell ($\sim 700\,^\circ$C) [77]. Since Te_2 has a bright transition only ~ 500 MHz away from the 493 nm Ba^+ transition, the spectroscopic signal is used as feedback to lock the length of the cavity to which the master laser is locked. The bandwidth of the laser after locking is estimated by dark-resonances spectroscopy of the Barium ion to be $\delta_g/2\pi \approx 100$ kHz.

  The output of the stabilized laser at 493 nm is divided into six different beams. Each light beam can be frequency-shifted and blocked independently by using free-space AOMs. The beams are coupled via single-mode optical fibers to the trap setup where the polarization is carefully adjusted. The laser radiations are used for:

  - A close-to-resonance beam, vertically polarized, is used as the main cooling beam.
  - A close-to-resonance beam, left-circularly-polarized is used to drive the $\Delta m = -1$ transition, for optical pumping and fast excitation.
  - A close-to-resonance beam, right-circularly-polarized beam is used to drive the $\Delta m = +1$ transition, for optical pumping and fast excitation.
  - A ~ 100 MHz blue-detuned beam, right-circularly-polarized is used to drive the $\Delta m = -1$ transition and is planned to be used as pump beam for EIT-cooling, in a scheme similar to the one shown in Ref. [78].
  - A ~ 100 MHz blue-detuned beam, horizontally-polarized is used to drive the $\Delta m = 0$ transition and is planned to be used as probe beam for EIT-cooling.

[16] A HighFinesse WS/7 for 986 nm, 650 nm and 413 nm, and a Bristol 671 for 1228 nm and 1762 nm.

  - A close-to-resonance beam is used coupled in the same fiber as the 650 nm repumper and the photo-ionization beams, in order to easily load ions in the trap.

  The power of these beams can be adjusted from microwatts to a maximum power of several milliwatts, and switched at a speed of tens of nanoseconds.

- **650 nm.** This laser light is generated by a Toptica DL pro system, with an output power of ≈ 30 mW. The frequency is locked to an optical cavity with a finesse of about 5000 using the PDH scheme. The linewidth of the laser after locking is $\delta_r/2\pi \approx 100$ kHz, estimated by dark-resonances spectroscopy of a trapped ion. The output of the laser is coupled to a double-pass AOM and divided in three main beams, which are then coupled into single-mode fibers. These three beams are:

  - The main repumper beam. This beam enters the chamber with vertical polarization, superimposed with the 493 nm cooling beam.
  - Loading beam. This beam is coupled into a single mode fiber together with 493 nm and 413 nm beams to provide easy loading of ions in the trap.
  - Fast-pulsed beam. This beam is coupled to a fiber-integrated amplitude modulator[17] after the AOM. This modulator can generate laser pulses with rise time of ≈ 2 ns and up to 30 mW power. These capabilities are not used in this thesis.

- **1762 nm**. This laser light is produced by a Koheras Adjustik Thulium doped fiber laser system. The output power is 50 mW, but since the laser defectively emits in two different modes with a frequency difference of about 70 MHz and orthogonal polarizations, we filter out half of the emitted power. The wavelength of the used mode is locked to an optical cavity with finesse $\mathcal{F} \approx 193000$ using the PDH scheme. Details about the feedback scheme used can be found in Ref. [46]. The linewidth of the laser after locking has been estimated by spectroscopic measurements on the ion to be ≈ 630 Hz [79]. After passing it through an AOM for fine frequency tuning and switching, it is polarization filtered and coupled into a single-mode fiber. Finally, there are 2 mW of power available at the position of the ions, with tunable polarization and focusing, allowing efficient addressing of single ions and different Zeeman transitions.

  Due to the limited available power and intensity stability issues, this laser is going to be replaced by a customized Toptica diode system and a fiber amplifier.

- **614 nm**. This laser light is produced by a Toptica DL-SHG system. A master diode laser at 1228 nm is frequency-doubled using a non-linear crystal in a bow-tie optical resonator. The master laser can be locked to an optical cavity using the PDH scheme, although during all the experiments discussed in this thesis it was free-running, and the wavelength was monitored using a wavemeter. The output power is 1 mW. After coupling it to an AOM and a single-mode fiber, there are 300 μW available at the trap setup.

[17] Jenoptic AM660 fiber EOM

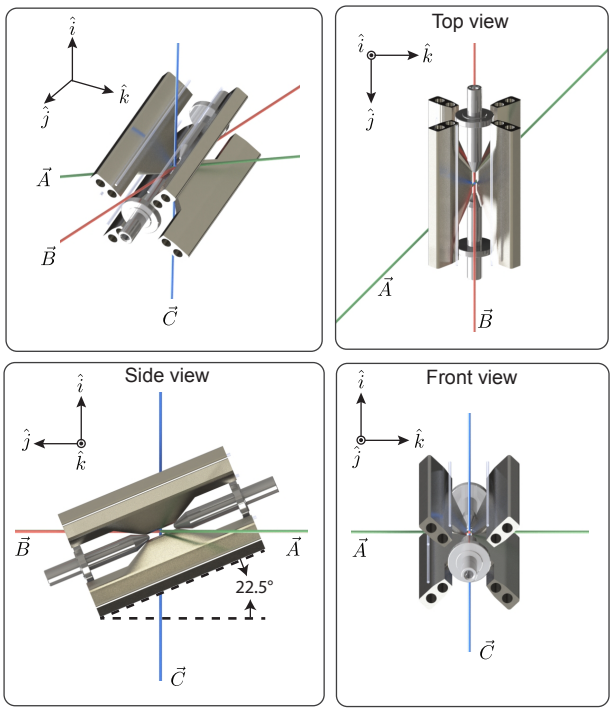

Figure 3.8: Linear Paul trap laser directions. The three directions used for the laser beams driving the ions are denoted $\vec{A}, \vec{B}$ and $\vec{C}$. The $\hat{j}$ and $\hat{k}$ vectors lie in the horizontal plane, parallel to the bottom flange of the vacuum chamber (and the optical table) and the vector $\hat{i}$ is vertical. The trap is tilted 22.5° with respect to the $\hat{k}$ vector. Axis $\vec{A}$ (green) is used for the 493 nm Doppler cooling and 650 nm repumper beams. Axis $\vec{B}$ (red) is used for optical pumping and excitation of the ions, with σ^-– and σ^+–polarized 493 nm beams. Additionally, the axis $\vec{B}$ is used for the photo-ionization 413 nm beam. The axis $\vec{C}$ (blue) is used for the beam driving the 1762 nm transition. The axis used for detection is parallel to the axis $\hat{k}$.

- **413 nm**. The laser light used for photo-ionization is produced directly by a Nichia NDVA416T laser-diode mounted in a Toptica DL100 system. The system can output up to 45 mW, but is operated at 10 mW. The laser is operated free-running and the wavelength is monitored with a wavemeter. The laser beam is coupled together with a 493 nm and a 650 nm laser beam into the same optical-fiber, ensuring the mutual alignment of the three beams when loading ions into the trap.

Laser access

In order to provide optical clearance to the center of the trap through all the viewports, the Paul trap is tilted with respect to the horizontal plane, as shown if Fig. 3.5. The presence of the objectives entails additional restrictions for the laser access to the center of the trap, but the objective holders are designed to provide enough clearance for all the lasers.

The axes used for the different lasers are shown in Fig. 3.8. The HALOs are not displayed for the sake of clarity. The horizontal axis $\vec{A} = (-\hat{j}+\hat{k})/\sqrt{2}$ is used for the

Doppler-cooling beam at 493 nm and the 650 nm repumper beam. This provides a good overlap between the propagation direction of the beam and the three motional directions of the atoms in the trap, which is a condition for efficient cooling.

The horizontal axis $\vec{B} = -\hat{j}$ is used for driving electronic σ-transitions in the atom, and therefore for optical pumping. Additionally, the $\vec{B}$ axis is used for the photo-ionization beam (see Sec. 3.3.5), and planned for a pump beam for EIT cooling. The axis $\vec{B}$ is tilted 22.5° with respect to the axis of the trap. Axes $\vec{A}$ and $\vec{B}$ are parallel to the bottom flange. The axis $\vec{C} = \hat{i}$, normal to the bottom flange, is used for the 1762 nm laser beam to address the qubit transition. The axes of the trap, which also correspond to the direction of the ion motional-modes, $\hat{x}$, $\hat{y}$ and $\hat{z}$, can be written as a function of the vector $\hat{i}$, $\hat{j}$ and $\hat{k}$ (Fig. 3.8) as

$$\hat{x} = \frac{1}{\sqrt{2}}\cos\frac{\pi}{8}\hat{i} + \frac{1}{\sqrt{2}}\sin\frac{\pi}{8}\hat{j} + \frac{1}{\sqrt{2}}\hat{k} \tag{3.12}$$

$$\hat{y} = \frac{1}{\sqrt{2}}\cos\frac{\pi}{8}\hat{i} + \frac{1}{\sqrt{2}}\sin\frac{\pi}{8}\hat{j} - \frac{1}{\sqrt{2}}\hat{k} \tag{3.13}$$

$$\hat{z} = -\sin\frac{\pi}{8}\hat{i} + \cos\frac{\pi}{8}\hat{j} \tag{3.14}$$

All of the lasers, except the 1762 nm laser, are focused down to a waist size of about 20 μm in the center of the trap, which is larger than the spacing between different ions ($\sim$ 5 μm) and therefore illuminate several ions simultaneously. The 1762 nm beam is focused using a custom combined beam-expander and focusing objective[18] to a waist diameter of about 5 μm.

3.3.4 Control system

The control of experiment sequences and parameters is done through the home-made "TrICS"[19] software. This software centralizes the control of most of the devices used in the experiment, allowing the setting of parameters such as the detuning and power of lasers, the voltages driving the Paul trap, the length of the optical cavities used for laser locking, switching of lasers, etc. It also handles the read-out of the photon counter, cavities temperatures, photodiode intensities, etc.

All of the synchronous processes needed in the experiments presented in this thesis are handled through a home-made device, the so-called "PulseBox" [80,81]. The PulseBox, also controlled through TriCS, has 32 digital outputs that can generate pulses with rise time shorter than 1 ns, with durations ranging from nanoseconds to seconds and programmable delays. These pulses are used as switching signals for the AOMs controlling the laser beams and other devices. Additionally, the PulseBox can host up to 16 direct-digital-synthesizers (DDS) for the generation of phase-coherent RF pulses, and up to 8 digital inputs. The PulseBox, therefore, is used to generate experimental sequences which are composed by laser pulses, scanning of parameters such as laser detuning, counting of the photons emitted by the atoms. The PulseBox also allows the triggering of in-sequence actions through the detection of pulses in

[18] Lens-optics
[19] Trapped ion control software

the input channels. The electronic pulses generated by the Pulsebox have a time precision and jitter well bellow one nanosecond [80].

3.3.5 Loading

The loading of $^{138}Ba^+$ into the trap is done through photo-ionization of neutral Barium in the vicinity of the trap's center. The neutral Barium is deposited as compressed-powder in two cylindrical ovens, with internal radius about 2 mm and about 3 cm long. The ovens, partially visible in Fig. 3.5, are located close to the trap, and oriented towards its center. In order to expel neutral Barium, the oven is resistively heated-up up to about 550 K by applying a current of 6 A.

The photo-ionization of the neutral atoms is then achieved through a two-photon process with a single 413.243 nm focused laser beam, which crosses the atomic beam in the center of the trap [61]. The first step of the photo-ionization drives an intercombination line from the $^1S_0$ to the $^3D_1$ state. From there, the energy of a second 413 nm photon is enough to unbind the electron. Additionally, a 493 nm and a 650 nm laser beams are co-propagated in a single-mode fiber, in order to cool and detect the ions when trapped, ensuring their relative alignment. At this stage, the detection is done using a camera, to be able to count the number of trapped ions. The loading of ions is probabilistic, happening at random times. With a photon-ionization beam of 0.5 mW, we achieve an average loading rate of $\approx$ 2 ions/min. After loading and cooling, the ion can be stored in the trap for periods of up to two weeks, even without continuous laser cooling.

One of the disadvantages of this method is that using $^3D_1$ as intermediate state, does not allow an efficient emission of fluorescence, because it is a metastable state, with a half-life in the order of 10^7 s [82]. With other approches where the first step is a dipole-allowed transition (typically used when trapping Ca), the measurement of the fluorescence allows the tuning of the wavelength of the photo-ionization laser and measurement of the atomic flux. A more efficient photo-ionization process for Barium with a dipole-allowed transition is described in Ref. [83].

3.4 Spectroscopy of Ba^+

In the following, the different spectroscopy techniques used to characterize the transitions used in our experiments are presented. The spectra obtained are used to estimate different parameters related with the trapping and driving of the ions.

3.4.1 Resonance fluorescence spectrum

The resonance fluorescence spectrum is measured by continuously driving a trapped ion with close-to-resonance cooling (493 nm) and repumper (650 nm) beams, while varying the detuning Δ_r of the repumper beam. Both beams are linearly polarized and drive all possible transitions between the involved states. The magnetic field

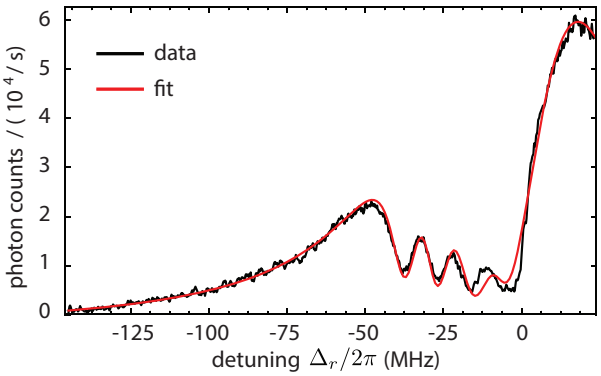

Figure 3.9: Resonance fluorescence spectrum. Emission spectrum of a single $^{138}Ba^{+}$ ion in the presence of magnetic field, as a function of repumper detuning Δ_r. The data (black curve) is fitted using the steady-state solution of the eight-level Bloch equations (red curve). From the fit, unknown parameters of the driving fields can be estimated (see main text).

applied using the coils prevents population trapping in the stretched states of the $5D_{3/2}$ ($m_j = \pm 3/2$) manifold. As discussed in Section 3.2.2, the presence of a magnetic field splits the energies of the electronic states, yielding eight non-degenerate levels: two in the $6S_{1/2}$ manifold, two in the $6P_{1/2}$ manifold and four in the $6P_{3/2}$ manifold. The evolution of the system can be described using an eight-level Bloch equations set, which can be deduced following the same procedure as the one presented in Section 2.3.2, but considering all the possible excitation and decay channels between the eight states [61]. Due to its complexity, this set of equations does not have a general analytical solution, but can be solved numerically using different methods. These methods are included in the available quantum optics computation toolboxes, such as the Quantum Optics Toolbox for Matlab [84], the Quantum Toolbox in Python (QuTiP) [85] or the Julia Framework for Open Quantum Dynamics (QuantumOptics.jl) [86].

An example of a measured spectrum as a function of the repumper detuning Δ_r is shown in Fig. 3.9 (black curve), where several peaks and valleys are observed. They are due to the dynamics of the eight-level system, and correspond to partial population trapping in dark states, as discussed in Section 2.3.2. The numerically calculated steady state solution for the total population of the $6P_{1/2}$ manifold can be fitted to the measured spectrum (Fig. 3.9, red curve) in order to estimate unknown parameters such as Rabi frequencies, laser detunings, magnetic field magnitude, laser linewidths and laser polarizations. From the data shown in Fig. 3.9, the Rabi frequency and detuning of the cooling beam are estimated to be $\Omega_g/2\pi = (23 \pm 1)\,\mathrm{MHz}$ and $\Delta_g/2\pi = (24 \pm 1)\,\mathrm{MHz}$. The Rabi frequency of the repumper beam is estimated to be $\Omega_r/2\pi = (14.7 \pm 0.3)\,\mathrm{MHz}$. The magnitude of the magnetic field is not extracted from this spectrum, but instead from the spectrum of the 1.7 μm transition, as explained in the following section.

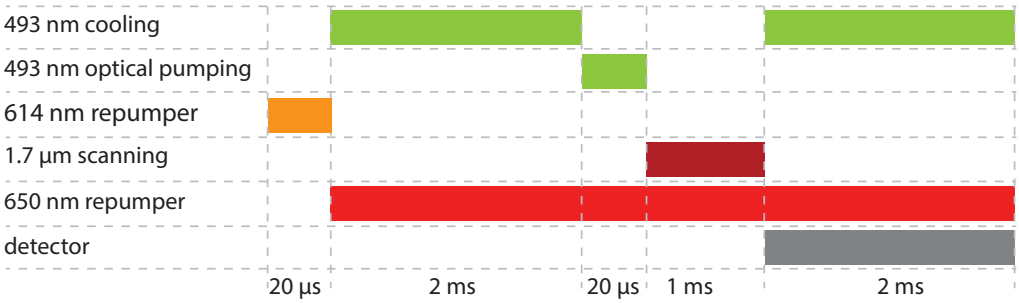

Figure 3.10: Optical qubit transition spectroscopy sequence. Sequence used for the spectroscopy of the 1.7 μm transition. The only scanned parameter is the detuning of the 1.7 μm pulse.

3.4.2 The optical qubit transition

Spectroscopy of the 1.7 μm quadrupolar transition is performed using the pulsed sequence shown in Fig. 3.10. First, the ion is illuminated with a 614 nm repumper for 20 μs in order to depopulate de $5D_{5/2}$ manifold. After this stage nearly 100% of the population is in the cooling levels ($6S_{1/2}$-$6P_{1/2}$-$5D_{3/2}$). Then, the ion is Doppler-cooled for 2 ms by the 493 nm cooling beam and the 650 nm repumper. Afterwards, the ion is illuminated with the 493 nm optical-pumping beam, which is left-circular polarized about the quantization axis, set by the magnetic field. This optical pumping beam can excite only the $|6S_{1/2}, m_j = +1/2\rangle \rightarrow |6P_{1/2}, m_j = -1/2\rangle$ transition. After 20 μs of optical pumping the population of the $|6S_{1/2}, m_j = -1/2\rangle$ state p_- is higher than 99.98%. The ion is then illuminated with the 1.7 μm beam, with a detuning $\Delta_{\text{o.q.}}$ which is scanned for different repetitions of the sequence. Depending on this detuning, the population may or may not be transferred to one of the states of the $5D_{5/2}$ metastable manifold depending on $\Delta_{\text{o.q.}}$. To discriminate if the population was transferred the same lasers used for cooling are turned on; if the ion emits light is said to be in a 'bright' state, and it means that it was not transferred to the metastable state. If it does not emit light we call it 'dark', and it means that the population is trapped in one of the metastable states, which are outside the cooling-cycle transitions. This technique is known as *electron-shelving* [87]. During this period of 2 ms (which is much shorter than the natural decay rate of the metastable state) a detector is turned on and the emitted photons are counted. The number of photons collected without any 1.7 μm pulse is used to define the excitation probability equal to zero (maximum fluorescence rate), and the number of photons detected when the ion is dark, is used to define the excitation probability equal to one.

The sequence is repeated 100 times with the same detuning $\Delta_{\text{o.q.}}$ in order to gather statistics about the mean excitation probability of the 1.7 μm pulse. Fig. 3.11a shows the spectrum of the 1.7 μm transition, where the detuning $\Delta_{\text{o.q.}}$ is scanned in a range of 35 MHz with 4000 different data points. The zero detuning reference is set arbitrarily. The spectrum clearly shows all of the quadrupole allowed transitions from the initially prepared state ($|6S_{1/2}, m_j = -1/2\rangle$), including carriers and motional sidebands. To observe the excitation spectrum starting from the $|6S_{1/2}, m_j = +1/2\rangle$ state, it is necessary to invert the polarization of the optical

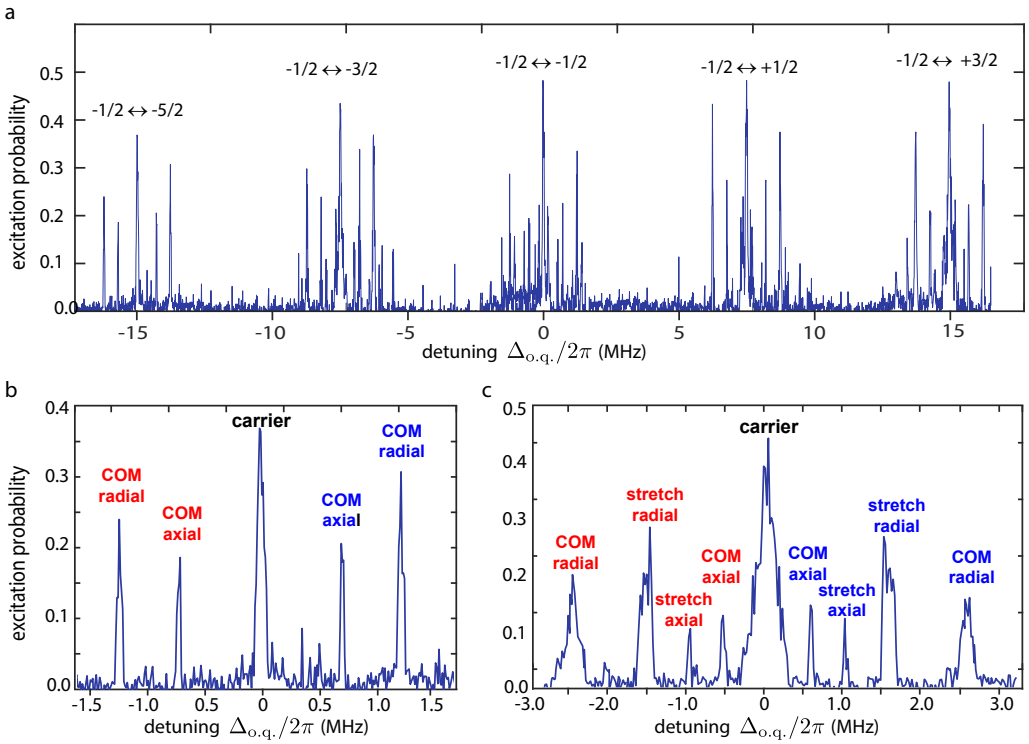

Figure 3.11: Optical qubit transition spectra. a. Excitation spectrum of the 1.7 μm transition from the initial ground state $6S_{1/2}$, $m_j = -1/2$ of a single ion. The plot shows the five different quadrupole-allowed carrier transitions and their respective sidebands. The carrier transitions are separated by ≈ 7.48 MHz, corresponding to a Zeeman spliting of the $5D_{5/2}$ states produced by a magnetic field with magnitude $B \approx 4.45$ G. **b.** Carrier and first sideband of the $|6S_{1/2}, m_j = -1/2\rangle \leftrightarrow |5D_{5/2}, m_j = -5/2\rangle$ transition for a single ion. Blue and red sidebands are labelled with the respective colors **b.** Carrier and first sideband transitions of the $|6S_{1/2}, m_j = -1/2 \leftrightarrow |5D_{5/2}, m_j = -5/2\rangle$ transition for two ions. Note that the trap parameters used during the acquisition of the spectra **a** and **b** are different (see main text).

pumping beam only.

From the spectrum of Fig. 3.11a it is possible to deduce the magnitude of the applied magnetic field, since the energy difference between different carrier transitions corresponds directly to the Zeeman splitting of the $5D_{5/2}$ state. The observed splitting is (7.48 ± 0.04) MHz, which, using Eq. 3.1, corresponds to a magnetic field magnitude $|\vec{B}| = (4.45 \pm 0.03)$ G.

Fig. 3.11b shows a narrower frequency range scan of the $|6S_{1/2}, m_j = -1/2\rangle \leftrightarrow |5S_{5/2}, m_j = -5/2\rangle$ transition for a single ion, where the first red and blue secular motional sidebands are clearly displayed. The axial trapping frequency is the frequency difference between the COM modes to the carriers, $\omega_z/2\pi = (0.69 \pm 0.01)$ MHz. In the same way, the radial trapping frequencies are measured to be $\omega_{x,y}/2\pi = (1.22 \pm 0.04)$ MHz. The presented spectrum does not have enough resolution to show separate peaks for the two radial motional mode due to saturation effects. To precisely measure the position of these peaks, it is necessary to reduce the intensity of the excitation laser. Doing this shows a splitting of the axial frequencies of about

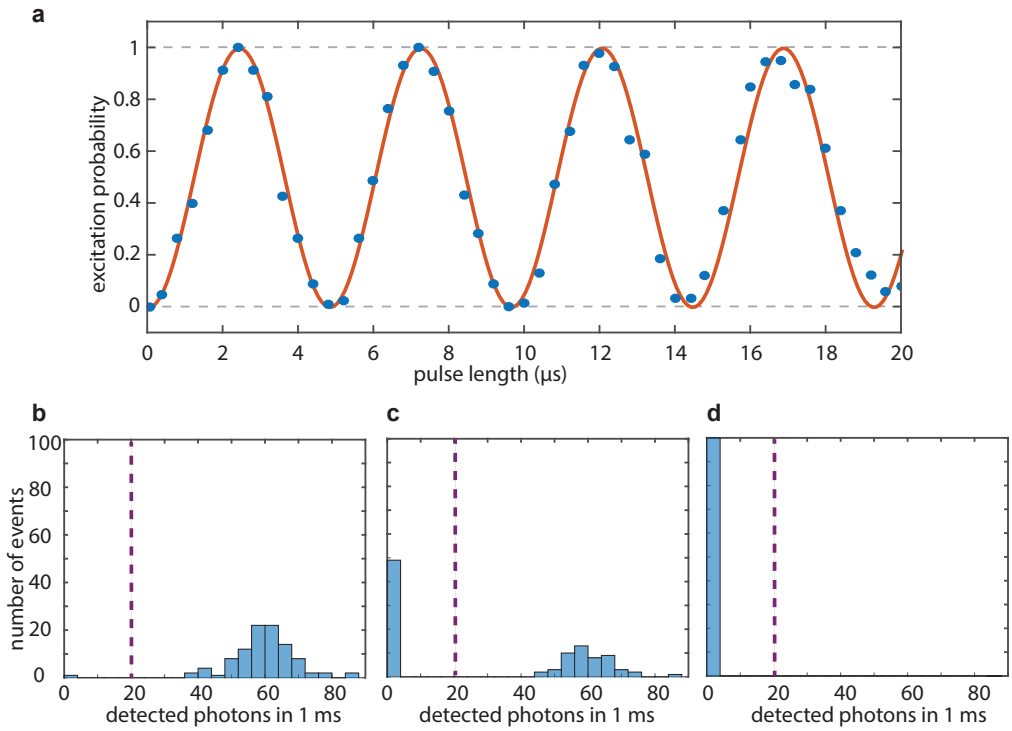

Figure 3.12: Rabi oscillations in the optical qubit transition. a. Rabi oscillations in the $|6S_{1/2}, m_j = -1/2\rangle \leftrightarrow |5D_{5/2}, m_j = -5/2\rangle$ carrier transition. Four full Rabi oscillations are displayed, with a Rabi frequency of $\Omega_{\text{o.q.}}/2\pi = (0.208 \pm 0.001)$ MHz. **b, c and d** show detection histograms for pulse lengths 0, 1.2 an 7.2 μs respectively. The purple dashed line shows the discrimination threshold between the dark and bright states.

30 kHz.

Fig. 3.11c shows the excitation spectrum of one ion when two ions are trapped in a chain along the z-axis. In this case there is a second motional mode in each oscillation direction. The trapping parameters are different from those used in Fig. 3.11b, so that the axial modes have frequencies $\omega_{z,\text{COM}}/2\pi \approx 0.6\,\text{MHz}$ and $\omega_{z,\text{stretch}}/2\pi \approx 0.6\,\text{MHz}$, whereas in the radial direction $\omega_{x,y,\text{COM}}/2\pi \approx 1.5\,\text{MHz}$ and $\omega_{x,y,\text{stretch}}/2\pi \approx 2.6\,\text{MHz}$.

Rabi oscillations

Rabi oscillations between two electronic states can be observed by fixing the detuning of the 1.7 μm beam such that is on resonance with one of the transitions, and scanning its pulse length. Fig. 3.12a shows Rabi oscillations in a single ion using a sequence similar to the one shown in Fig. 3.10a, but with the detuning of the 1.7 μs pulse resonant with the $|6S_{1/2}, m_j = -1/2\rangle \leftrightarrow |5D_{5/2}, m_j = -5/2\rangle$ carrier transition. The pulse length is varied from 0 to 20 μs.

As the linewidth of the driving laser is narrow enough to excite only the carrier transition, the effect of a laser pulse with length t and phase φ is given by the

operator

$$\hat{R}(\theta,\varphi) = \exp\left[\theta/2(\cos\varphi\hat{\sigma}_x + \sin\varphi\hat{\sigma}_y)\right] \tag{3.15}$$

where $\theta = \Omega_{\text{o.q.}}t$ is known as *pulse area*, $\Omega_{\text{o.p.}}$ is the Rabi frequency of the driven transition, and the Pauli operators $\hat{\sigma}_x$ and $\hat{\sigma}_y$ are defined as in Eq. 2.47, by labelling the two electronic states involved as

$$|g_-\rangle \equiv |6\mathrm{S}_{1/2}, m_j = -1/2\rangle \tag{3.16}$$
$$|e\rangle \equiv |5\mathrm{D}_{5/2}, m_j = -5/2\rangle, \tag{3.17}$$

which form our optical qubit. If the initial state is the ground state $|g_-\rangle$, the probability of exciting the state $|e\rangle$ is given by

$$P_e(t) = \left|\langle e|\hat{R}(\theta,\phi)|g_-\rangle\right|^2 \tag{3.18}$$
$$= \frac{1}{2}(1-\cos\theta), \tag{3.19}$$

as predicted also by Eq. 2.70. It is worth noticing that, for a quadrupole S↔D transition, the induced electric-quadrupolar moment $\hat{Q}$ couples to the gradient of the magnetic field, i.e.,

$$H_I = \hat{Q}\nabla E(t). \tag{3.20}$$

In this case, the resonant Rabi frequency for the transition connecting the states $|S, m_s, j\rangle \leftrightarrow |D, m_D, j'\rangle$ when driven with plane wave, is theoretically defined as [35]

$$\Omega = \left|\frac{eE_0}{2\hbar}\langle \mathrm{S}, m_S, j|(\vec{\epsilon}\cdot\vec{r})(\vec{k}\cdot\vec{r})|\mathrm{D}, m_D, j'\rangle\right|, \tag{3.21}$$

where $\vec{\epsilon}$ is the polarization of the driving beam, $\vec{k}$ its wavevector, E_0 its amplitude and $\vec{r}$ is the position operator of the electron (relative to the nucleus). Different from the dipole transitions case, in quadrupole transitions the Rabi frequency depends on the field gradient instead of the field amplitude, but the Rabi oscillation exhibits the same behaviour. As already mentioned Eq. (3.21) is valid when the driving field is a plane wave. In our experiments this is not true since we use strongly focused beams, and therefore, corrections to this equation must be applied. A general expression in terms of the quadrupole momentum operator can be found in Ref. [35].

The oscillations in Fig. 3.12 display a Rabi frequency of $\Omega_{\text{o.q.}}/2\pi = (0.208 \pm 0.001)$ MHz and a π-pulse time of $(2.40 \pm 0.01)\,\mu$s. A pulse of length 2.4 μs almost completely transfers the population to the metastable state, with more than 99.5% efficiency. Fig. 3.12b, c and d show the detection histograms for 100 experimental repetitions of three different pulse lengths. The detected distributions for a bright and dark ion do not overlap, and the background and dark counts are negligible.

Longer measurements show that the contrast of the Rabi oscillations decreases to 50% at about 200 μs. The contrast at longer times is mostly limited by the

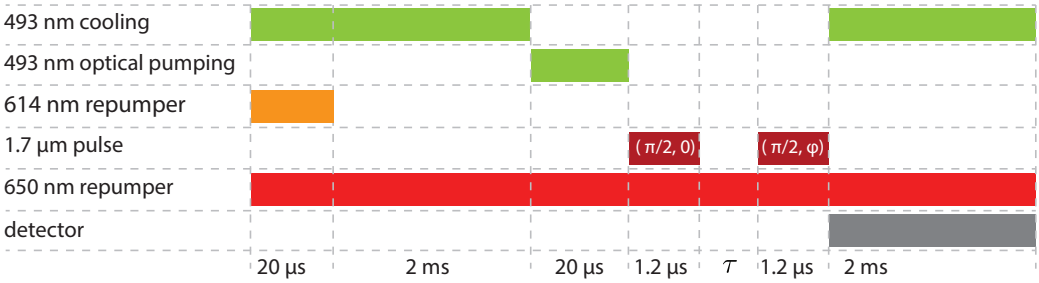

Figure 3.13: Optical qubit transition Ramsey experiment sequence. Sequence used for measurement of Ramsey fringes in the optical qubit transition. Two 1.7 μm $\pi/2$-pulses separated by a delay time τ drive the optical qubit transition. The scanned parameter is the phase φ of the second pulse, respective of the phase of the first pulse. Different time delays allows us to deduce the coherence time of the qubit.

intensity fluctuations of the driving beam, the ion motion and the 50 Hz oscillation of the magnetic field due to the electical supply line frequency. The latter can be compensated by synchronising the experiments with the supply line, although this strongly limits the repetition rate. More details can be found in Ref. [79].

Ramsey fringes

To benchmark the coherence of the light-atom interaction and the coherence of the atomic transition in our setup we measure Ramsey fringes. This method permits not only to obtain information about the populations, but also of the phase evolution of the atom with respect to the driving field. To do so, after Doppler cooling and preparing the ion in the initial state $|g_-\rangle$, we apply two laser pulses with pulse area $\theta = \pi/2$, and with a relative phase difference φ in the rotating frame, separated by a delay time τ. The phase of the first pulse is set as the reference phase. The action of the two different pulses is represented by the operators $\hat{R}(\pi/2, 0)$ and $\hat{R}(\pi/2, \varphi)$, defined in Eq. 3.15. The first pulse prepares the coherent superposition

$$\frac{1}{\sqrt{2}}(|g_-\rangle + e^{-i\frac{\pi}{2}}|e\rangle). \tag{3.22}$$

During the time τ, the atom evolves freely (i.e., not through the interaction with the laser field), meaning that the relative phase between the states involved can change, i.e, the state evolves to

$$\frac{1}{\sqrt{2}}(|g_-\rangle + e^{i(-\frac{\pi}{2}+\varphi_{\text{free}})}|e\rangle). \tag{3.23}$$

The action of the second pulse depends on the accumulated phase during the free evolution. If the accumulated phase during the free evolution is $\varphi_{\text{free}} = 0$ in the rotating frame, i.e., there is no phase evolution, the second pulse will produce the state

$$\frac{1}{\sqrt{2}}\left[\left(e^{-i\varphi} - 1\right)|g\rangle + i\left(e^{i\varphi} + 1\right)|e\rangle\right], \tag{3.24}$$

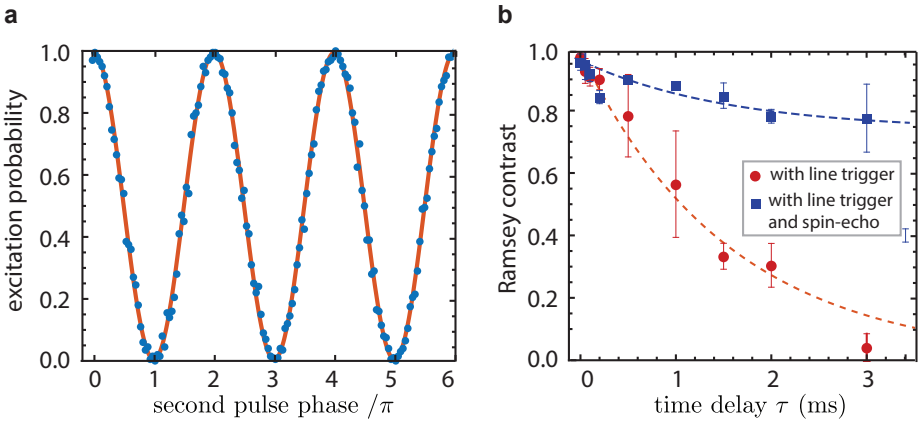

Figure 3.14: Ramsey fringes of the optical qubit. a. Ramsey fringes with zero delay ($\tau = 0$). The observed contrast is close to 1. **b.** Measured contrast for delay times of up to 3.5 ms. The red points correspond to the estimated contrast when synchronizing the experiments with the phase of the 50 Hz supply line, which oscillates at 50 Hz. The blue squares show how the coherence can be further improved by adding a spin-echo pulse (see main text). The segmented lines are only a guide to the eye. Measurements by L. Slodička [79].

so that the probability of finding the ion in the excited state after the two pulses is

$$P_e = \frac{1}{2}(1 + \cos\varphi). \tag{3.25}$$

On the other hand, if during the free evolution the phase changes, the probability of finding the ion in the excited state is

$$P_e = \frac{1}{2}[1 + \cos(\varphi - \varphi_{\text{free}})]. \tag{3.26}$$

Due to fluctuations in the magnetic field, the phase evolution does not occur at a constant rate. This effect together with fluctuations in the Rabi frequency due to changes in pulse intensity, causes the contrast of the Ramsey fringes to decrease for increasing delay times.

Fig. 3.13 shows the sequence used for Ramsey experiments in our system. A first experiment to test the coherent interaction between laser pulses and atom consists in sending the two Ramsey pulses with no time delay, and scanning the phase of the second pulse. Fig. 3.14a shows the result of such an experiment. At zero delay no dephasing is expected, and the data is well described by Eq. (3.25). The measured contrast is 98.7 ± 0.8 %, and the small deviation from the theoretical curve proves the high degree coherence between the two pulses and the degree of control of the qubit superposition.

Fig. 3.14b show the results of a second experiment, with measured contrast of the Ramsey fringes for delay times τ ranging from 0 to 3.5 ms, synchronizing the experiments with the supply line oscillating at 50 Hz (red circles). The contrast

decreases to half its initial value (coherence time) in ≈ 1.6 ms. Contrast reduction due to phase fluctuations with frequencies higher than $1/\tau$ can be compensated by adding a *spin-echo* pulse in between the two Ramsey pulses [42]. A spin-echo pulse is a $R(\pi, 0)$–pulse, which inverts the relative direction of the phase evolution, and compensates for it when the free-evolution time of the ion is the same before and after it. The blue squares is Fig. 3.14b show how the coherence time is improved up to more than 3 ms by adding a single spin-echo pulse. The effectiveness of the spin-echo pulses in reverting the free phase evolution suggests that the main source of decoherence is low frequency noise, most likely slow variations of the magnetic field changing the Zeeman splitting between states, whereas the remaining coherence losses are due to high frequency field noise and other decoherence mechanisms such as motion-induced decoherence [88].

3.4.3 The ground state RF qubit

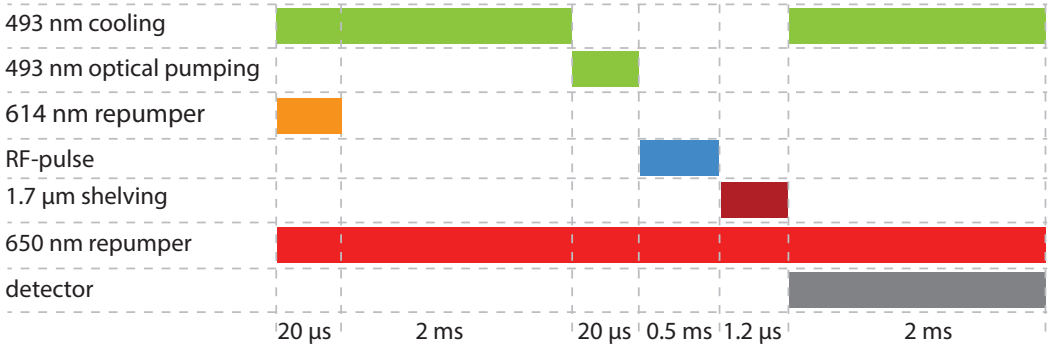

Figure 3.15: Sequence for spectroscopy of the RF ground state transition. Sequence used for the spectroscopy of the RF transition between the $|6S_{1/2}, m_j = -1/2\rangle$ and $|6S_{1/2}, m_j = +1/2\rangle$ states. The scanned parameter is the frequency ω_{RF} of the RF pulse. In order to discriminate between the occupation of both states through fluorescence detection, a π-pulse in the $|6S_{1/2}, m_j = -1/2\rangle \leftrightarrow |5S_{5/2}, m_j = -5/2\rangle$ is used to shelve the population of the $|6S_{1/2}, m_j = -1/2\rangle$ state.

The applied magnetic field lifts the energy degeneracy of the ground states $|g_-\rangle = |6S_{1/2}, m_j = -1/2\rangle$ and $|g_+\rangle = |6S_{1/2}, m_j = +1/2\rangle$. For the applied magnetic field with amplitude 4.45 G, an energy splitting of 12.45 MHz between both ground states is expected. We drive this magnetic-dipole transition using a single-loop antenna (diameter ≈ 10 cm) located close to the bottom view port. The antenna is driven with an RF signal produced by a DDS from the PulseBox, which is amplified to reach a power of ≈ 100 mW. Fig. 3.15 shows the sequence used for spectroscopy of the transition. After optically pumping into the state $|g_-\rangle$, a 0.5 ms RF pulse with variable frequency ω_{RF} is applied in order to drive the transition. To measure the population of the states $|g_-\rangle$ or $|g_+\rangle$ after the RF pulse, the population of $|g_-\rangle$ is shelved with more than 99% efficiency to the $|5D_{5/2}, m_j = -5/2\rangle$ state, using a π-pulse on the optical qubit transition. Therefore, in the detection stage, when the fluorescence lasers are turned on (493 nm and 650 nm), an ion emitting fluorescence corresponds to an ion projected in the $|g_+\rangle$ state, and a dark ion corresponds to a projection in $|g_-\rangle$.

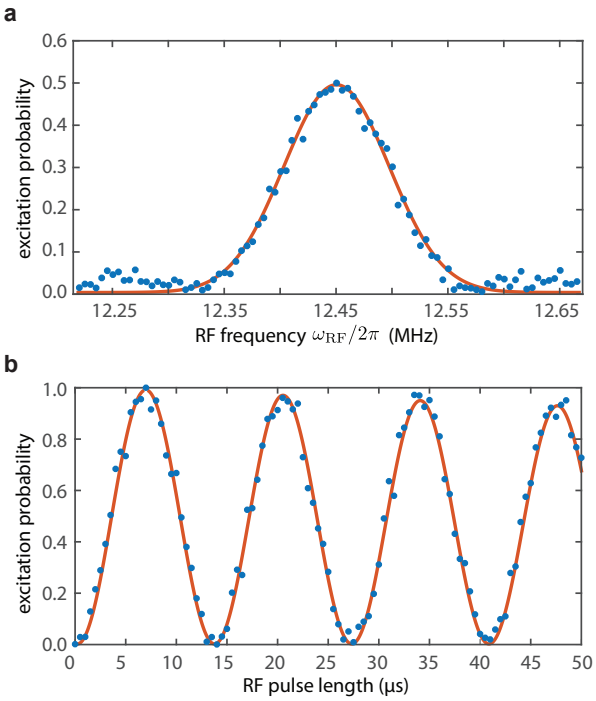

Figure 3.16: RF qubit spectroscopy and Rabi oscillations. a. Spectrum of the carrier RF-qubit transition. The resonance frequency is $\omega_{RF}/2\pi = (12.45 \pm 0.01)$ MHz. **b.** Rabi oscillations between the two ground states. The measured Rabi frequency is $\Omega_{RF}/2\pi = (73.75 \pm 0.02)$ kHz.

Fig. 3.16a shows the spectrum of the carrier RF ground state transition, using 500 μs square RF pulses. A scan over a broader range of frequencies does not show motional sidebands, due to the small Lamb-Dicke parameter of the transition ($\eta \sim 10^{-9}$). The resonance frequency is $\omega_{RF}/2\pi = (12.45 \pm 0.01)$ MHz, from which the magnetic field is estimated to be (4.450 ± 0.005) G, in agreement with the value estimated from the 1.7 μm transition spectroscopy $(4.43 \pm 0.3$ G).

Rabi oscillations

To observe Rabi oscillations on this transition we use a sequence similar to the one shown in Fig. 3.15, except that the frequency of the RF pulse is fixed to $\omega_{RF}/2\pi = 12.45$ MHz and scanning the length of the pulse. Fig. 3.16b shows the measured Rabi flops, where each point represents the estimated probability of ending in the $|g_+\rangle$ state, from 100 repetitions of the sequence for a given pulse length. The measured Rabi frequency is $\Omega_{RF}/2\pi = (73.75 \pm 0.02)$ kHz, and the length for a π-pulse is estimated to be 6.77 ± 0.02 μs. The fitted curve shows a decaying contrast, which is faster than for the optical qubit. This is due to the faster loss in coherence caused by the higher sensitivity to magnetic field fluctuations, since the Landé factor in the ground state qubit are almost twice those of the optical transition.

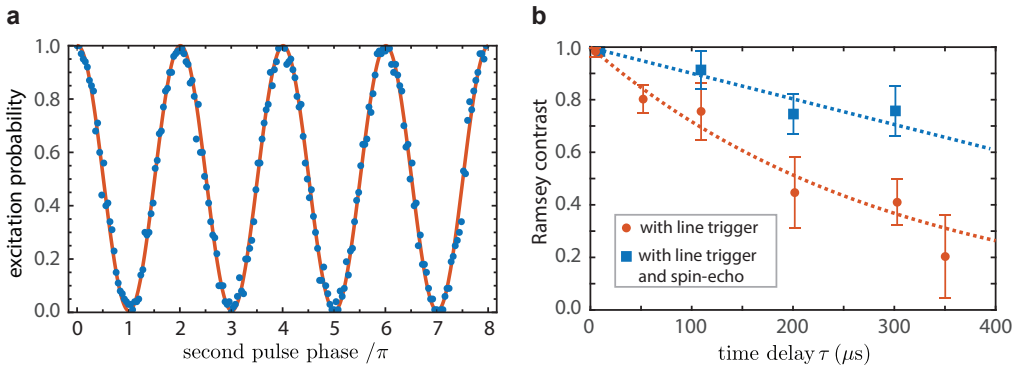

Figure 3.17: Ramsey fringes of the RF-qubit. a. Ramsey fringes at $\tau = 0$ delay. **b.** Contrast of the Ramsey fringes for different delay times, with line-trigger (red points) and with line-trigger and a spin-echo pulse (blue squares). The segmented lines are merely guides to the eye.

Ramsey fringes

To further characterize the coherence of the RF-qubit, we measure Ramsey fringes, as discussed for the case of the optical qubit in Section 3.4.2. Fig. 3.17a shows Ramsey fringes for zero delay between the two $\pi/2$-pulses and scanning of the phase of the second pulse. The measured contrast of $(99.8 \pm 0.1)\%$ proves a high degree of coherent control of the qubit. 3.17b shows the contrast of the measured Ramsey fringes for time delays ranging from 0 to 400 μs, using line-trigger (red dots) and line trigger together with a spin-echo pulse (blue squares). From the evolution of the contrast the coherence time is estimated to be ≈ 304 μs without spin-echo. The addition of a spin-echo pulse further increases the coherence time and shows that the coherence time is mostly limited by magnetic field fluctuations.

The obtained coherence times fulfil the requirements for the experiments presented in the following chapters, imposing no significant detriment in the quality of the measured data. However, in order to perform more demanding experiments, such as quantum computation with trapped ions, further improvements in the stability of the driving fields and the magnetic fields would be required.

3.5 Micromotion compensation

The excess of micromotion is detrimental to most of the experiments presented in this thesis. It causes Doppler broadening of the transitions, induces motional decoherence and, as we will see in Chapter 4, affects the interference of fields emitted by different ions.

The amplitude of the different secular motional modes can be reduced using laser cooling, even down to the ground state. On the contrary, the micromotion it is always present, although, it amplitude can be minimized and thereby detrimental effects reduced. The ion is said to have 'excess micromotion', when the amplitude of the micromotion is not the minimum possible. The cause for such a situation

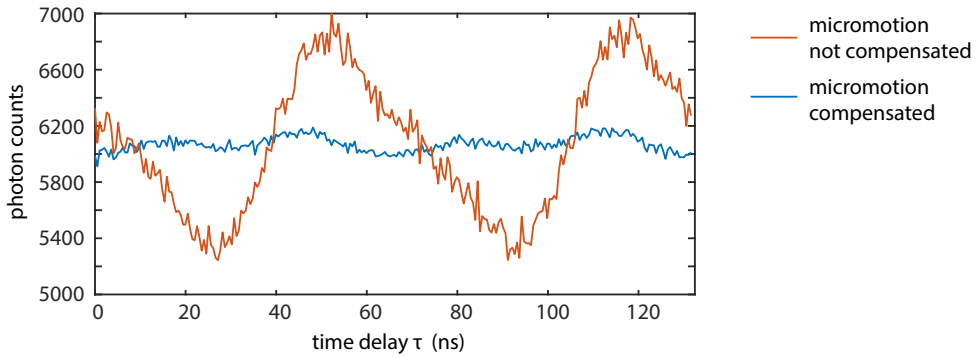

Figure 3.18: Micromotion compensation. Number of photons detected in a bin of 512 ps with a time delay τ from the 'triggering' pulse (synchronized with the RF drive). The red curve show two full oscillations of the amount of emitted photons due to micromotion, with exactly the same period as the RF-driving. The blue curve show the same experiment after compensation of the micromotion using the top compensation electrode pair.

is that the minimum of the RF pseudopotential does not coincide with the DC confinement saddle point. Although the used traps are designed for these two points to coincide, the presence of stray electric fields can separate them. To compensate for the presence of these stray fields, DC voltages are applied to the compensation electrodes shown in Fig. 3.2.

There are several iterative methods that can be used to find the voltages needed to compensate for excess of micromotion [62]. Most of this methods are based on the observation and minimization of the effects of the effective Doppler modulation of the laser driving the ions due to micromotion.

In our experiment, we compensate micromotion by measuring and reducing the correlations between the RF signal driving the trap and the number of photons emitted when continuously Doppler-cooling the ion [62]. These correlations are expected since the micromotion is a periodic motion phase-locked to the driving field, causing an effective Doppler detuning of the lasers used for cooling. This modulates the Rabi frequency of the laser fields driving the internal transition of the ion, and therefore, the photon scattering rate.

Since micromotion may be present in the three possible orthogonal directions, we use a laser beam propagating in a direction with overlap with the three directions of the motional modes of the ion. To measure the correlation of the number of photons emitted and the trap drive, we derive generates 10 ns square 'triggering' pulses with repetition rate synchronized with the period T of the RF signal driving of the trap ($T = 2\pi/\omega_{\mathrm{RF}} \approx 66.007$ ns). Then, using the PicoHarp 300, we measure the number of photon counts in bins of 512 ps, separated by a time delay τ from the triggering pulses, and integrate over 30 s, detecting more the 1.5 million photons. Fig. 3.18 shows the results before (0 V on the compensation electrodes) and after micromotion compensation, using one of the pair of compensation electrodes (260 V). The voltage of the compensation electrodes is scanned until the minimum possible amplitude is obtained. In the shown case, the amplitude was reduced by a factor of more than 15. The same procedure is repeated with the other pair of compensation electrodes

until no oscillations are observed (contrast bellow 1%).

3.6 Summary

In this chapter we have presented the main components of our experimental setup, including the trap, the collection optics, the different detectors and detection configurations. We have also presented the spectroscopy of the transitions used in this thesis, showing the achievable Rabi frequencies, Ramsey fringe contrasts and coherence times of the two qubit transitions. The results show the high level of coherent control of single atomic ions. The measured coherence times, although improvable, are well inside the regime needed for the realization of the experiments reported in this thesis. Should longer coherence times be required, there are several ways to improve them, e.g., by diminishing the fluctuations of the magnetic field using active stabilization or a magnetic shield around the setup, and by improving the frequency and intensity stability of the lasers.

The capability of performing coherent control of the qubits shown here, together with high efficiency single-mode detection is crucial for entanglement generation and characterization using single photons with controllable phase (Chapter 4). The optical quality of the collection optics and high efficiency of the pumping are a key feature for the precise imaging experiments presented in Chapter 5.

4

Interference of single photons emitted by entangled atoms

4.1 Introduction: Light emitted by correlated matter

The emission properties of a set of atoms can be different from the naïve expectation that if an atom emits light with an emission rate γ , then N atoms will emit with a rate $N\gamma$. This is true when the atoms are thermally excited and photons are randomly emitted. However, when the atoms are coherently excited such that there is a defined phase relation between their internal states, the emission rate can grow as high as $N^2\gamma$ as was first suggested by R. H. Dicke in his seminal work [89]. This effect, dubbed *superradiance*, is due to the "spontaneous phase-locking of the atomic dipoles" [90], which can occur, for example, through direct dipole-dipole interaction when the separation between atoms is smaller than the emitted wavelength. The opposite effect, namely the reduction of the emission rate dubbed *subradiance*, can also occur in some situations. Detailed discussion of this phenomenon can be found in Refs. [90,91] and extensive review of different experiments studying this an related phenomena can be found in Ref. [92].

The phase-locking of the atomic dipoles can also occur through other mechanisms, such as the spontanous creation of entanglement between the atoms [93, 94]. Collective emission and absorption properties of entangled emitters have been extensively studied in ensembles of neutral atoms [95–97] where, in general, the number and position of the atoms fluctuates, and the precise control of the quantum state of each emitter is challenging.

The phase-locking of the dipoles can also be achieved by controlled creation of entanglement between different atoms instead of spontaneous creation. The interference of coherently emitted photons from an array with a definite number of well-localized atoms (well bellow the emission wavelength), in a well-characterized entangled state can give rise to a direction-dependent modification of the emission rate [98, 99]. In this case, contrary to the original scenario proposed by Dicke, the modification of the emission rate does not rely on the proximity of the atoms and

it is still present for arbitrarily large separation between them. Strictly speaking, this effect is not superradiance, since the enhancement and inhibition of the decay rate occur in a particular observed optical mode and vanish when integrated over the entire space. Nevertheless, the modification of the emission through this mechanism is of fundamental interest, since it arises directly from the entanglement in the atomic systems, and allows us to directly 'optically observe' the entanglement by measuring the photon interference signal. Furthermore, the possibility of engineering the emission rate and pattern of a set of emitters by controlling their internal state opens a new paradigm for optical physics experiments.

To observe the coherent emission of light from such a entangled chain of atoms it is necessary to achieve simultaneously sub-wavelength atom localization, high-fidelity entanglement generation and atom-light coupling strong enough to detect an optical signal at very low photon flux. The experimental platform of trapped ions presented in the previous chapter has enabled excellent control over position and entanglement with well-defined and steadily increasing numbers of particles [26,100, 101], motivated mostly by the pursuit of the realization of a quantum computer. Meanwhile, the pursuit of on-demand single photons, strong atom-light coupling, and fast quantum state readout has advanced the collection efficiency of light from single emitters [66,102–104]. In our laboratory, these developments are put together, giving us precise control of the internal states and positions of the ions as well as efficient measurement of the emission of single photons. This, therefore, allows the investigation of the effects of entanglement in collective atom-light interactions in the few-atom limit, and allows us to study how the emission properties of atoms in entangled states differ from those in separable states [105,106].

In this chapter we present the first observation of controlled emission of a single photon into a given free-space optical mode, emitted jointly by a pair of ions prepared in a well-characterized entangled state. The ions are effectively separated by a distance of about 60 cm, which can be tuned dynamically during the experiment with sub-wavelength precision. The modification in the emission that we observe corresponds directly to the path interference of single emitted photons, and arises from the entanglement present in the two-atom state. With the presented arrangement we directly observe both enhancement and inhibition of single-photon emission from the atoms by controlling their interferometric distance. As mentioned before, although reminiscent of superradiance, the observed modification of the emission due to interference occurs in the observed optical mode, and it is not a global modification of the spontaneous decay rate. The global modification due to direct dipole-dipole interaction is negligible for the atom-atom distance studied in our experiment.

The approach presented in this chapter could be used as an alternative to methods based on the tomographic reconstruction of the atom state in order to estimate the entanglement. We experimentally prove this by showing that the emission rate modification is qualitatively different for separable and entangled states. The contrast of the photon interference signal can, in some cases, be directly related to the amount of entanglement. Furthermore, as the entangled state is sensitive to differences in the local magnetic fields at the position of each atom, we use the interference signal to precisely measure the field gradient. In the following, we present the theoretical background, a detailed description of the experiment, as well as a the results and possible applications. The main results and some parts of this chapter

have been published in Ref. [107]

4.2 Entanglement-modified emission rate

In order to have a simple picture of the origin of the interference of photons emitted by entangled atoms, we follow the description in Ref. [98]. Let us consider a chain of N equally spaced emitters at positions $\vec{R}_i$ $(i = 1, \ldots, N)$, with two internal levels $|e\rangle$ and $|g\rangle$. When the transition $|e\rangle \to |g\rangle$ occurs, a photon with wavelength λ is emitted. We will consider that the emitters are uniformly separated by a distance d, which is much larger than the wavelength λ such that the dipole-dipole interaction can be neglected. We will also consider that the initial state of the emitters is a symmetric entangled W-state, i.e., a symmetric superposition of all the states having only one emitter being in the state $|e\rangle$ and all the rest in $|g\rangle$,

$$|\mathrm{W}\rangle = \frac{1}{\sqrt{N}} \left(|e, g, g \cdots g\rangle + |g, e, g \cdots g\rangle + \cdots |g, g, g \cdots e\rangle.\right) \tag{4.1}$$

A generalization of these states are the so-called Dicke states, with n_e emitters being in the state $|e\rangle$ and $N - n_e$ emitters in the state $|g\rangle$, is given by

$$|\mathrm{W}_{n_e, N-n_e}\rangle = \binom{N}{n_e}^{-1/2} \sum_k \mathcal{P}_k |S_{n_e, N-n_e}\rangle. \tag{4.2}$$

$\mathcal{P}_k$ is an operator producing all the possible different permutations with equal number of n_e emitters in $|e\rangle$ and $|S_{n_e, N-n_e}\rangle$ is defined by

$$|S_{n_e, N-n_e}\rangle = \prod_{\alpha=1}^{n_e} |e_\alpha\rangle \prod_{\beta=n_e+1}^{N} |g_\beta\rangle. \tag{4.3}$$

For example, for $N = 4$ and $n_e = 2$, the Dicke state is given by

$$\begin{aligned} |\mathrm{W}_{2,2}\rangle \;=\; & \frac{1}{\sqrt{6}} \left(|e, e, g, g\rangle + |e, g, e, g\rangle + |g, e, e, g\rangle \right. \\ & \left. + |e, g, g, e\rangle + |g, e, g, e\rangle + |g, g, e, e\rangle\right). \end{aligned} \tag{4.4}$$

If the considered transition is an electric dipole transition, the positive part of the electric field at the position $\vec{r} = r\vec{n}$ in the far-field region, is proportional to

$$\hat{E}^+ = \frac{e^{ikr}}{r} \sum_j \vec{n} \times (\vec{n} \times \vec{p}_{ge}) e^{-i\varphi_j} \hat{s}_j^- \tag{4.5}$$

where $k = 2\pi/\lambda$, $\vec{p}_{ge}$ is the dipole moment of the transition $|e\rangle \to |g\rangle$, with dipole operator $\hat{s}_j^- = |g\rangle_j\langle e|$, and φ_j is the phase of a photon at the position $\vec{r}$ emitted by

the emitter j at position $\vec{R}_j$, relative to the origin, i.e.,

$$\varphi_j(\vec{r}) = \varphi_j = k\vec{n} \cdot \vec{R}_j. \tag{4.6}$$

The field intensity detected at the position $\vec{r}$ is given by

$$I = \langle \hat{E}^- \hat{E}^+ \rangle, \tag{4.7}$$

Where $\hat{E}^- = \hat{E}^{+\dagger}$. For simplicity, we now consider the case where the direction of detection and dipole moment are orthogonal, such that $\vec{p}_{ge} \cdot \vec{n} = 0$. Under this consideration, and omitting a constant factor, the dimensionless positive part of the electric field is proportional to

$$\hat{E}^+ = \sum_j e^{-i\varphi_j} \hat{s}_j^-, \tag{4.8}$$

and therefore, the detected intensity is proportional to the dimensionless intensity

$$\begin{aligned} \mathrm{I}(\vec{r}) &= \sum_{i,j} \langle \hat{s}_i^+ \hat{s}_j^- \rangle e^{i(\varphi_i - \varphi_j)}, & (4.9) \\ &= \sum_i \langle \hat{s}_i^+ \hat{s}_i^- \rangle + \left(\sum_{i \neq j} \langle \hat{s}_i^+ \rangle \langle \hat{s}_j^- \rangle e^{i(\varphi_i - \varphi_j)} \right) \\ &\quad + \left(\sum_{i \neq j} \left(\langle \hat{s}_i^+ \hat{s}_j^- \rangle - \langle \hat{s}_i^+ \rangle \langle \hat{s}_j^- \rangle \right) e^{i(\varphi_i - \varphi_j)} \right). & (4.10) \end{aligned}$$

The first summation in Eq. (4.10) corresponds to the population of the $|e\rangle$ state, the second summation corresponds to the expectation values of the dipole operator, and the third to the quantum correlations of the considered states. In the case of a separable state such as the one in Eq. (4.3) it is found that $\langle \hat{s}_i^+ \hat{s}_j^- \rangle = \langle \hat{s}_i^+ \rangle \langle \hat{s}_j^- \rangle = 0$ for $i \neq j$, i.e., both the dipole moment and the correlation vanish, so that the detected intensity is in this case proportional to

$$\mathrm{I}_{|S_{n_e, N-n_e}\rangle} = \sum_{i=1}^{n_e} = n_e, \tag{4.11}$$

which is constant, meaning that each emitter radiates independently. Note that since there are separable states with non-vanishing dipole moment this is not true for all separable states, as we will discuss later in this section.

Contrary to separable states, for entangled W-states the correlations are always non-vanishing due to the presence of entanglement, and the interference term in Eq. (4.10) will always be present. The key point to understand the interference is that the discussed atomic state after the emission does not allow us to distinguish which emitter actually emitted the photon. On the other hand, for a separable state $|S_{n_e, N-n_e}\rangle$ it is possible to tell which atom emitted the photon by measuring their state.

As there is not a simple expression for the general N emitter W-state, lets consider the simple case of $|\mathrm{W}_{1,2}\rangle$. The emission intensity for the three-emitter state $|\mathrm{W}_{1,2}\rangle$, with only one emitter being in the state $|e\rangle$ is calculated to be proportional to [98].

$$\mathrm{I}_{|\mathrm{W}_{1,2}\rangle} = 1 + \frac{2}{3}\sum_{i<j=1}^{3}\cos(\varphi_i - \varphi_j). \tag{4.12}$$

The maximum detected intensity occurs when the emissions of the three emitters at the position of the detector are in phase, i.e., $\varphi_1 = \varphi_2 = \varphi_3$. For this example the maximum is $\mathrm{I}^{\max}_{|\mathrm{W}_{1,2}\rangle} = 3$, which can be decomposed as

$$\mathrm{I}^{\max}_{|\mathrm{W}_{1,2}\rangle} = n_e + \max(\text{interference term}) \tag{4.13}$$

where n_e accounts for the incoherent emission from the emitters. The detected intensity can be tuned by varying the distance between emitters or changing the direction of detection. The maximum intensity for the general case of W-states considered can be calculated as [98]

$$\mathrm{I}^{\max}_{|\mathrm{W}_{n_e,N-n_e}\rangle} = n_e + n_e(N - n_e). \tag{4.14}$$

For the particular case of $N = 2$ and $n_e = 1$ that we will study experimentally later in this chapter, the expected interference signal is

$$I_{|\mathrm{W}_{1,1}\rangle} = 1 + \cos(\varphi_1 - \varphi_2). \tag{4.15}$$

The maximum and minimum intensities are in this case 2 and 0, respectively.

In summary, the emission from separable states $|S_{n_e,N-n_e}\rangle$ does not exhibit interference, and the detected intensity is proportional to the number n_e of emitters in the excited state. On the other hand, entangled $|\mathrm{W}_{n_e,N-n_e}\rangle$ states exhibit interference in their emission, so that the measured emission intensity will depend of the direction and distance of the detection. Notice that none of these states are general separable or entangled states. In the following, we will discuss the interference properties of more general states of two emitters relevant for our experiment.

4.2.1 General case of two emitters

The most general pure state of two two-level emitters, denoted emitter A and emitter B, can be written as

$$|\beta\rangle = a|g,e\rangle + b|e,g\rangle + c|e,e\rangle + d|g,g\rangle, \tag{4.16}$$

where $a, b, c, d \in \mathbb{C}$ and $|a|^2 + |b|^2 + |c|^2 + |d|^2 = 1$. This state does not have a fixed number of excitations but instead a superposition: the probability of having two excitations is $|c|^2$, the probability of having one excitation is $|a|^2 + |b|^2$ and the probability of having no excitation is $|d|^2$.

In order to quantify the entanglement of the atomic state, let us introduce the *concurrence*, also called *amount of entanglement* [108]. The concurrence $\mathcal{C}$, in the case of two qubits, is a real number $\mathcal{C} \in [0,1]$ quantifying the amount of entanglement in the system, such that $\mathcal{C} = 0$ for separable states, $\mathcal{C} \neq 0$ for entangled states and $\mathcal{C} = 1$ for maximally entangled states. The concurrence can be calculated in the case of pure states as [109]

$$\mathcal{C} = |\langle\beta|\tilde{\beta}\rangle|, \tag{4.17}$$

where $\tilde{\beta}$ is defined as

$$\tilde{\beta} = (\hat{\sigma}_y \otimes \hat{\sigma}_y)|\beta^*\rangle, \tag{4.18}$$

and $|\beta^*\rangle$ is the complex conjugate of the vector $|\beta\rangle$. The concurrence of the state $|\beta\rangle$ is then given by

$$\mathcal{C}_{|\beta\rangle} = 2|cd - ab|. \tag{4.19}$$

Following the treatment introduced in the former section, the intensities of the emission produced by the state $|\beta\rangle$ will be proportional to $\mathrm{I}(\vec{r})$, defined in Eq. (4.10), which in this case can be written explicitly as

$$\begin{aligned} \mathrm{I}_{|\beta\rangle} \;=\; & |a|^2 + |b|^2 + 2|c|^2 \\ & + 2\Re\left[(c^*b + a^*d)(a^*c + d^*b)e^{i(\varphi_A - \varphi_B)}\right] \\ & + 2\Re\left[\{a^*b - (c^*b + a^*d)(a^*c + d^*b)\}\, e^{i(\varphi_A - \varphi_B)}\right], \end{aligned} \tag{4.20}$$

where φ_A and φ_B are the phases of the field emitted by emitter A and B at the position of the detector, $\Re$ means real part and * denotes the complex conjugate. The first line of Eq. (4.20) represents the incoherent contribution of each part of the superposition, which corresponds directly to the sum of probabilities of single and double excitations (double excitations will produce two photons). The second line, as before, contains the product of the expectation values of the dipole operators, and the third line the correlation terms. This expression can by simplified to

$$\mathrm{I}_{|\beta\rangle} = |a|^2 + |b|^2 + 2|c|^2 + 2\Re\left(a^*be^{i(\varphi_A - \varphi_B)}\right), \tag{4.21}$$

from which it is clear that the interference term is present only when both a and b are non zero. The maximum and minimum intensity are calculated to be proportional to

$$\mathrm{I}^{\max}_{|\beta\rangle} = |a|^2 + |b|^2 + 2|c|^2 + 2|ab|, \tag{4.22}$$

$$\mathrm{I}^{\min}_{|\beta\rangle} = |a|^2 + |b|^2 + 2|c|^2 - 2|ab|, \tag{4.23}$$

The maximum interference amplitude $\mathcal{A} = \mathrm{I}^{\max} - \mathrm{I}^{\min} = 4|ab| = 2$ occurs for

maximally entangled states ($\mathcal{C} = 1$) of the form

$$\frac{1}{\sqrt{2}}(|g,e\rangle + e^{i\phi}|e,g\rangle), \tag{4.24}$$

which correspond to states which have maximal quantum correlations and dipole operator expectation values equal to zero (see Eq. (4.20)). The visibility for these states is $\mathcal{V} = (\mathrm{I}^{\max} - \mathrm{I}^{\min})/(\mathrm{I}^{\max} + \mathrm{I}^{\min}) = 1$. For separable states ($\mathcal{C} = 0$), the maximum interference amplitude achievable is $\mathcal{A} = 1$ and visibility $\mathcal{V} = 1/2$, which occurs for states with maximum dipole operators expectations values and vanishing correlations. The visibility of the general state $|\beta\rangle$ is given by

$$\mathcal{V}_{|\beta\rangle} = \frac{2|ab|}{|a|^2 + |b|^2 + 2|c|^2}. \tag{4.25}$$

4.2.2 The single excitation subspace

The most interesting feature of the studied interference occurs in the single excitation subspace, spanned by the basis $\{|g,e\rangle, |e,g\rangle\}$, which corresponds to all the states with a fixed number of excitations $n_e = 1$. A general state in this subspace is

$$|\xi\rangle = a|g,e\rangle + b|e,g\rangle, \tag{4.26}$$

with $|a|^2 + |b|^2 = 1$. In this case the concurrence is $\mathcal{C}_{|\xi\rangle} = 2|ab|$ and has the same value as the visibility $\mathcal{V}_{|\xi\rangle} = 2|ab|$. Therefore, the measurement of a full interference fringe can be directly used to quantify the entanglement. Separable states in this subspace, i.e., $|e,g\rangle$ and $|g,e\rangle$ do not exhibit interference, and hence $\mathcal{V} = \mathcal{C} = 0$. Oppositely, maximally entangled states such that $|a| = |b| = \frac{1}{\sqrt{2}}$ have maximum visibility $\mathcal{V} = \mathcal{C} = 1$.

This result is still valid for mixed states in this subspace when detecting in the far field, as demonstrated in Ref. [110]. In that case the density matrix can be written as

$$\rho = \begin{pmatrix} \rho_{eg,eg} & \rho_{eg,ge} \\ \rho_{ge,eg} & \rho_{ge,ge} \end{pmatrix} \tag{4.27}$$

such that $\mathcal{C}(\rho) = \mathcal{V}(\rho) = 2|\rho_{eg,ge}|$.

There is not a general relation between the observed interference of N emitters and the amount of entanglement, mostly because defining measures of multipartite entanglement is not straight forward as in the case of two emitters. However, it is possible to define bounds for the minimum entanglement present in the emitting system when observing some degree of interference in some particular cases, as shown in Ref. [110].

Ions are excellent candidates for studying the predictions presented here because atomic localizations well bellow the emission wavelength can be readily achieved. Furthermore our setup features a collection efficiency which allows for experiments

at the single photon level. In the following section, we present an experiment in which we prepare an entangled state of two trapped ions and observe tuning of the emission rate by interference of single photons. In particular, we aim to compare the interference of single photons emitted by a pair of atoms, prepared in the states

$$|\psi\rangle = \frac{1}{\sqrt{2}}(|g,e\rangle + e^{i\phi}|e,g\rangle), \tag{4.28}$$

$$|\zeta\rangle = |eg\rangle, \tag{4.29}$$

$$|\xi\rangle = \frac{1}{2}(|g\rangle + |e\rangle)(|g\rangle + |e\rangle). \tag{4.30}$$

The first state is an entangled state, which we generate optically using the so-called Cabrillo scheme [9]. The other two are separable states with a fixed and a superposition of number of excitations, respectively. Each of these three states have different interference properties as we shall see in the next section.

4.3 Entanglement of separated atoms via single photon detection

There are several ways to create entanglement in a chain of trapped ions. The most robust approaches are based on the realization of conditional logic gates between different ions by taking advantage of their motional coupling. Such methods include the realization of the so-called Cirac-Zoller gate [38,111], the Mølmer-Sørensen gate [112,113] and the geometric phase gate [114,115]. These kinds of gates can generate high fidelity entanglement between several ions and have been the cornerstone in the development of quantum computing with trapped ions. However, since they rely on the coupling of the ions to the same motional mode, they cannot be used to generate entanglement between distant ions.

Another approach to generate entanglement between ions is through the detection of single photons emitted by the trapped ions. One of the methods based on this approach consists of first entangling the internal state of the ions with, e.g., the polarization of an emitted photon. Thereafter, by performing a Bell measurement of the state of photons emitted by different ions, it is posible to swap the entanglement to create ion-ion entanglement. This method was first demonstrated for two distant trapped ions by Moehring et al. [116] and relies on the coincident detection of two photons emitted by the separated ions.

A second method based on the detection of emitted photons was proposed by Cabrillo et al. [9]. This method requires the detection of only one photon emitted by the ion pair undergoing a Raman transition. The photon is detected in an interferometric arrangement, such that it is not possible to distinguish which ion emitted it. The detection of a photon in such a setup projects the state of the ions into an entangled state. This method was first demonstrated with trapped ions in our laboratory by Slodička et al. [117], and is the entanglement generation method that we use in the experiments presented in this thesis. This approach is more efficient than methods requiring the detection of two photons for the currently achievable

single photon detection efficiencies [79]. Furthermore, it allows us to demonstrate fully optical creation and characterization of entanglement when combined with the observation of single photon interference presented in this thesis.

In the following section, a detailed description of the Cabrillo entangling scheme and its implementation is provided.

4.3.1 The Cabrillo scheme

The Cabrillo scheme [9] is based on the detection of a single photon emitted during a Raman process in one of the atoms. To illustrate how it works, let us consider two atoms, A and B, at different locations, both prepared in the ground state $|g_-\rangle$, see Fig. 4.1. Each atom is excited to a short-lived intermediate state $|i\rangle$, which can decay to a different ground state $|g_+\rangle$, through the spontaneous Raman process $|g_-\rangle \rightarrow |i\rangle \rightarrow |g_+\rangle$. If this Raman process is successful, the atom will emit a single photon with the wavelength and polarization corresponding to the $|i\rangle \leftrightarrow |g_+\rangle$ transition. The state after driving the Raman process for each atom, with probability p_e, is given by

$$|s,n\rangle_j = \sqrt{1-p_e}|g_-,0\rangle + \sqrt{p_e}|g_+,1\rangle e^{i\phi_{\mathrm{D},j}+i\phi_{\mathrm{L},j}}, \tag{4.31}$$

where s represents the internal state of the atom $j = \mathrm{A}$ or B, and n is the photon occupation number of the emitted field, $\phi_{\mathrm{L},j}$ is the phase of the laser driving the transition $|g_-\rangle \rightarrow |i\rangle$ at the position of the atom j and $\phi_{\mathrm{D},j}$ is the phase acquired by the photon emitted by the atom j on its way to the position of a single photon detector. If both atoms undergo the same Raman process, the total state of the system is then given by

$$\begin{aligned} |s_\mathrm{A}, s_\mathrm{B}, n_\mathrm{A}, n_\mathrm{A}\rangle \;=\; & (1-p_e)|g_-,g_-,0,0\rangle \\ & +\sqrt{p_e(1-p_e)}\Big(e^{i(\phi_{\mathrm{L,A}}+\phi_{\mathrm{D,A}})}|g_+,g_-,1,0\rangle \\ & +e^{i(\phi_{\mathrm{L,B}}+\phi_{\mathrm{D,B}})}|g_-,g_+,0,1\rangle\Big) \\ & +p_e e^{i(\phi_{\mathrm{L,A}}+\phi_{\mathrm{L,B}}+\phi_{\mathrm{D,A}}+\phi_{\mathrm{D,B}})}|g_+,g_+,1,1\rangle. \end{aligned} \tag{4.32}$$

If the detection modes of the emission of atoms A and B are overlapped and the photons emitted from both atoms are indistinguishable, the detection of a single photon will project the state of both atoms onto the entangled state

$$|\psi^\phi\rangle = \frac{1}{\sqrt{2}}\Big(|g_+,g_-\rangle + e^{i\phi}|g_-,g_+\rangle\Big) \tag{4.33}$$

with probability $2p_e(1-p_e)$, and where the phase ϕ is defined as

$$\phi = (\phi_{\mathrm{L,B}} - \phi_{\mathrm{L,A}}) + (\phi_{\mathrm{D,B}} - \phi_{\mathrm{D,A}}). \tag{4.34}$$

If the single photon detection efficiency η is the same for both atoms, then the overall probability of creating the state $|\psi^\phi\rangle$ is $2\eta p_e(1-p_e)$.

Since the single photon detection efficiency η in our setup is typically in the few percent range, the detection of a single photon could correspond to the projection onto $|g_+, g_+\rangle$ as well. In this case, each of the two atoms emits one photon, but only one is detected due the imperfect efficiency. In general, APDs or PMTs cannot distinguish between the detection of a single photon or two simultaneous photons, and therefore, even for perfect light collection, a click in the detectors can project the atoms' state onto $|g_+, g_+\rangle$. To avoid this, the probability of successful Raman process p_e has to be kept small, such the probability p_e^2 of projection onto $|g_+, g_+\rangle$ is negligible. However, this also reduces the overall probability of generating the aimed state $|\psi^\phi\rangle$. The choice of p_e is therefore a trade-off between the overall success probability and the fidelity of the obtained state. In our experiment we set $p_e \approx 6\%$, such that the probability of double excitation p_e^2 is 0.36 %.

As mentioned before, this scheme does not rely on the proximity of the atoms and is an efficient way to create entanglement between distant atoms in the low detection efficiency regime, since it does not require the coincidence detection of photons. Controlling the phase ϕ of the generating state and being able to produce the same state in a repeatable manner requires phase stability of the detection path and the exciting lasers. This requirement can be challenging, but is achievable with current technology. Another requirement is that the photons detected from different atoms have to be indistinguishable in all the degrees of freedom. In this way, a single detected photon does not contain any information about which atom emitted it. This can be achieved be detecting photons in a single spatial and polarization mode by filtering out photons in other modes, although at the cost of reducing the collection efficiency, as we will see in the next section.

An important feature of the generated state is that it belongs to a *decoherence-free subspace*. This means that if one of the states forming the qubit dephases with respect to the other, e.g. after a time $|g_+\rangle$ evolves into $e^{i\phi_t}|g_+\rangle$, the dephasing occurs equally for both parts of the superposition, and therefore is only a trivial global phase, i.e.,

$$|\psi^\phi\rangle = \frac{1}{\sqrt{2}}(|g_+, g_-\rangle + e^{i\phi}|g_-, g_+\rangle) \rightarrow \frac{1}{\sqrt{2}}(e^{i\phi_t}|g_+, g_-\rangle + e^{i(\phi+\phi_t)}|g_-, g_+\rangle) = e^{i\phi_t}|\psi^\phi\rangle$$

Hence, if both atoms are subject to the same magnetic field fluctuations, an entangled bipartite qubit such as $|\psi^\phi\rangle$ will lose coherence much slower than a qubit stored in a single atom. Furthermore, using ground states as qubit states as we do in our experiment also suppresses the decoherence due to spontaneous emission. The coherence time of the entangled state in the ground state decoherence-free subspace is expected to be orders of magnitude longer than a qubit encoded in a single atom, as demonstrated in Ref. [118], where coherence times of more than 20 s were achieved.

4.3.2 Entanglement generation

To implement the Cabrillo scheme we trap and Doppler cool two $^{138}Ba^+$ ions along the symmetry axis of our linear Paul trap, separated by a distance $z \simeq 5.2$ μm. The HALO objectives (see Chapter 3) are used to collect and collimate part of the light emitted by the ions. A distant mirror at distance $d/2 \simeq 30$ cm from the trap

axis outside the vacuum chamber superimposes the emission of both ions, so that their spatial mode is overlapped and coupled to a single mode fiber. The whole setup is depicted in Fig. 4.1a. A magnetic field $\vec{B}$ is applied along the axis used for the pumping and excitation beams (see Fig. 3.8), defining a quantization axis and Zeeman splitting the electronic levels.

The electronics states involved in the Cabrillo entangling scheme are $|g_-\rangle = |6S_{1/2}, m_j = -1/2\rangle$, $|i\rangle = |6P_{1/2}, m_j = +1/2\rangle$ and $|g_+\rangle = |6S_{1/2}, m_j = +1/2\rangle$. The ions are prepared in the initial state $|g_-, g_-\rangle$ by optical pumping using a 493 nm σ^--polarized beam driving the transition $|6S_{1/2}, m_j = +1/2\rangle \leftrightarrow |6P_{1/2}, m_j = -1/2\rangle$, and a 650 nm repumper beam, driving all possible transitions between the $5D_{3/2}$ and $6P_{1/2}$ manifolds (Fig. 4.1b). After optical pumping, the ions are prepared in $|g_-, g_-\rangle$ with more than 99.98% probability. The population of this state is measured using the electron-shelving technique presented in Section 3.4.3.

Thereafter, a weak σ^+-polarized beam driving the transition $|g_-\rangle \rightarrow |i\rangle$ is sent to the ions (Fig. 4.1c). The Rayleigh length of the beam is bigger than the separation of the ions, so they are excited with approximately the same probability (measured in Section 4.3.2). If one of the ions is excited to the $|i\rangle$ state, it can spontaneously decay to the $5D_{3/2}$ manifold emitting a 650 nm photon, to the $|g_-\rangle$ state emitting a 493 nm σ^+-polarized photon or to the $|g_+\rangle$ state emitting a 493 nm π-polarized photon. The intensity and length of the pulse is such that the probability of success of the Raman process $|g_-\rangle \rightarrow |i\rangle \rightarrow |g_+\rangle$ is $p_e \approx 6\%$, as discussed in the next section. If the emission from different ions is indistinguishable in the detector, the detection of a single 493 nm π-polarized photon projects the ions onto a entangled state such as the one in Eq. (4.33). To avoid the detection of single photons that would lead to the projection onto a different state, the 650 nm photons are filtered out with more than 99.99% efficiency using a laser line filter[1] (Fig. 4.1a). This filter has transmittance of 97% at 493nm. 493 nm σ^+-polarized photons are filtered out using a PBS, given that in the collimated beam they are mostly vertically polarized, allowing us to filter out more than 99.5% of these photons. After these filtering steps, more that 99.49% of the photons coupled to the single mode fiber (SMF in Fig. 4.1a) are π-polarized 493 nm photons, the detection of which leads to generation of entanglement.

The phase ϕ of the generated entangled state of Eq. (4.34), provided that in our setup $d \gg z$, is given explicitly by

$$\phi = kz + kd, \tag{4.35}$$

where $k = 2\pi/\lambda$. Therefore, the phase ϕ of the entangled state can be tuned by either changing the separation z between the ions or by changing the length of the optical path connecting them. In our experiment we take the second approach: we tune the phase ϕ by changing the position of the mirror with sub-wavelength precision by varying the voltage applied to a piezoelectric transducer attached to the mirror holder. In contrast to changing the separation z between the ions, this method does not introduce additional heating of the motional modes.

There are some crucial points that have to be experimentally addressed to achieve high fidelity entanglement generation. First, the photon whose detection generates

[1] Semrock FF01-494-20-25

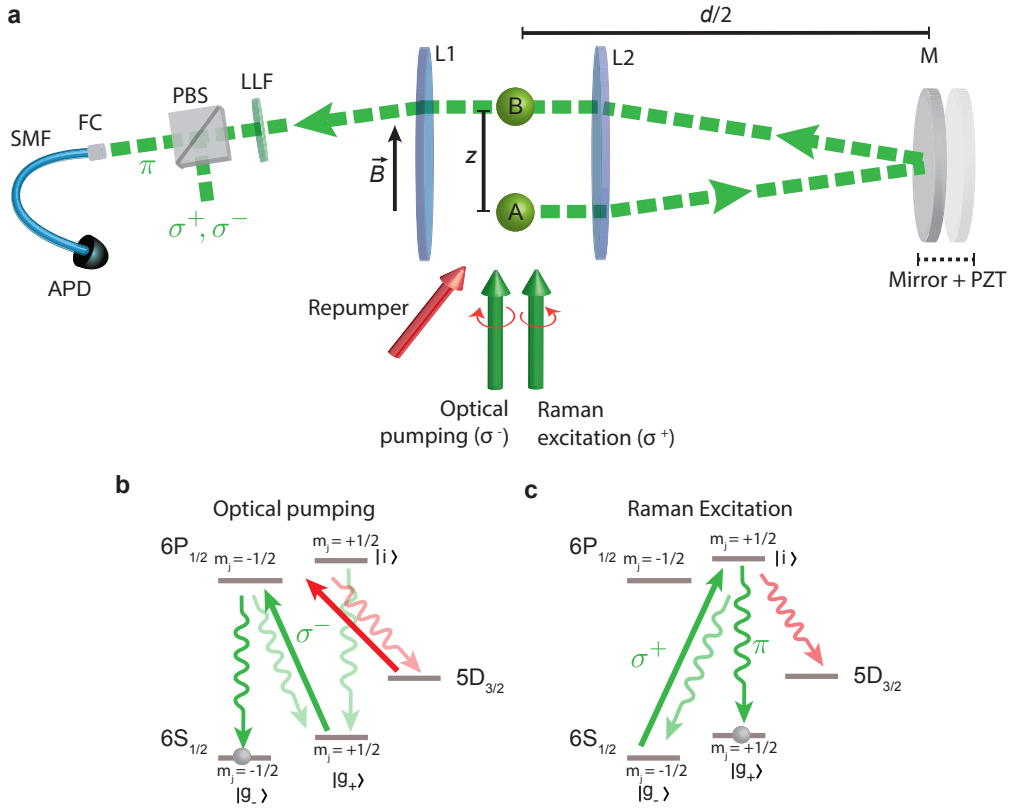

Figure 4.1: Cabrillo entangling scheme implementation. a. Two $^{138}Ba^{+}$ ions, A and B, are trapped and cooled in a linear Paul trap, separated by a distance $z \simeq 5.2\,\mu$m. The radiation fields are collimated using two identical in-vacuum HALO objectives (L1 and L2). A mirror (M) at a distance $d/2 \simeq 30\,$cm superimposes the emissions from the ions so that they are coupled to a common spatial mode. The mirror is mounted on piezoelectric transducers (PZT) that allow fast sub-wavelength control of the ion-ion distance in the common optical mode. A laser line filter (LLF) filters out photons with wavelength other than 493 ± 20 nm. A polarizing beam splitter (PBS) selects π-polarized photons, which are coupled to a single-mode fiber (SMF) using a fiber collimator (FC) and detected by an avalanche photodiode (APD). **b.** A 493 nm σ^{-}-polarized laser beam, parallel to the magnetic field $\vec{B}$ and a 650 nm repumper are used to prepare the initial state $|g_-, g_-\rangle$. **b.** A weak 493 nm σ^{-}-polarized laser beam is use to drive the Raman process $|g_-\rangle \rightarrow |i\rangle \rightarrow |g_+\rangle$, which when successful results in the emission of a π-polarized photon from the ions.

entanglement must not carry information about which ion emitted it. This means that all the photons detected have to be identical, and that all the photons detected have the same probability of coming from any of the ions. This could be achieved by equally coupling the emission of both ion to the detected optical mode, and by exciting both ions with the exact same probability. Second, the photon whose detection generates entanglement must not carry information about which ion emitted it. A second important experimental issue, is that in order to create repetitively the same entangled state we need to be able to control the value of the entanglement phase ϕ. In the following, we address these points.

Calibration of the excitation pulse

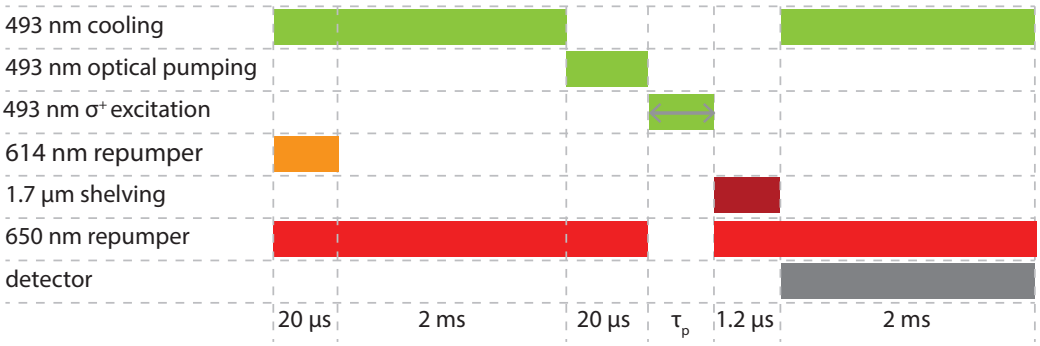

Figure 4.2: Sequence for calibration of the excitation pulse length. After Doppler cooling and pumping both ions into the initial state $|g_-\rangle$, the weak σ^+-polarized pulse with variable length τ_p is sent to the ions, driving the $|g_-\rangle \rightarrow |i\rangle$ transition. Then the population not transferred to the $|g_+\rangle$ is shelved to the $5D_{5/2}, m_j = -5/2$ state. Finally, the fluorescence of each ion is measured independently and simultaneously using two APDs (see main text).

To avoid the excitation of both ions up to a negligible level in comparison with the single excitation events, the strength of the exciting pulse has to be small. At the same time, decreasing the excitation probability reduces the rate of entanglement generation. Due to this trade-off between entangled state fidelity and achievable entanglement generation rate we chose $p_e \approx 6\%$. To create an entangled state such as in Eq. (4.33) it is also necessary that both ions are excited equally. To calibrate the intensity and length of the pulse we measure the population of both ground state $|g_-\rangle$ and $|g_+\rangle$ of each ion individually after applying the excitation pulse. The populations are measured by shelving the state $|g_-\rangle$ and measuring the fluorescence thereafter (Section 3.4.3). The sequence used for this purpose is shown in Fig. 4.2. The sequence is repeated with different excitation pulse lengths, in the 0 - 1 μs range using an AOM and keeping the input laser power and detuning constant. In order to check that both ions are excited with the same strength to $|i\rangle$ after the optical pumping, we measured independently and simultaneously the fluorescence from each ion with a detection setup similar to the one in Fig. 3.6c, but using the left-side HALO only, and coupling the emission of each ion to an independent APD. The results of such a scan for each ion are shown in Fig. 4.3. The fluorescence intensity corresponding to 100% of the populations being in the state $|g_+\rangle$ is set by the maximum fluorescence measured during Doppler cooling with the same detection configuration. The independent exponential fits show that a pulse of $\tau_p = 48$ ns

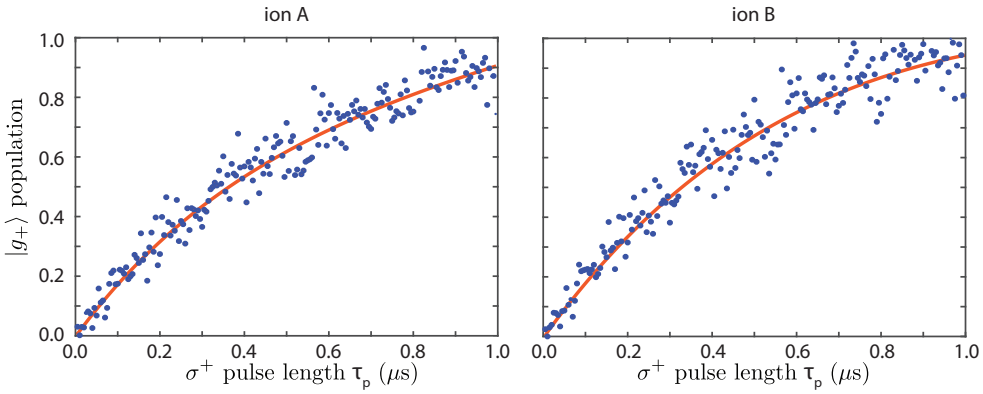

Figure 4.3: Excitation pulse length calibration. Probability of ending in the state $|g_+\rangle$, for ion A and ion B. The independent exponential fits show that a pulse of $\tau_p = 48$ ns corresponds to a probability of 6 ± 1, equal for both ions.

corresponds to 6 ± 1 % probability of having a successful Raman process, equally for both ions. Note that the 48 ns corresponds to the length of the square envelope RF pulse sent to the AOM generating the optical pulse, although, as this RF pulse is shorter than the rise time of the AOM (70 ns), the resulting pulse has a symmetrical triangular shape, with an average power of 95 nW and a FWHM of 29 ns (measured with a fast photodiode). The shape of this pulse does not play role in the experiment.

Note that Fig. 4.3 shows the statistical average of the populations of the $|g_+\rangle$ for each ion, where each point represents 100 repetitions of the same experiment. However, it does not mean that, for example, sending a 48 ns pulse will excite both simultaneously with 6 % probabilities. By looking at the detection correlations between photons detected by either APD, we estimate that the probability of exciting both ions with a 48 ns pulse are 1 ± 1 %.

Photon indistinguishability

A crucial ingredient in the Cabrillo scheme is that in order to project the state of the atoms into a symmetric entangled state such as the one in Eq. (4.33), the photon detected in the common optical mode should not provide information about which ion emitted it. Therefore, photons emitted by different atoms ideally have to be completely indistinguishable from each other. To characterize the degree of indistinguishability of these photons, we measure the second order temporal correlation function $g^2(\tau)$ of the detected field. This function quantifies the temporal correlations between the detection of two consecutive photons, separated by a delay time τ. The value of $g^2(\tau = 0)$ directly quantifies the degree of indistinguishability of two fields [119]. To be able to measure correlations at times much shorter than the detector dead time we slightly modify the detection setup shown in Fig. 4.1a to realize a Hanbury-Brown-Twiss detection scheme. This is achieved by replacing the single-mode fiber (SMF) by a single-mode-fiber beamsplitter, and coupling its outputs to independent APDs, as shown in Fig. 4.4a. Each detected photon is then time tagged with 4 ps resolution and the obtained detection histories are then analysed to extract the values of $g^2(\tau)$ using time bins of 512 ps.

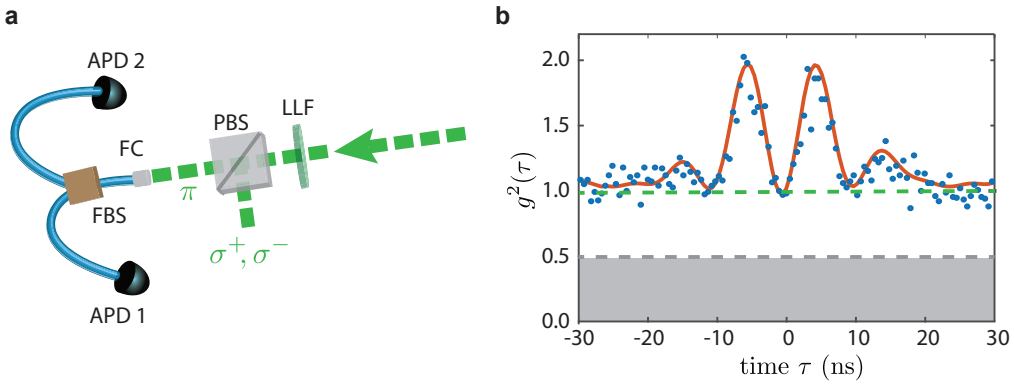

Figure 4.4: Indistinguishability of the detected photons from different ions. a. Hanbury-Brown-Twiss detection configuration for measuring of the second order temporal correlation function of the detected field $g^2(\tau)$. The overlapped photons emitted by different ions are filtered in wavelength using a laser line filter (LLF) which let only 493 nm photons pass and in polarization using a PBS, and then coupled to a 50/50-single-mode-fiber beamsplitter (FBS). The photons at each output of the beamsplitter are detected with two different APDs (APD1 and APD2). Each detected photon is time-tagged using the PicoHarp 300. **b.** Measured $g^2(\tau)$ function, normalized to $g^2(\tau \to \infty)$. The second order correlation at zero delay is estimated to be $g^2(\tau = 0) = 0.99 \pm 0.06$, corresponding to near perfectly indistinguishable photons. The dashed green line shows the ideal value $g^2(\tau = 0) = 1$ for totally indistinguishable fields, whereas the grey dashed line shows the $g^2(\tau = 0) = 1/2$ for fully distinguishable fields.

While the PBS and the single-mode fibers ensure that the detected photons have the same polarization and spatial mode, the indistinguishability could be reduced by the fact that the detection rate from the ion A amounts to only 60% of the detection rate from the ion B. This imbalance is due to larger optical losses for the ion A due to additional propagation through an in-vacuum lens, optical viewports and imperfect reflectivity on the distant mirror. Additionally, there is a significant mode mismatch after propagation along the long path with respect to the fiber coupled mode. This imbalance can be compensated by a precise angular adjustment of the distant mirror and of the fiber coupler, reducing the detection rate of ion B to equal to that from the ion A. To achieve this, first, the mirror is blocked and the fiber coupler is misaligned so that the detected rate from atom B equals the previously measured detected rate from atom A. Then the mirror is uncovered, and its tilt is adjusted while scanning its distance to the trap until achieving maximum interference visibility.

The obtained $g^2(\tau)$ after optically correcting the detection unbalance is shown in Fig. 4.4b, where the data points are normalized by the measured $g^2(\tau \to \infty)$. The ideal value for totally indistinguishable fields is $g^2(\tau = 0) = 1$ in this normalization (green dashed line in Fig. 4.4b), whereas $g^2(\tau = 0) \leq 1/2$ corresponds to fully distinguishable fields (grey area in Fig. 4.4b). The second order correlation at zero delay is estimated to be $g^2(\tau = 0) = 0.99 \pm 0.06$, corresponding to near perfectly indistinguishable photons.

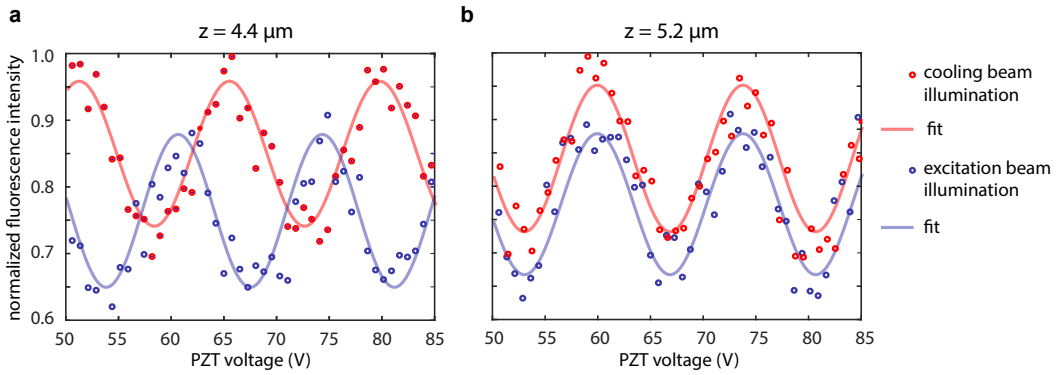

Figure 4.5: Interference phase control. The appropriate distance matching the phases of the interference signal produced by illuminating the ions with the cooling and the excitation beams is found by scanning the mirror distance $d/2$ with the PZTs while recording the ions fluorescence intensity alternately produced by illuminating with the cooling or excitation beam, for different trap tip voltages (ion separations) **a.** Interference patterns at ion distance $z = 4.4$ μm (tip voltages = 700 V). The interference signals show a phase difference 1.6 $\pm$ 0.2 rad.**b.** Interference patters at ion distance $z = 5.2$ μm (tip voltages = 400 V). The interference signals show a phase difference 0.2 $\pm$ 0.2 rad. Both signals are normalized to the maximum detected fluorescence rate.

Phase control

To monitor, define and lock the length of the interference path between the ions which sets the entangling phase ϕ we record the intensity of the resonant fluorescence during the Doppler cooling stage. Due to interference in the emitted fluorescence of the two ions, the detected intensity gives us information about the relative phase of both detected fields. The cooling and excitation beams do not copropagate, and therefore, the relative phase of the interference signal when using either of these beams varies depending on the separation z of the ions. To make the monitoring and selection of the phase easy, we match the interference signals by finding the appropriate ion separation z by symmetrically changing the trap tip voltages until reaching a value where the relative phase between both signals is zero. Fig. 4.5 shows the resonance florescence intensity when illuminating alternately the two ions with the cooling and the excitation beams (with polarization adjusted such that no optical pumping occurs), while scanning the distance of the mirror d. Fig. 4.5a show the case of both interference signals with $z = 4.4$ μm, exhibiting a relative phase of 1.6 $\pm$ 0.2 rad, and Fig. 4.5b shows the case of relative phase 0.2 $\pm$ 0.2 rad for $z = 5.2$ μm. The latter is the setting used in the entanglement experiment.

Hence, by locking the distance of the mirror to a point where the interference during the cooling stage is maximum we can create an entangled state with phase $\phi = 0$. Conversely, locking the distance of the mirror to an interference minimum corresponds to the creation of a entangled state with $\phi = \pi$. Other phases can be set by choosing other locking points.

The visibility of the fringes shown is Fig. 4.5 does not correspond to the one achieved during the actual entanglement generation and emission from entangled

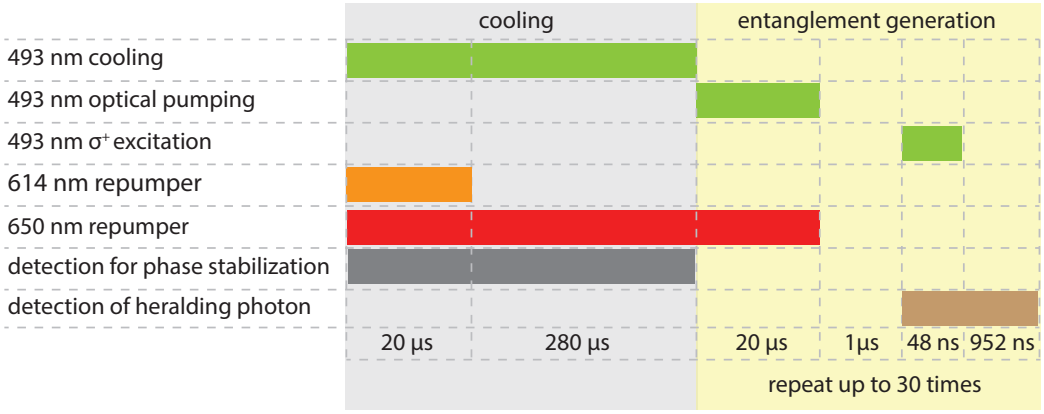

Figure 4.6: Sequence for entanglement generation. The sequence used for entanglement generation consists of two stages. In a first stage (grey shaded area) the ions are Doopler cooled. The fluorescence detected during this stage in the common optical mode is used to stabilize the interference phase (Section 4.3.2). In the second stage (yellow shaded) both ions are prepared in the initial state $|g_-, g_-\rangle$ via optical pumping, and then the weak 48 ns excitation pulse is sent. Starting simultaneously the APD is gated for 1 μs. If a single photon is detected during this period, the entanglement process is successful, if not, the entanglement generation stage is repeated up to 30 times.

states experiments. In that case, the visibility is optimized to achieve the value $V = 0.37 \pm 0.02$. The visibility is mostly limited by the motion of the ions [120].

Experimental sequence for entanglement generation

So far, we have shown that the requirements needed to generate entanglement using the Cabrillo scheme are fulfilled. We now show how these different ingredients are combined to generate entanglement. To do so, we use the setup presented in Fig. 4.1 and the sequence shown if Fig. 4.6. This sequence is composed of two stages: First, a cooling stage, and second, an entanglement generation stage. In the first stage the ions are pumped into the cooling manifold and Doppler-cooled for 300 μs. The fluorescence detected during this period is used to stabilize the interference phase between the two ions by slightly adjusting the position of the distant mirror and keeping the detected fluorescence at a given level.

In the second stage, i.e., the entanglement generation stage, the ions are prepared in the initial state $|g_-, g_-\rangle$ by optical pumping with the 493 nm σ^--polarized beam and the 650 nm repumper. Thereafter, the ions are weakly excited in the $|g_-\rangle \rightarrow |i\rangle$ transition with the 48 ns σ^+-polarized pulse. Starting simultaneously with the excitation pulse, the APD is gated during 1 μs. If a "heralding" photon is detected in the common optical mode defined by the optical fiber, the PBS and the filter, the process of entanglement generation is successful. If this is the case, a characterization stage is initiated (not shown in the figure). If no photon is detected, the entanglement generation stage is repeated, including the inital state preparation. The generation stage is repeated up to 30 times, and if no photon is detected in these 30 attempts, the cooling stage is repeated. This is necessary in order to avoid decoherence due to motional heating and phase uncertainty due to mechanical drifts of the mirror

position that can lead to phase uncertainty.

Following this procedure, we achieve a heralding-photon detection rate, corresponding to the number of entanglement events, of $5.02\,\mathrm{s}^{-1}$. This rate is mostly limited by the overall detection efficiency $\eta \approx 0.002$, constrained primarily by the NA $= 0.40$ of the in-vacuum lenses, which allow us to collect $\approx 6\%$ of the spontaneous emission from the desired transition in the common mode. Additional optical losses are caused by the lenses and viewports, reflections from the distant mirror, the rest of the optical elements and imperfect coupling into the single-mode fiber, with combined transmission $T \approx 0.07$. The quantum efficiency of the APD is $\approx 70\%$.

The detection of a single photon at the end of the generation stage is not a proof of generation of entanglement. After the detection of the heralding photon a state characterization stage is performed. The presence of entanglement in the ion pair is confirmed in typical experiments by performing full tomography of the state [121], or by measuring some observable that acts as an entanglement witness [122, 123]. In our experiment we characterize the entanglement by measuring "parity oscillations" [113], as presented in the next section.

4.3.3 Entanglement characterization

The method used to generate entanglement ideally creates the state $\frac{1}{\sqrt{2}}(|g_+, g_-\rangle + e^{i\phi}|g_-, g_+\rangle)$ with a phase ϕ which is independent of any absolute laser phase. Instead, it depends only on geometrical parameters defining the relative phase of photons emitted by different ions. The phase ϕ is not related to the absolute phase of the 1.7 μm laser or the RF radiation that could be used to perform state tomography. Therefore, state tomography cannot be properly performed when using the presented entangling scheme. Instead, a method that does not rely on the phase relation of the analysing pulses and the entanglement phase is required.

The approach that we take is the measurement of parity oscillations [113]. This method permits us to access the elements of the state's experimentally generated density matrix ρ^ϕ which contribute to the overlap with the desired theoretical state $|\psi^\phi\rangle$, allowing the calculation of the fidelity of the created state $F = \langle\psi^\phi|\hat{\rho}^\phi|\psi^\phi\rangle$. This method is based on Ramsey-like interference measurements and gives a direct estimation of the coherence between the $|g_-, g_+\rangle$ and $|g_+, g_-\rangle$ states. Furthermore, it requires only global qubit rotations, and therefore, single ion laser addressing is not necessary.

The most general density matrix for a two-qubit system, with qubit states $|g_-\rangle$ and $|g_+\rangle$ is given by

$$\hat{\rho} = \begin{pmatrix} \rho_{g_-,g_-} & \rho_{g_-g_-,g_+g_-} & \rho_{g_-g_-,g_-g_+} & \rho_{g_-g_-,g_+g_+} \\ \rho^*_{g_-g_-,g_+g_-} & \rho_{g_+,g_-} & \rho_{g_+g_-,g_-g_+} & \rho_{g_+g_-,g_+g_+} \\ \rho^*_{g_-g_-,g_-g_+} & \rho^*_{g_+g_-,g_-g_+} & \rho_{g_-,g_+} & \rho_{g_-g_+,g_+g_+} \\ \rho^*_{g_-g_-,g_+g_+} & \rho^*_{g_+g_-,g_+g_+} & \rho^*_{g_-g_+,g_+g_+} & \rho_{g_+,g_+} \end{pmatrix}, \tag{4.36}$$

First rotation	Second rotation	Measurement Result
–	–	$\rho_{g_-,g_-} + \rho_{g_+,g_+} - (\rho_{g_+,g_-} + \rho_{g_+,g_-})$
$\hat{R}(\pi/2,0)_{\mathrm{G}}$	–	$2\Re(\rho_{g_-g_+,g_+g_-} - \rho_{g_-g_-,g_+g_+})$
$\hat{R}(\pi/2,\pi/4)_{\mathrm{G}}$	–	$2\Re(\rho_{g_-g_+,g_+g_-}) + 2\Im(\rho_{g_-g_-,g_+g_+})$
$\hat{R}(\pi/2,\pi/2)_{\mathrm{G}}$	–	$2\Re(\rho_{g_-g_+,g_+g_-} + \rho_{g_-g_-,g_+g_+})$
$\hat{R}(\pi/2,\pi/2)_{\mathrm{G}}$	$\hat{R}(\pi/2,0)_{\mathrm{G}}$	$2\Re(\rho_{g_-g_+,g_+g_-} - \rho_{g_-g_-,g_+g_+})$
$\hat{R}(\pi/2,\pi/2)_{\mathrm{G}}$	$\hat{R}(\pi/2,\pi/2)_{\mathrm{G}}$	$\rho_{g_-,g_-} + \rho_{g_+,g_+} - (\rho_{g_+,g_-} + \rho_{g_+,g_-})$

Table 4.1: Parity operator expectation values after applying global rotations to the experimental state $\hat{\rho}$. $\Re$ and $\Im$ symbolises real and imaginary part respectively.

with $\hat{\rho}^\dagger = \hat{\rho}$ and $\mathrm{Tr}(\hat{\rho}) = 1$. The parity operator for two states is defined as

$$\hat{P} = |g_-g_-\rangle\langle g_-g_-| + |g_+g_+\rangle\langle g_+g_+| - |g_-g_-\rangle\langle g_+g_+| - |g_+g_+\rangle\langle g_-g_-|, \tag{4.37}$$

so that its expectation value is given by

$$\langle\hat{P}\rangle = \mathrm{Tr}(\hat{P}\hat{\rho}) = \rho_{g_-,g_-} + \rho_{g_+,g_+} - (\rho_{g_-,g_+} + \rho_{g_+,g_-}). \tag{4.38}$$

To access the value of the coherence terms of the density matrix we can apply global qubit rotations over the generated ion states. The rotations can be composed by one or two pulses in the RF transition connecting the $|g_-\rangle$ and $|g_+\rangle$ states (Section 3.4.3). Such a global rotation is defined by the operator

$$\hat{R}(\theta,\phi_R)_{\mathrm{G}} = \hat{R}(\theta,\phi_R)_{\mathrm{A}} \otimes \hat{R}(\theta,\phi_R)_{\mathrm{B}}, \tag{4.39}$$

where $\hat{R}(\theta,\phi_R)_{A(B)}$ are defined as in Eq. 3.15 and A(B) designate each ion. If two pulses $\hat{R}(\pi/2,\pi/2)_{\mathrm{G}}$ and $\hat{R}(\pi/2,\phi_R)_{\mathrm{G}}$ are applied consecutively before measuring the parity operator, the expectation value of the parity operator is given by

$$\left\langle\hat{P}(\phi_R)\right\rangle = \mathrm{Tr}\left(\hat{P}\hat{R}(\pi/2,\phi_R)_{\mathrm{G}}\hat{R}(\pi/2,\pi/2)_{\mathrm{G}}\hat{\rho}\hat{R}(\pi/2,\pi/2)^\dagger_{\mathrm{G}}\hat{R}(\pi/2,\phi_R)^\dagger_{\mathrm{G}}\right). \tag{4.40}$$

The outcome of the measurement of the parity operator after different sequences of global rotations are shown in Table 4.1.

In the case of the pure state $|\psi^\phi\rangle = \frac{1}{\sqrt{2}}(|g_-,g_+\rangle + e^{i\phi}|g_+,g_-\rangle)$, the parity signal after the rotations $\hat{R}(\pi/2,\phi_R)_{\mathrm{G}}\hat{R}(\pi/2,\pi/2)_{\mathrm{G}}$ is given by

$$\left\langle\hat{P}(\phi_R)\right\rangle_{|\psi^\phi\rangle} = \cos(2\phi_R + \phi). \tag{4.41}$$

For imperfect experimentally generated states, this signal can be phase-shifted, reduced in amplitude or show offsets.

The fidelity of the experimentally generated state $\hat{\rho}$ with respect to the state

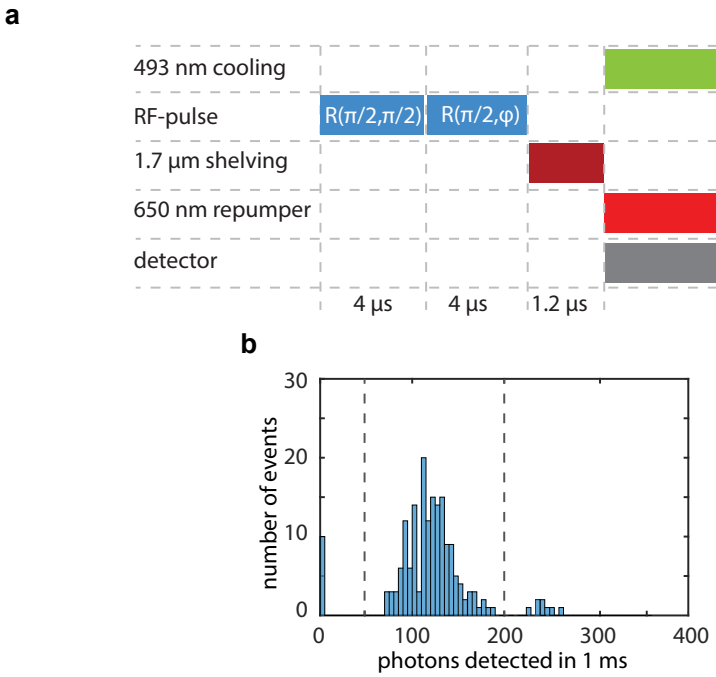

Figure 4.7: Sequence for measurement of the parity operator. a. The sequence used for measurement of the parity operator consist of RF-qubit rotations followed by shelving of the $|g_-\rangle$ state and measurement of the fluorescence of both ions. **b.** Histogram of the detected fluorescence after shelving without any qubit rotation. The dashed vertical lines mark the treshold between three different fluorescence levels (see main text). By integration of the number of events in each region, the estimated populations of the experimental state are $\rho_{g_-,g_+} + \rho_{g_+,g_-} = 91 \pm 3\,\%$, $\rho_{g_-,g_-} = 5 \pm 1\,\%$ and $\rho_{g_+,g_+} = 4 \pm 2\,\%$.

$|\psi^{\phi=0}\rangle$ can be estimated from the parity measurements, and is explicitly given by

$$F = \langle\psi^{\phi=0}|\hat{\rho}|\psi^{\phi=0}\rangle = \frac{1}{2}\left[\rho_{g_-,g+} + \rho_{g_+,g-} + 2\Re(\rho_{g_-g_+,g_+g_-}).\right] \tag{4.42}$$

All the terms in this expression can be obtained by global rotations and measurements of the parity operator. The presence of entanglement in the ion pair can be proven by measuring $F > 1/2$. However, the measurement of parity oscillations only does not give an exact value for the amount of entanglement of the system, but can be used to set lower bounds for the concurrence or entanglement of formation [113, 124].

To measure parity oscillations we perform the global rotations using coherent RF pulses in resonance with the Zeeman transition connecting the two ground states $|g_-\rangle$ and $|g_+\rangle$, as previously presented in Section 3.4.3. For the external applied magnetic field with magnitude $B = 0.453\,\mathrm{mT}$ the Zeeman splitting is 12.7 MHz. After the qubit rotations are performed, a global shelving pulse resonant with the $|g_-\rangle \leftrightarrow |5\mathrm{D}_{5/2}, m_j = -5/2\rangle$ transition[2], transforming superpositions in the $\{|g_-\rangle, |g_+\rangle\}$ basis onto the $\{|5\mathrm{D}_{5/2}, m_j = -5/2\rangle, |g_+\rangle\}$ basis. Thereafter, the cooling beams are turned on and the fluorescence emitted by the ions in the common optical

[2]The beam configuration is the same as the one discussed in Sec. 3.3.3

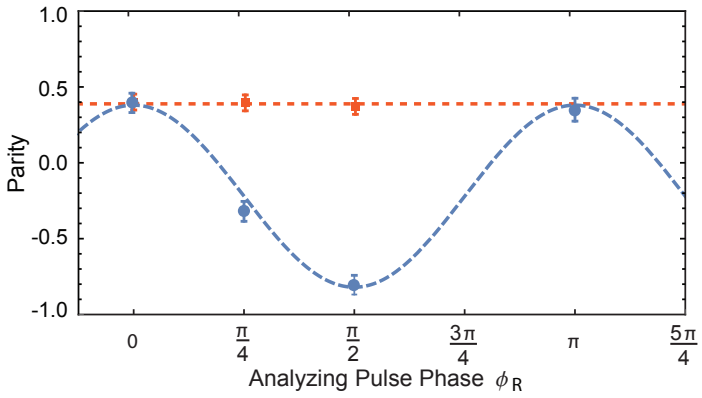

Figure 4.8: Parity oscillations. Orange squares: Measured expectation values of the parity operator after a single global rotation $\hat{R}(\pi/2, \phi_R)$ is applied. Blue points: Measured expectation value of the parity operator when the global rotations $\hat{R}(\pi/2, \pi/2)$ and $\hat{R}(\pi/2, \phi_R)$ are applied.

mode is detected by the APD. Since the length of the applied pulses is much shorter than the mechanical drifts of the mirror's position, the detected fluorescence rate is the same as during the cooling stage, allowing the estimations of the populations of the rotated state. This parity oscillation measurement sequence is executed only if a heralding photon is detected.

Fig. 4.7a shows the sequence used for detection of the populations and parity operator. Fig. 4.7b shows the fluorescence detection histogram after shelving without applying any qubit rotation and containing 185 entangling events. This histogram is separated in three regions, the left-side region corresponds to both ions being in a dark state, the center-region corresponds to one ion being in a dark state and one in a bright state, and the right-side region corresponds to both ions being in a bright state. The threshold between these regions is set by independent measurements of the fluorescence histograms of a single ion. The integrated number of events in each region corresponds to the populations ρ_{g_-,g_-}, $\rho_{g_-,g_+} + \rho_{g_+,g_-}$ and ρ_{g_+,g_+} respectively. Notice that since the fluorescence emitted by both ions is coupled identically to the same APD it is not possible to measure ρ_{g_-,g_+} and ρ_{g_+,g_-} separately. From these measurements we estimate that the experimentally created entangled state has populations $\rho_{g_-,g_+} + \rho_{g_+,g_-} = 91 \pm 3\,\%$, $\rho_{g_-,g_-} = 5 \pm 1\,\%$ and $\rho_{g_+,g_+} = 4 \pm 2\%$, corresponding to a parity value of 0.80 ± 0.6. The presence of population in the $|g_-, g_-\rangle$ state is mostly due to dark counts in the detector and the detection of background and scattered light during the entanglement generation. The measured population in the $|g_+, g_+\rangle$ ions is mostly due to the non-vanishing probability of creating double excitations and imperfections in the shelving pulse. Since the measurement presented in Section 4.3.2 shown that both ions are excited equally, we assume that the generated state has populations $\rho_{g_-,g_+} = \rho_{g_+,g_-} = \frac{1}{2}(\rho_{g_-,g_+} + \rho_{g_+,g_-}) = 45.5 \pm 1.5\,\%$.

Fig. 4.8 shows the expectation value of the parity operator after applying one or two global rotations on the generated state with phase $\phi = 0$ set during the preparation. The orange squares correspond to only one rotation $\hat{R}(\pi/2, \phi_R)$ applied, and showing a constant behaviour independent of the rotation phase ϕ_R. According to Table 4.1, this means that both the imaginary and real parts of coherences ρ_{g_-,g_-,g_+,g_+} are zero. This result is expected since in the realized experiment there

is no mechanism that can generate these kinds of coherences. The blue points in Fig. 4.8 show the results after applying two pulses generating consecutively the rotations $\hat{R}(\pi/2, \pi/2)$ and $\hat{R}(\pi/2, \phi_R)$, exhibiting the expected oscillatory behaviour. The amplitude and offset fitted curve oscillates with period π and amplitude equal to 1.19 ± 0.06.

Using Eq. (4.42), the fidelity of the generated state can be calculated from the populations measurement and from the measured parity oscillations points, which, combining the statistics of all the measured points, is estimated to be $F = 0.65 \pm 0.2 > 1/2$, proving the presence of entanglement. The fidelity is primarily limited by the motion of the ions, as studied in Ref. [79], and could be improved by further cooling the ions with techniques such as EIT cooling or sideband cooling, although using these additional cooling techniques would be detrimental for the repetition rate of the full experiment since they require longer cooling times. Other effects reducing the fidelity are the atomic recoil during Raman scattering, initial state preparation imperfections and qubit decoherence. The latter comes from the fact that even though the created state lies in a decoherence-free subspace, the ions are taken out from it during the parity measurements.

Since there is no a physical mechanism to generate far-off diagonal coherences in the realized state and since the measurements show so, we neglect all the coherences but $\rho_{g_+g_-,g_-g_+}$ and estimate the concurrence of the generated state from the measured elements only. The general definition of the concurrence for bipartite mixed state is given by

$$\mathcal{C}(\rho) = \max(0, \lambda_1 - \lambda_2 - \lambda_3 - \lambda_4), \tag{4.43}$$

where $\lambda_1 > \lambda_2 > \lambda_3 > \lambda_4$ are the eigenvalues of the matrix

$$\aleph = \sqrt{\sqrt{\rho}\tilde{\rho}\sqrt{\rho}}, \quad \text{with} \quad \tilde{\rho} = (\hat{\sigma}_y \otimes \hat{\sigma}_y)\rho^*(\hat{\sigma}_y \otimes \hat{\sigma}_y). \tag{4.44}$$

The concurrence for our generated state is estimated to be $\mathcal{C}(\rho) = 0.31 \pm 0.10$, Moreover, using the general inequality for density matrices between populations and coherences $\rho_{n,n}\rho_{m,m} \leq |\rho_{n,m}|^2$, we have numerically inspected that the presence of coherences neglected in our approximation do not decrease the value of the concurrence.

4.4 Interference of single photons emitted by a pair of entangled atoms

We have considered theoretically how the emission of entangled atoms can interfere and lead to enhancement and inhibition of the detected field. Furthermore, we have shown experimental results demonstrating creation of entanglement between effectively separated ions using interference. In this section we present the observation of interference in the spontaneous emission of a single photon into free space, emitted jointly by a pair of ions prepared in an entangled state. To do so, we use the setup presented in Fig. 4.1, where two ions are trapped adjacently but share a

common optical mode in which their effective optical separation is $d \simeq 60$ cm. With this arrangement, it is possible to directly observe both enhancement and inhibition of single-photon emission from the ions by controlling the optical distance between them in the common mode. This distance can be set dynamically during an experimental sequence with sub-wavelength precision and in times well below the lifetime of the entangled state.

To understand the interference process, let us consider that the theoretical target entangled state $|\psi^{\phi}\rangle$, discussed in Sections 4.3.1 and 4.3.2, is subject to a second Raman process $|g_-\rangle \rightarrow |e\rangle \rightarrow |g_+\rangle$. Only the component of the entangled state remaining in $|g_-\rangle$ can absorb a photon from the exciting pulse and emit a second π-polarized photon. If such a process is completed, the state of the joint ions-photon system is

$$|\psi'^{\phi}\rangle = \frac{1}{\sqrt{2}}\left(|0,1\rangle + e^{i(\phi_{\mathrm{L,A}}-\phi_{\mathrm{L,B}})}|1,0\rangle\right)|g_+,g_+\rangle \tag{4.45}$$

The field states $|1,0\rangle$ and $|0,1\rangle$ correspond to the emission of a single photon from atom A or B. The detection of this "witness" photon in the common mode projects the atoms onto the unnormalized state

$$|\psi'^{\phi}_p\rangle = \frac{1}{\sqrt{2}}(1 + e^{i(\phi_{\mathrm{L,A}}-\phi_{\mathrm{L,B}}+\phi'_{\mathrm{D,A}}-\phi'_{\mathrm{D,B}})}e^{i\phi})|g_+,g_+\rangle, \tag{4.46}$$

where $\phi'_{\mathrm{D,A}} - \phi'_{\mathrm{D,B}} = kd'$ is the optical phase difference in the common mode when the witness photon is detected. Therefore, the probability of detecting a single witness photon is

$$P \propto \left|\langle\psi'^{\phi}_p|\psi'^{\phi}_p\rangle\right|^2 = 1 + \cos(\phi - \phi'), \tag{4.47}$$

where $\phi' = (\phi_{\mathrm{L,B}} - \phi_{\mathrm{L,A}}) + (\phi'_{\mathrm{D,B}} - \phi'_{\mathrm{D,A}})$. The witness photon detection probability is modulated by the phase difference $\Delta\phi = \phi - \phi'$ between the heralding and witness detection events. This effect is a consequence of entanglement between the two emitters and corresponds to enhancement or inhibition of the emission probability in the common mode due to single-photon path interference. Eq. 4.10 can indeed be obtained using the theory presented in Section 4.2 and is a generalization of Eq. 4.15 for W-like states with arbitrary phase ϕ.

From Eq. 4.47 it is clear that the probability of detecting a single photon in the common optical mode depends on the difference between the phase of the entangled state ϕ and the "detection phase" ϕ'. This phase difference $\Delta\phi$ can be set by rapidly changing the position of the distant mirror from $d/2$ to $d'/2$ between the two detection events, namely the detection of the single photon creating the entanglement and the second detection of the witness photon probing the entanglement. This change is done in under $220\,\mu$s, allowing precise phase control in short times without motional excitation of the ions. Since the distance z between the ions is kept constant during this process, the phase difference is given by $\Delta\phi = k(d' - d)$.

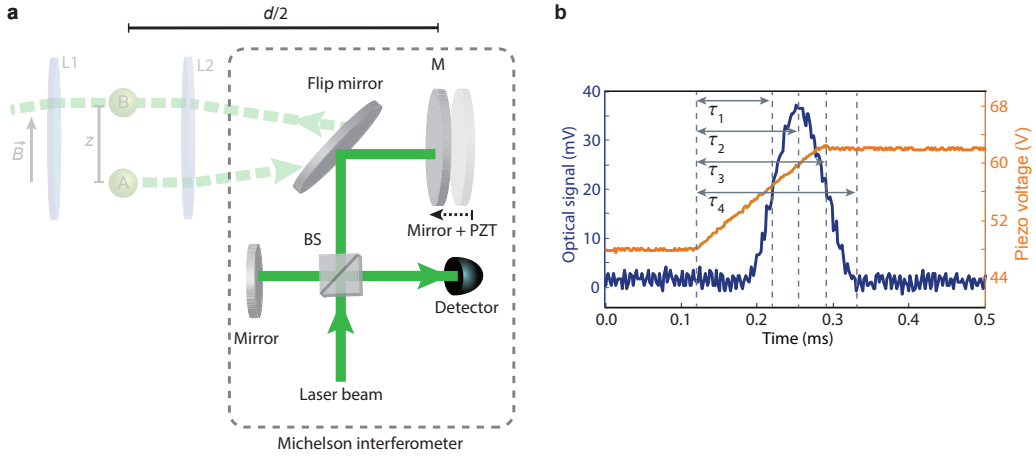

Figure 4.9: Calibration of the fast phase change. a. A Michelson interferometer attached to the setup is enabled by a flip mirror, allowing the fine calibration of the PZT-mirror voltage-displacement time response. **b.** The distant mirror is displaced by the length corresponding to a full interference fringe by applying a fixed $\simeq 200\,\mu$s linear voltage ramp of 14.0 V (orange trace) to the PZT transducers. The phase difference given by the position of the mirror at a given time is measured by recording the interferometric signal (blue trace). Different phase differences are then set by emitting and detecting the second photon at different time delays τ_i (grey arrows, see main text).

4.4.1 Fast phase tuning

The fast change in the mirror distance is achieved by ramping the voltage of the piezoelectric transducers. A voltage ramp, in contrast to an abrupt voltage step is used to prevent inducing high-frequency vibrations in the mirror that can lead to phase uncertainty. After detecting a heralding photon, a linear voltage ramp with amplitude $\Delta U = 14.0\,\text{V}$ and duration $\Delta T = 200\,\mu$s is applied to the PZTs, displacing the mirror by $(d'-d)/2 = \lambda/2$, corresponding to $\Delta\phi = 2\pi$ (a full interference fringe). Different phase differences $\Delta\phi$ are then obtained by sending the excitation pulse and detecting the witness photon after different variable delay times τ_i relative to the start of the ramp.

For the fine calibration of the phase change $\Delta\phi$ as a function of the delay τ we implement a simple method using the fact that the photon emission from the entangled atom pair depends only on the *relative* phase $\Delta\phi$. A Michelson interferometer is inserted into the experiment using a flip mirror (Fig. 4.9a). The signal of the interferometer is recorded for the voltage ramp described above (Fig. 4.9b) with a laser beam with the same frequency as the $\lambda = 493\,\text{nm}$ excitation beam. The times used in the experiment are $\tau_0 = 60\,\mu$s for $\Delta\phi = 0$, $\tau_1 = 93\,\mu$s for $\Delta\phi = \pi/2$, $\tau_2 = 129\,\mu$s for $\Delta\phi = \pi$, $\tau_3 = 164\,\mu$s for $\Delta\phi = 3\pi/2$ and $\tau_4 = 203\,\mu$s for $\Delta\phi = 2\pi$. To obtain the phase difference $\Delta\phi = 5\pi/2$ we apply a larger voltage step of 18.0 V and a delay time of $220\,\mu$s. The mirror position drifts occur on time scales (~ 10 s) longer than those used in the experiments, making the method robust against them. The angular alignment of the distant mirror is adjusted every 1 h by maximizing the visibility of the interference fringes shown in Fig. 4.5.

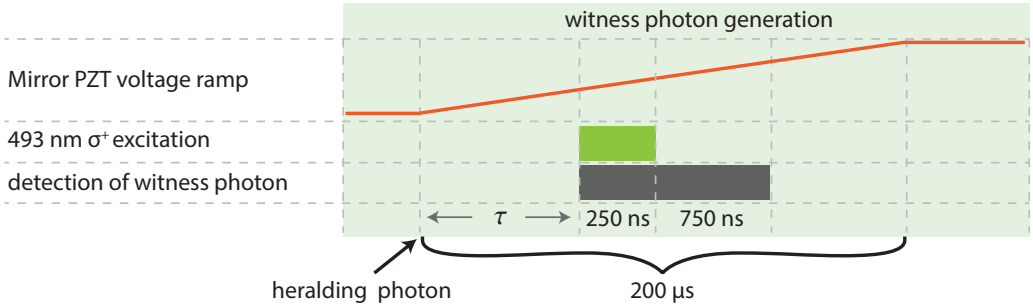

Figure 4.10: Sequence for witness photon generation. When a photon heralding the creation of entanglement is detected, a voltage ramp is applied to the PZT of the mirror. Depending of which phase difference $\Delta\phi$ is aimed (see main text), the pulse creating the witness photon and the signal triggering the APD are sent with variable delay τ after the start of the ramp.

4.4.2 Experimental sequence and results

The experimental sequence for interference between entangled ions (Fig. 4.10) is triggered by the detection of a photon creating entanglement, and in replacement of the entanglement characterization sequence described in Section 4.3.3. The linear voltage ramp applied to the piezoelectric transducer (Fig. 4.9b) is triggered by the detection of a heralding photon. After a variable delay τ relative to the start of the ramp, an APD detection window of 1 μs is opened. Simultaneously, a Raman excitation pulse, stronger than the pulse used to create entanglement, is sent to the ions. This pulse has a probability $p_{\mathrm{w}} = 80 \pm 2\,\%$ of successfully driving the $|g_-\rangle \rightarrow |g_+\rangle$, with 250 ns length and 15.8 μW mean power. It can be set substantially stronger than the entanglement generation pulse because the ion pair in the state $|\psi\rangle$ cannot absorb multiple photons. The sequence is repeated at a rate $704\,\mathrm{s}^{-1}$, achieving an entanglement generation rate of $5.02\,\mathrm{s}^{-1}$ and an average witness photon detection rate of $0.47\,\mathrm{min}^{-1}$.

We measure the witness photon detection probability P by counting the number of witness photons per herald photon for a given phase change $\Delta\phi$. The results of the measurement, together with the amplitude- and offset-fitted model from Eq. (4.47), are plotted in Fig. 4.11. The maximum and minimum measured probabilities are $P(\Delta\phi = 0) = (2.10 \pm 0.07) \times 10^{-3}$ and $P(\Delta\phi = \pi) = (1.17 \pm 0.12) \times 10^{-3}$. All the blue circles shown in Fig. 4.11 (entangled state data) correspond to accumulations of 9 hours, except the first blue circle which corresponds to 40 hours.

The visibility V obtained by the fitted model implies a concurrence of the entangled atom pair $\mathcal{C}_{\mathrm{wit}} = V = 0.27 \pm 0.03$, in agreement with the concurrence of the bipartite density matrix inferred from parity measurements $\mathcal{C}(\rho_{\mathrm{par}}) = 0.31 \pm 0.10$.

For comparison we measure the photon detection rate for a separable two-ion state $|\zeta\rangle = |g_+, g_-\rangle$. This state is prepared by optically pumping both ions into the $|g_-\rangle$ state, followed by a 1.76 μm addressed shelving pulse on the $|g_-\rangle \leftrightarrow |5D_{\frac{5}{2}}, m_j = -\frac{5}{2}\rangle$ transition on ion B and a global RF π-pulse between the $|g_-\rangle$ and $|g_+\rangle$ states of both ions, before unshelving the ion B. We trigger the emission of a witness photon from this state by using an excitation beam with the same parameters used for

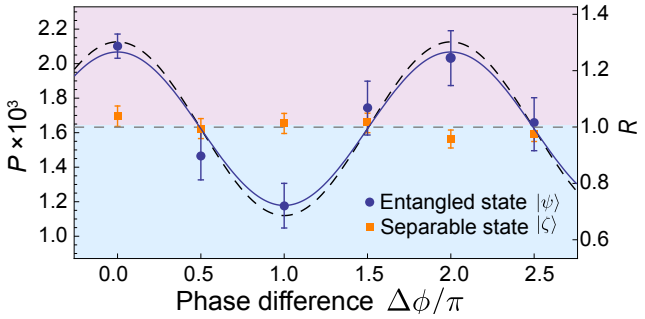

Figure 4.11: Probability of single photon detection from a entangled state. Absolute (P) and relative (R) witness photon probability from the atom pair as a function of the phase difference $\Delta\phi$ for the entangled state $|\psi\rangle$ (blue circles) and the separable state $|\zeta\rangle$ (orange squares). Error bars correspond to the Poissonian error from photon counting. The blue solid curve is the amplitude and offset fitted scattering model for the entangled state, while the black dashed curve shows the expected probability from the independent estimation of its concurrence. The grey dashed line is the average of the fitted curve. The witness photon detection probability for $|\psi\rangle$ is maximally enhanced at $\Delta\phi = 0,\ 2\pi$ and maximally suppressed at $\Delta\phi = \pi$. The photon detection probability for $|\zeta\rangle$ is constant within the measurement uncertainty.

emitting a photon from the state $|\psi\rangle$. The witness photon detection probability for $|\zeta\rangle$, which is the mean number of photons detected per prepared state, is shown in Fig. 4.11 (orange squares) as a function of the optical phase $\Delta\phi$. In contrast to the entangled state $|\psi\rangle$, the photon probability $P_{|\zeta\rangle}$ for the separable state $|\zeta\rangle$ is independent of the phase difference, with an average detection probability $P_{\text{sep}} = (1.63 \pm 0.05) \times 10^{-3}$. The observed visibility for this states is ≈ 0, in agreement with the expected vanishing concurrence of the state. We define the relative probabilities $R = P(\Delta\phi)/P_{\text{sep}}$, so that $R > 1$ ($R < 1$) represents enhanced (suppressed) detection probability relative to this separable state. The relative scale is shown in Fig. 4.11, right vertical axis. Because states $|\psi\rangle$ and $|\zeta\rangle$ both contain a single ion in $|g_-\rangle$, we expect the mean detection probabilities from each state to be equal. The mean of the fitted interference curve for $R_{|\psi\rangle}$ in Fig. 4.11 is 0.99 ± 0.08, in close agreement with the mean of $R_{|\zeta\rangle}$.

The results presented up to here are therefore in agreement with the prediction stating that in the single excitation subspace, spanned by $\{|g_-, g_+\rangle, |g_+, g_-\rangle\}$, the visibility of the observed interference corresponds to the amount of the entanglement in the ion pair (Section 4.2.2). Therefore, that measurement of the visibility, together with measurements of the populations can be used to prove the presence of entanglement.

For the most general state of the bipartite system $|\beta\rangle = a|g_-, g_+, \rangle + b|g_+, g_-, \rangle + c|g_-, g_-, \rangle + d|g_+, g_+\rangle$, the probability of detecting a single photon is proportional to the expression in Eq. 4.21. The visibility of the interference fringes for the state β signal is given by Eq. 4.25, showing that a separable state outside the single excitation subspace can still lead to interference if it has a non-fixed (a superposition) number of excitations. Hence, in general the expected visibility does not correspond to the concurrence. For the separable state $|\xi\rangle = \frac{1}{2}(|g_-\rangle + |g_+\rangle) \otimes (|g_-\rangle + |g_+\rangle)$, where $a = b = c = d = 1/2$, the visibility is $V_{|\xi\rangle} = \frac{1}{2}$, while the concurrence is

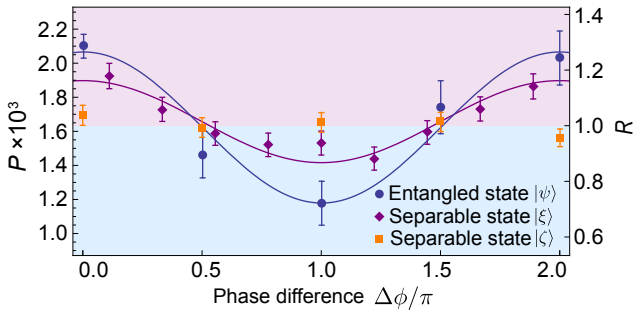

Figure 4.12: Probability of single photon detection from different states. The measured probability of single photon detection from the separable state $|\xi\rangle$ is shown with purple diamonds. The fitted amplitude corresponds to a visibility $V_{|\eta\rangle} = 0.15 \pm 0.08$. The measured data for the entangled state $|\psi\rangle$ (blue circles) and for the separable state $|\zeta\rangle$ (orange squares) presented in Fig. 4.11 are shown for reference.

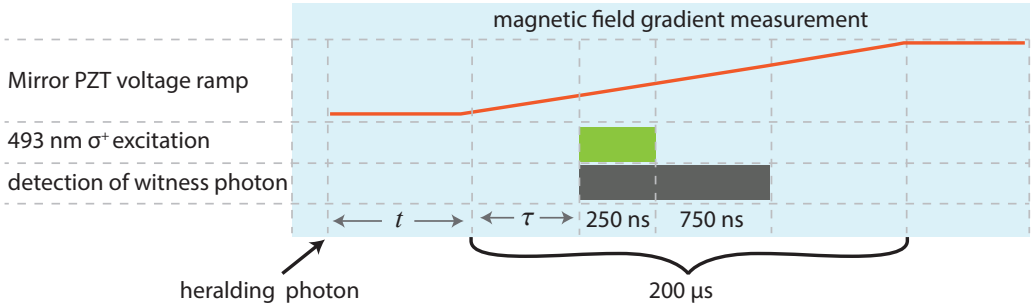

Figure 4.13: Sequence used for the measurement of the magnetic field gradient. After the detection of a photon heralding the entanglement, a waiting time t is added before starting the voltage ramp of the mirror's PZT. After starting the ramp, the time delays $\tau_0 = 60\,\mu$s and $\tau_1 = 93\,\mu$s are used in order to generate the mirror displacement corresponding to $\Delta\phi = 0$ and $\Delta\phi = \pi/2$, respectively.

$\mathcal{C}_{|\eta\rangle} = 0$. The single photon detection probability for the state $|\xi\rangle$, prepared using RF global pulses on the $|g_-\rangle \rightarrow |g_+\rangle$ transition, is shown in Fig. 4.12. We observe a visibility $V_{|\xi\rangle} = 0.15 \pm 0.08$, which is approximately, as expected, half the visibility $V_{|\psi\rangle} = \mathcal{C}_{\text{wit}} = 0.27 \pm 0.03$ measured for the entangled state.

4.5 Optical measurement of magnetic field gradient

The witness photon detection probability P is also sensitive to any phase accumulated by the entangled state between the emission of herald and witness photons. For example, the presence of a weak static magnetic field gradient between the ions induces a linear evolution of the entangled state phase ϕ due to the linear Zeeman effect, namely [125, 126].

$$\phi \rightarrow \phi + \frac{g\mu_B}{\hbar}\Delta B(\text{A,B})t \tag{4.48}$$

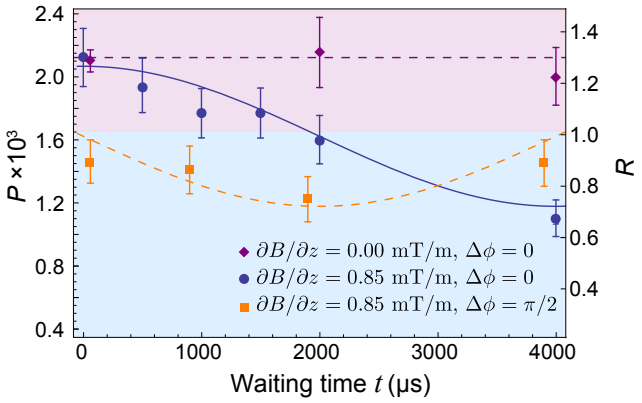

Figure 4.14: Effect of a magnetic field gradient. Absolute (P) and relative (R) witness photon probability when $\Delta\phi = 0$ (blue circles) and $\Delta\phi = \pi/2$ (orange squares) for waiting times t in the presence of a magnetic field gradient compared to the same measure in the absence of a magnetic field gradient (purple diamonds) with $\Delta\phi = 0$. The blue curve is amplitude and period fitted to the measured data for $\Delta\phi = 0$ (blue points), while the orange dashed curve is a $\pi/2$ phase shifted version of this fit, showing with the $\Delta\phi = \pi/2$ measured data. The dashed purple line shows constant enhancement in the absence of magnetic field gradient.

Where ΔB(A,B) is the difference of the field magnitudes at the positions of ions A and B, μ_B is the Bohr magneton, t is the time of the evolution and $g \simeq 2$ is the Landé factor of the $|g_\pm\rangle$ state. The magnetic field difference ΔB(A,B) can therefore be inferred from the acquired phase during the evolution.

We measure the magnetic field gradient due to an external permanent magnet by recording the evolution of the witness photon emission probability with a variable waiting time between the herald and witness photons. This is in practice achieved by adding a waiting time t between the detection of the heralding photon and the start of the PZT voltage ramp (Fig. 4.13). The actual phase difference between the heralding and witness photon is therefore $\Delta\phi + \frac{g\mu_B}{\hbar}\Delta B(\text{A,B})t$.

The results are shown in Fig. 4.14 for mirror displacements corresponding to $\Delta\phi = 0$ (blue) and $\Delta\phi = \pi/2$ (orange). Oscillations observed in both signals correspond to a linear evolution of the entanglement phase with a $\pi/2$ phase shift with respect to each other. The period of the oscillation obtained from the fit (blue curve in Fig. 4.14) of the data for $\Delta\phi = 0$ is 8.0 ± 0.5 ms. The orange curve is the same fit shifted by $\pi/2$, and shows agreement with the measured data for $\Delta\phi = \pi/2$. The period of the oscillation implies a magnetic field gradient of ΔB(A,B) = 0.85 ± 0.05 mT/m along the ion crystal. The same measurement is taken in absence of magnetic field gradient for $\Delta\phi = 0$ (Fig. 4.14, purple diamonds), where the signal remains constant since dephasing effects are negligible on the measured time scale. The coherence time of the entangled state in the decoherence-free subspace is expected to be orders of magnitude longer than the time scale of the shown phase evolution [118].

4.6 Summary and outlook

In this chapter we have described how the presence of entanglement in a pair of ions can change their emission properties. To do so, we have first reviewed the scheme applied to generate entanglement and the setup used to interferometrically detect single photons emitted by either ion, with almost perfect indistinguishability of the emitters. The fidelity, and therefore the visibility of the interference of single photons emitted by the pair of entangled ions, is largely limited by the atomic motion. After Doppler cooling, the amplitude of the atomic motion in the trap is ≈ 30 nm in both radial directions. This motion, which is a superposition of the in-phase and out-of-phase modes, produces a fundamental uncertainty in the atomic positions at the moment of the emission, and a corresponding phase uncertainty in the emitted photon. A mathematical description of this decoherence mechanism can be is found in the Supplementary Information of [117]. The effect of the motion can be reduced, e.g., by performing sideband cooling to the ground state of motion. However, experimental sequences including ground state cooling have a duration nearly ten times longer that of sequences with Doppler cooling only, lowering the entanglement rate dramatically and making them impractical. The long cooling times are mostly due to the small Lamb-Dicke parameter ($<1\%$) in the quadrupole transition which could be used for sideband cooling. In the near future, EIT cooling, which in principle requires less time than sideband cooling and can address multiple motional modes simultaneously, will be implemented. Other effects reducing the fidelity are the atomic recoil during Raman scattering, initial population imperfections and qubit decoherence (the system is taken out of the decoherence-free subspace for parity measurements, with a coherence time $\sim 120\,\mu$s). In spite of the achieved fidelity, we have shown that there is a clear relation between entanglement and interference.

The agreement between measurements of entanglement using single-photon interference visibility and independent measurements of internal states populations confirms that the observed interference can be employed for the estimation of entanglement between distant particles, without any requirement on coherent control over internal atomic states [109, 110, 127]. Such a scheme is also applicable to quantum objects with different internal structures and emission spectra [128], and should allow the observation of entanglement between non-identical atoms or general disparate quantum emitters [100, 127, 129, 130]. However, the average witness photon count rate achieved in our experiment ($0.47\ \text{min}^{-1}$) limits the practical use for those purposes, and significant improvements in the efficiency of the detection must be developed in order to show the utility of the scheme beyond a proof of principle.

Both the creation and detection of entanglement are performed fully optically, although the measurement of the populations of the involved states, which is necessary to show that the interference is a proof of entanglement, is done via the electron shelving technique. However, this also could be done fully optically, without additional lasers (See Section 3.3.3. in Ref. [131]). The free-space configuration imposes no fundamental constraints on the direction of emission, the number of entangled particles, or their mutual distance. The phases of the emitters in the detected optical mode can be tuned arbitrarily, allowing the observation of the complete interference signal; this is in contrast to Fabry-Perot cavity systems [105, 106] in which the relative phase of the emitters is restricted to 0 or π by the cavity mode.

While super- and subradiance, i.e., modifications of the global spontaneous emission rate, have been previously observed with a pair of trapped atoms [132], here we have shown the control of the single-photon emission rate into a selected free-space optical mode using entanglement. This opens the way to experimental studies of optical properties of entangled states of a few well-controlled emitters [98,110,127,133] such as trapped ions as presented here, or neutral atoms in more versatile trapping configurations [14].

The spatial differences of various environmental factors are mapped directly into interference of photons from entangled particles through the evolution of the phase of the entangled state, as shown here for the case of magnetic field gradients. This points to potential applications in quantum metrology [134]; together with all-optical preparation of distant entangled states [116, 117] and recent developments in the stabilization of large fiber networks [135], the technique presented here may enable the development of ultra-sensitive optical gradiometers [136].

5

Apparent displacement of a single atom due to spin-orbit coupling of light

5.1 Introduction

Electromagnetic radiation can carry angular momentum as spin angular momentum and orbital angular momentum. The first corresponds to the rotating electric and magnetic fields of circularly polarized radiation, while the latter arises from the disposition of the wavefronts of the fields [137]. Spin and orbital angular momenta can transform into each other and be converted to mechanical angular momentum when interacting with matter [138, 139]. The conversion between spin and orbital angular momenta has been predicted and recently observed, as in the case of the spin-Hall effect of light, where the trajectory of light beams impinging on dielectric interfaces depends on the spin-orbit interaction of light [140–142]. Spin-orbit interaction of light has also been studied in the case of single emitters. Effects such as strong directionality of the emission and absorption by single quantum emitters are the subject of study of a new field, so-called "chiral quantum optics" [143]. While several experiments have shown such effects in the emission and absorption of photons into waveguides [144, 145], with applications in quantum networking, this effect has not been observed for a single emitter radiating into free space.

In this chapter we present a theoretical and experimental study of the spin-orbit coupling of angular momentum of single photons spontaneously emitted from a single atom. The presence of orbital angular momentum is evidenced by a slight tilt in the direction of emission, which depends on the change of angular momentum experienced by the atom during the emission. This effect, already predicted by Charles G. Darwin more than 80 years ago [146], is measured as a displacement in the apparent position of the emitter imaged with a lens. In this experiment, the photons are detected in a direction where they carry solely orbital angular momentum. In this configuration, the apparent position of the emitter is shifted depending on the change of angular momentum of the ion. We observe this displacement by comparing the locations of the images of the ion formed by photons with opposite orbital angular momenta.

We discuss the generalization for arbitrary orbital angular momentum superpositions and shown that, in some imaging configuration, the apparent displacement of the position of the emitter can be bigger than the detected wavelength. In the limit of a very small numerical aperture imaging system, the displacement can become arbitrarily large. We present experimental results using a nano-sized emitter, whose emission pattern can be tuned to be any dipole superposition, leading to large apparent displacements. Furthermore, we study the connection of these results with the phenomenon of weak value amplification and optical current vortices and discuss the applications of the presented phenomena in metrology, as well as its possible impact in microscopy.

The results presented in this chapter are part of a collaborative work between our laboratory and Stefan Walser, Jürgen Volz and Arno Rauschenbeutel from the Atom Institute of the Vienna University of Technology (TU Wien). The experiment with a single atom was performed in the Barium laboratory in Innsbruck, whereas the experiment with the nano-emitter was performed in Vienna. The main results an some parts of this chapter have been pubished in Ref. [147].

5.2 Spin and orbital angular momentum of atoms and light

5.2.1 Angular momenta of an atom

Electrons bound to an atom have a quantized angular momentum with respect to the center of mass of the atom. The total angular momentum $\vec{J}$ of an electron is the sum of the different contributions corresponding to orbital angular momentum $\vec{L}$ and its spin angular momentum $\vec{S}$, i.e.,

$$\vec{J} = \vec{L} + \vec{S}. \tag{5.1}$$

The orbital angular momentum corresponds to its external angular momentum and the spin to the internal one. To describe the angular momentum of an electron a set of quantum numbers is used. In modern atomic physics these quantum numbers are the principal quantum number, the azimuthal quantum number, the magnetic quantum number and the spin projection quantum number:

- The principal quantum number $n = 1, 2, 3, \ldots$ describes the shell to which the electron belongs, or "how far away" from the nucleus the electron is orbiting.
- The azimuthal quantum number l determines the subshell of the electron and the magnitude of the orbital angular momentum L. This magnitude can be obtained through the relation

$$L^2 = \hbar^2 l(l+1), \tag{5.2}$$

with $l = 0, 1, \ldots, n-1$. Traditionally, the value of this quantum number is represented by the letter S for the case of $l = 0$, P for $l = 1$, D for $l = 2$, etc.

- The magnetic quantum number m_l describes the specific spatial distribution of the electron spatial wavefunction in the subshell. The projection L_z of the total orbital angular momentum with respect to a quantization axis z is calculated as

$$L_z = m_l \hbar, \tag{5.3}$$

  with $m_l = -l, -l+1, \ldots, l-1, l$.

- The spin projection number m_s describes the intrinsic angular momentum of the electron. The projection of this angular momentum along the quantization axis is given by

$$S_z = m_s \hbar \tag{5.4}$$

  For the case of an electron, m_s can take the values -1/2 and +1/2.

The total angular momentum of an atom is the sum of angular momenta of each electron and the nucleus, and is a conserved quantity for an isolated atom. The interactions between the angular momenta of the electrons and nucleus give rise to the hyperfine energy level structure of the atom. In the case of $^{138}Ba^+$, the angular momentum of the nucleus vanishes, so that there is no hyperfine structure.

If an electronic shell is full, its total angular momentum adds to zero. Therefore, for the case of singly ionized alkaline earth metals such as $^{138}Ba^+$, the total angular momentum of the atom is the one of the outermost electron. In this thesis, we define the energetic and angular momentum state of this electron by the notation

$$n\, l_j, m_j, \tag{5.5}$$

where $j = s + l$. So for example, the ground state manifold is composed by the state $6S_{1/2}, m_j = -1/2$ and $6S_{1/2}, m_j = +1/2$, both states with principal quantum number $n = 6$, electron spin $s = 1/2$, azimuthal quantum number $l = 0$ (S) and $m_j = 0 - 1/2 = -1/2$ and $m_j = 0 + 1/2 = +1/2$, respectively. The states in the $6P_{1/2}$ manifold share the same quantum number, except for the azimuthal quantum number, which in this case is $l = 1$ (P).

5.2.2 Angular momentum of light

Light can carry angular momentum in two ways: as spin angular momentum (SAM) and orbital angular momentum (OAM). The spin orbital angular momentum is present in light with some degree of circular polarization, whereas the (intrinsic) orbital angular momentum is present in light whose wavefronts have some helicity on its wavefronts [148]. Note that there is also an extrinsic angular momentum of light, which corresponds to light propagating with respect to a displaced reference frame [137].

For a classical light field oscillating with angular frequency ω, the spin angular momentum density can be written in an operational way following the so-called

electric-magnetic democracy formalism [148–151] as

$$\vec{s} = \frac{1}{4\omega}\Im\left[\epsilon_0\vec{E}^* \times \vec{E} + \mu_0\vec{H}^* \times \vec{H}\right], \tag{5.6}$$

where $\vec{E}$ is the electric field and $\vec{H}$ is the magnetic field. The orbital angular momentum density can be written as

$$\vec{L} = \vec{r} \times \vec{p}_{\mathrm{o}}, \tag{5.7}$$

where $\vec{p}_{\mathrm{o}}$ is the *orbital canonical linear momentum density*, defined as

$$\vec{p}_{\mathrm{o}} = \frac{1}{4\omega}\Im\left[\epsilon_0\vec{E}^* \cdot (\nabla)\vec{E} + \mu_0\vec{H}^* \cdot (\nabla)\vec{H}\right], \tag{5.8}$$

where the notation $\vec{A} \cdot (\nabla)\vec{B} = A_x\nabla B_x + A_y\nabla B_y + B_z\nabla B_z$ is used. The linear momentum density $\vec{p}$ is defined as

$$\vec{p} = \vec{p}_{\mathrm{o}} + \vec{p}_{\mathrm{s}}, \tag{5.9}$$

consisting of both orbital (o) and spin (s) parts, and it is proportional to the Poynting vector averaged over one field oscillation cycle [149]. The spin part is defined as

$$\vec{p}_{\mathrm{s}} = \frac{1}{2}(\nabla \times \vec{s}). \tag{5.10}$$

Orbital angular momentum can be decomposed in longitudinal orbital angular momentum and transverse orbital angular momentum. The longitudinal orbital angular momentum corresponds to an orbital angular momentum vector along the propagation direction of the field. This kind of OAM can be found, for example, in vortex beams, where the orbital angular per photon is quantized and determined by the topological charge $l = 0, \pm 1, \pm 2$, etc. On the other hand, transverse angular momentum corresponds to an orbital angular momentum vector perpendicular to the direction of propagation. This last case can be found in, e.g., strongly focused beams or in the emission field of circular dipoles, as we study in this thesis.

5.3 Conservation of angular momentum in the spontaneous emission

5.3.1 Orbital and spin angular momentum in the emitted field

Let us consider now the process of spontaneous emission where an atom decays from an excited state to a ground state emitting a photon with wavelength λ. Depending on the state of the atom before and after the emission, the atom may change its angular momentum. Fig. 5.1 shows the three different possibilities for the $6\mathrm{P}_{1/2} \rightarrow 6\mathrm{P}_{1/2}$ dipole transition in $^{138}\mathrm{Ba}^+$. The change of angular momentum of the atom

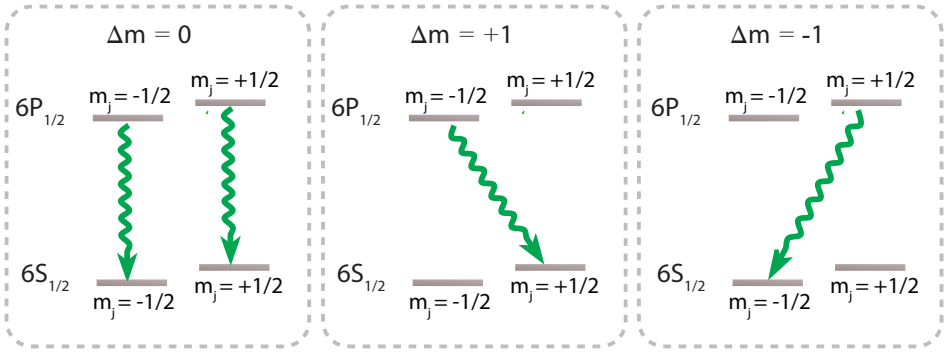

Figure 5.1: Dipole transitions and change of angular momentum. The three cases of change angular momentum $\Delta m = 0, +1, -1$ of an atom before and after spontaneous emission.

$\hbar\Delta m = \hbar(m_f - m_i)$ is given by the difference in the magnetic quantum number of the atom before (m_i) and after (m_f) the decay. The first case (Fig. 5.1, left) corresponds to the decay $6\mathrm{P}_{1/2}, m_j = +1/2 \rightarrow 6\mathrm{P}_{1/2}, m_j = +1/2$ and $6\mathrm{P}_{1/2}, m_j = -1/2 \rightarrow 6\mathrm{P}_{1/2}, m_j = -1/2$. In this case the angular momentum of the atom is unchanged, i.e., $\hbar\Delta m = 0$. This kind of transition is usually called a π-transition. The other two cases shown in Fig. 5.1 correspond to $\hbar\Delta m = +\hbar$ (Fig. 5.1, center), named σ^+–transition, and to $\hbar\Delta m = -\hbar$ (Fig. 5.1, right), named σ^-–transition. The emission pattern of these transitions correspond to the emission of π, σ^- and σ^+ dipoles, and the probability of detecting a single photon in a given direction is given by Eqs. (3.6) and (3.7).

Let us now study the case of a spontaneously emitted photon in a $\Delta m = +1$ or $\Delta m = -1$ electric dipole transition. In this case, the final angular momentum of the atom differs by a quantum $\hbar$ from the initial one. As conservation of the total angular momentum imposes, this angular momentum must be contained in the emitted photon as spin or orbital angular momentum. Therefore, the photon is expected to have angular momentum along the quantization axis. Whether this angular momentum is present as SAM or OAM depends on the direction of emission of the photon. In general, for any direction, the expectation values of the spin and orbital angular momenta of the photon along the quantization axis z are given by [152]

$$\langle s_z \rangle = \Delta m \frac{2\cos^2\theta}{1+\cos^2\theta}\hbar, \tag{5.11}$$

$$\langle l_z \rangle = \Delta m \frac{\sin^2\theta}{1+\cos^2\theta}\hbar \tag{5.12}$$

respectively, where θ is the polar angle with respect to the quantization axis. For $\Delta m = \pm 1$ the expectation values of the spin and orbital angular momenta always add to $\mp\hbar$, independent of the direction of observation, as expected from the change of angular momentum in the atom. A photon detected in the z direction carries angular momentum solely in the form of spin angular momentum, i.e., it has right circular polarization $-\frac{1}{\sqrt{2}}(\hat{x} + i\hat{y})$ for a $\Delta m = +1$ transition and left circular polarization $\frac{1}{\sqrt{2}}(\hat{x} - i\hat{y})$ in the case of a $\Delta m = -1$ transition. For a photon detected in a direction $\hat{r}$ on the equatorial xy-plane ($\theta = \pi/2$) the polarization is linear, parallel to $\hat{r} \times \hat{z}$, irrespective of the $\Delta m = \pm 1$ transition, and therefore, the photon does not carry

spin angular momentum. In the following, we show that the wavefronts in these directions have a spiralling shape, and carry the angular momentum.

Wavefronts of the radiated field

The field emitted by $\Delta m = +1$ and $\Delta m = -1$ dipole transitions corresponds to the radiation of a dipole rotating clockwise or counterclockwise in the xy-plane. In that plane, the wavefronts are spirals with opposite orientations (Fig. 5.2a). This is a classical property of the field, and can be calculated from the Maxwell equations for radiative dipoles. A detailed deduction is presented here.

The classical field due to an oscillating dipole in the far field is given by (see section 7.6 in [42])

$$\vec{E}_q^{(+)}(\vec{r},t) = \frac{1}{4\pi\epsilon_0 c^2}\left[(\hat{\varepsilon}_q\cdot\hat{r})\hat{r} - \hat{\varepsilon}_q\right]\frac{\ddot{d}_q^{(+)}(t_r)}{r}, \tag{5.13}$$

where d is the dipole moment, $\hat{\varepsilon}$ is the dipole orientation: $\hat{\varepsilon}_0 = \hat{z}$ for a linear dipole and $\hat{\varepsilon}_{\pm 1} = \mp\frac{1}{\sqrt{2}}(\hat{x} \pm i\hat{y})$ for a rotating dipole in the xy-plane; and t_r is the retarded time $t_r = t - r/c$. The product $\hat{\varepsilon}_q \cdot \hat{r}$ in spherical coordinates can be written as

$$\hat{\varepsilon}_q\cdot\hat{r} = \sqrt{\frac{4\pi}{3}}Y_1^q(\theta,\phi), \tag{5.14}$$

where $Y_p^q(\theta,\phi)$ are spherical harmonics. In the cases of dipole π–transition ($p = 1$, $q = 0$) and a dipole $\sigma^{\pm}$–transition ($p = 1$, $q = \pm 1$) the spherical harmonics are given by

$$Y_1^0(\theta,\phi) = \sqrt{\tfrac{3}{4\pi}}\cos\theta, \tag{5.15}$$

$$Y_1^{\pm 1}(\theta,\phi) = \mp\sqrt{\tfrac{3}{8\pi}}\sin\theta e^{\pm i\phi}. \tag{5.16}$$

Since the dipole moment is proportional to the external oscillatory driving field $E^{(\pm)} \sim e^{\mp i\omega t}$, and considering that the emitted light is in the near resonant regime, the scattered light has a frequency close to the transition energy ω. In this approximation the second temporal derivative of the dipole moment is given by

$$\ddot{d}^{(+)} \approx -\omega^2 d^{(+)} \approx -\omega^2 e^{-i\omega t}. \tag{5.17}$$

Therefore, in the case of the $\sigma^{\pm}$ dipoles, the electric field in the far field is given explicitly by

$$\vec{E}(\vec{r},t)_{\pm 1} = \frac{1}{4\pi\epsilon c^2}\left[\pm\sqrt{\frac{3}{8\pi}}\sin\theta e^{\pm i\phi}\hat{r} + \hat{\varepsilon}_{\pm 1}\right]\frac{\omega^2 e^{(-i\omega t_r)}}{r}, \tag{5.18}$$

It is convenient to decompose the field in its three spherical components,

$$\vec{E}(\vec{r},t)_{\pm1,\hat{r}} = \pm\frac{1}{4\pi\epsilon_0 c^2}\left(\sqrt{\frac{3}{8\pi}}-\frac{1}{\sqrt{2}}\right)\sin\theta e^{\pm i\phi}\frac{\omega^2 e^{-i\omega t_r}}{r}, \tag{5.19}$$

$$\vec{E}(\vec{r},t)_{\pm1,\hat{\phi}} = \frac{1}{4\pi\epsilon_0 c^2}\frac{1}{\sqrt{2}}\sin\theta e^{i(\pm\phi-\frac{\pi}{2})}\frac{\omega^2 e^{-i\omega t_r}}{r}, \tag{5.20}$$

$$\vec{E}(\vec{r},t)_{\pm1,\hat{\theta}} = \mp\frac{1}{4\pi\epsilon_0 c^2}\frac{1}{\sqrt{2}}\cos\theta e^{\pm i\phi}\frac{\omega^2 e^{-i\omega t_r}}{r}. \tag{5.21}$$

The phases of these three components depend on the spatial coordinates r and ϕ and the time t (through the retarded time t_r), and are given by

$$\psi_{\pm1,\hat{r}} = \pm\phi-\omega t_r \tag{5.22}$$

$$\psi_{\pm1,\hat{\phi}} = \pm\phi-\omega t_r-\pi/2 \tag{5.23}$$

$$\psi_{\pm1,\hat{\theta}} = \pm\phi-\omega t_r. \tag{5.24}$$

The wavefronts, i.e., all the points where the field has the same phase at a given time $t=t_0$, can be described by the parametric equation

$$r(\phi) = n\lambda+\frac{\lambda}{2\pi}(\mp\phi+\varphi_0+\omega t_0+\pi/2) \tag{5.25}$$

$$= \lambda(n\mp\frac{\phi}{2\pi})+\text{cte}, \tag{5.26}$$

for dipole orientations $\varepsilon_{\pm1}^{\hat{}}$, respectively, and where $\lambda=2\pi c/\omega$, $n\in\mathbb{N}$ and cte is a constant. These correspond to Archimedean spirals around the z axis, with opposite growing sense for σ^+ and σ^- dipoles. A given phase at a given time repeats spatially after a distance λ from the origin. This is a characteristic of a field carrying transverse orbital angular momentum $l_z=\mp\hbar$.

Following the same calculations for the case of the linearly oscillating dipole ($\Delta m=0$) leads to

$$\vec{E}(\vec{r},t)_0 \approx \frac{1}{4\pi\epsilon_0 c^2}\left[\frac{3}{4\pi}\cos\theta\hat{r}+\hat{z}\right]\frac{-\omega^2 e^{-i\omega t_r}}{r}. \tag{5.27}$$

The wavefronts are, for a given phase φ_0 at a time t_0, described by a constant radius

$$r(\theta,\phi)=n\lambda+\frac{\varphi_0}{k}+\omega t_0=\text{cte}', \tag{5.28}$$

therefore, they are spherical wavefronts without any spiralling and they do not carry orbital angular momentum.

5.3.2 Apparent displacement of the emitter

The spiral shape of the wavefronts of the field emitted in dipole transition with $\Delta m=\pm1$ causes an apparent displacement of the emitters due the presence of

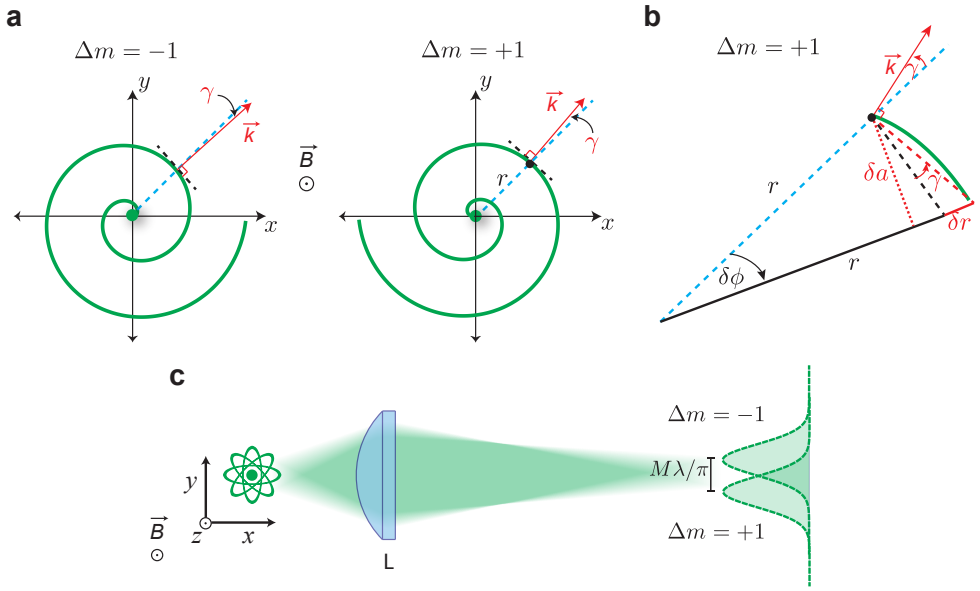

Figure 5.2: Wavefront of the field and apparent displacement of the emitter a. Spiral wavefronts in the equatorial xy-plane for $\Delta m = -1$ and $\Delta m = +1$ transitions (quantization axis $\vec{B}$ along z). γ is the angle between the radial direction (blue, dashed line) and the propagation direction $\vec{k}$. **b.** For a small angle $\delta\phi$, the spiral length increases by $\delta r = \lambda\,|\delta\phi|/(2\pi)$, which causes the tilt $\gamma = -\Delta m\,\delta r/\delta a = -\Delta m\,\frac{1}{2\pi}\frac{\lambda}{r}$. When observed from the $\hat{x}$ direction, the angular tilt γ translates into a shift $\delta y = -\Delta m\,\frac{\lambda}{2\pi}$, and a displacement $\Delta y = \frac{\lambda}{\pi}$ between the transitions. **c.** The images of the atom for the two transitions, formed by an optical system (L) with magnification M, are separated by a distance $M\Delta y = M\lambda/\pi$.

transverse angular momentum. This can be understood from geometrical arguments, as we present now.

For a fixed phase of the radiated field, e.g. $\psi = 0$, the wavefronts are defined by the parametric equation (5.26), $r(\phi) = \lambda(n - \Delta m\frac{\phi}{2\pi})$, where ϕ is the azimuthal angle and $n \in \mathbb{N}$. The direction $\vec{k}$ of propagation of the photons, defined perpendicular to the wavefronts, is slightly tilted with respect to the radial direction (see Fig. 5.2a). The tilt angle $\gamma(r)$ has opposite values depending on the transition $\Delta m = \pm 1$, and corresponds to an apparent displacement of the origin of the photons perpendicular to the direction of observation (Fig. 5.2). When observing along the $\hat{x}$ direction, the displacement of the apparent and actual atom locations is [153]

$$\Delta y = \mp\frac{\lambda}{2\pi} \tag{5.29}$$

for $\Delta m = \pm 1$ (see Fig. 5.2b). Therefore, if the emitter is imaged with a magnification M with optical axis in the equatorial plane ($\theta = \pi/2$), this effect is observed as a displacement $M\lambda/\pi$ between the centroids of the images for the $\Delta m = +1$ and $\Delta m = -1$ transitions (see Fig. 5.2c).

The apparent displacement of the position of the atom depending in which photons are detected is a signature of the presence of orbital angular momentum in the

atom emission. Here we have used a simple geometrical deduction, but it can be extracted analytically in different ways, as presented in the following sections. The predicted displacement of the images from by photons emitted by $\Delta m = +1$ and $\Delta m = -1$ transition is $\lambda/2\pi = 157.1$ nm for the considered 493 nm transition in $^{138}Ba^{+}$. This is a sub-wavelength distance but still of the same order of magnitude as the wavelength and much larger than distances measurable with current microscopy techniques. In Section 5.5 we present an experiment in which this displacement is measured using the emission of a single $^{138}Ba^{+}$ ion.

5.4 Measurement of the orbital angular momentum of the field

The apparent displacement of the position of an emitter depending on the orbital angular momentum can be understood from the discussed geometrical arguments. In this section we study the effect from a quantum measurement point of view, and we generalize the results to arbitrary elliptical dipoles.

At any point $\vec{r}$, the local orbital angular momentum of the quantized emitted field is given by the operator

$$\hat{\vec{L}} = \vec{r} \times \hat{\vec{p}}, \tag{5.30}$$

where $\hat{\vec{p}} = -i\hbar\vec{\nabla}$ is the linear momentum density operator and the origin of the coordinate system is the the position of the emitter. The local orbital angular momentum per photon in a given direction can be measured by detecting them behind a small aperture at position $\boldsymbol{r}_0$. Let us assume that at the position of this small aperture there is a lens which forms an image of the emitter at a distance d from the lens. The presence of angular momentum orthogonal to the direction of propagation of the photons causes a transverse displacement of the image formed by the light passing the aperture, with respect to the center of symmetry of the image plane. The center of symmetry is the point in which the optical axis intersects the image plane, which we use as a the origin of the coordinate system there. The displacement $\langle\vec{q}\rangle$ of the center of mass of the far-field image in this coordinate system corresponds to expectation values of the transverse linear momentum components $\langle\hat{\vec{p}}^{w}_{\vec{q}}\rangle$ per photon at the position of the aperture. The relation between angular momentum and displacement is given by

$$\langle\vec{q}\rangle = \frac{d}{\hbar k}\langle\hat{\vec{p}}^{\mathrm{w}}_{\vec{q}}\rangle = \frac{d}{\hbar k}\frac{1}{r_0}\langle\hat{\vec{L}}^{\mathrm{w}}_{\vec{q}}\rangle. \tag{5.31}$$

This kind of measurement where only a part of the total field is sampled can be interpreted in the framework of weak measurements, and we indicate the expectation values with the superscript w [154]. In a weak measurement, only a small portion of the total wavefuntion is used to estimated the so-called weak value of an operator. Using the language of weak measurements, the pre-selected state is in this case the full wavefunction of the field emitted by the dipole. The weak value of the photons' orbital angular momentum (or the transverse linear momentum) is given at the

position of the lens by [149]

$$\langle \hat{L}_q^{\mathrm{w}} \rangle = r_0 \cdot \langle \hat{p}_q^w \rangle = r_0 \cdot \frac{\langle \tilde{\mathbf{\Psi}}_{\mathrm{post}} | \hat{p}_q | \mathbf{\Psi} \rangle}{\langle \tilde{\mathbf{\Psi}}_{\mathrm{post}} | \mathbf{\Psi} \rangle}, \tag{5.32}$$

where $\tilde{\mathbf{\Psi}}_{\mathrm{post}}$ is the part of the wavefunction (the electric field) that passes the aperture (the post-selected state). The orbital angular momentum components transverse to the optical axis result in a transverse linear momentum at the aperture that leads in turn to a displacement of the diffracted beam in the far field.

This discussion holds in general true, even when there is no lens located at the position of the aperture. However, for practical reasons, a lens with focal distance f and focused a the position of the emitter will be considered to define the aperture and a second lens with focal length f' to form the image. An ideal lens applies a phase transformation to light that passes the aperture, such that any wave originating from a single point in the focal plane is transformed into a plane wave. For any such wave, the average wavevector and thus the average transverse momentum is conserved.

5.4.1 Calculation of the centroid position in optical imaging

To calculate the displacement of the image centroid of a dipole emitter in a typical imaging system, let us consider the above relation between angular momentum and transverse linear momentum when the collecting lens has an aperture with diameter D. We consider the situation where the angular momentum of the light with respect to the origin fixed by the position of the emitter is fully transverse to the optical axis of the imaging system (x axis) and we set our quantization axis (z axis) along the angular momentum direction. The imaging system consists of a lens with focal length f located at a distance f from the emitter. In this situation, the electric fields of the three elementary dipoles π, σ^+ and σ^- at the objective are, for small aperture ($D \ll f$), given by

$$\tilde{\mathbf{\Psi}}_{\pi}(\rho, \phi) = \frac{1}{f} \hat{e}_z e^{i\varphi}, \tag{5.33}$$

$$\tilde{\mathbf{\Psi}}_{\sigma^{\pm}}(\rho, \phi) = \frac{1}{\sqrt{2}} \left(\pm \frac{i}{f} \hat{e}_y + \frac{\rho}{f^2} \hat{e}_\rho \right) e^{i\varphi}, \tag{5.34}$$

where ρ and ϕ are polar coordinates in the aperture plane, y and z are Cartesian coordinates in the aperture plane, $\hat{e}_x$, $\hat{e}_y$, $\hat{e}_z$ and $\hat{e}_\rho$ are the unit vectors in the respective direction, and $\varphi = k\sqrt{\rho^2 + f^2}$. Fig. 5.3 shows the used coordinate system. $\tilde{\Psi}_{\pi,\sigma^{\pm}}$ are the parts of the electric field that pass through the aperture from the corresponding dipoles. Since the emitter is in the focal plane of the objective, the latter applies the transformation $e^{-i\varphi}$ on the light and removes the phase factor in Eqs. (5.33) and (5.34), which is dropped in the following. In the case where the light has no orbital angular momentum, the transformation of the objective results in a beam with planar wavefronts perpendicular to the optical axis. Consequently, the light has no linear momentum transverse to the optical axis. For the case where the incoming light has orbital angular momentum along the z axis, the wavefronts

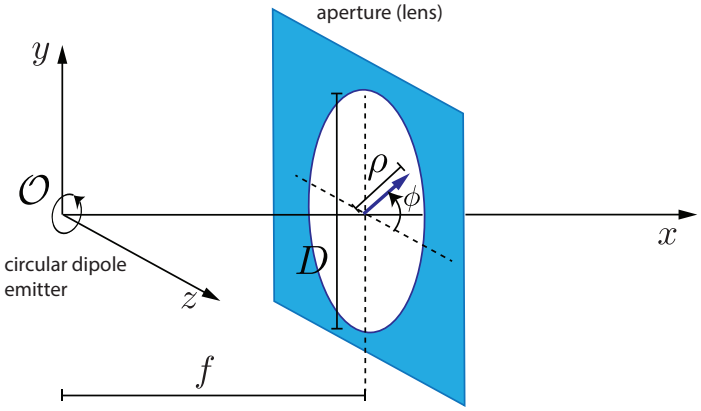

Figure 5.3: Coordinate system for the calculation of imaging displacement. An emitter is located at the origin $\mathcal{O}$ of the coordinate system. The quantization axis is chosen along the z and the optical axis along x. An aperture (lens) with diameter D is located at a distance f from the emitter. On the plane $x = f$ we define the polar coordinates (ρ, ϕ).

after the objective are tilted with respect to the optical axis and the light has linear momentum in a direction transverse to the optical axis. Measuring the displacement of the waveform's center of mass from the optical axis $\langle q \rangle$ at distance d from the objective ($d \gg D$) then corresponds to a measurement of the expectation value of the transverse angular momentum component per photon $\langle \hat{L}_q^{\mathrm{w}} \rangle$ or the linear transverse momentum component $\langle \hat{p}_q^w \rangle$ of the photons at the position of the aperture where $q \in (\rho, \phi)$. The actions of the momentum operators $\hat{p}_q$ on the wave are

$$\hat{p}_q \tilde{\Psi}_{\sigma^\pm} = -\frac{i\hbar}{f^2\sqrt{2}} \hat{e}_q, \tag{5.35}$$

as well as $\hat{p}_q \tilde{\Psi}_\pi = 0$.

We now consider the general case of a photon that originates from a superposition of σ^+ and σ^- dipole emissions, i.e.,

$$\mathbf{\Psi} = \alpha \Psi_{\sigma^+} + \beta \Psi_{\sigma^-}, \tag{5.36}$$

with $|\alpha|^2 + |\beta|^2 = 1$, and we have defined the complex valued amplitude ratio or *dipole polarization ratio* as

$$\epsilon = (\alpha + \beta)/(\alpha - \beta). \tag{5.37}$$

The field of the arbitrary dipole is therefore written as

$$\mathbf{\Psi} = \frac{1}{\sqrt{2}} \left(\frac{i}{f}(\alpha - \beta)\hat{e}_y + \frac{\rho}{f^2}(\alpha + \beta)\hat{e}_\rho \right). \tag{5.38}$$

The weak value of the momentum operator of the field emitted by the dipole of

Eq. (5.36), along the i direction can therefore be calculated as

$$\langle \hat{p}_i^w \rangle = \frac{\langle \mathbf{\Psi} | (\hat{p}_i \tilde{\mathbf{\Psi}}) \rangle}{\langle \mathbf{\Psi} | \tilde{\mathbf{\Psi}} \rangle}, \tag{5.39}$$

where $\tilde{\Psi}$ represents the part of the field that is collected by the aperture. Each of this brackets can by integrated directly assuming that Ψ and $\tilde{\Psi}$ are the same function, but restricting the limit of the integral to those of the aperture, leading to

$$\langle \hat{p}_y^w \rangle = \frac{\hbar}{f} \frac{\Re(\epsilon)}{1 + |\epsilon|^2 \mathrm{NA}^2/2}, \tag{5.40}$$

$$\langle \hat{p}_z^w \rangle = 0. \tag{5.41}$$

Here, we defined the numerical aperture $\mathrm{NA} = D/(2f)$. Therefore, from Eqs. (5.40) and (5.41), together with the relation between transverse linear momentum and displacement of the centroid of the images (Eq. (5.31)), it can be seen that the image only exhibits a transverse displacement along the axis which is perpendicular to both the optical axis and the quantization axis.

5.4.2 Microscopy set-up

In a microscopy set-up, the image is not formed at infinity, but with second lens with focal length f'. In this case, the expected displacement is obtained by replacing d by f'. Hence, the expected displacement on the screen is

$$\langle \hat{y} \rangle = \frac{1}{\hbar k} M \langle \hat{L}_y^w \rangle = \frac{\lambda}{2\pi} M \frac{\Re(\epsilon)}{1 + |\epsilon|^2 \mathrm{NA}^2/2}, \tag{5.42}$$

where $M = f'/f$ is the magnification of imaging the system. Eq. (5.40) has two noteworthy consequences. First, for small numerical aperture ($\mathrm{NA} \ll |\epsilon|$) and ϵ real, the displacement of the centroid increases linearly in ϵ, i.e.,

$$\langle \hat{y} \rangle \simeq -\epsilon M \frac{\lambda}{2\pi}. \tag{5.43}$$

Second, in the case of circular polarization $\epsilon = \pm 1$ we recover the displacement

$$\Delta y = \frac{\langle \hat{y} \rangle}{M} = \pm \frac{\lambda}{2\pi} \tag{5.44}$$

derived above.

Outside of the linear regime, the apparent displacement reaches a maximum

$$\Delta y_{\max} = \mp \lambda / (\sqrt{8} \pi \mathrm{NA}) \tag{5.45}$$

for $\epsilon = \pm\sqrt{2}/\mathrm{NA}$. Remarkably, this implies that the displacement of the apparent position of the emitter can take arbitrarily large positive and negative values for small numerical apertures. For example, with $\mathrm{NA} = 0.23$, the distance between the

two extremal apparent displacements is as large as the optical wavelength λ. These large displacements are reached for $\epsilon = \pm 6.3$, i.e., when the polarization of the dipole is almost linear along the optical axis of the imaging system. In this case, the absolute value of the corresponding expectation values of the local orbital angular momentum per photon at the aperture significantly exceed $\hbar$, the total angular momentum per emitted photon. Such "supermomentum" [155] is an example of weak value amplification common to structured optical fields, in which the local expectation value of an operator can take values outside its eigenspectrum [149,156].

5.4.3 Fourier optics

The position of the centroid can be also calculated using Fourier optics. Using this approach, the electric fields produced by three linear dipoles oriented along the axes x, y and z in the image plane are given by [157]

$$\vec{E}_x = -iE_0 \cdot \frac{\mathrm{NA}^2}{\rho} J_2(\tilde{\rho})(\cos\varphi \hat{e}_y + \sin\varphi \hat{e}_z), \tag{5.46}$$

$$\vec{E}_y = E_0 \cdot \frac{\mathrm{NA}}{\rho} J_1(\tilde{\rho}) \hat{e}_y, \tag{5.47}$$

$$\vec{E}_z = E_0 \cdot \frac{\mathrm{NA}}{\rho} J_1(\tilde{\rho}) \hat{e}_z, \tag{5.48}$$

respectively, in the small NA approximation. J_n is the n^{th} Bessel function of the first kind and $\tilde{\rho} = \rho \cdot k \cdot \mathrm{NA} \cdot f/f'$. Additionally we have defined

$$E_0 = \frac{\mu\omega^2}{4\pi\epsilon_0^2 c^2}. \tag{5.49}$$

The approximate electric fields of Eq. (5.46)-(5.48) are valid in the small NA limit, i.e., $\mathrm{NA} \approx D/(2f)$. The final image of an arbitrary superposition of these dipole fields is given by the intensity of the linear superposition of the respective electric fields. Doing this for the dipoles considered above, the apparent displacement derived in Eq. (5.42) is recovered.

5.4.4 Full numerical calculation of the images

Until now the calculations of the displacement of the image centroids have been restricted to the case of small NA. In general, it is not possible to obtain analytical expressions for arbitrary large NA and arbitrary dipole orientations. Nevertheless, it is possible to numerically calculate the intensity distribution in the image plane by a full propagation of the electromagnetic fields through the optical system. To do so, we follow the approach presented in Chapter 3 and 4 of Ref. [158] and use Wolfram Mathematica to solve the numerical integrals. Fig. 5.4 shows the images of elliptical dipoles with different polarization ratios ϵ. Fig. 5.5 shows the numerically calculated relative displacement of the center of mass of the images. In Fig. 5.5 it is clearly visible that by decreasing the numerical aperture of the imaging system the maximum apparent displacement increases. Also, it is possible to see that for

polarization ratios $\epsilon = \pm 1$ the displacement is well described by the approximation $M\lambda/2\pi$ and that for small apertures and $|\epsilon < 1|$ the displacement depends linearly on ϵ.

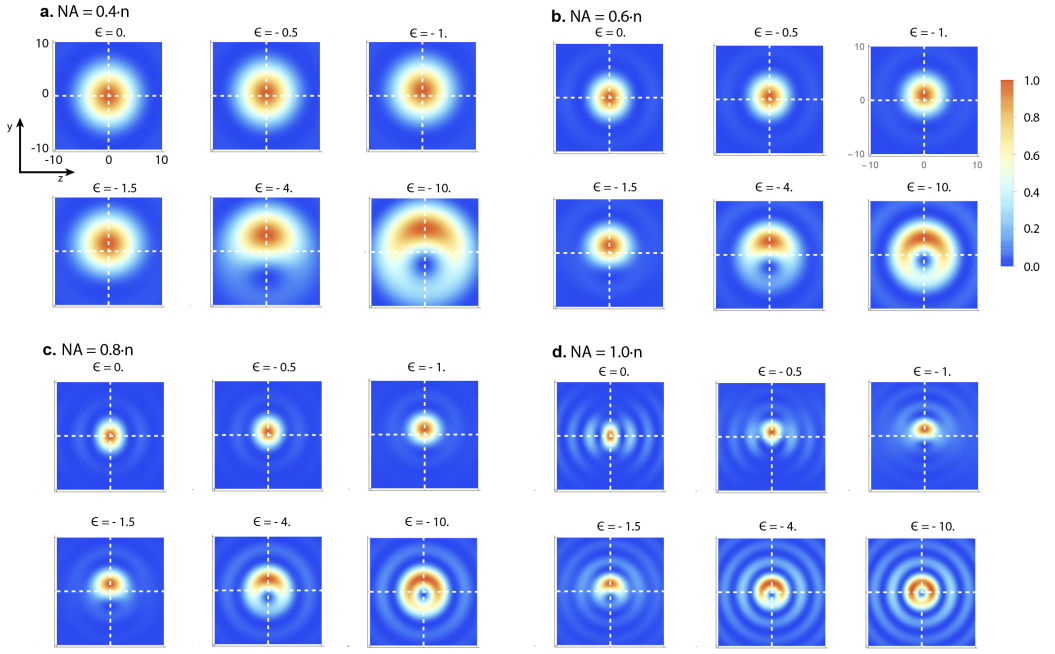

Figure 5.4: Numerically calculated images of different dipoles. Full field calculation of the image of dipoles with different dipole polarization ratios ϵ and imaged using different numerical apertures NA. n is the diffraction index of the medium surrounding the emitter, in our case $n \approx 1$ (vacuum). The horizontal and vertical axes are in units of $M\lambda/10$

5.5 Observation of the apparent displacement of a single $^{138}Ba^{+}$ ion

To experimentally study the displacement of the image of a dipole emitter due to the presence of transverse orbital angular momentum in the emitted field we image a single atom. We prepare the emission of single photons by a specific dipole transition with a given Δm from a single $^{138}Ba^{+}$ atomic ion. The chosen dipole transition is the cooling transition, with $\lambda = 493.41\,\text{nm}$, whose emission can be detected efficiently in our experimental setup.

5.5.1 Experimental setup

To measure the described effect, we trap a single $^{138}Ba^{+}$ ion in the linear Paul trap described in Chapter 3. The magnetic field $\vec{B}$ defining the quantization axis is chosen to be parallel to the pumping beams ($\vec{B}$ axis in Fig. 3.8), with magnitude $B = 0.45\,\text{mT}$. In this way, the optical axis defined by the position of the HALOs is orthogonal to the quantization axis (see Fig. 5.7 and Chapter 3). Photons propa-

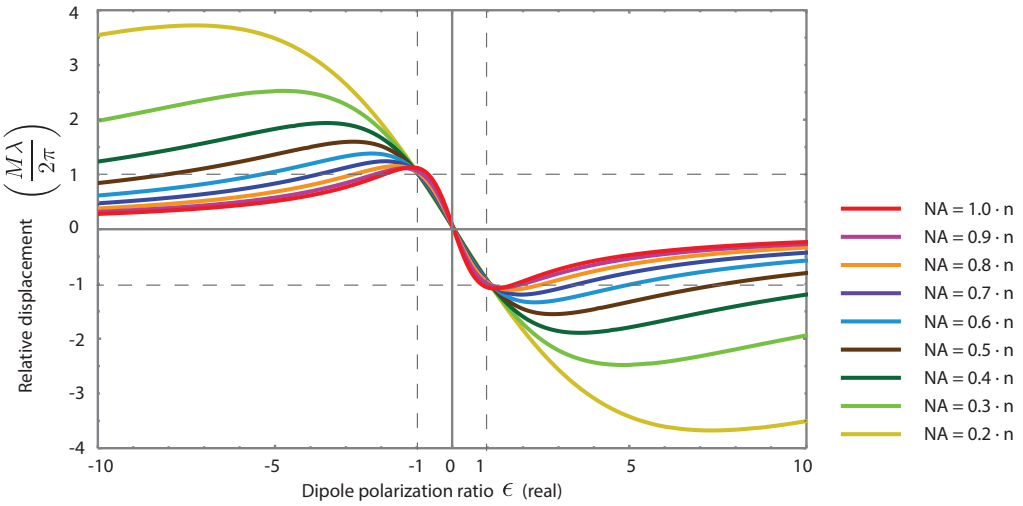

Figure 5.5: Predicted center of mass apparent displacement without small NA approximations. Predicted apparent displacement of the center of mass of the images of dipoles for different NA as a function of the dipole polarization ratio ϵ, for real ϵ, *i.e.*, elliptical rotating dipole calculated using full field propagation. The dashed lines show that for clockwise and anticlockwise circular rotating dipoles ($\epsilon = 1$ and $\epsilon = -1$ respectively), the displacement of the center of mass of the image corresponds to $M\lambda/(2\pi)$ and $-M\lambda/(2\pi)$ respectively.

gating in this axis carry solely orbital angular momentum.

We prepare the emission in a given transition by first Doppler-cooling the ion with the 493 nm cooling and 650 nm repumper laser beams, reducing the extension of the motional atomic wavepacket, which is after cooling given by ~ 36 nm. This is followed by optically pumping to one of the ground states. For example, when preparing the emission of a $\Delta m = +1$ photon, we pump to the $6S_{1/2}, m_j = -1/2$ with a σ^-–polarized 493 nm laser beam. After that, we apply a short σ^+–polarized 493 nm laser pulse which excites the atom to the state $6P_{1/2}, m_j = +1/2$, as shown in Fig. 5.6b. From that excited state the atom can spontaneously decay back to the $6S_{1/2}, m_j = -1/2$, through a $\Delta m = +1$ transition, to the $6S_{1/2}, m_j = +1/2$ through a $\Delta m = 0$ transition, or to the $6D_{3/2}$ manifold. During this transition the atom emits a photon that can be collected by the high numerical aperture objective and directed to the camera through the imaging system. Additional filter elements (Fig. 5.7) allow the detection of photons emitted only in the $\Delta m = +1$ transition at 493 nm. To detect photons from the opposite transition ($\Delta m = -1$), the polarization of the optical pumping and excitation beams are exchanged, as shown Fig. 5.6c.

The imaging system is shown in Fig. 5.7. The in-vacuum high numerical aperture objective (L1) with focal length $f_1 = 25$ mm and with numerical aperture NA= 0.40 partially collects the emission of the single atom, defining the axis of the imaging system along the x-axis of the coordinate reference system shown in the figure, orthogonal to the quantization axis.

In this configuration, photons from $\Delta m = 0$ ($\Delta m = \pm 1$) transitions are horizontally (vertically) polarized when propagating along the optical axis. However,

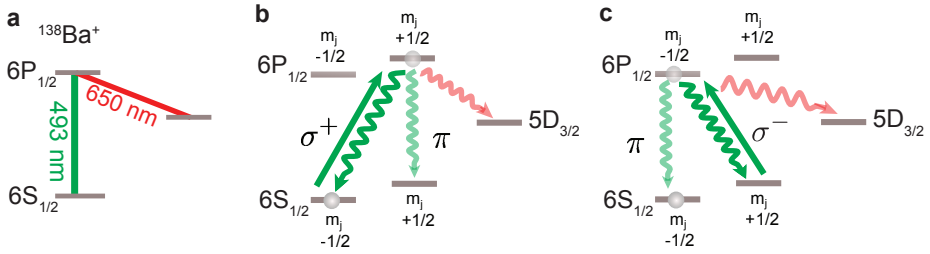

Figure 5.6: Electronic dipole transitions used to measure apparent displacement a. Levels and transitions of $^{138}Ba^{+}$ used in this experiment. **b.** In order to emit a $\Delta m = +1$ photon an ion initially prepared in the state $6S_{1/2}, m_j = -1/2$ is excited by a circular-right polarized laser beam at 493 nm. **c.** In order to emit a $\Delta m = +1$ photon the atom prepared initially in the $6S_{1/2}, m_j = +1/2$ is excited by a circular-left polarized laser beam. Photon originating from other possible decay channels are filtered out using polarization and wavelength filtering.

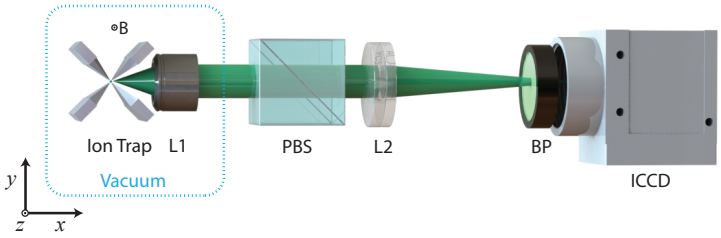

Figure 5.7: Imaging system for the detection of apparent displacement. A single $^{138}Ba^{+}$ ion is confined the linear Paul trap. A magnetic field $\vec{B}$ along $\hat{z}$ defines the quantization axis. Fluorescence light is collected in the $\hat{x}$ direction by a high numerical aperture, in-vacuum lens (L1), and a second lens (L2) forms a focus on an intensified CCD camera. A polarization beam splitter (PBS, Thorlabs PBS511) filters out photons with polarization parallel to the quantization axis (π–polarized photons), while a bandpass filter (BP) filters out photons with wavelength other than 493 ± 1 nm.

photons emitted in directions around the optical axis are also collected by the HALO lens. For not-so-small numerical aperture imaging systems, photons collected far from the optical axis have slightly different polarizations. An ideal PBS paired with the NA = 0.40 objective used here removes 99.998% of photons from the π transitions and transmits 97.3% of the photons from the σ transitions. The actual used PBS has a polarization extinction ratio of 1000:1, so that, after polarization filtering more than 99.8% of the detected photons come from a σ transition. The image is not significantly changed by the imperfect filtering at this numerical aperture, as shown in the simulations presented in Fig. 5.9.

The light emitted during the cooling and optical pumping stages is filtered out by blocking the acquisition of the CCD sensor. The results shown here were obtained using an intensified CCD camera (ICCD, Andor iStar A-DH334T-18H-63, with a pixel size of $13 \times 13\,\mu m^2$). The fast gating provided by the intensifier enables the collection of single photons only from the desired transition, by opening short detection windows after cooling and pumping are finished. Fig. 5.8 shows the sequence and timing used in the experiment. Complementary results where obtained using

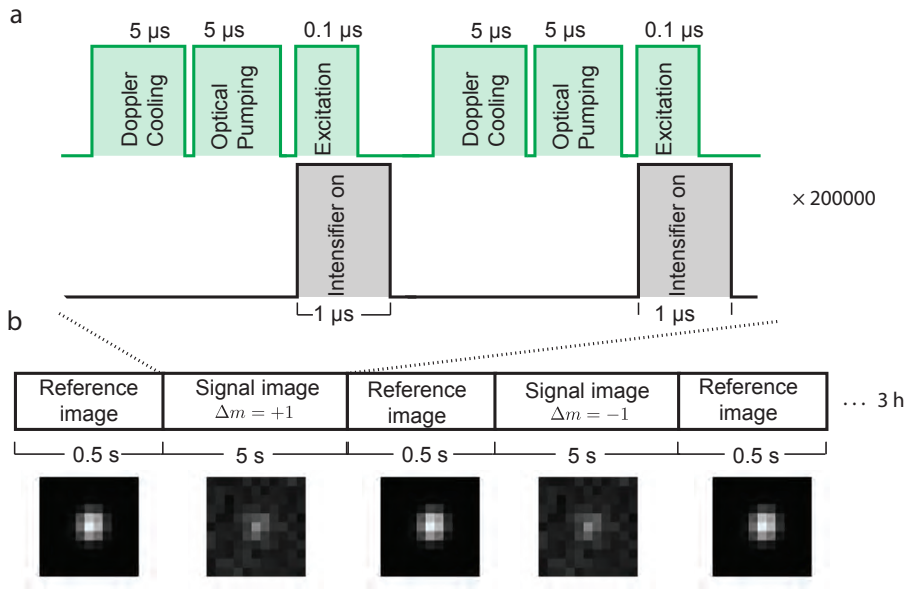

Figure 5.8: Experimental sequence. **a**. Timing of the sequence used to generate photons in a given transition. The sequence is repeated during 5 s, **b**. A reference image of 0.5 s is taken before and after the 5 s accumulation of the desired photons. The acquisition is directly alternated between images with photons coming from the $\Delta m = -1$ and $\Delta m = +1$ transitions.

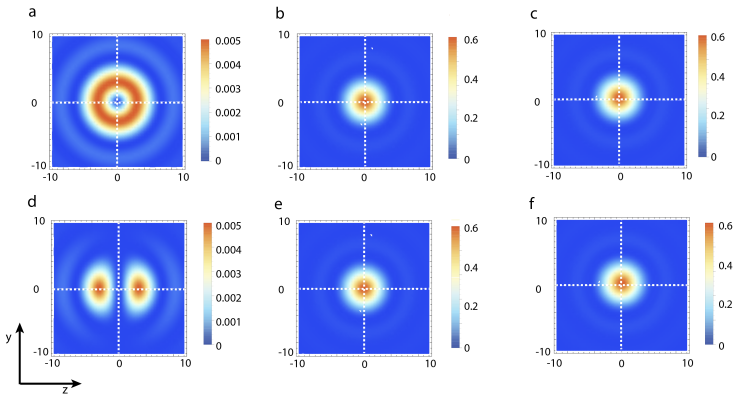

Figure 5.9: Effect of polarization filtering in the position of the centroid of the image. Calculated intensity distribution for NA = 0.4 in the image plane for a dipole oriented along the optical axis **a**, oriented orthogonal to the optical axis **b**, and a circular dipole which is the superposition of them, **c**. **d, e** and **f** show the image of these dipoles when placing a PBS between the two lenses forming the imaging system. The contribution of the longitudinal dipole (**a** and **d**), as can be seen from the colour scale, is orders of magnitudes smaller than the contribution of the transversal one (**b** and **e**). Vertical and horizontal axes are in units of $M\lambda/2\pi$.

an EMCCD camera and an optical chopper, as presented in Section 5.5.3.

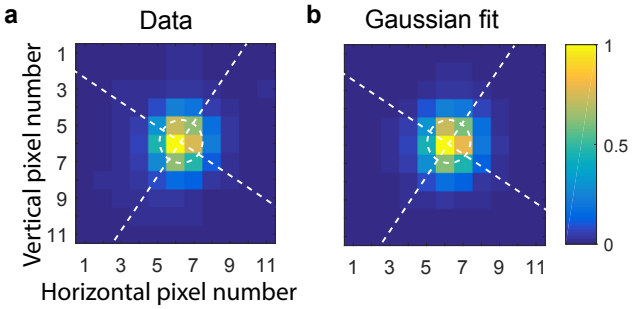

Figure 5.10: Normalized image and fit. **a.** Acquired image of a single ion during Doppler-cooling. **b.** Seven parameter 2D Gaussian fit with pixelation applied for comparison. The white lines show the major and minor axes of the fitted Gaussian and the circles show the 1σ width of the fit.

5.5.2 Image characteristics and stability

The image of the atomic ion formed using the presented imaging system corresponds to the point-spread function of the imaging system, which is well approximated in our case by a two-dimensional Gaussian. The detected images are analyzed by fitting to a Gaussian profile with seven free parameters $(z_0, y_0, \sigma_z, \sigma_y, A, O, \theta)$, (z_0, y_0) being the coordinates of the centroid, σ_z and σ_y the standard deviation along the major and minor axes, A the amplitude, O an offset and θ rotation angle with respect to the CCD sensor axis. Although the Gaussian fitting method is in general informationally sub-optimal [159], it does not introduce significant parameter estimation errors in the measured NA$< n_{\text{med}}$ regime (where n_{med} is the refraction index surrounding the emitter), and non-diffraction-limited regime [160]. The image of the atom detected on the CCD camera is a non diffraction-limited Gaussian profile, characterized by widths $2\sigma_z = 30.1(4)\,\mu$m and $2\sigma_y = 28.4(4)\,\mu$m (Fig. 5.10). In a diffraction-limited system these widths are expected to be $\sim 8\,\mu m$[1]. We suspect that these large differences arise from the misposition of the in-vacuum objectives along the optical axis, since, unfortunately, the nanopositioning stages on which they are mounted are not operative and a precise adjustment was not possible.

To precisely estimate the magnification of the optical system we image two ions trapped in the Paul trap. Spectroscopy of the quadrupole electronic transition of the ions allow us to measure the trap frequencies. These frequencies are used to calculate the equilibrium position of the pair of atoms and their mutual distance. Then, using the same quadrupole transition we shelve either ion in a dark state. In this way we can image each ion separately using their fluorescence, without changing their distance. From the independent images, the centroid position of each ion is extracted and their relative distance in the image plane is calculated. The magnification is computed as the quotient of their distance in image and object plane, which is $M = 5.40(7)$.

The expected displacement of $M \times 157.1\,$nm is 35 times smaller than the width of the images. Even if the angular resolution of visible radiation in a diffraction-limited system with aperture D is considered to be λ/D, and where any object

[1]Calculated using the formula of the Airy Radius $r = 0.61\lambda/\text{NA}$ and considering the magnification stated bellow

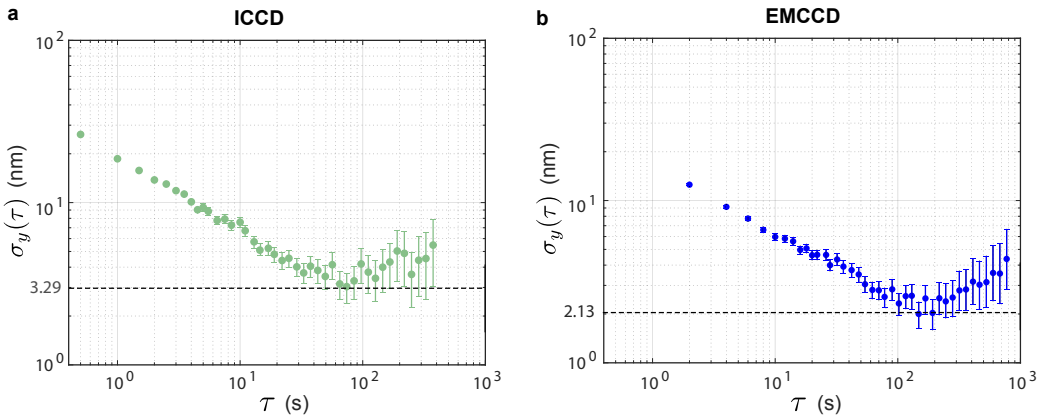

Figure 5.11: Stability of the ion imaging system. Allan variance of the vertical position of the atom as a function of the accumulation time τ of the images, using an ICCD camera (**a**) and EMCCD camera (**b**) for comparison.

smaller than this size is observed as a diffraction limited spot, the centroid of the spot can be measured, in principle, with arbitrarily high precision. This precision scales up with the number N of photons detected, provided that the signal-to-noise ratio is larger than 1 [161, 162]. The noise restricting the precision can be classified in two types: shot noise, where the precision of the localization of the centroid scales as $N^{-1/2}$, and background noise created by CCD readout noise, dark current, background light, *etc*, where the precision scales as N^{-1} [162]. In our experiment, using the sequence shown in Fig. 5.8, the overall photon detection rate is $\sim$ 1600 photons/s and is mostly limited by the ion preparation sequence repetition rate, the numerical aperture of the imaging system and the quantum efficiency of the camera. Given that our optical system is not diffraction-limited, the scaling of the precision is under-optimal. Nevertheless, it is still possible to achieve few nanometers precision by accumulating photons for several hours.

The long accumulation time introduces a new source of error in the position estimation that originates from mechanical drifts in the imaging system. This inaccuracy can be overcome by a measurement and compensation of the mechanical drifts, as soon as the time scale on which they occur is much longer than each camera exposure.

The stability of the imaging system can be characterized by the Allan variance of the fitted centroids of the detected images [163]. This gives a measure of the position uncertainty depending of the accumulation time τ. This is done by taking N_P pictures with exposure time t, adding them in bins of duration $\tau = nt$, where n is an integer number smaller than $N_\mathrm{P}/2$. Each binned image is fitted to a seven parameter Gaussian function, from where the centroid is extracted. For comparison, we also use, besides the ICCD camera, an EMCCD camera (Andor iXon DU-897). The EMCCD camera, in spite of having a bigger pixel size ($16 \times 16\,\mu\mathrm{m}^2$), has a better resolution (see Section 3.3.2). In the case of the EMCCD camera we take 2000 images with 2 s exposure time with the atom emitting resonant florescence at maximum rate, and in the case of the ICCD camera we take 3000 images with 0.5 s exposure time. In both cases, the dead time between images is negligible. Fig. 5.11 shows the vertical position uncertainty (relevant for the experiment) extracted with this method. For the EMCCD we get a minimum uncertainty in the vertical position

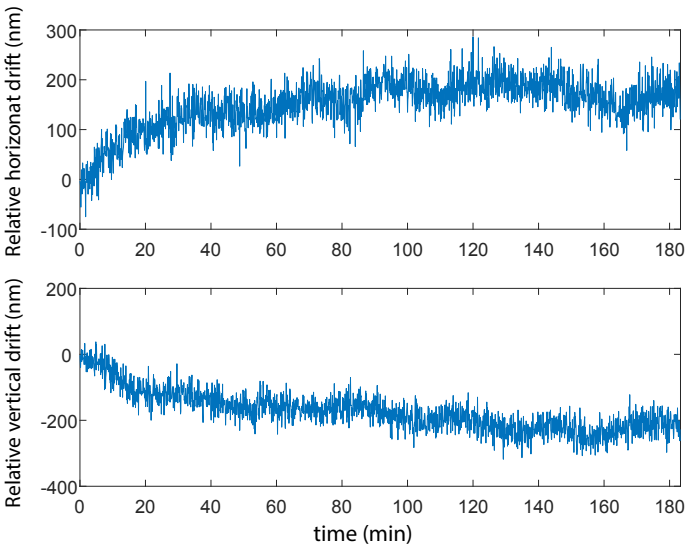

Figure 5.12: Long term mechanic drift of the imaging system. Vertical and horizontal positions of the centroid of the fitted reference images, over a period of 180 min.

of 2.13(41) nm for 148 s accumulations, while for the ICCD setup the minimum is 3.29(71) nm for 74 s accumulations. In the logarithmic plot shown in Fig. 5.11 the shot noise dominates the linear behavior of the decreasing part, where the long y-intercept of the line is mostly limited by the limited numerical aperture of our collection lens L1 (NA = 0.4) and the size of the spot in the camera, which is not diffraction limited. The increasing part of the curve is dominated by mechanical drifts in the system.

To compensate for the mechanical drifts in the actual experiment, we use the acquisition of long-exposure images during the cooling stage (Fig. 5.8b) to obtain a real-time "reference" of the particle position. Figs. 5.8a shows the full experimental sequence. This sequence is repeated for 3 h, and the analysed pictures correspond to accumulation of photons in a 11 × 11 pixel sub-area of the CCD sensor. The mechanical drift of the centroid fitted images used as reference are shown in Fig. 5.12, where we see that in a period of 3 h, the image drift a maximum of ≈ 200 nm in both vertical and horizontal axes. The rapid oscillations correspond to statistical noise.

5.5.3 Results

After the data collection using the sequence shown in Fig. 5.8 is finished, each reference image is fitted. The mean centroid position of two consecutive reference images is used to correct for the drifts in the signal image acquired in between them. All the corrected signal images are added up and fitted using the seven free parameter function. Finally, we compare the centroid positions of the added-up reference and signal images to determine their relative displacement. The uncertainty of the displacement is extracted from the 1σ confidence intervals using χ^2 analysis, given its relation with the real noise sources [161].

The obtained results are shown in Fig. 5.13, corresponding to a displacement of

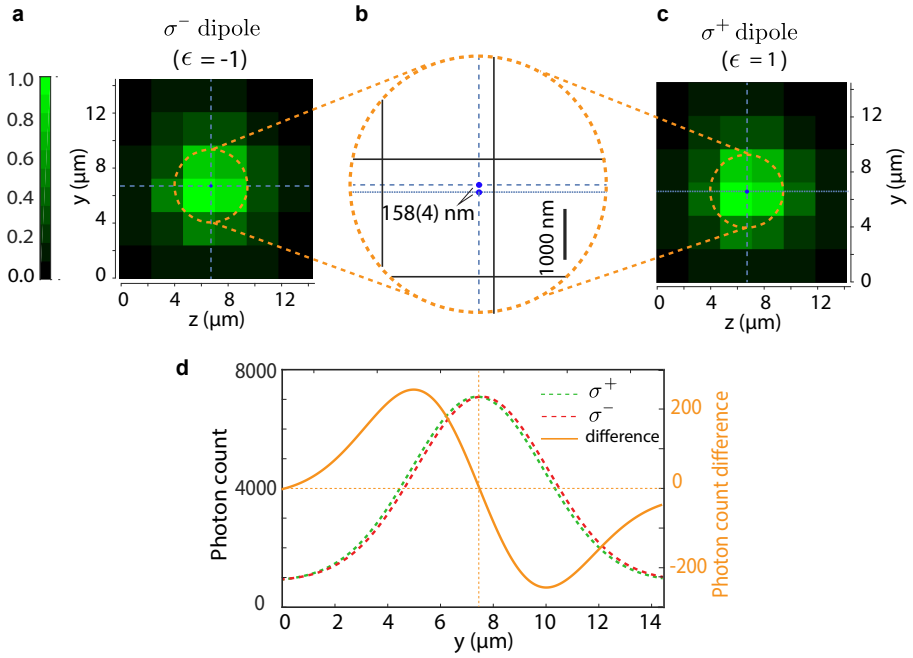

Figure 5.13: Apparent displacement of the emitters. **a, c,** Measured images (normalized to maximum pixel count rate) of a single atom for the σ^- and σ^+ transitions. The blue lines and blue points indicate the centroid of the image obtained by a 2D Gaussian fit to the data. The orange circle represents the 1σ-width. **b,** Zoom of the center of images **a** and **c**. The two blue points show the centroid position of the fitted σ^- (upper point) and σ^+ (lower point) images. **d,** Vertical cross section of the Gaussian fits for σ^+ (green dashed curve, left scale) and σ^- (red dashed curve, left scale) polarizations. The orange curve shows the difference of both fits (right scale).

$\Delta y = 158(4)\,\mathrm{nm}$ in the object plane between the image formed by $\Delta m = +1$ and $\Delta m = -1$ photons, and a small displacement of unknown origin in the horizontal axis of $6(2)\,\mathrm{nm}$. The obtained value for the displacement in the object plane and its uncertainty as function of the number of accumulated single images is shown in Fig. 5.14. The uncertainty of the measured displacement converges logarithmically to the expected value as the number of photons increase (see inset in Fig. 5.14). The results are in good agreement with the expected λ/π value, proving that for the measured emission direction, the photons carry transverse orbital angular momentum. Furthermore, this also shows that while the detected photons from $\Delta m = +1$ or $\Delta m = -1$ transitions are indistinguishable in polarization, they carry detectable opposite orbital angular momentum.

Direct comparison of signal images

A simplified analysis is done by considering the displacement between consecutive signal images, which corresponds to the accumulations of $\Delta m = +1$ or the $\Delta m = -1$ photons during periods of 5 s alternately. This analysis is valid since the time separation between consecutive images is much shorter than the characteristic time of the mechanical drifts.

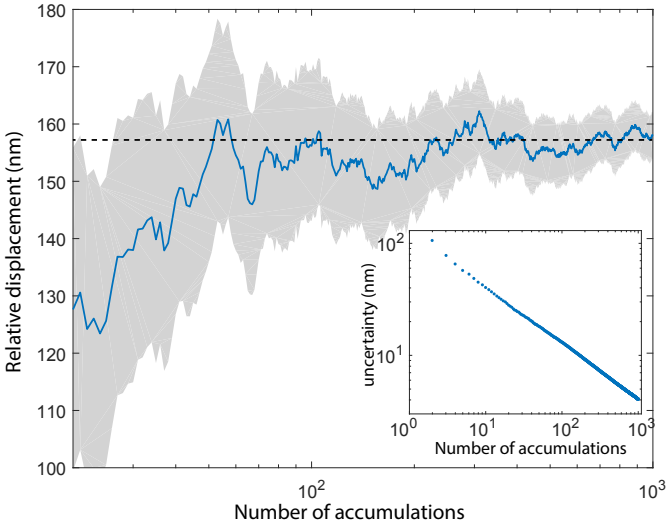

Figure 5.14: Convergence of the measured relative displacement of the atom. Convergence of the estimated relative displacement between the counter rotating circular atomic dipoles σ^+ and σ^- (blue line) and uncertainty (grey area) versus the number of signal images accumulated after drifts correction. The dashed line shows the expected value $\lambda_1/\pi = 157.1$ nm. The inset shows the evolution of the uncertainty in logarithmic scale as the number of accumulated images increases.

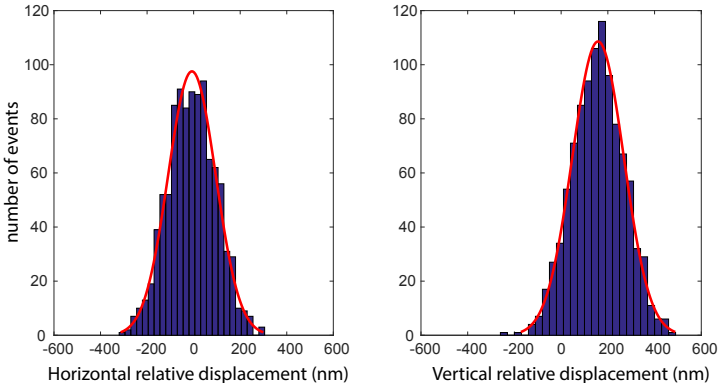

Figure 5.15: Direct comparison of consecutive ion images Histograms of the horizontal and vertical relative displacements of pairs of consecutive signal images formed by photons coming from the $\Delta m = -1$ and $\Delta m = +1$ atomic transitions, for 2000 image pairs. The histograms show a clear average vertical displacement, and an average zero horizontal displacement. Each histogram is fitted to a normal distribution from which we extract an average horizontal relative displacement of 7(6) nm and standard deviation of 106(4) nm, while for the vertical displacement we get an average of 158(6) nm and standard deviation of 112(4) nm. The stated errors correspond to the 1σ-confidence intervals of the fits.

Fig. 5.15 shows the histograms of the relative horizontal and vertical displacement between consecutive $\Delta m = +1$ and $\Delta m = -1$ images, when comparing 2000 different pairs. Each histogram is fitted to a normal distribution from where we ex-

tract an average relative displacement in the horizontal axis of 7(6) nm and standard deviation 106(4) nm, while for the vertical axis we get an average relative displacement of 158(6) nm and standard deviation 112(4) nm. The error of these quantities correspond to the 1σ-confidence intervals of the fits. These results are shown in Fig. 5.15 and agree with the more precise analysis presented above.

Results obtained using a EMCCD camera

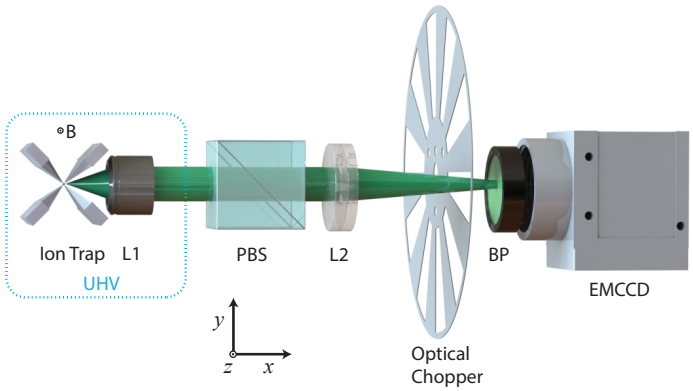

Figure 5.16: Imaging setup with an EMCCD Camera. An optical chopper is added in front of the camera to block the path of photons being emitted during the preparation stage.

During the realization of this experiment we used an EMCCD camera (EMCCD, Andor iXon DU-897) in addition to the ICCD camera which results are shown above. While the main advantage of using an ICCD camera, i.e., fast gating of the photon detection, is not present in the EMCCD, we where able to find positive results by mechanically gating the detection of photons in the CCD camera. In this case an optical chopper is used for blocking the optical path during the cooling and optical pumping stages. The use of an optical chopper reduces more than 1000 times the photon generation rate due its limited spinning frequency. At the maximum spinning frequency, the shortest gating windows achieved corresponds to 700 μs. Despite the slow gating allowed by this setup, using the EMCCD camera provides a higher quantum efficiency and resolution, and a slightly improved image stability (see Fig. 5.11b). The used setup is described in Fig. 5.16. In order to avoid additional mechanical drifts and vibrations due to the mechanical chopper, we detach it from the rest of the experiment by hanging it from the ceiling.

Figs. 5.17a and b depict the experiment sequence used with the EMCCD camera and the optical chopper. An exposure of 2 s is used for the reference pictures of the atom during the extended cooling stage. The sequence for the emission of photons in a given transition is repeated during 60 s and accumulated in a "signal" image. The detection rate (∼20 photons/s) of the desired photons is mainly limited by the maximum rotation speed of the optical chopper. In this case we repeat the full sequence for approximately 7 h, then we exchange the polarization of the optical pumping beam and excitation pulse and accumulate photons with opposite angular momentum for another 7 h, adding up to a total of 14 h for the full experiment.

The obtained results when using the EMCCD camera are $\Delta y = 160(10)$ nm for

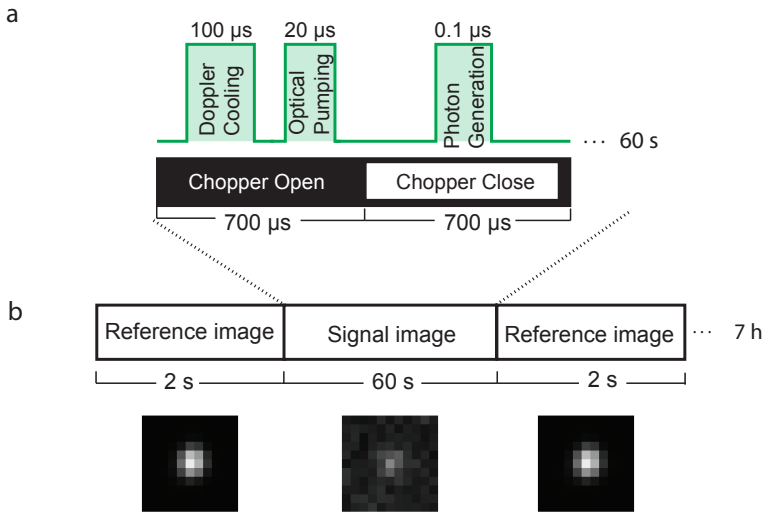

Figure 5.17: **a** Sequence timing used for generations of photons from a given transition when using the EMCCD camera, repeated during 60 s. The repetition rate is given by the maximum chopper rotation speed. **b**. Reference images with maximum fluorescence rate from the photos are taken before and after the accumulation of the desired photons to keep track of the mechanical drift of the imaging system.

the vertical displacement and small horizontal displacement of 5(10) nm compatible with the expected value. The higher uncertainty is due to the higher levels of noise, since the CCD sensor is exposed to the background noise for longer periods of time than in the ICCD setup and the chopper is less effective in blocking it (see vertical offset in Fig. 5.11).

5.6 Displacement of the apparent position of a nano-emitter

In Section 5.4 we have seen that the apparent displacement of the emitter is a universal effect, present in any dipole with a degree of circular polarization, i.e., it is not restricted to atoms. Furthermore, we have predicted that the observed apparent displacement of the emitter depends on the numerical aperture of the imaging system as well as on the polarization ratio ϵ of the considered dipole. Studying these dependences using a single ion is demanding, since it would require the preparation of quantum superpositions of the emission of a single atom and increasing the numerical aperture of the in-vacuum lens, which maximum is restricted by the trap geometry. Given these difficulties, a test of our predictions is realized using a different dipole emitter: a sub-wavelength sized gold nanoparticle. Such nanoparticles are used as markers in super-resolution microscopy of biological research [164, 165]. Being a spherically symmetric emitter, the polarization of a nanoparticle's dipole coincides with the polarization of the illuminating field, which can be controlled precisely.

In the experiment realized in Vienna by Stefan Walser, Jürgen Volz and Arno Rauschenbeutel, a 100 nm-diameter gold nanoparticle is placed in the center of a

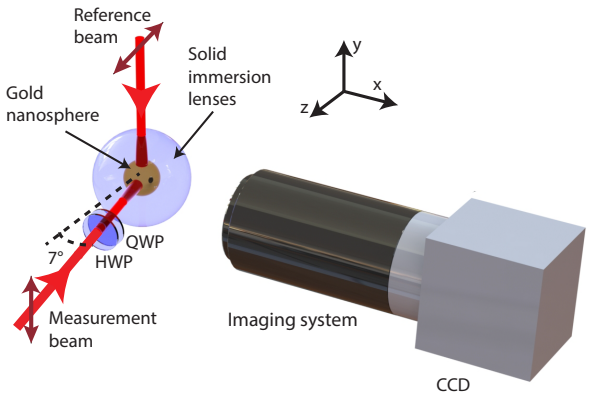

Figure 5.18: Nanosphere experimental setup. A gold nanosphere is located in the gap between two solid immersion lenses, filled with index matching oil to prevent reflections. The particle scatters light alternatively from a reference beam with fixed linear polarization and a measurement beam whose polarization is adjusted using half- (HWP) and quarter-wave (QWP) plates. The scattered light is collected by a microscope objective and imaged onto a CCD camera.

glass sphere with refractive index $n = 1.46$ by depositing it on an optical nanofibre [166] and surrounding it by two fused silica 2.5 mm-radius hemispherical solid immersion lenses. The $\sim 200\,\mu$m gap between the lenses is filled with index matching oil to prevent any reflection near the particle from either the nanofibre or the lenses. The nanoparticle is illuminated by a laser beam (vacuum wavelength $\lambda_2 = 685\,$nm) with adjustable polarization and the scattered light is imaged onto a CCD camera through the sphere and a microscope (Fig. 5.18).

To test the dependence of the position apparent displacement on the NA, two different microscope objectives are used with the same nominal magnification but different numerical apertures, resulting in NA $= 0.41$ and NA $= 0.61$ when including the silica sphere refraction index, and measured magnifications 21.9(2) and 20.1(1), respectively. The apparent displacement of the nanoparticle is measured by fitting a two-dimensional Gaussian function to its image, using alternately the beam with adjustable polarization and a linearly polarized reference beam. The measurements, averaged over 125 individual realisations for each polarization setting, are shown in Fig. 5.19. For $|\epsilon| < 2$, within experimental errors, a very good agreement of the measurements with the expected linear increase of the displacement with ϵ is observed, independent of the numerical aperture. For larger $|\epsilon|$, the linear approximation is not valid and the experimental data follows approximately the theoretical approximation of Eq. (5.42) (dashed lines). The apparent positions of the nanoparticle imaged with right and left circular polarizations ($\epsilon = \pm 1$) are displaced relative to each other by 145(6) nm for NA $= 0.41$ and 146(4) nm for NA $= 0.61$, in agreement with the expected value $2\Delta y = \tilde{\lambda}_2/\pi \approx 150\,$nm, where $\tilde{\lambda}_2 = \lambda_2/n$ is the laser wavelength in the index matching oil. The displacement increases for larger values of $|\epsilon|$, and the total displacement between counter-rotating elliptical polarizations reaches 430(7) nm ($\simeq \tilde{\lambda}_2$) for $\epsilon = \pm 5.67$, a shift four times larger than the diameter of the gold nanoparticle. Additional details about this experiments can be found in Ref. [147] and in the Ph.D Thesis of Stefan Walser [167].

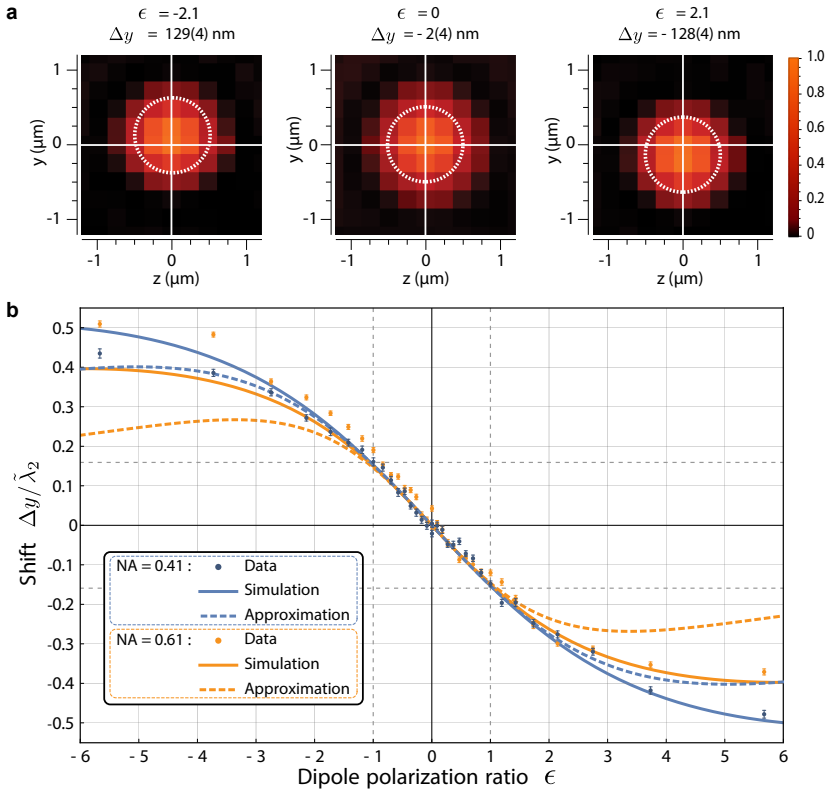

Figure 5.19: Apparent displacement of a gold nanosphere. a, Measured images of the nanoparticle for $\epsilon = \pm 2.1$ and $\epsilon = 0$ for NA $= 0.41$. The white cross indicates the position of the nanoparticle obtained from the reference image. The dashed circle with a diameter of 500 nm indicates the 1σ width of the image obtained from a Gaussian fit and is centred around the apparent position of the nanoparticle. **b,** Relative displacement of the image of the particle as a function of ϵ, measured for two different NAs. The error bars indicate the 1σ statistical error. The dashed curves are the theoretical approximation of Eq. (5.42) and the solid curves are the displacements obtained by numerical simulations of the field propagation. The dashed grey lines show the case of circularly polarized emitters. Figure made by S. Walser.

5.7 Relation with optical current vortices

There is a close connection between the measurement of emitter apparent displacement higher than $\lambda/2\pi$ (weak value amplification) and the appearance of momentum vortices in the emitted light field [168–170]. This connection is depicted in Fig. 5.20 which plots the field distribution of the emitted light in the lens plane, projected into different polarization bases and for different states of the emitter.

Optical spin-orbit coupling manifests itself in the azimuthal depending phase of axially symmetric dipole fields. For example, the right circularly polarized dipole about the optical axis (row 1 in Fig. 5.20) is a superposition of a right circular polarized field with orbital angular momentum $\hat{L}_x = 0$ and a left circular polarized field with $\hat{L}_x = 2\hbar$. Therefore, the phase of the field projected in the circular left basis (E_L) is point-symmetrical and shows a strong azimuthal dependence(Fig. 5.20

row 1, column 3), and a singular point (vortex) in the intersection of the lens plane and the symmetry axis of the dipole. The vertical polarization projection E_V is constant along the vertical axis of the plot, and the intensity distribution for different NA (Fig. 5.20 row 1, columns 6 to 8) do not show a displaced image.

Similarly, the linear dipole along the optical axis, $\vec{d}(\epsilon = \infty)$ (Fig. 5.20, row 6), consists of equal superposed circular fields with orbital angular momentum $\hat{L}_x = \pm\hbar$ opposed to their spin $\hat{S}_x = \mp\hbar$. The phase of the field projected in both circular the circular basis left E_L and right E_R shows a point-symmetry with a singular point in the intersection of the lens plane and the symmetry axis of the dipole. The vertical polarization projection E_V is constant along the vertical axis of the plot. The intensity distribution for different NA do not show a displaced image.

For $0 < \epsilon < \infty$ the vertical projection E_V of $|\psi\rangle$ has a pronounced vertical phase gradient due to orbital angular momentum $\hat{L}_z$. This gradient Fourier transforms to a displacement along y in the image plane. The image fields are both displaced and distorted depending on ellipticity and aperture, as already shown in Fig. 5.4. For small numerical apertures the image of the elliptical dipole is close to a displaced aperture point-spread function.

Furthermore, for $0 < \epsilon < \infty$ the circular components of the elliptical dipole fields have off-axis momentum-current vortices (phase singularities in the E_R and E_L plots in Fig. 5.20) [168–170]. As shown in columns 2 and 3, the phase singularities in the E_L and E_L projections move from the edge ($\rho/f = 1$) to the optical axis ($\rho/f = 0$) as ϵ increases from 1 to ∞. The image plane distributions provide a graphical illustration of the apparent position displacement. The displacement of the image is maximum when the vortex is located close to the edge of the lens aperture, and therefore, it depends on the NA of the lens, as shown in Fig. 5.5.

The elliptical dipoles may be displaced by an amount Δy that corresponds to momentum larger than the field largest momentum eigenmode due to the weak amplification effect, and that scales inversely with the NA, according to the weak value amplification rule (see Fig. 5.5 and Eq. 5.5). This weak value amplification is an example of supermomentum in single-photon field. The centroid is maximally displaced when the vortices are in the edge of the collection aperture, which in the case of NA ~ 0.6 occurs when $\epsilon \sim 2$.

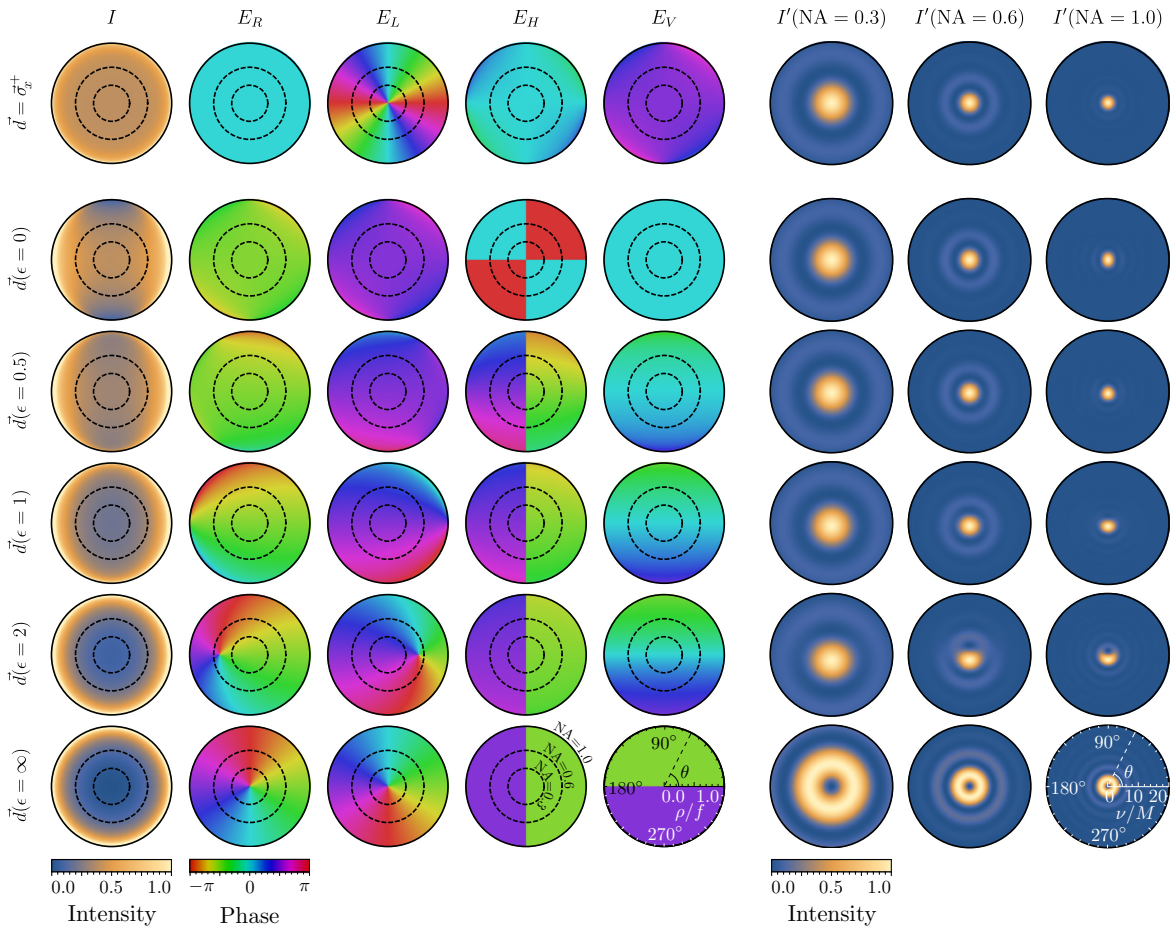

Figure 5.20: Momentum vortices and weak value amplification. The plots show the field distribution of the emitted light at the lens plane for different polarization projection and different states of the emitter alongside corresponding intensity distributions in the image plane. **(Left five columns)** Field intensity I and phase in the local linear (E_H,E_V) and local circular (E_R, E_L) polarization bases of the dipoles shown at left by an apodized orthographic projection. This projection is identical to the field distribution after collimation by an ideal spherical lens. The fields are plotted in radial coordinates $\rho/f = \sin(\phi)$ to an aperture half-angle $\phi_a = \pi/2$ at which the orthographic projection diverges. Dashed circles indicate NA= 0.3, 0.6. **(Right three columns)** Corresponding images I' calculated by full propagation of the optical dipole fields for NA= 0.3, 0.6 and 1. For NA<1 the images are calculated by a truncated Hankel transform. I' is plotted in radial coordinates ν/M with units $\lambda/2\pi$. The colour scale is normalized to the maximum of each image. **(Row 1)** the dipole circularly polarized about the optical axis. **(Rows 2–6)** dipoles with increasing polarization ratio ϵ. The corresponding images for negative ϵ can be obtained by reflecting the images along the horizontal axis. Figure by D. H. Higginbottom.

5.8 Implications and applications

5.8.1 Implications in positioning and imaging techniques

The presented phenomenon can affect different techniques used for the localization of remote objects even beyond the optical regime. As soon as an object can emit or reflect waves with transverse angular momentum the effect is present. Thus, it may affect the localization of remote objects imaged with radar or sonar techniques [171, 172], or even alter the apparent position of astronomical objects detected through their emission of gravitational waves [173, 174].

We speculate that the most notorious case where the studied effect can have important consequences is in super-resolution microscopy techniques. In modern super-resolution microscopy it is possible to achieve image resolutions two orders of magnitude smaller than the systematic apparent displacement demonstrated here [175, 176]. Small deviations from an ideal linear dipole emission typically considered in this kind of techniques can lead to the presence of transverse orbital angular momentum in the emitted field, and therefore, to uncertainties and deviations of the actual position of a marker. Taking into account the presented effect, the determination of the position of an emitter with using an optical system with NA = 1, at a wavelength of $\lambda \approx 628\,\mathrm{nm}$ with an accuracy of 1 nm, requires the scattered light to be more than 99.99 % linearly polarized, i.e., $|\Re(\epsilon)| < 0.01$ (see Supplementary information in Ref. [147].

Residual components with transversal angular momentum in the detected light in super-resolution microscopy are in general present, and therefore the discussed effect takes place. These components in the detected field can be a consequence of the presence of non-linearly polarized components in the illuminating field, and/or due to the non-elastic scattering of the used marker, even under ideal linearly polarized illumination. The first case occurs, e.g., when a strongly-focused linearly-polarized illumination is used to excite the emitter, as typically done in super-resolution microscopy. In this case, the paraxial approximation is not valid, and near the focus, the field exhibits both transverse and longitudinal angular momenta, which then can be transferred to the detected field [177].

The second case in which non-linear polarization components can appear in the detected fields comes from the fact that commonly-used microscopy markers can emit as elliptically polarized emitters. Markers such asnanorods, or even nanospheres with small deformations exhibit complex-valued anisotropic polarizability, due to spurious reflections or plasmonic effects, and can, therefore, transform perfectly linearly polarized excitation light to light with some degree of elliptical polarization that features a transverse component of the angular momentum [178]. Even a spurious internal reflection on surfaces slightly not-normal to the illumination axis can lead to phase shifts in the reflected field, and therefore to elliptically polarized components in the detected field. A reflection of 4% and a tilting angle between different surfaces of the marker of 20° can lead to local ellipticities of up to $\epsilon = 0.2$ which would lead to an apparent displacement of about 20 nm for an emitter with scalar polarizability.

We speculate that another way in which non-linear dipole field components can appear in the detected light is due to the use of bio-labels, dyes, organic dipolar molecules, etc., as markers, which in general, do not absorb and emit as perfectly linear dipoles. Even for a molecule that, in view of its structural geometry, could fulfil this requirement, this assumption seems to be unphysical. If a molecule is immersed in a gaseous, liquid, or solid medium, molecular collisions, temperature-induced vibrations, and/or strain-induced static distortions will occur. This will lead to a broadening and results in spectral overlap of transitions of different linear polarizations. In this case, angular momentum can be transferred between the molecule and the light upon both, absorption and emission. If the illumination light features some degree of elliptical polarization, the fluorescence photons can also exhibit elliptical polarization. Moreover, in the presence of spectral broadening, the emitter will generally feature a complex-valued anisotropic polarizability, i.e., its dipole will be elliptical even for perfectly linearly polarized illumination light and, depending on its orientation, polarization-dependent position apparent displacement will result. Given the fact that molecular transitions are broadened by about 6 orders of magnitude in a room-temperature environment, the question is thus not whether the mixing of transitions occur but only how strong it is. We are not aware of studies that investigate this issue to the precision required to rule out the importance of ellipticity-dependent apparent displacement. We expect that, stimulated by our work, such studies will be carried out in the near future.

Given the fact that the apparent displacements do not occur for linearly polarized dipoles, one might be led to think that they are also small for small elliptical polarization components. However, as we experimentally demonstrated, in certain situations (small NA), this is precisely when the apparent displacement can become large. Thus, any spurious elliptical polarization component of the detected light may lead to a wavelength-scale systematic apparent displacement of the centroid.

Note that, for larger ϵ, an accuracy of, e.g., 1 nm could still be reached by employing an algorithm that not only uses position but also polarization of the dipole as fit parameters for the recorded point-spread function, although requiring the number of detected photons to be increased by several orders of magnitude [147,159].

5.8.2 Applications in optical sensing

The apparent displacement of the emitters depends on the local properties of the illumination and the orientation of their dipoles, and therefore, the displacement can be used to measure these properties. As an example, the presented effect could be used in conjunction with an array of trapped particles to measure the local polarization of an illumination laser. If the illuminating laser has different degrees of circular polarization at the position of the particles, this is translated into different apparent displacement in the image of each particle, see Fig 5.21a. If the distance between particles is known, information about the local polarization of the beam can be extracted from the images.

Another example is the sensing of magnetic field directions using arrays of trapped atoms. As the studied effect depends on the direction of the optical axis and the quantization axis, small variation of the magnetic field direction at the po-

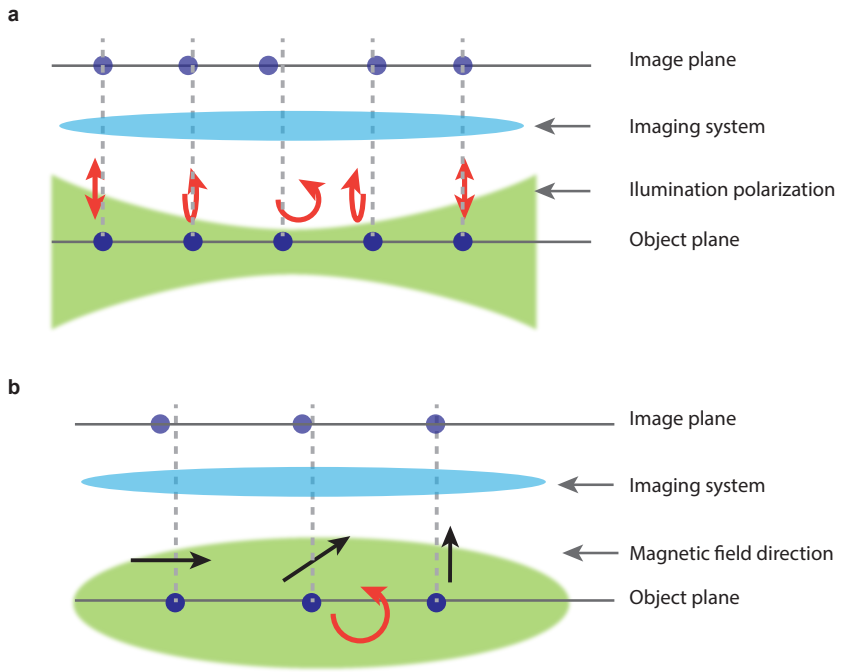

Figure 5.21: Examples of applications in metrology. a. The local polarization (red arrows) of an illumination beam (green) can be measured by observing the apparent displacement of the image of a nano-particle array. **b.** The local direction of the magnetic field (black arrows) can be measured by observing the apparent displacement of a chain of trapped ions excited by a field with constant circular polarization.

sition of the different atoms can be studied by imaging the atoms. If there is such a variations on the magnetic field direction, this would be translated into different apparent displacements for each atom, as shown in Fig 5.21b.

5.8.3 Applications in selective detection and coupling

In some cases, depending of the NA of the imaging system and on the dipole polarization ratio ϵ, it is possible to spatially separate photons emitted by dipole with opposite ϵ. Fig. 5.22 show two examples where this is possible. In the top row, the images of a dipole with $\epsilon = -5$ and $\epsilon = +5$ are displayed. 73% of the photons emitted by the $\epsilon = -5$ dipole are detected in the top half of the image screen, whereas 73% of the photons emitted by the $\epsilon = -5$ are detected in the bottom half of the image. Therefore, if an emitter emits a photon which is in a superposition of dipole fields with $\epsilon = \pm 5$, which gets detected in the top half of the image, we can say with 73% confidence that it was emitted by the $\epsilon = -5$ component of the superposition, and *vice versa*. It is possible to define areas of interest in the image plane where this confidence increases up to more than 99% (red circles in Fig. 5.22).

The bottom row of Fig. 5.22 shows a second example, with NA = 1.0. In that case, photons emitted by a dipole with $\epsilon = -1$ and $\epsilon = +1$ can be distinguished also with 73% confidence by looking at which half of the screen they where de-

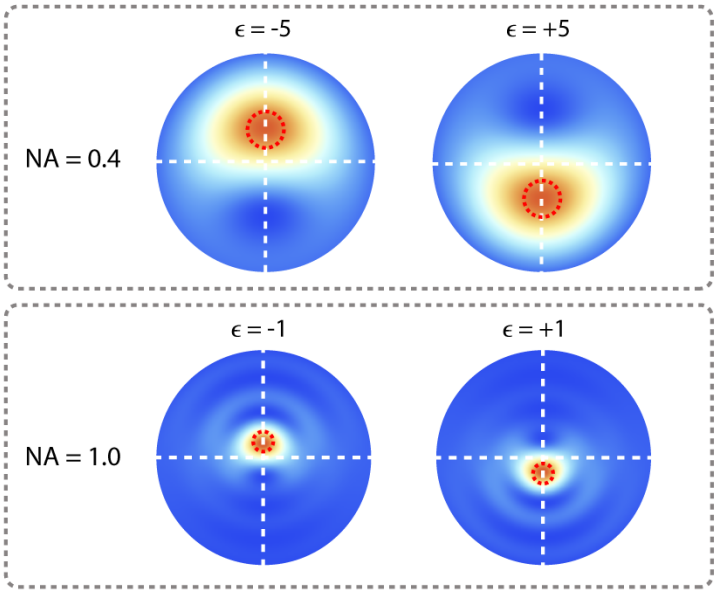

Figure 5.22: Dipole selective detection. Images of dipoles with opposite ϵ and using an imaging system with NA = 0.4 and 1.0. Depending where a photon is detected, we can distinguish from which dipole was emitted. The region marked with a red circle show the area where it would be possible to distinguish with more than 99%.

tected on. Restricting the area of interest in the screen to the ones shown in the figure, this confidence also increases up to 99%. The case of $\epsilon = \pm 1$ is of particular interest in atomic physics, since this corresponds to the emission of photons from $\sigma^{\pm}$–transitions, corresponding to projections to different atomic states. This could be used, for example, to create directional coupling between different atoms. If a second atom is located in the image plane of the first one, where the image intensity peak of the σ^{+}–dipole is located, then only photons coming from the σ^{+} transition would be absorbed by the second atom. Conversely, if another atom is located in the image plane of the first one, where the image intensity peak of the σ^{-}–dipole of this is located, then only photons coming from the σ^{-}–transition would be absorbed by the second atom. This can be useful to implement free-space chiral atomic networks, with applications in quantum networking and communications [143].

5.9 Summary and outlook

In this chapter we have studied the coupling of spin and angular momentum on the emitted field of single fundamental emitters. We have theoretically and experimentally shown that the presence of transverse orbital angular momentum can lead to the apparent displacement of the position of the emitter. We have demonstrated that, in the case of imaging a single ion, this apparent displacement, in spite of being a sub-wavelength effect, is still well above the achievable resolution with state of the art imaging systems.

The most surprising results appear in the case of small numerical aperture imag-

ing systems, where the apparent displacement can reach values higher than the wavelength. We have discussed how these results are in agreement with the weak-measurement and weak-value amplification formalism.

The apparent displacement of the emitter position is present even for ideal, focussed, aberration-free imaging systems. It is a fundamental and universal phenomenon, and should not be confused with positioning error due to an imperfect optical system or biased analysis tools [159]. As we have discussed, this phenomenon has implications in super-resolution microscopy, but also offers opportunities for metrology or quantum networking.

The results presented here, although developed for fundamental dipole optical emitters, are still valid for any multipole optical emitter, such as an atom emitting photons in a quadrupole transition. In that case, the angular momentum eigenspectrum of the emitted field includes photons carrying higher angular momentum, namely $2\hbar$, and therefore higher displacements are expected. Furthermore, the discussed effect does not belong to the optical spectrum only, but to any emitter (or scatterer) emitting waves carrying transverse angular momentum, as is the case of sound waves, radio waves or gravitational waves [179].

6

A new setup for quantum electrodynamics studies and for improved light collection

6.1 Introduction and motivation

The spontaneous emission rate of atoms can be enhanced or inhibited in several ways. As already discussed in Chapter 4, one way to achieve modification in the spontaneous emission rate is through dipole-dipole interactions, namely sub- and superradiance type effects [89–92]. Observing large modifications of the spontaneous emission in trapped ions using this approach is in general difficult, since the Coulomb interaction restricts the minimum achievable interatomic distance. Nevertheless, some degree of modification has been shown for the case of two ions. In Ref. [132] an enhancement of $\sim 1.5\%$ and an inhibition of $\sim 1.2\%$ by locating two ions 1470 nm away from each other. As we have experimentaly studied in Chapter 4, the limitations imposed by the Coulomb forces can be partially overcome using entanglement, achieving a modification of the spontaneous emission rate of up to 30% that does not depend on the interatomic distance. However, this is not a global modification of the spontaneous emission rate of, and only a directional effect. In the case of neutral atoms, the Coulomb interaction is not a limitation, and modification of the spontaneous emission has been demonstrated with large atomic ensembles [180].

Another way to enhance or reduce the rate of spontaneous emission of an atom is modifying the electromagnetic vacuum mode structure interacting with the atom [181, 182]. The electromagnetic mode structure interacting with the atoms can be altered by placing them close to dielectric interfaces [183], between two mirrors [184] or inside photonic structures which pruduce a bandgap [185] . In particular, large enhancement of the emission from a single atom has been achieved using high-finesse cavities [186–189]. Recently, a 5-fold enhancement in the spontaneus emission rate has been demonstrated placing a single atom in a fiber cavity [190]. Furthermore, in the realm of solid state emitters, enhancement by a factor of more than 100 has been observed using microcavities [191]. The opposite effect, i.e., inhibition of the spontaneous emission, remains more elusive, and only few experiments have demon-

strated large modifications, see for example Ref. [192] where the rate of spontaneous emission of a single Rydberg atom was reduced by a factor of 20, or Ref. [193] where the emission rate of a solid state emitter was reduced by a factor of ~ 10. The main limitation in all the mentioned experiments is that by using standard approaches it is not possible to restrict all the spatial vacuum modes surrounding the emitter.

It is a common assumption in the field of cavity electrodynamics that to achieve total inhibition of the spontaneous emission it is necessary to place the atom in between mirrors that cover the full solid angle around it, restricting all the vacuum modes resonant with the atom, see for example Ref. [194]. On the contrary, given the point symmetry of the emission of atoms, it is still possible to restrict all the vacuum modes covering only the half solid angle. This can be achieved by placing the atoms in the center of a concave hemispherical mirror, as theoretically predicted in Ref. [195]. By taking this approach it is possible to achieve both inhibition and enhancement of the spontaneous emission, depending on the radius R of the hemispherical mirror, provided that the mirror is close enough to the atom to allow temporal interference of the field emitted in opposite directions. This condition can be written as $2R/c \ll 1/\Gamma$, where c is the speed of light and Γ is the free-space decay rate of the observed transition. If $R = n\lambda/2$, where n is an integer and λ is the wavelength of the observed atomic transition, an atom located in the center of curvature of the mirror lies in a node of the vacuum mode density and inhibition is observed. Conversely, if the radius is $R = n\lambda/2 + \lambda/4$, an atom located in the center of curvature lies in an anti-node, an enhancement is observed. If the mirror is not a hemisphere, but a spherical mirror with NA < 1 only partial modification is expected. Fig. 6.1 shows the expected modification of the decay rate of a dipole transition depending on the numerical aperture of a perfectly reflective spherical mirror. Furthermore, other effects such as ground and excited level shifts depending on the size of the mirror have been predicted [195].

In this Chapter we present the new "Panopticon" apparatus for the integration of a high quality hemispherical mirror (NA ≈ 1) and a trapped ion for the realization of the paradigmatic situation described above. In addition to the fundamental components of such a setup, i.e., the hemispherical mirror and a Paul trap, a high numerical aperture lens (NA $= 0.7$) is used to collimate the emission and direct it to a detector. The design and construction of such an apparatus presents multiple technical challenges which are discussed in this Chapter, including

- The construction and characterization of a hemispherical mirror with constant radius of curvature. The effects discussed above vanish rapidly if the radius of curvature is not constant. We aim to fabricate a hemispherical mirror with a radius of curvature RMS error not larger than $\lambda = \lambda/10$ over all the surface. The radius of curvature must be tunable through thermal expansion of the substrate.

- The trap design. The used Paul trap must provide full optical clearance between the trapped ion an the hemispherical mirror. Additionally, it must provide optical clearance for the collection of the emitted light through the high NA lens and for laser access. Ideally, the trap should also provide the possibility of trapping several ions simultaneously in a stable fashion to provide enough flexibility for other experiments.

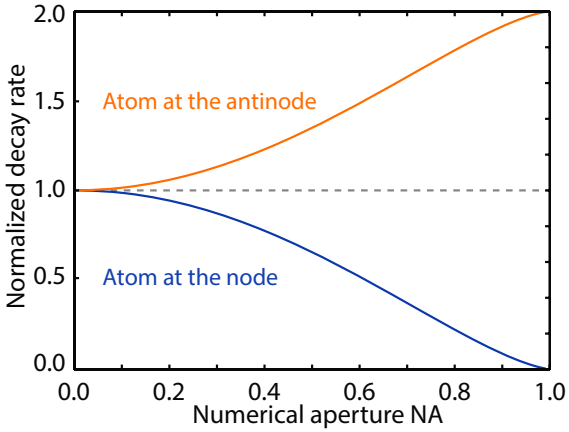

Figure 6.1: Modification of the emission of an atom in the center of a hemispherical mirror. Depending on the radius and numerical aperture of a spherical mirror it is possible to observe inhibition or enhancement of the spontaneous emission rate of an atom located in its center of curvature. If the radius of the mirror is $R = n\lambda/2$, the center of curvature is a node of the vacuum mode density and inhibition is expected (blue curve). If the radius of the mirror is $R = n\lambda/2 + \lambda/4$, the center of curvature is an anti-node of the vacuum mode density and enhancement is expected (blue curve). Perfect inhibition and enhancement are achieved only in the case that half of the space is covered by the mirror (NA = 1). In this plot a mirror with perfect reflection is assumed. Figure taken from Ref. [195].

- The design and characterization of the high NA lens used for collection aim at diffraction limited performance, enabling interference and imaging experiments such as the ones presented in Chapters 4 and 5.
- The design of the vacuum vessel. All these elements have to be placed in an ultra high vacuum environment, and their relative position should be adjustable in-situ.

Besides the fundamental quantum electrodynamics experiments accessible with the implementation of this new setup, it will also provide record photon collection efficiencies for ion trap setups without cavities. For the optical dipole orientation, the expected photon collection efficiency is 38 % without considering enhancement of the spontaneous emission effects. This substantially improves the precision of any optical measurement of atomic properties and properties of the fields interacting with the atom. The improved collection and absorption rates enabled by this kind of setup could be used to implement a quantum network without cavities.

Note that some of the features exhibited by a setup consisting of a hemispherical mirror, such a high collection efficiency and improved single photon absorption, can be achieved using an atom in the focus of a parabolic mirror [66, 196]. However, in this approach the enhancement and inhibition of the spontaneous emission due to QED effects vanish at realistic machinable parabolic mirrors [196]. Other approaches consist in using a combination of a high NA lens collecting the light emitted by an atom and a mirror retroreflecting the collected light. Although changes in the decay rates have been observed using this approach [197], the maximum modifications are

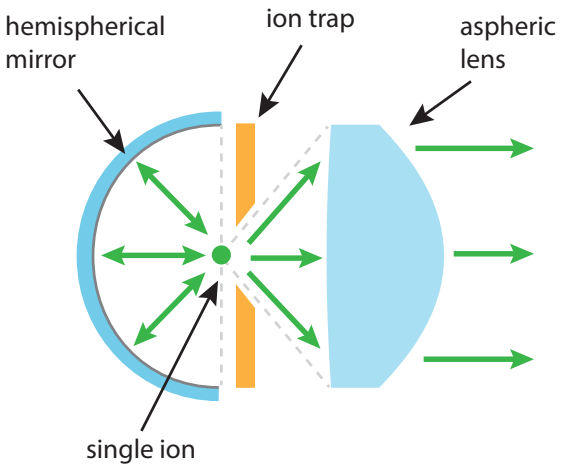

Figure 6.2: Main components of the Panopticon setup. The green arrows show the propagation of the emitted field.

limited by the achievable numerical apertures of the collecting lens in trapped ions systems.

6.2 The Panopticon setup

The main feature of the Panopticon setup[1] is the ability to confine a single atomic ion in the center of a hemispherical mirror. The ion trap needs to provide full optical clearance between the trapped ion and the mirror. Additionally, in order to provide a large capture of the emitted field, a large NA aspheric lens (NA = 0.7) is positioned opposite to the mirror, such that its focal point lies at the position of the ion. Therefore. the trap needs also to provide optical clearance for the solid angle captured by the asphere. Fig. 6.2 shows a scheme with the main components of the Panopticon setup. In this section we describe the design and construction of each of these main components, and how to assemble them together.

6.2.1 The hemispherical mirror

The main component of the Panopticon setup is the concave hemispherical mirror. To be able to observe large modification of the spontaneous emission of an atom located in its center, optical surface precision is required over the full numerical aperture. The best macroscopic round objects ever fabricated are spheres with a surface deviation of only 17 nm peak-to-valley [199]. This surface quality is achieved by randomly rotating the sphere between two polishing tools, for periods of several days. Unfortunately, this technique cannot be applied to concave spherical surfaces, and in general, until now, there was no technique able to produce a surface precision

[1] The Panopticon setup owes its name to a type of institutional building proposed by the English philosopher and social theorist Jeremy Bentham [198]. In this kind of building, a single watchman located in a central tower can observe all the inmates of the institution, which are located in cells with optical clearance around the tower.

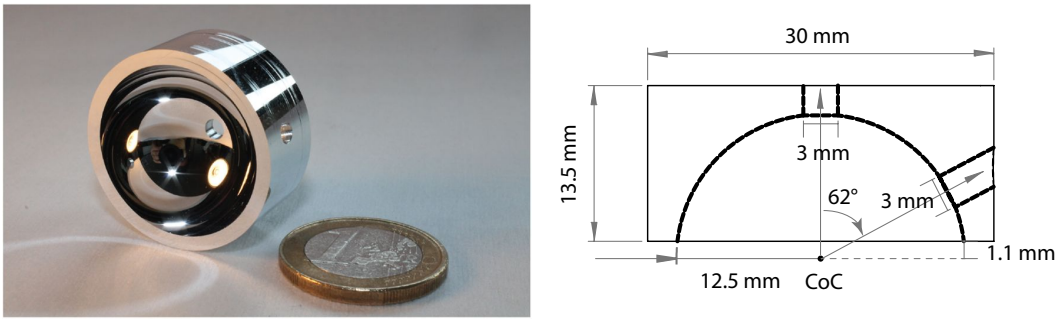

Figure 6.3: Fabricated hemispherical mirror. Photograph of a fabricated hemispherical mirror and a euro coin for comparison. The sketch on the right side shows a cross section with the relevant dimensions of the fabricated mirror. Note the 3 mm diameter drilled holes which provide radial laser access to the center of curvature (CoC) of the mirror, where the ion will be located.

similar to that of convex sphere. As a reference, the probably roundest convex objects ever fabricated (prior to our work) has a peak-to-valley deviation of 163 nm [199].

In a collaborative work with The Australian National University (ANU) we have been able to produce hemispherical mirrors with RMS form error consistently below 25 nm, a maximum peak-to-valley error of 88 nm, and a radius of curvature of $\approx$ 12.5 mm. The mirrors were fabricated by D. B. Higginbottom by diamond turning a cylindrical aluminium 6061 substrate with a CNC (computer numerical controlled) nano-lathe[2]. To achieve low surface deformation, an in-situ white-light interferometer was implemented on the lathe, permitting the calibration of the tool with sub-nanometer precision prior to the machining. A detailed description of the fabrication and characterization of the mirrors can be found in Refs. [200, 201].

Fig. 6.3 shows a fabricated mirror intended to be used in the experiment, with a surface RMS error of 18.1 nm and a peak-to-valley error of 116.5 nm. There are two drilled holes (3 mm diameter) which provide laser access to the center of curvature, where the ion will be located (see Section 6.2.4). One of them is located along the optical axis of the mirror and the other at 62° from the center with respect to the optical axis. The NA of this mirror is 0.996 (half aperture 85°), which is not a limitation of the fabrication process but is planned to provide optical clearance (1.1 mm) to the trapped ion for a laser beam orthogonal to the mirror's optical axis. The reflectivity of the mirror is the one of the substrate (0.92 for aluminium 6061 at 493 nm), and it could be improved by applying a highly reflective thin film coating to the mirror. The concave shape of the mirror makes it difficult to realize this in a uniform fashion, and it would be detrimental for the overall surface quality using standard techniques[3]. Detrimental effect are expected also from standard polishing techniques. Fig. 6.4 shows the expected modification of the spontaneous emission considering the measured surface form, reflectivity and the effect of the drilled holes. Considering form and reflectivity, the maximum expected

[2]Nanotech 250UPL, Moore Precision Tools

[3]New developments in Atomic Layer Deposition (ALD) have shown promising results in uniform coating of complex 3D structures, see for example https://www.laseroptik.de/en/coating-guide/production-methods/ald

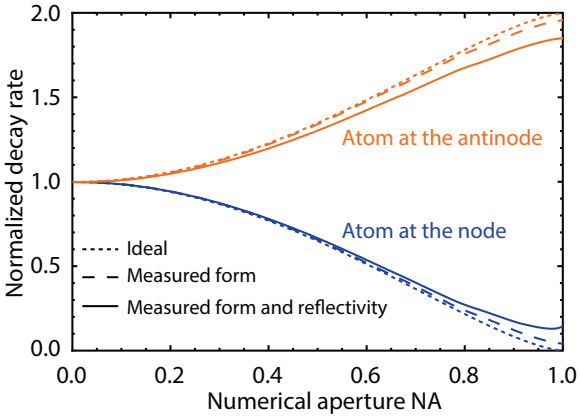

Figure 6.4: Expected performance of the fabricated mirror. Modification of the spontaneous emission rate considering the achieved form, and the achieved form and reflectivity of the substrate. The numerical aperture NA=0.996 is not distinguishable from NA=1.0 in the shown plot. Considering form and reflectivity, the maximum expected enhancement and inhibition of the spontaneous emission rate correspond to 88% of its ideal value.

enhancement and inhibition of the spontaneous emission rate correspond to 88% of their ideal value. The main deviation from the ideal case comes from the limited reflectivity of the material.

To tune the radius of curvature of the mirror, we rely on the uniform thermal expansion of the substrate. The coefficient of thermal expansion of aluminium 6061 at room temperature is 23.5×10^{-6} K^{-1}. To achieve a difference in the radius of curvature of $\lambda/4 \approx 123.3$ nm (with $\lambda = 493$ nm) it is necessary to change the temperature by 0.42 K. Resistively heating the mirror under a single-shot white-light ZYGO interferometer has shown tunability over the desired range in a uniform fashion, and no indication of surface distortion due to thermal expansion. Nevertheless, small variations in environmental temperature could lead to drifts in the radius of curvature, so that active stabilization of the temperature of the mirror is necessary. To do so, the mirror will be mounted in an aluminium holder, whose temperature is measured using two UHV compatible temperature sensors[4], and stabilized using vacuum compatible heating wires[5].

6.2.2 The aspheric lens

To capture and collimate the light emitted by the ion, an aspheric lens is located opposite to the hemispherical mirror, as shown in Fig. 6.2. The main advantages of using an aspheric lens instead of a multi-lens objective is the simple compact design and reduced spherical and other optical aberrations. The low aberrations play a crucial role in future experiments related with spatial properties of emitted and absorbed photons, as well as interference experiments with photons emitted by atoms in different traps and detection of quantum features of the atomic motion.

[4]Thermistors BC101B1K, Littelfuse®

[5]Insulated Nichrome wires NC-32, LakeShore Cryotronics®

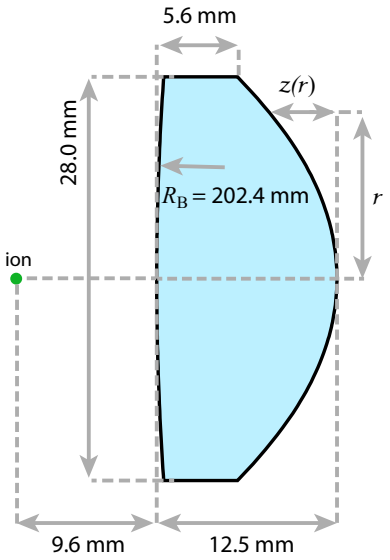

Parameter	Value
R_F	14.56 mm
k	−0.776
A_4	$-3.2022806 \times 10^{-6}\,\mathrm{mm}^{-3}$
A_6	$-2.9002661 \times 10^{-8}\,\mathrm{mm}^{-5}$
A_8	$-9.6249910 \times 10^{-11}\,\mathrm{mm}^{-7}$
A_{10}	$-1.0236456 \times 10^{-13}\,\mathrm{mm}^{-9}$
A_{12}	$4.5511459 \times 10^{-16}\,\mathrm{mm}^{-11}$
A_{14}	$3.3201252 \times 10^{-18}\,\mathrm{mm}^{-13}$
A_{16}	$-8.7645298 \times 10^{-21}\,\mathrm{mm}^{-15}$

Figure 6.5: Aspheric lens dimension. The surface facing the ion is spherical with a radius of curvature R_B, whereas the aspheric face is defined by the Eq. (6.1). The ion is positioned 9.6 mm away from the front surface. The table shows the aspheric surface lens design parameters.

The asphere, designed and fabricated by Asphericon GmbH, has NA = 0.7, a working distance of 9.60 mm and an effective focal length of 16.05 mm. The design was optimized using Zemax OpticStudio to achieve a diffraction-limited single lens with ultra-low wavefront aberrations at 493 nm. These features are needed for future interference experiments between different traps and for high resolution imaging of the emission pattern. The dimensions of the designed asphere are shown in Fig. 6.5. The surface facing the ion has a designed constant radius of curvature $R_B = 202.303\,\mathrm{mm}$, whereas the opposite face is a rotationally symmetric asphere defined by the equation

$$z(r) = \frac{r^2}{R_F\left(1+\sqrt{1-(1+k)\frac{r^2}{R_F^2}}\right)} + \sum_{i=2}^{n=8} A_{2i} r^{2i}. \tag{6.1}$$

The values of the parameters R_F, k and A are listed in the table in Fig. 6.5.

Three pieces of the designed asphere were fabricated using S-TIH53 glass substrate[6], with refractive index $n_g \approx 1.85$, Abbe number $v_g = 23.59$ (at 546 nm). The manufacturing process includes CNC grinding and polishing as first step. In order to reduce surface irregularities, a process called "ion beam figuring" is used. In this process ion beams are hit at specific regions of the surface. Finally, an anti-reflecting coating for 493 nm is applied using "plasma-assisted physical vapour deposition". All this step were performed using Asphericon GmbH technology. Fig. 6.6a shows a photograph of one of the aspheres and Fig. 6.6b shows the achieved wavefront quality[7]. RMS wavefronts distortion below 37 nm and peak-to-valley distortion below

[6]Ohara Corporation, quoted absorption coefficient of 0.951% at 488 m. Data sheet at https://www.oharacorp.com/pdf/estih53.pdf

[7]The wavefront distortions were measured using a high-resolution wavefront sensor, Phasics

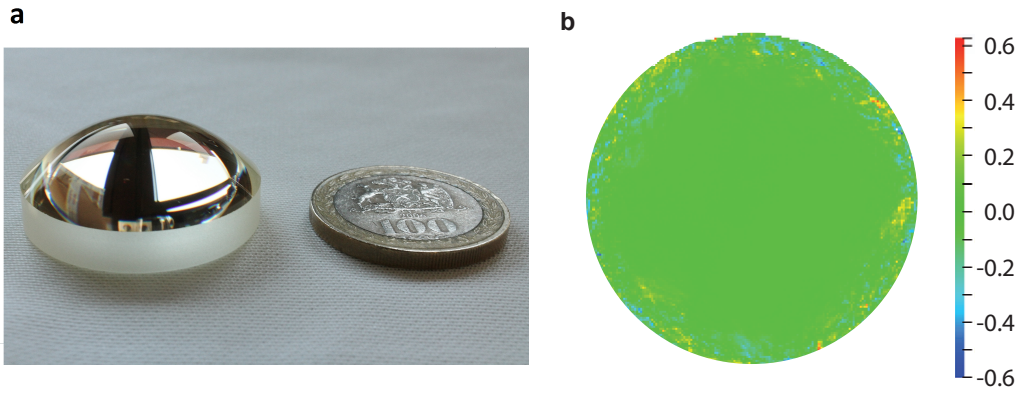

Figure 6.6: Fabricated aspheric lens. a. Photograph of one of the three fabricated aspheric lenses together with a hundred chilean pesos coin, giving the scale (the coin has the same dimensions as a one euro coin). **b.** Measured wavefront distortion of one of the aspheres. The color scale is in units of $\lambda = 493$ nm. Provided by Asphericon GmbH.

700 nm over all of the numerical aperture were systematically achieved. The reflections in the coated surfaces where measured to be smaller than 0.4% for incidence angle of up to 40°, and the transmissivity measured with a laser beam perpendicular to the surface at the center of the lens was 95%, in agreement with the quoted values. Both measurements where done with a laser beam with 493 nm wavelength.

The lens is mounted in an aluminium holder, which allows for laser access to the focal point of the lens from several directions (see Section 6.2.4), and with negligible reduction of the numerical aperture.

6.2.3 The ion trap

The main challenge in the design of an ion trap compatible with the Panopticon setup, is that the trap should provide full optical clearance between the trapped ion and the hemispherical mirror, and between the ion and the aperture defined by the aspheric lens. This could be achieved using, for example, a needle trap [202], although this approach allows the trapping of only one ion in a stable fashion without excess of micromotion. It is desirable to be able to trap several ions stably, since the built setup could then be used for a broader range of experiments. There are some designs which partially comply with the optical access and stable trapping of several ions criteria, including, for example, the miniaturized segmented "High Optical Access Trap 2.0" developed by the Sandia National Laboratories[8]. However, this kind of miniaturized traps needs to be operated under cryogenic conditions to achieve optimal performance, which increases the complexity of the setup. The approach that we take here is the fabrication of a monolithic slotted pseudo-planar macroscopic trap. A simplified scheme of the designed trap geometry is shown in Fig. 6.7, where an ion is trapped above the front surface, providing full clearance on the side of the hemispherical mirror and clearance corresponding to the NA = 0.7 of the aspheric lens through the slot.

SID4-307, at Asphericon GmbH

[8]Information about this trap can be found in https://www.osti.gov/servlets/purl/1239095

The geometry shown in Fig. 6.7 generates an RF trapping pseudo-potential in the x and y directions, whereas trapping along the z direction is provided by the DC potential generated primarily by the DC electrodes DC1 and DC2. Note that the DC votages applied to the electrodes DC,3 DC4, DC5 and DC6 also contribute, although weakly, to the trapping potential in the z direction.

The fabrication of such a trap is challenging, but is doable with current subtractive 3D laser micro-machining technology. The basic idea is to 3D laser machine a monolithic dielectric substrate with the required shape, from now on "3D printing", including "trenches" to separate different regions. Then, the surfaces are coated with a conductor, i.e., gold, creating isolated electrodes in each region surrounded by trenches. Fig. 6.8 depicts this basic idea combining 3D-printing and coating to create electrodes.

The required precision of the dielectric substrate fabrication can be achieved by "laser carving" techniques, provided by companies such as FEMTOprint SA. The 3D-printing technology used by this company consists in using strongly-focused high-power laser pulses to locally change the refractive index of the substrate. Then a photo-chemical process is used to remove the material with altered refraction index. Using this technique on, e.g., fused silica, the carved features can reach an average roughness below 100 nm, whereas the untouched surfaces can reach an average roughness below 5 nm. Additional polishing can reduce the roughness below 50 nm, though with detrimental effects in surrounding areas.

Conductive coating of the surfaces by means of evaporation of a thin layer of titanium ($\sim$ 2 nm) and a thick layer of gold ($\sim$ 200 nm) can be performed in-house in our clean room, typically followed by gold electroplating to increase the thickness of the electrodes to $\sim 5\ \mu$m.

Trapping potential simulations

The trap geometry presented in Fig. 6.7 is the result of systematic optimization considering multiple aspects. The different dimensions and positions of the electrodes were varied to optimize the achievable trapping frequencies for $^{138}Ba^{+}$ ion, trap depth, trap capacitance, residual axial RF field and ion-electrode distance, constrained by the required optical clearance and laser access to the ion. For these purposes, the produced electric potentials are simulated via finite element analysis using the software COMSOL Multiphysics® 4.4. In these simulations, besides the fields produced by the trap electrodes, the presence of the hemispherical mirror is considered and its surface is considered to be grounded.

Fig. 6.9 shows the simulated trapping potential, including the DC and RF contributions. The RF pseudo-potential minimum of the presented trap geometry is located 157 μm away from the front plane, making the distance of a trapped ion and the closest electrode equal to 453 μm. For comparison, in our "Innsbruck" style blade trap this distance is 707 μm. Small distances between ion and electrodes increases the heating rate of ions due to surface noise and other effects [203]. Keeping this distance relatively large (above $\sim 300\,\mu$m) is important to minimize these effects.

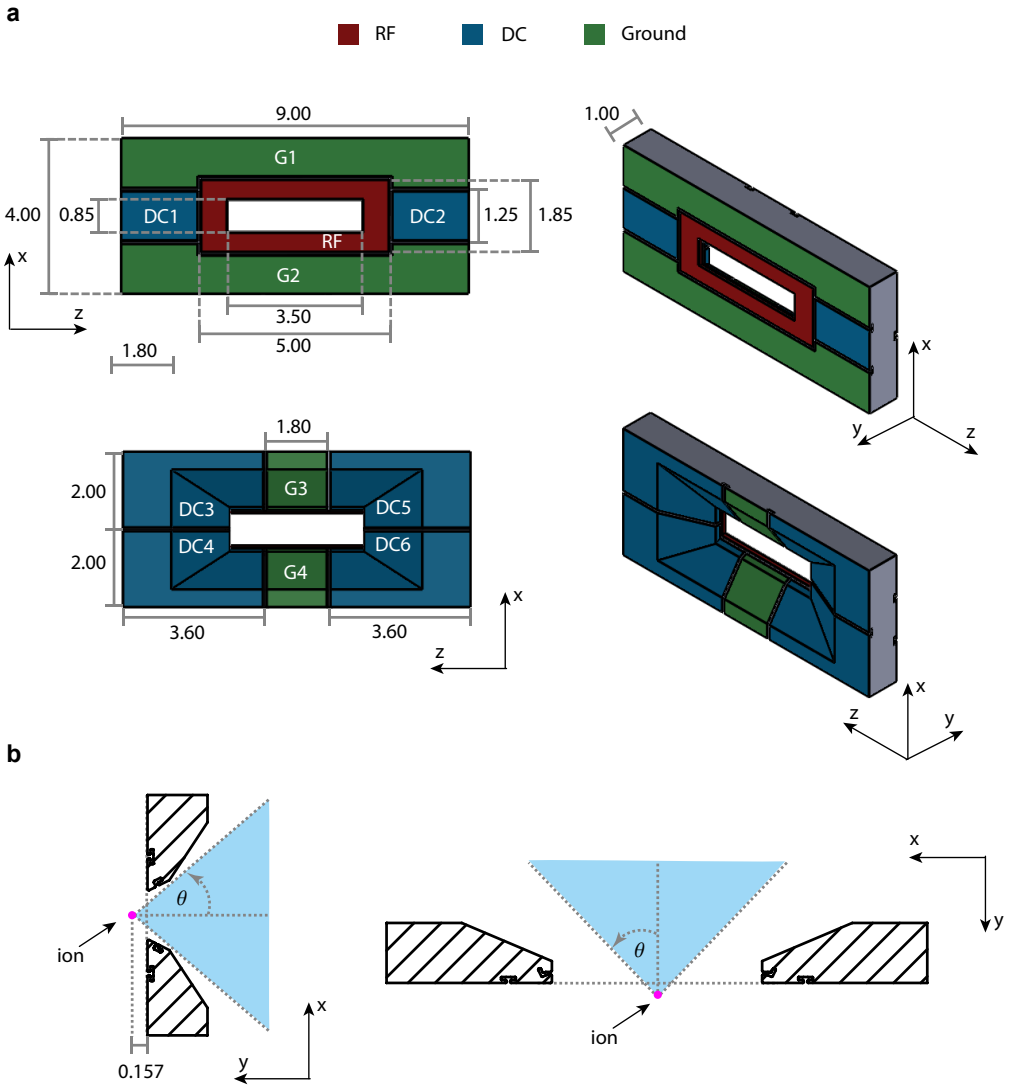

Figure 6.7: Ion trap design a. Simplified design of a 3D-printed ion trap. The RF, DC and ground electrodes lay on the facets of a 3D-printed substrate. All the shown dimension are in mm. **b.** Transverse cuts of the trap showing the optical clearance provided by the design. On mirror side ($y > 0$) there is full clearance, and on the side of the lens the optical clearance (light blue area) is slightly bigger than the required $\theta = \arcsin \mathrm{NA} \approx 44.4°$. The RF pseudo-potential minimum, and therefore the position of the ion, is located 0.157 mm away from the front plane of the trap. The text in white shows the name of each electrode.

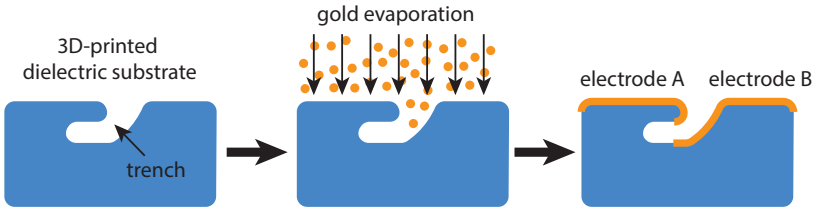

Figure 6.8: Electrode separation through 3D-printing and coating. First, a dielectric substrate is "3D-printed". This substrate includes all the features, including the trenches needed to separate electrodes. Then, the surfaces are coated with a conductor (gold). The geometry of the printed trenches provides electric insulation between different regions, defining different electrodes.

Fig. 6.9c shows the trapping potentials along each coordinate axis. The potentials along x and z are symmetric about the trap center, while along the y axis it is asymmetric, as typically observed in surface traps [202]. Depending on the voltage applied to the different electrodes, the trapping frequencies of the trapping directions can be varied. Table 6.1 shows the trapping frequencies and trap depths obtained from the simulations for a $^{138}Ba^{+}$ ion.

The simulations also show that independent control of the voltage applied to the electrodes DC3, DC4, DC5 and DC6 is enough for compensation of micromotion in all directions. Simulations with different trench geometries and dimensions were carried out. The most relevant trench parameter, i.e., the electrode-electrode separation provided by the trench, was varied between 50 μm and 150 μm. The variations in this range have a negligible effect on the trapping potential shape and the obtained trapping frequencies, but have a significant effect on the achievable breakdown voltages between electrodes. The dimensions used for the actual trap will be set by the results of in-laboratory voltage breakdown tests being performed at the time of writing with samples fabricated by FEMTOprint SA. The goal of these tests is to determine the maximum DC and RF voltages that can be applied to the electrodes considered in our design in realistic experimental conditions, which is expected to be in the order of several kV.

The actual trap

Although the trap design to be fabricated has the same core geometry as the one presented in Fig. 6.7, it includes additional features. Fig. 6.10 shows a render of the actual design. All the electrodes in the front, i.e., DC1, DC2, RF, G1 and G2, are extended to reach the back plane. There, together with the electrodes DC3 , DC4, DC5, DC6, G3 and G4, are prolonged into conductive traces to reach an area not covered by the mirror nor the lens (Fig. 6.10b). In this way, the trap can be wire-bonded and connected to the voltage supplies in a printed circuit board (PCB), without cables in the area of optical clearance. The extended area is also used to clamp the trap to the PCB using the drilled holes.

Additionally, grooves in the front face will be carved in the substrate (during the 3D-printing process). These grooves improve the clearance of the laser beams

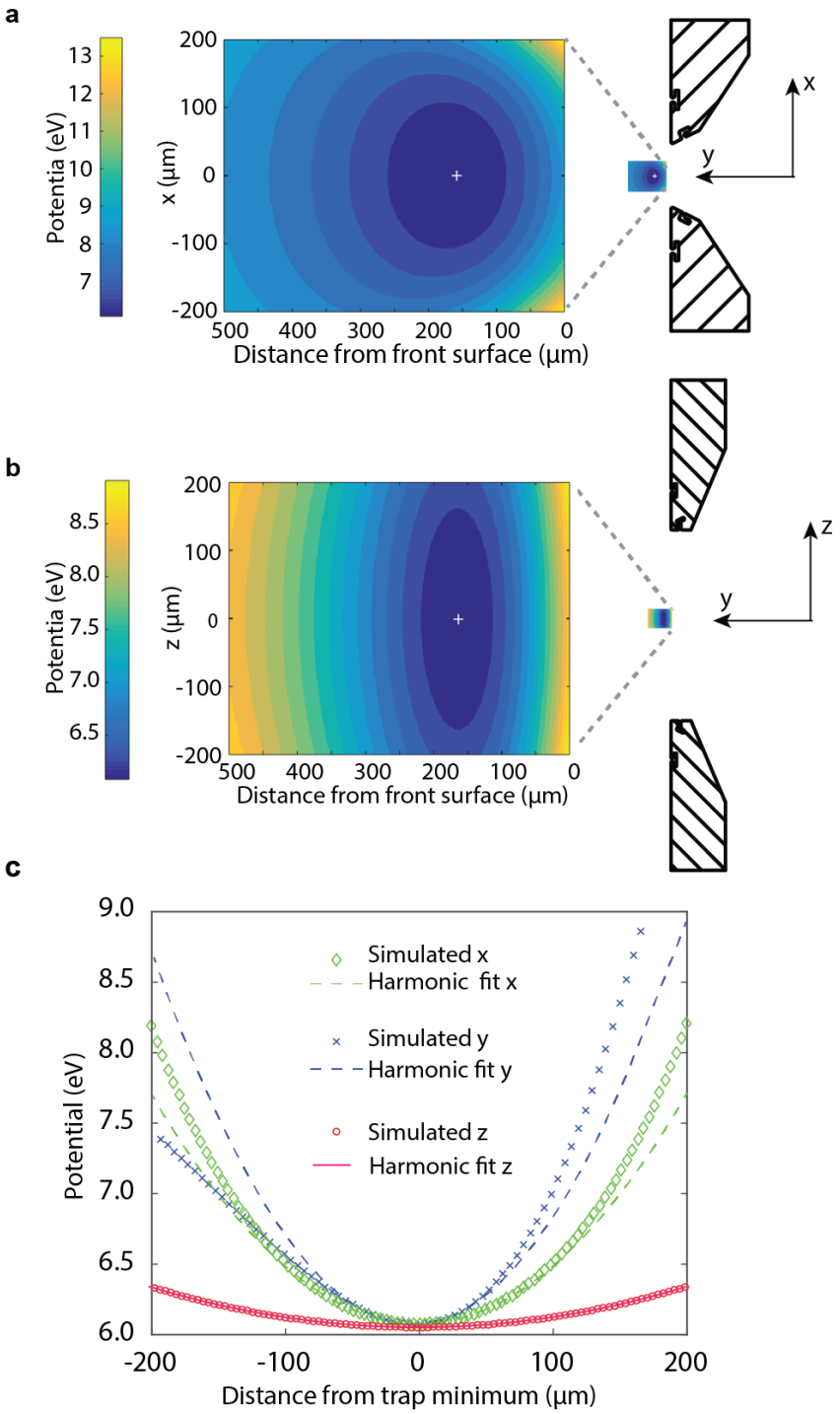

Figure 6.9: Simulated trapping potential of the 3D-printed trap. a. Simulated trapping potential in the $x-y$ plane. The white cross shows the position of the minimum. **b.** Trapping potential in the $y-z$ plane. **c.** Trapping potential along the x, y and z axis. The potentials along x and z are symmetric around the trap center, whereas the potential along y is asymmetric. Close to the center, in a range of $\sim 100\,\mu$m, the potentials are well approximated by harmonic potentials. The parameters used for the plots shown here correspond to "config. 1" in Table 6.1.

	config.1	**config. 2**	**config. 3**
RF freq. $\Omega_{\mathrm{RF}}/2\pi$ (MHz)	16.0	16.0	16.0
RF amplitude U_{RF}(V)	1000	1500	2000
DC1,2 (V)	200	300	400
DC3,4,5,6 (V)	82	123	164
$\omega_x/2\pi$ (MHz)	1.33	2.16	2.96
$\omega_y/2\pi$ (MHz)	1.57	2.34	3.07
$\omega_z/2\pi$ (MHz)	0.51	0.62	0.72
Trap depth (eV)	2.4	4.9	8.2

Table 6.1: Trap driving parameters and resulting trap frequencies and depths, obtained by finite elements simulations. Three different configurations are shown. DC1 and DC2 correspond to the "endcap" electrodes shown in Fig. 6.7, while DC3, DC4, DC5 and DC6 are the electrodes in the back plane. In the three configurations the electrodes G1, G2, G3 and G4 are grounded.

that propagate close to the surface, reducing the light scattered by the trap. This is of particular importance when addressing single ions using a strongly focused 1.7 μm laser. The conical vertical grooves shown Fig. 6.10a mimic the divergence of such a laser with additional 100μm of optical clearance. The horizontal cylindrical grooves give enough optical clearance for an axial cooling beam. Fig. 6.10c shows all the planned axes for laser access to the position of the ions. The vertical axis (blue in Fig. 6.10c) will be used for the 1.7 μm laser beam and compensation of micromotion, the horizontal axis (red)) will be used for optical pumping, compensation of micromotion photo-ionization beams, the diagonal beam (green) will be used for Doppler-cooling, and the axis parallel to the optical axis (yellow) for compensation of micromotion.

We have performed simulations of the generated trapping potential for this design. The differences with the results of the simulations of the simplified version presented above are negligible.

6.2.4 The full optical setup

The optical setup, consisting of the hemispherical mirror, the aspheric lens and the ion trap has to be set in place in a robust and stable manner, while still providing enough degrees of freedom for correct alignment. The holders and positioners have to be compatible with the ultra-high vacuum environment needed to trap single atomic ions in a stable way. To do so, we designed the mounting system shown in Fig. 6.11. In this setup, all the elements are carefully designed in order to provide the required laser access and optical clearance. The position of the mirror and the lens can be independently set by using the xyz-nanopositioners[9] shown in the figure. The positioners have a step of 1 nm in each direction, a position read resolution of 1 nm and a maximum displacement of 12 mm.

[9]SmarAct SLC-1720-S-UHVT

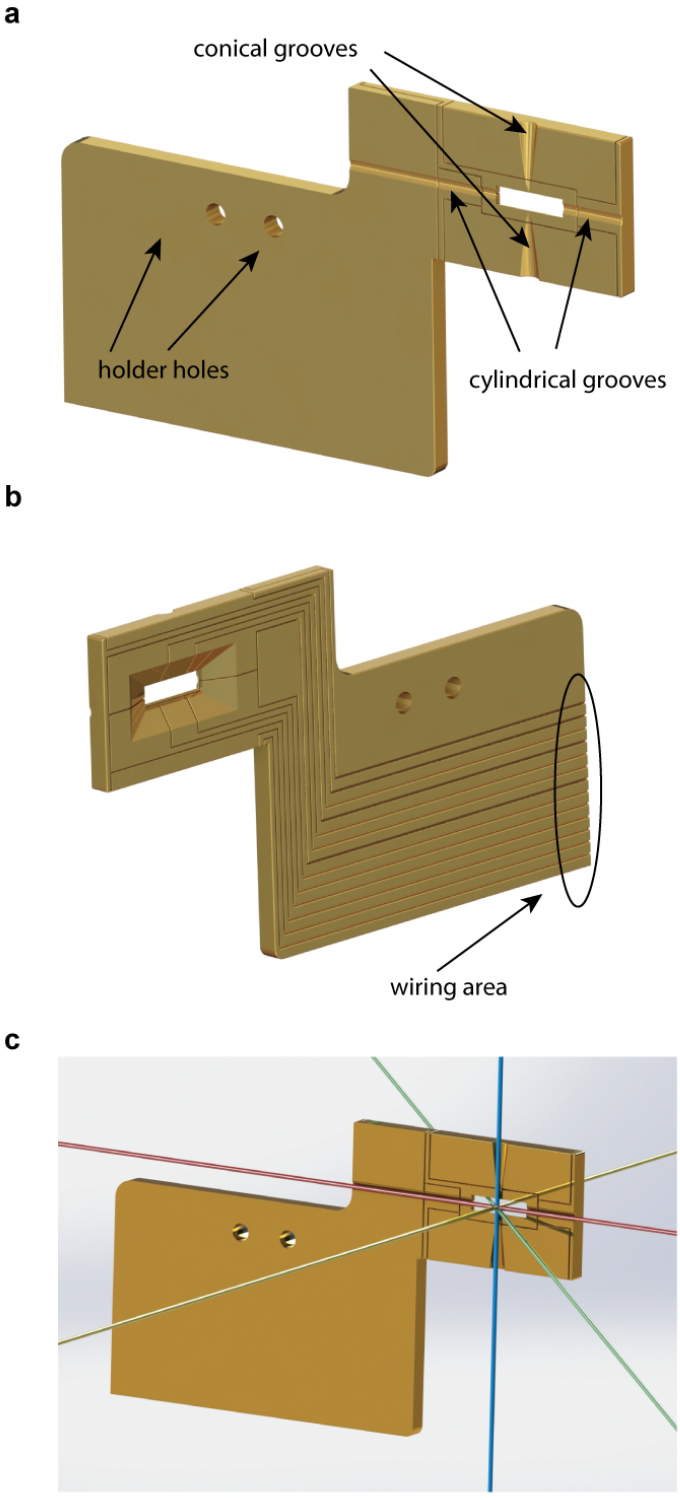

Figure 6.10: Full design of the ion trap. a. Front side of the designed Paul trap. Cylindrical and conical grooves are carved in the substrate in order to minimize the scatter of laser beams propagating close to the surface. All the electrodes in the front are extended to the back plane through the edges. Holes are drilled to hold the trap using screws. The position and number of holes is referential only. **b.** In the back plane all the electrodes are extended into rails, which are used for wire-bonding and connecting the voltage supplies. **c.** The trap and the four planned laser axes.

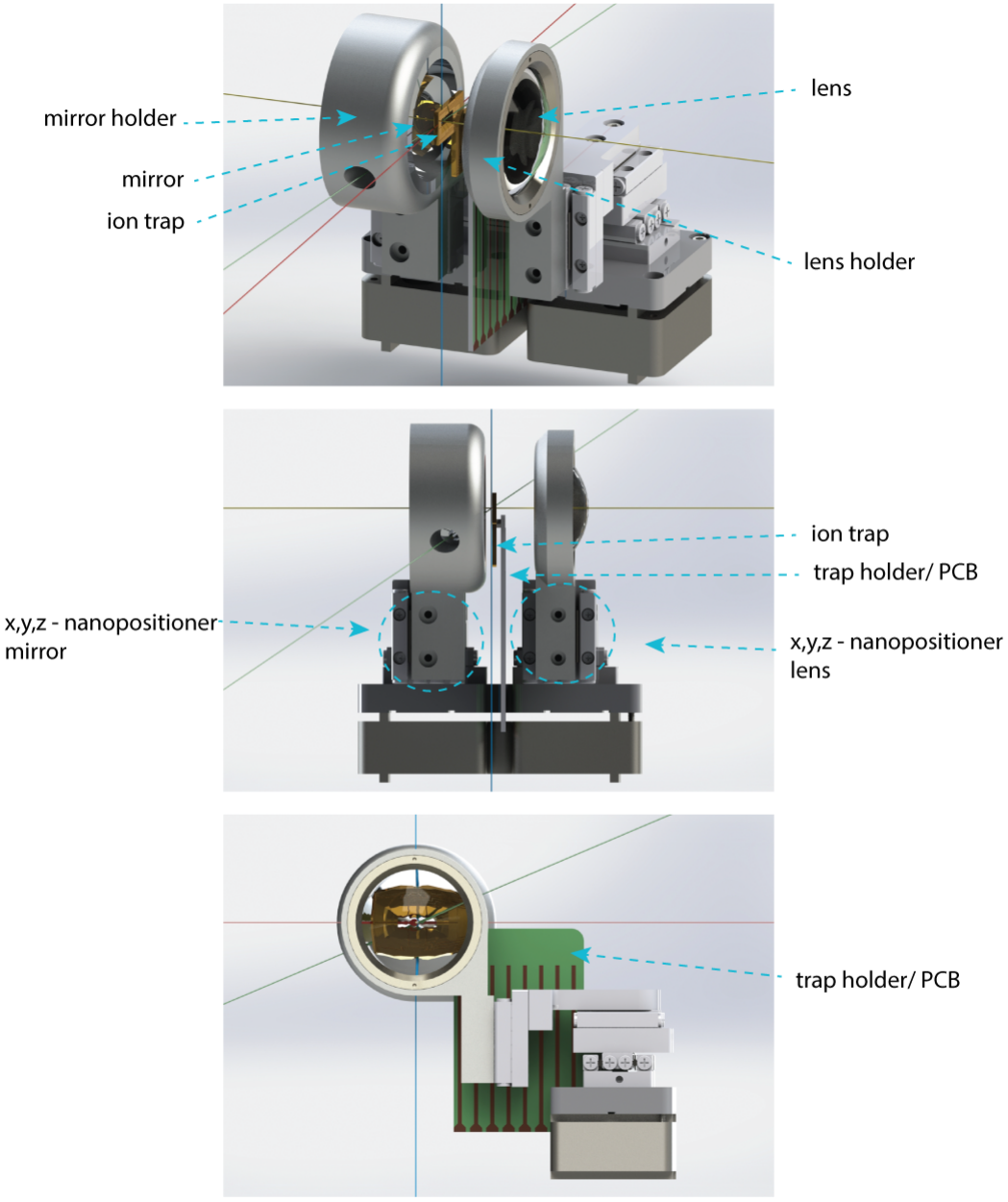

Figure 6.11: Panopticon optical setup. The mirror and lens are mounted on independent xyz–nanopositioners, whereas the position of the ion trap is fixed. The ion trap is attached to a PCB structure with insulating screws and washers. The PCB will hold filtering electronics for the DC electrodes. The coloured lines show the planned laser axes.

6.3 The vacuum vessel

The Panopticon optical setup will be placed in a ultra-high vacuum environment. To achieve this we have designed the vacuum vessel shown in Fig. 6.12. The main component of the vacuum vessel is an 8"–CF spherical octagon vacuum chamber[10]. The chamber provides the required access for laser beams (see Fig. 6.11).

A customized 6-way CF cross is attached to the main chamber, providing enough flanges to connect a vacuum valve[11], a vacuum gauge[12], the electric feedthroughs for the wiring the nanopositioners, a non-evaporable getter (NEG) pump[13] and a viewport.

The main pumping is done with a combined ion and NEG pump[14] attached to the main chamber. During the activation of the NEG part, the pump can reach temperatures close to 450° C. This temperature is not compatible with the maximum temperature to which the nanopositioners can be exposed (150° C). In order to avoid damage of the nanopositioners, the pump is retracted from the main chamber using a spacer, and a two-layer aluminium heat shield is placed between the pump and the positioners (see Fig. 6.12). According to simulations performed by the pump manufacturer, this is enough to prevent damage to the positioners.

The vacuum vessel has all the necessary viewports to provide access to the center of the trap using the planned axes (see Fig. 6.11), including a CF-160 viewport in the top of the chamber. All the viewports are anti-reflection coated for all the wavelengths needed to load, cool and control $^{138}Ba^{+}$ ions. The viewport used for transmitting the light emitted by the ion and collimated by the aspheric lens has optical quality surface, with wavefronts aberrations below $\lambda/10$ over all the surface (with $\lambda = 493$ nm).

The electrical connections needed to drive the ion trap, to heat an atom dispenser and to measure and control the temperature of the mirror are done through feedthroughs in the customized CF-160 bottom flange. This customized flange also has a CF-16 viewport intended for 1.7 μm laser addressing of individual trapped ions.

Three pairs of magnetic field coils are attached to some of the main chamber flanges in order to provide a homogeneous magnetic field in the center of the trap.

6.3.1 Loading stage

To provide a source of atoms inside the vacuum chamber we have designed a loading stage that simultaneously contains a resistively heated Ba dispenser and a laser ablation target. The resistively heated dispenser is a reliable way to produce a flux

[10]Kimball Physics, MCF800-SphSq-G2E4C4A16.
[11]VAT 54132-GE02
[12]Bayard-Alpert ion gauge, Agilent UHV-24
[13]SAES CapaciTorr Z-400.
[14]SAES NEXTorr D 100-5

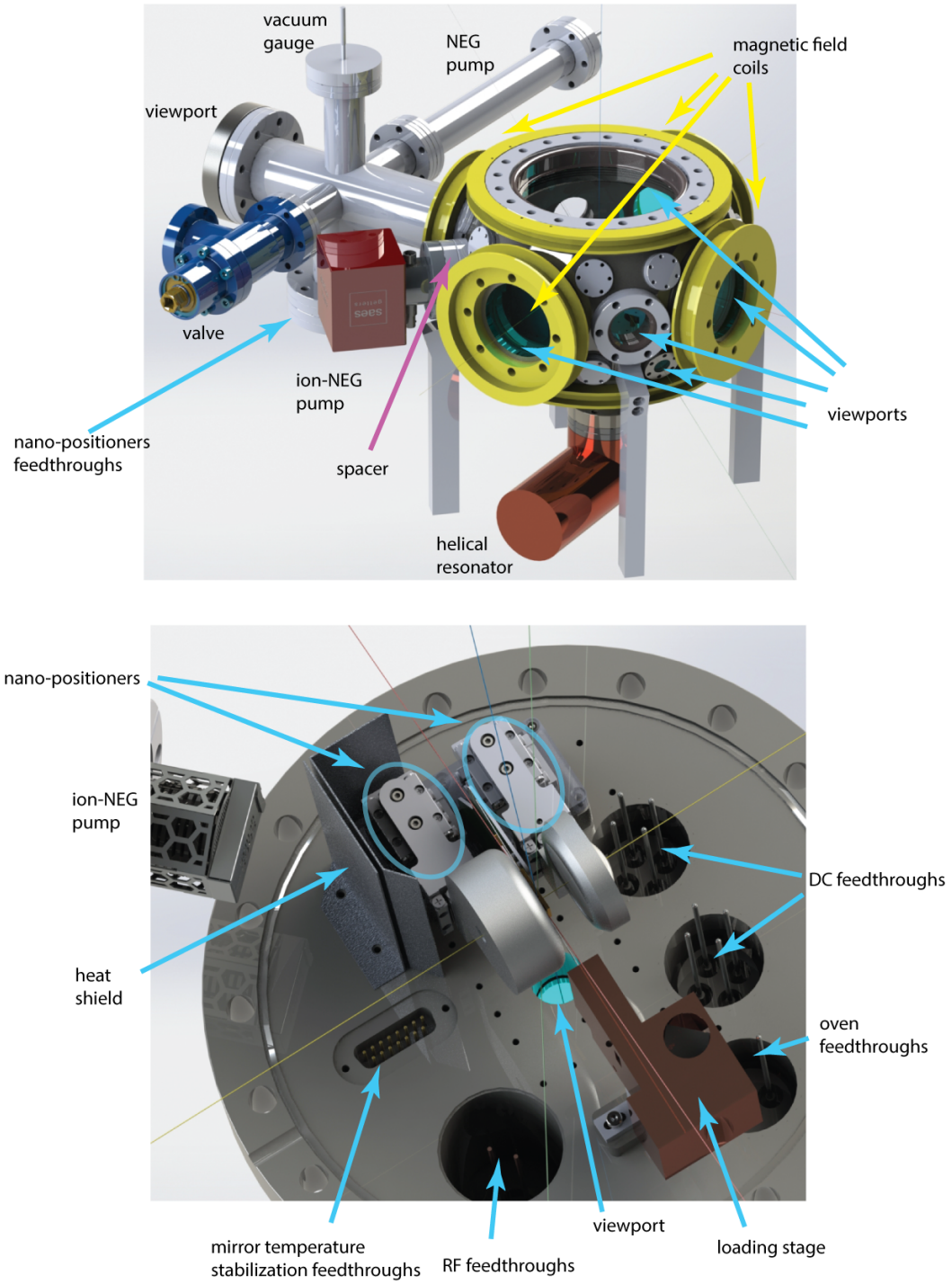

Figure 6.12: Vacuum vessel main components. See details in the main text.

of neutral atoms in the center of the trap, which are then ionized using the photo-ionization laser (see Section 3.3.5). This process is, however, slow, and produces an excess of heat inside the vacuum chamber that can have some detrimental effects on the operation of ion traps.

Laser ablation from a target is an alternative way, which has been proved to be more efficient and less detrimental for ion traps operation (see for example Ref. [204]). In this case, short and strong laser pulses are applied on a Ba target to produce neutral and ionized atoms, which eventually reach the center of the trap. It has been experimentally shown that instead of using a pure Ba target, targets containing $BaTiO_3$ or BaO produce higher Ba^+ yields [205], making loading more efficient.

Fig. 6.13 shows the designed loading stage, where both a resistive oven (dispenser) and a $BaTiO_3$ ablation target are located. The holder is made of macor® ceramic, which exhibits a low thermal and electric conductance. Both the target and the oven are enclosed in a copper shield, which simultaneously provides thermal insulation and prevents the ablated Barium from spreading into the rest of the chamber. This is important to avoid coating the viewports in the long term. Two holes in the front are used to collimate the atomic flux and direct it to the center of the ion trap. As the ablation process spreads atoms in every direction, a mirror and a hole in the shield are used for the ablation laser pulses. This configuration prevents a high atomic flux from exiting the shield and directly coat the viewport used for the ablation laser. Furthermore, the shield has two small circular apertures to collimate the atomic flux into the center of the trap, and a small square aperture in the side, which will allow for direct monitoring of the oven temperature with a thermal camera through a infra-red transmissive germanium viewport.

A broad range of pulsed laser sources can produce the pulses needed for ablation. An example of such a source is a pulsed nitrogen laser, with wavelength 337 nm and energy per pulse of 150 μJ [15]. This wavelength is compatible with our coated viewports.

6.4 Current status

At the time of writing of this thesis, the fabrication of the components of the new apparatus is almost complete. The main vacuum components such as the vacuum chamber, the combined pump, the vacuum valve, the coated viewports, the sealing blanks and feedthroughs have been pre-baked and put together, achieving a pressure below 10^{-10}mbar, without activating the NEG pump. During this test we were not able to identify any leak in the vacuum vessel.

The components of the main in-vacuum optical setup (see Fig. 6.11) are ready to be assembled. The design of the ion trap has been approved for fabrication by the manufacturing company. Only details about the final dimensions of the trenches need to be set. The final dimension of these trenches will depend on the results of

[15] for example, a Stanford Research Systems nitrogen laser NL100 reaches the requirements.

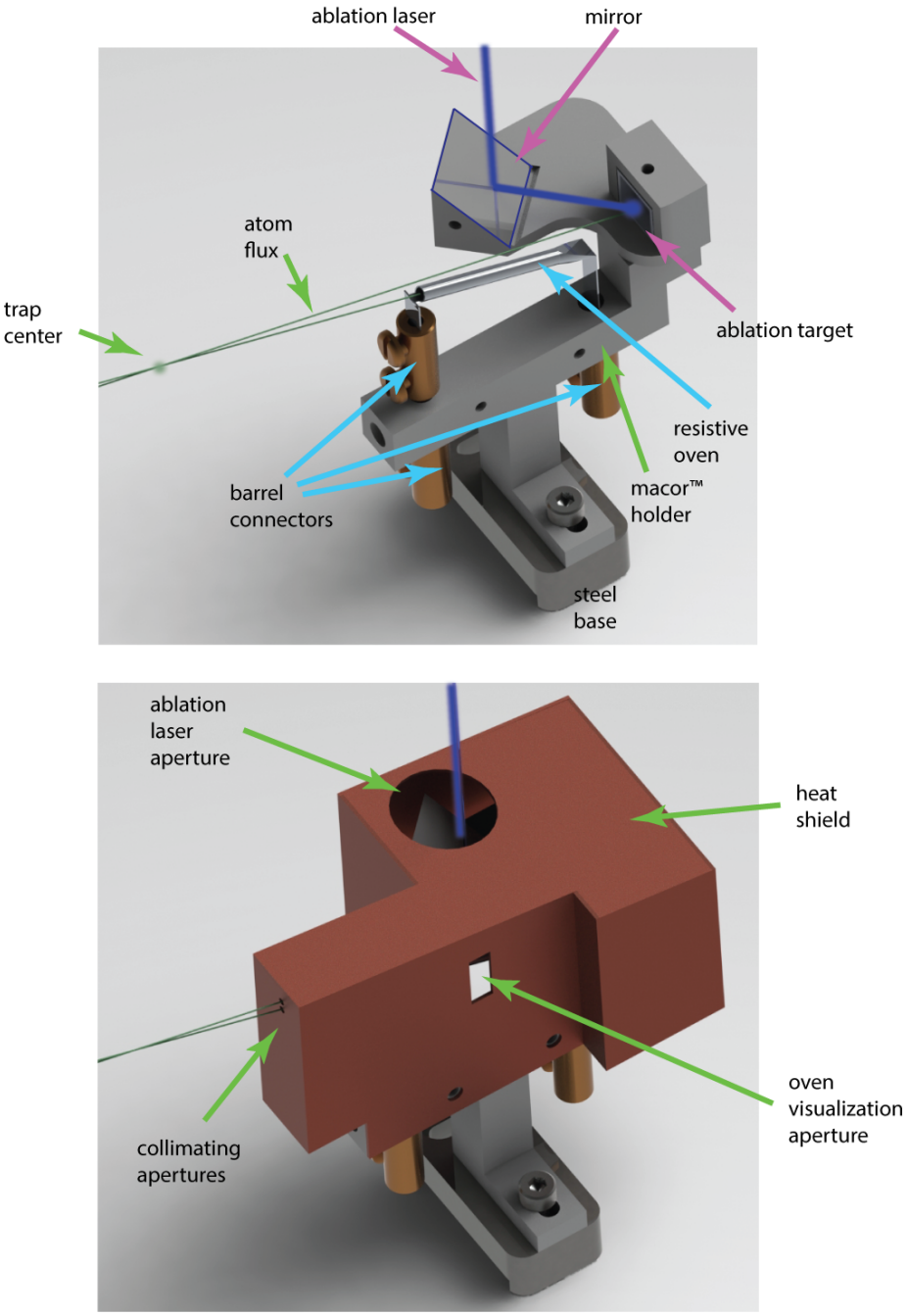

Figure 6.13: Loading stage. Design of a loading stage combining a resistive Barium oven and a target for laser ablation. See details in the main text.

the breakdown voltages, obtained from tests samples already fabricated. The final design of the PCB holding and connecting the trap is not yet defined. The holders of the mirror and lens and the positioners are ready to be used. The loading stage is currently being fabricated, and the ablation target and oven have been already ordered. As all the rest of the equipment needed for trapping and observing ion is operative, the first tries with the new setup should be then performed during the course of this year.

6.5 Summary and outlook

In this chapter we have presented the design of a new setup which will allow studies of quantum electrodynamics effects, improved collection efficiency of single photons emitted by a single atom. We have presented the design and construction of the main optical components of such a setup, namely the hemispherical mirror and the aspheric lens, and shown how the strict requirements on their fabrication are fulfilled.

In particular, an unprecedented precision on the fabrication of macroscopic concave hemispherical mirrors have been achieved, which will give us access to enhancement and inhibition of the spontaneous emission of a single atom of more than 96%. The technique used for their fabrication could be extended to the precise fabrication of other concave surfaces, allowing for more exotic quantum electrodynamics situations. One example of that, proposed by Yves Colombe, would be the fabrication of a mirror with a $\lambda/4$ radius step, such as the one shown in Fig. 6.14. Such a mirror will allow to enhance the spontaneous emission in the modes collected by a lens, while inhibiting the rest. In such a way, collection efficiencies close to 100% could be achieved.

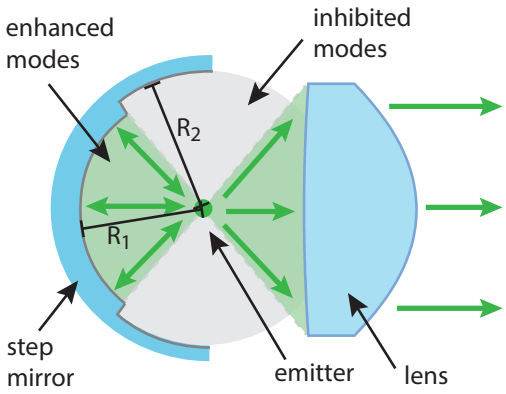

Figure 6.14: Step mirror concept. A mirror with radius of curvature $R_1 = n\lambda/2$ around the center and $R_2 = n\lambda/2 + \lambda/4$ would permit to enhanced the emission of photons in the collected solid angle while inhibiting the emission outside. Idea proposed by Yves Colombe.

We have also presented the design of a monolithic high optical access ion trap, with macroscopic dimensions. Such a trap is compatible with the optical access aspects required for the observation of the quantum electrodynamics effects. The achievable trapping parameters are similar to those achievable with designs such as our "Innsbruck-style" trap for $^{138}Ba^{+}$, and can be even better for lighter species

such as $^{40}Ca^{+}$.

The design of this new trap exploits new 3D-printing technologies and the basic concept of use trenches to separate electrodes can be extended to more complex trap geometries, including segmented traps or traps designed for trapping 2D or 3D ion crystals, with high optical access to the trapped particles. The high optical access achieved by the trap could also be used in fiber cavity setups [206, 207].

We have also presented the design of the complete setup, which includes a state of the art vacuum vessel and fast loading of ions in the trap via laser ablation. The construction of several of these setups would permit to perform experiments related with remote entanglement distribution and quantum networking without cavities.

The physical phenomena that we aim to study with this setup, such as strong inhibition and enhancement of the spontaneous emission, are not restricted to atomic ions, but in general, could be observed from any quantum emitter. Therefore, the optical setup presented here could be used with other systems with promising prospects in quantum networking and communications, such as quantum dots or diamond spin qubits [208, 209].

7 Conclusion and outlook

The experimental platform provided by trapped ions features aspects that other platforms find difficult to achieve simultaneously. Among these features are the high degree of control, the localization of the particles, the long trapping and coherence times and the high collection efficiency of photons emitted into free space. In this thesis, by taking advantage of these unique combination of features, two key experiments regarding fundamental quantum optical properties of the emission of single atoms have been presented.

In the first experiment we have shown how quantum information properties of a pair of atoms, namely the presence of entanglement, can affect their single photon emission rate. This effect proved to be useful in experimentally detecting entanglement in a purely optical fashion, with prospects of detecting of entanglement of extended quantum systems. We have also shown how this effect can be used to implement optical gradiometers, where entanglement could be used to test field differences in separated locations, provided that we can create entanglement between atoms at different locations.

In the second experiment we have studied a fundamental property of the field emitted by single atoms: its spin-orbital angular momentum coupling. We have for first time shown that photons emitted in certain directions carry solely orbital angular momentum. Due to this orbital angular momentum, the image of a single atom can be displaced with respect to its actual position. The high stability of our photon collection and imaging system enabled us to measure this effect with nanometer precision. We have discussed in detail the possible implications of this phenomenon, which does not affect not only atoms but any fundamental emitter, for the achievable precision and accuracy of current position determination and imaging techniques. However, besides the limitations that this phenomenon implies, it also provides new ways to measure local properties of fields, such as local polarization of light, or direction of magnetic fields.

Furthermore, we have presented the design of a new ion trapping apparatus, which will allow us to study fundamental electrodynamics effects. We have presented the results of the fabrication of the key components, namely a hemispherical mirror with optical-quality terminated surface, and an aspheric lens with numerical

aperture NA = 0.7 and wavefronts aberrations bellow the original goal. We have also presented the design of a macroscopic, monolithic ion trap with high optical access, which is compatible with the optical access requirements of the optical system.

The realization of the new apparatus will not only enable experiements on quantum electrodynamics as mentioned above, but also substantially increase the collection of the emission of the light emitted by the ions. Therefore, this would improve the precision and accuracy of any quantum optics experiment performed in the apparatus, and allow for faster qubit read-out. It will also make any experiment based on the detection of single photons faster, making it promising for fast generation of remote entanglement using photons as a bus. The Cabrillo scheme presented in Chapter 4 has been recently used for the first demonstration of on-demand generation of entanglement between distant qubits using photons in the optical regime as a bus [209]. By using the Cabrillo entangling scheme distributed over several nodes composed of our newly developed traps, we envisage a competitive alternative to cavity-based realizations of quantum networks.

Bibliography

[1] T. Ritz, A. Damjanović, and K. Schulten, "The quantum physics of photosynthesis," *ChemPhysChem*, vol. 3, no. 3, pp. 243–248, 2002. 1

[2] P. Würfel and U. Würfel, *Physics of solar cells: from basic principles to advanced concepts*. John Wiley & Sons, 2016. 1

[3] M. Ahmadi, B. X. R. Alves, C. Baker, W. Bertsche, E. Butler, A. Capra, C. Carruth, C. Cesar, M. Charlton, S. Cohen, *et al.*, "Observation of the 1s–2s transition in trapped antihydrogen," *Nature*, vol. 541, no. 7638, pp. 506–510, 2017. 1

[4] A. Reiserer and G. Rempe, "Cavity-based quantum networks with single atoms and optical photons," *Reviews of Modern Physics*, vol. 87, no. 4, p. 1379, 2015. 1

[5] A. Einstein, B. Podolsky, and N. Rosen, "Can quantum-mechanical description of physical reality be considered complete?," *Physical Review*, vol. 47, no. 10, p. 777, 1935. 1

[6] A. Einstein, M. Born, and H. Born, *The Born-Einstein letters: friendship, politics, and physics in uncertain times. correspondence between Albert Einstein and Max and Hedwig Born from 1916 to 1955 with commentaries by Max Born*. Macmillan, New York, 2005. 1

[7] R. Jozsa and N. Linden, "On the role of entanglement in quantum-computational speed-up," in *Proceedings of the Royal Society of London A: Mathematical, Physical and Engineering Sciences*, vol. 459, pp. 2011–2032, The Royal Society, 2003. 1

[8] A. K. Ekert, "Quantum cryptography based on Bell's theorem," *Physical Review Letters*, vol. 67, no. 6, p. 661, 1991. 1

[9] C. Cabrillo, J. Cirac, P. García-Fernández, and P. Zoller, "Creation of entangled states of distant atoms by interference," *Physical Review A*, vol. 59, pp. 1025–1033, 1999. 1, 4.2.2, 4.3, 4.3.1

[10] W. H. Zurek, "Decoherence and the transition from quantum to classical—revisited," in *Quantum Decoherence*, pp. 1–31, Springer, 2006. 2.1

[11] H. Häffner, C. F. Roos, and R. Blatt, "Quantum computing with trapped ions," *Physics Reports*, vol. 469, no. 4, pp. 155–203, 2008. 2.1

[12] K. Blaum, Y. N. Novikov, and G. Werth, "Penning traps as a versatile tool for precise experiments in fundamental physics," *Contemporary Physics*, vol. 51, no. 2, pp. 149–175, 2010. 2.1, 1

[13] Z. Hu and H. Kimble, "Observation of a single atom in a magneto-optical trap," *Optics Letters*, vol. 19, no. 22, pp. 1888–1890, 1994. 2.1

[14] D. Barredo, S. de Léséleuc, V. Lienhard, T. Lahaye, and A. Browaeys, "An atom-by-atom assembler of defect-free arbitrary two-dimensional atomic arrays," *Science*, vol. 354, no. 6315, pp. 1021–1023, 2016. 2.1, 4.6

[15] I. Bloch, "Ultracold quantum gases in optical lattices," *Nature Physics*, vol. 1, no. 1, pp. 23–30, 2005. 2.1

[16] Y. Chu and M. D. Lukin, "Quantum optics with nitrogen-vacancy centers in diamond," *arXiv preprint arXiv:1504.05990*, 2015. 2.1

[17] A. Prehn, M. Ibrügger, R. Glöckner, G. Rempe, and M. Zeppenfeld, "Optoelectrical cooling of polar molecules to submillikelvin temperatures," *Physical Review Letters*, vol. 116, no. 6, p. 063005, 2016. 2.1

[18] A. Beveratos, I. Abram, J.-M. Gérard, and I. Robert-Philip, "Quantum optics with quantum dots," *The European Physical Journal D*, vol. 68, p. 377, Dec 2014. 2.1

[19] A. Shnirman, G. Schön, and Z. Hermon, "Quantum manipulations of small josephson junctions," *Physical Review Letters*, vol. 79, no. 12, p. 2371, 1997. 2.1

[20] K. J. Morse, R. J. Abraham, A. DeAbreu, C. Bowness, T. S. Richards, H. Riemann, N. V. Abrosimov, P. Becker, H.-J. Pohl, M. L. Thewalt, *et al.*, "A photonic platform for donor spin qubits in silicon," *Science Advances*, vol. 3, no. 7, p. e1700930, 2017. 2.1

[21] S. Bertaina, S. Gambarelli, A. Tkachuk, I. Kurkin, B. Malkin, A. Stepanov, and B. Barbara, "Rare-earth solid-state qubits," *Nature Nanotechnology*, vol. 2, no. 1, pp. 39–42, 2007. 2.1

[22] R. Miller, T. Northup, K. Birnbaum, A. Boca, A. Boozer, and H. Kimble, "Trapped atoms in cavity qed: coupling quantized light and matter," *Journal of Physics B: Atomic, Molecular and Optical Physics*, vol. 38, no. 9, p. S551, 2005. 2.1

[23] W. Paul, "Electromagnetic traps for charged and neutral particles," *Reviews of Modern Physics*, vol. 62, no. 3, p. 531, 1990. 2.1

[24] Y. Wang, M. Um, J. Zhang, S. An, M. Lyu, J.-N. Zhang, L.-M. Duan, D. Yum, and K. Kim, "Single-qubit quantum memory exceeding ten-minute coherence time," *Nature Photonics*, vol. 11, no. 10, p. 646, 2017. 2.1

[25] G. Wilpers, P. See, P. Gill, and A. G. Sinclair, "A monolithic array of three-dimensional ion traps fabricated with conventional semiconductor technology," *Nature Nanotechnology*, vol. 7, no. 9, p. 572, 2012. 2.1

[26] T. Monz, P. Schindler, J. T. Barreiro, M. Chwalla, D. Nigg, W. A. Coish, M. Harlander, W. Hänsel, M. Hennrich, and R. Blatt, "14-qubit entanglement: Creation and coherence," *Physical Review Letters*, vol. 106, p. 130506, 2011. 2.1, 4.1

[27] J. Zhang, G. Pagano, P. W. Hess, A. Kyprianidis, P. Becker, H. Kaplan, A. V. Gorshkov, Z.-X. Gong, and C. Monroe, "Observation of a many-body dynamical phase transition with a 53-qubit quantum simulator," *Nature*, vol. 551, no. 7682, p. 601, 2017. 2.1

[28] W. Paul and H. Steinwedel, "Ein neues Massenspektrometer ohne Magnetfeld," *Zeitschrift für Naturforschung A*, vol. 8, no. 7, pp. 448–450, 1953. 2.2.1

[29] H. G. Dehmelt, "Radiofrequency spectroscopy of stored ions : Storage," *Advances in Atomic and Molecular Physics*, vol. 3, pp. 53–72, 1968. 2.2.1

[30] D. Leibfried, R. Blatt, C. Monroe, and D. Wineland, "Quantum dynamics of single trapped ions," *Reviews of Modern Physics*, vol. 75, no. 1, p. 281, 2003. 2.2.2

[31] M. D. Hughes, B. Lekitsch, J. A. Broersma, and W. K. Hensinger, "Microfabricated ion traps," *Contemporary Physics*, vol. 52, no. 6, pp. 505–529, 2011. 2.2.3

[32] D. Bouwmeester, A. Ekert, A. Zeilinger, *et al.*, *The physics of quantum information*, vol. 3. Springer, Berlin, 2000. 2.2.3

[33] D. H. Dubin, "Theory of structural phase transitions in a trapped coulomb crystal," *Physical Review Letters*, vol. 71, no. 17, p. 2753, 1993. 2.2.4

[34] A. Steane, "The ion trap quantum information processor," *Applied Physics B: Lasers and Optics*, vol. 64, no. 6, pp. 623–643, 1997. 2.2.4

[35] D. F. James, "Quantum dynamics of cold trapped ions with application to quantum computation," *Applied Physics B: Lasers and Optics*, vol. 66, no. 2, pp. 181–190, 1998. 2.2.4, 2.2.5, 2.3.3, 2.3.3, 3.1, 3.3, 3.4.2, 3.4.2

[36] P. Richerme, "Two-dimensional ion crystals in radio-frequency traps for quantum simulation," *Physical Review A*, vol. 94, no. 3, p. 032320, 2016. 2.2.4

[37] H. Casimir and D. Polder, "The influence of retardation on the London-van der Waals forces," *Physical Review*, vol. 73, no. 4, p. 360, 1948. 2.2.6

[38] J. I. Cirac and P. Zoller, "Quantum computations with cold trapped ions," *Physical Review Letters*, vol. 74, no. 20, p. 4091, 1995. 2.3, 2.3.3, 4.3

[39] C. Cohen-Tannoudji, J. Dupont-Roc, G. Grynberg, and P. Thickstun, *Atom-photon interactions: basic processes and applications*. Wiley Online Library, 1992. 2.3.1

[40] P. A. Dirac, "The fundamental equations of quantum mechanics," in *Proceedings of the Royal Society of London A*, vol. 109, pp. 642–653, The Royal Society, 1925. 2

[41] M. F. Frenzel, "Atoms and photons-their interaction dynamics," *arXiv preprint arXiv:1212.4339*, 2012. 2.3.1

[42] D. A. Steck, "Quantum and atom optics, lecture notes," *Oregon Center for Optics and Department of Physics, University of Oregon*, vol. 47, 2007. Available at https://http://atomoptics-nas.uoregon.edu/~dsteck/teaching/quantum-optics/. 2.3.1, 2.3.1, 3.2.2, 3.4.2, 5.3.1

[43] F. Arecchi and R. Bonifacio, "Theory of optical maser amplifiers," *IEEE Journal of Quantum Electronics*, vol. 1, no. 4, pp. 169–178, 1965. 4

[44] S. Stenholm, "The semiclassical theory of laser cooling," *Reviews of modern physics*, vol. 58, no. 3, p. 699, 1986. 2.3.3, 2.3.4, 2.3.4

[45] F. Diedrich, J. Bergquist, W. M. Itano, and D. Wineland, "Laser cooling to the zero-point energy of motion," *Physical Review Letters*, vol. 62, no. 4, p. 403, 1989. 2.3.3

[46] N. Röck, "Quantum manipulation on the Barium quadrupolar transition," Master's thesis, Universität Innsbruck, 2011. Available at https://quantumoptics.at/en/publications/master-diploma-theses. 2.3.4, 3.3.3

[47] C. Monroe, D. Meekhof, B. King, S. R. Jefferts, W. M. Itano, D. J. Wineland, and P. Gould, "Resolved-sideband raman cooling of a bound atom to the 3d zero-point energy," *Physical Review Letters*, vol. 75, no. 22, p. 4011, 1995. 2.3.4

[48] C. Roos, D. Leibfried, A. Mundt, F. Schmidt-Kaler, J. Eschner, and R. Blatt, "Experimental demonstration of ground state laser cooling with electromagnetically induced transparency," *Physical Review Letters*, vol. 85, no. 26, p. 5547, 2000. 2.3.4

[49] G. Birkl, J. A. Yeazell, R. Rückerl, and H. Walther, "Polarization gradient cooling of trapped ions," *EPL (Europhysics Letters)*, vol. 27, no. 3, p. 197, 1994. 2.3.4

[50] E. A. Dijck, A. Mohanty, N. Valappol, M. N. n. Portela, L. Willmann, and K. Jungmann, "Lifetime of the $5d\,^2D_{5/2}$ level of $^{138}Ba^+$ from quantum jumps with single and multiple ba^+ ions," *Phyisical Review A*, vol. 97, p. 032508, 2018. 3.1

[51] T. Harty, D. Allcock, C. J. Ballance, L. Guidoni, H. Janacek, N. Linke, D. Stacey, and D. Lucas, "High-fidelity preparation, gates, memory, and readout of a trapped-ion quantum bit," *Physical Review Letters*, vol. 113, no. 22, p. 220501, 2014. 3.1

[52] V. Schäfer, C. Ballance, K. Thirumalai, L. Stephenson, T. Ballance, A. Steane, and D. Lucas, "Fast quantum logic gates with trapped-ion qubits," *Nature*, vol. 555, no. 7694, p. 75, 2018. 3.1

[53] M. R. Dietrich, A. Avril, R. Bowler, N. Kurz, J. Salacka, G. Shu, and B. Blinov, "Barium ions for quantum computation," in *AIP Conference Proceedings*, vol. 1114, pp. 25–30, AIP, 2009. 3.1

[54] N. C. Lewty, B. L. Chuah, R. Cazan, B. Sahoo, and M. Barrett, "Spectroscopy on a single trapped 137 Ba+ ion for nuclear magnetic octupole moment determination," *Optics Express*, vol. 20, no. 19, pp. 21379–21384, 2012. 3.1

[55] T. Koerber, M. Schacht, W. Nagourney, and E. Fortson, "Radio frequency spectroscopy with a trapped Ba+ ion: recent progress and prospects for measuring parity violation," *Journal of Physics B: Atomic, Molecular and Optical Physics*, vol. 36, no. 3, p. 637, 2003. 3.1

[56] A. Gallagher, "Oscillator strengths of Ca II, Sr II, and Ba II," *Physical Review*, vol. 157, no. 1, p. 24, 1967. 3.1

[57] T. Sauter, R. Blatt, W. Neuhauser, and P. E. Toschek, "'Quantum jumps' observed in the fluorescence of a single ion," *Optics Communications*, vol. 60, no. 5, pp. 287–292, 1986. 3.1, 3.2.1

[58] F. Plumelle, M. Desaintfuscien, J. L. Duchene, and C. Audoin, "Laser probing of ions confined in a cylindrical radiofrequency trap," *Optics Communications*, vol. 34, no. 1, pp. 71–76, 1980. 3.1, 3.2.1

[59] R. Schneider and G. Werth, "Ion storage technique for very long living states: The decay rate of the 5D 3/2 state of Ba II," *Zeitschrift für Physik*, vol. 293, no. 2, pp. 103–106, 1979. 3.2.1

[60] P. Zeeman, "On the influence of magnetism on the nature of the light emitted by a substance.," *The Astrophysical Journal*, vol. 5, p. 332, 1897. 2

[61] D. Rotter, *Quantum feedback and quantum correlation measurements with a single Barium ion*. PhD thesis, Universität Innsbruck, 2008. Available at https://quantumoptics.at/en/publications/ph-d-theses. 3.3, 3.3, 3.3.5, 3.4.1

[62] D. J. Berkeland, J. D. Miller, J. C. Bergquist, W. M. Itano, and D. J. Wineland, "Minimization of ion micromotion in a paul trap," *Journal of Applied Physics*, vol. 83, no. 10, pp. 5025–5033, 1998. 3.3, 3.5

[63] A. Zverev and H. Blinchikoff, "Realization of a filter with helical components," *IRE Transactions on Component Parts*, vol. 8, no. 3, pp. 99–110, 1961. 3.3

[64] L. Slodička, G. Hétet, M. Hennrich, and R. Blatt, "Free space interference experiments with single photons and single ions," in *Engineering the Atom-Photon Interaction*, pp. 99–124, Springer, 2015. 3.3.2

[65] H. G. Barros, A. Stute, T. E. Northup, C. Russo, P. O. Schmidt, and R. Blatt, "Deterministic single-photon source from a single ion," *New Journal of Physics*, vol. 11, no. 10, p. 103004, 2009. 3.3.2

[66] R. Maiwald, A. Golla, M. Fischer, M. Bader, S. Heugel, B. Chalopin, M. Sondermann, and G. Leuchs, "Collecting more than half the fluorescence photons from a single ion," *Physical Review A*, vol. 86, no. 4, p. 043431, 2012. 3.3.2, 4.1, 6.1

[67] M. Ghadimi, V. Blūms, B. G. Norton, P. M. Fisher, S. Connell, J. M. Amini, C. Volin, H. Hayden, C.-S. Pai, D. Kielpinski, M. Lobino, and E. Streed, "Scalable ion–photon quantum interface based on integrated diffractive mirrors," *npj Quantum Information*, vol. 3, no. 1, p. 4, 2017. 3.3.2

[68] A. P. VanDevender, Y. Colombe, J. Amini, D. Leibfried, and D. J. Wineland, "Efficient fiber optic detection of trapped ion fluorescence," *Physical Review Letters*, vol. 105, no. 2, p. 023001, 2010. 3.3.2

[69] K. K. Mehta, C. D. Bruzewicz, R. McConnell, R. J. Ram, J. M. Sage, and J. Chiaverini, "Integrated optical addressing of an ion qubit," *Nature Nanotechnology*, vol. 11, no. 12, p. 1066, 2016. 3.3.2

[70] D. H. Slichter, V. B. Verma, D. Leibfried, R. P. Mirin, S. W. Nam, and D. J. Wineland, "Uv-sensitive superconducting nanowire single photon detectors for integration in an ion trap," *Optics Express*, vol. 25, no. 8, pp. 8705–8720, 2017. 3.3.2

[71] T. Nieddu, V. Gokhroo, and S. N. Chormaic, "Optical nanofibres and neutral atoms," *Journal of Optics*, vol. 18, no. 5, p. 053001, 2016. 3.3.2

[72] S. Gerber, D. Rotter, M. Hennrich, R. Blatt, F. Rohde, C. Schuck, M. Almendros, R. Gehr, F. Dubin, and J. Eschner, "Quantum interference from remotely trapped ions," *New Journal of Physics*, vol. 11, no. 1, p. 013032, 2009. 10

[73] J. D. Jackson, *Classical electrodynamics*. John Wiley & Sons, 2012. 3.3.2

[74] T. Plakhotnik, W. E. Moerner, V. Palm, and U. P. Wild, "Single molecule spectroscopy: maximum emission rate and saturation intensity," *Optics Communications*, vol. 114, no. 1-2, pp. 83–88, 1995. 3.3.2

[75] D. B. Higginbottom, L. Slodička, G. Araneda, L. Lachman, R. Filip, M. Hennrich, and R. Blatt, "Pure single photons from a trapped atom source," *New Journal of Physics*, vol. 18, no. 9, p. 093038, 2016. 3.3.2

[76] R. W. P. Drever, J. L. Hall, F. V. Kowalski, J. Hough, G. M. Ford, A. J. Munley, and H. Ward, "Laser phase and frequency stabilization using an optical resonator," *Applied Physics B*, vol. 31, no. 2, pp. 97–105, 1983. 3.3.3

[77] C. Raab, J. Bolle, H. Oberst, J. Eschner, F. Schmidt-Kaler, and R. Blatt, "Diode laser spectrometer at 493 nm for single trapped ba+ ions," *Applied Physics B*, vol. 67, no. 6, pp. 683–688, 1998. 3.3.3

[78] R. Lechner, C. Maier, C. Hempel, P. Jurcevic, B. P. Lanyon, T. Monz, M. Brownnutt, R. Blatt, and C. F. Roos, "Electromagnetically-induced-transparency ground-state cooling of long ion strings," *Physical Review A*, vol. 93, no. 5, p. 053401, 2016. 3.3.3

[79] L. Slodička, *Single ion - single photon interactions in free space*. PhD thesis, Universität Innsbruck, 2013. Available at https://quantumoptics.at/en/publications/ph-d-theses. 3.3.3, 3.4.2, 3.14, 4.3, 4.3.3

[80] P. Pham, "A general purpose sequencer for quantum computing," Master's thesis, Massachusetts Institute of Technology, 2005. 3.3.4

[81] P. Schindler, "Frequency sysnthesis and pulse shaping for quantum information processing with trapped ions," Master's thesis, Universität Innsbruck, 2008. Available at https://quantumoptics.at/en/publications/master-diploma-theses. 3.3.4

[82] A. Kramida, Yu. Ralchenko, J. Reader, and NIST ASD Team. NIST Atomic Spectra Database (ver. 5.5.6), [Online]. Available: https://physics.nist.gov/asd [2018, September 17]. National Institute of Standards and Technology, Gaithersburg, MD., 2018. 3.3.5

[83] G. Leschhorn, T. Hasegawa, and T. Schaetz, "Efficient photo-ionization for barium ion trapping using a dipole-allowed resonant two-photon transition," *Applied Physics B*, vol. 108, no. 1, pp. 159–165, 2012. 3.3.5

[84] S. M. Tan, "A quantum optics toolbox for matlab 5," 2002. Available at https://github.com/jevonlongdell/qotoolbox. 3.4.1

[85] J. Johansson, P. Nation, and F. Nori, "Qutip: An open-source python framework for the dynamics of open quantum systems," *Computer Physics Communications*, vol. 183, no. 8, pp. 1760 – 1772, 2012. 3.4.1

[86] S. Krämer, D. Plankensteiner, L. Ostermann, and H. Ritsch, "Quantumoptics.jl: A julia framework for simulating open quantum systems," *Computer Physics Communications*, vol. 227, pp. 109 – 116, 2018. 3.4.1

[87] H. Dehmelt, "Proposed $10^{14}\delta\nu/\nu$ laser fluorescence spectroscopy on Tl^+ mono-ion oscillator," in *Bulletin of the American Physical Society*, vol. 18, pp. 1521–1521, 1973. 3.4.2

[88] D. J. Wineland, C. Monroe, W. M. Itano, D. Leibfried, B. E. King, and D. M. Meekhof, "Experimental issues in coherent quantum-state manipulation of trapped atomic ions," *Journal of Research of the National Institute of Standards and Technology*, vol. 103, no. 3, p. 259, 1998. 3.4.2

[89] R. H. Dicke, "Coherence in spontaneous radiation processes," *Physical Review*, vol. 93, no. 1, p. 99, 1954. 4.1, 6.1

[90] M. Gross and S. Haroche, "Superradiance: An essay on the theory of collective spontaneous emission," *Physics Reports*, vol. 93, no. 5, pp. 301–396, 1982. 4.1, 6.1

[91] A. V. Andreev, V. I. Emel'yanov, and Y. A. Il'inskiˇ i, "Collective spontaneous emission (Dicke superradiance)," *Soviet Physics Uspekhi*, vol. 23, no. 8, p. 493, 1980. 4.1, 6.1

[92] M. G. Benedict and E. D. Trifonov, *6.2 Superradiance*, pp. 67–81. Berlin, Heidelberg: Springer Berlin Heidelberg, 2006. 4.1, 6.1

[93] M. O. Scully, E. S. Fry, C. R. Ooi, and K. Wódkiewicz, "Directed spontaneous emission from an extended ensemble of n atoms: Timing is everything," *Physical Review Letters*, vol. 96, no. 1, p. 010501, 2006. 4.1

[94] M. O. Scully and A. A. Svidzinsky, "The super of superradiance," *Science*, vol. 325, no. 5947, pp. 1510–1511, 2009. 4.1

[95] R. Schmied, J.-D. Bancal, B. Allard, M. Fadel, V. Scarani, P. Treutlein, and N. Sangouard, "Bell correlations in a Bose-Einstein condensate," *Science*, vol. 352, pp. 441–444, 2016. 4.1

[96] R. McConnell, H. Zhang, J. Hu, S. Ćuk, and V. Vuletić, "Entanglement with negative Wigner function of almost 3,000 atoms heralded by one photon," *Nature*, vol. 519, pp. 439–442, 2015. 4.1

[97] F. Haas, J. Volz, R. Gehr, J. Reichel, and J. Estève, "Entangled states of more than 40 atoms in an optical fiber cavity.," *Science*, vol. 344, pp. 180–183, 2014. 4.1

[98] R. Wiegner, J. von Zanthier, and G. S. Agarwal, "Quantum-interference-initiated superradiant and subradiant emission from entangled atoms," *Physical Review A*, vol. 84, p. 023805, 2011. 4.1, 4.2, 4.2, 4.2, 4.6

[99] G. S. Agarwal, "Quantum-entanglement-initiated super raman scattering," *Physical Review A*, vol. 83, p. 023802, 2011. 4.1

[100] T. R. Tan, J. P. Gaebler, Y. Lin, Y. Wan, R. Bowler, D. Leibfried, and D. J. Wineland, "Multi-element logic gates for trapped-ion qubits," *Nature*, vol. 528, pp. 380–383, 2015. 4.1, 4.6

[101] C. J. Ballance, V. M. Schäfer, J. P. Home, D. Szwer, S. C. Webster, D. T. C. Allcock, N. M. Linke, and T. Harty, "Hybrid quantum logic and a test of Bell's inequality using two different atomic isotopes," *Nature*, vol. 528, pp. 384–386, 2015. 4.1

[102] E. W. Streed, A. Jechow, B. G. Norton, and D. Kielpinski, "Absorption imaging of a single atom," *Nature Communications*, vol. 3, p. 933, 2012. 4.1

[103] G. Shu, C. Chou, N. Kurz, M. R. Dietrich, and B. B. Blinov, "Efficient fluorescence collection and ion imaging with the tack ion trap," *Journal of the Optical Society of America B*, vol. 28, pp. 2865–2870, 2011. 4.1

[104] P. Lodahl, S. Mahmoodian, and S. Stobbe, "Interfacing single photons and single quantum dots with photonic nanostructures," *Review of Modern Physics*, vol. 87, pp. 347–400, 2015. 4.1

[105] J. A. Mlynek, A. A. Abdumalikov, C. Eichler, and A. Wallraff, "Observation of Dicke superradiance for two artificial atoms in a cavity with high decay rate," *Nature Communications*, vol. 5, p. 5186, 2014. 4.1, 4.6

[106] B. Casabone, K. Friebe, B. Brandstätter, K. Schüppert, R. Blatt, and T. Northup, "Enhanced quantum interface with collective ion-cavity coupling," *Physical Review Letters*, vol. 114, p. 023602, 2015. 4.1, 4.6

[107] G. Araneda, D. B. Higginbottom, L. Slodička, Y. Colombe, and R. Blatt, "Interference of single photons emitted by entangled atoms in free space," *Physical Review Letters*, vol. 120, no. 19, p. 193603, 2018. 4.1

[108] S. Hill and W. K. Wootters, "Entanglement of a pair of quantum bits," *Physical Review Letters*, vol. 78, no. 26, p. 5022, 1997. 4.2.1

[109] M. Jakob and J. A. Bergou, "Quantitative complementarity relations in bipartite systems: Entanglement as a physical reality," *Optics Communications*, vol. 283, pp. 827–830, 2010. 4.2.1, 4.6

[110] J. Suzuki, C. Miniatura, and K. Nemoto, "Entanglement detection from interference fringes in atom-photon systems," *Physical Review A*, vol. 81, p. 062307, 2010. 4.2.2, 4.2.2, 4.6

[111] F. Schmidt-Kaler, H. Häffner, M. Riebe, S. Gulde, G. P. Lancaster, T. Deuschle, C. Becher, C. F. Roos, J. Eschner, and R. Blatt, "Realization of the Cirac–Zoller controlled-not quantum gate," *Nature*, vol. 422, no. 6930, p. 408, 2003. 4.3

[112] A. Sørensen and K. Mølmer, "Quantum computation with ions in thermal motion," *Physical Review Letters*, vol. 82, no. 9, p. 1971, 1999. 4.3

[113] C. A. Sackett, D. Kielpinski, B. E. King, C. Langer, V. Meyer, C. J. Myatt, M. Rowe, Q. A. Turchette, W. M. Itano, D. J. Wineland, and C. Monroe, "Experimental entanglement of four particles," *Nature*, vol. 404, pp. 256–259, 2000. 4.3, 4.3.2, 4.3.3, 4.3.3

[114] G. Milburn, S. Schneider, and D. James, "Ion trap quantum computing with warm ions," *Fortschritte der Physik*, vol. 48, no. 9-11, pp. 801–810, 2000. 4.3

[115] D. Leibfried, B. DeMarco, V. Meyer, D. Lucas, M. Barrett, J. Britton, W. M. Itano, B. Jelenković, C. Langer, T. Rosenband, *et al.*, "Experimental demonstration of a robust, high-fidelity geometric two ion-qubit phase gate," *Nature*, vol. 422, no. 6930, p. 412, 2003. 4.3

[116] D. L. Moehring, P. Maunz, S. Olmschenk, K. C. Younge, D. N. Matsukevich, L.-M. Duan, and C. Monroe, "Entanglement of single-atom quantum bits at a distance.," *Nature*, vol. 449, pp. 68–71, 2007. 4.3, 4.6

[117] L. Slodička, G. Hétet, N. Röck, P. Schindler, M. Hennrich, and R. Blatt, "Atom-atom entanglement by single-photon detection," *Physical Review Letters*, vol. 110, p. 083603, 2013. 4.3, 4.6

[118] H. Häffner, F. Schmidt-Kaler, W. Hänsel, C. Roos, T. Körber, M. Chwalla, M. Riebe, J. Benhelm, U. D. Rapol, C. Becher, and B. R., "Robust entanglement," *Applied Physics B*, vol. 81, pp. 151–153, 2005. 4.3.1, 4.5

[119] R. Loudon, *The quantum theory of light*. OUP Oxford, 2000. 4.3.2

[120] L. Slodička, G. Hétet, N. Röck, S. Gerber, P. Schindler, M. Kumph, M. Hennrich, and R. Blatt, "Interferometric thermometry of a single sub-doppler-cooled atom," *Physical Review A*, vol. 85, no. 4, p. 043401, 2012. 4.3.2

[121] C. Roos, G. Lancaster, M. Riebe, H. Häffner, W. Hänsel, S. Gulde, C. Becher, J. Eschner, F. Schmidt-Kaler, and R. Blatt, "Bell states of atoms with ultralong lifetimes and their tomographic state analysis," *Physical Review Letters*, vol. 92, no. 22, p. 220402, 2004. 4.3.2

[122] M. Bourennane, M. Eibl, C. Kurtsiefer, S. Gaertner, H. Weinfurter, O. Gühne, P. Hyllus, D. Bruß, M. Lewenstein, and A. Sanpera, "Experimental detection

of multipartite entanglement using witness operators," *Physical Review Letters*, vol. 92, no. 8, p. 087902, 2004. 4.3.2

[123] N. Friis, O. Marty, C. Maier, C. Hempel, M. Holzäpfel, P. Jurcevic, M. B. Plenio, M. Huber, C. Roos, R. Blatt, *et al.*, "Observation of entangled states of a fully controlled 20-qubit system," *Physical Review X*, vol. 8, no. 2, p. 021012, 2018. 4.3.2

[124] W. K. Wootters, "Entanglement of formation and concurrence.," *Quantum Information & Computation*, vol. 1, no. 1, pp. 27–44, 2001. 4.3.3

[125] F. Schmidt-Kaler and R. Gerritsma, "Entangled states of trapped ions allow measuring the magnetic field gradient produced by a single atomic spin," *Europhysics Letters*, vol. 99, p. 53001, 2012. 4.5

[126] T. Ruster, H. Kaufmann, M. Luda, V. Kaushal, C. Schmiegelow, F. Schmidt-Kaler, and U. Poschinger, "Entanglement-based dc magnetometry with separated ions," *Physical Review X*, vol. 7, no. 3, p. 031050, 2017. 4.5

[127] Z. Ficek and R. Tanaś, "Entangled states and collective nonclassical effects in two-atom systems," *Physics Reports*, vol. 372, pp. 369–443, 2002. 4.6

[128] G. Vittorini, D. Hucul, I. V. Inlek, C. Crocker, and C. Monroe, "Entanglement of distinguishable quantum memories," *Physical Review A*, vol. 90, p. 040302, 2014. 4.6

[129] G. Kurizki, P. Bertet, Y. Kubo, M. K., P. D., P. Rabl, and J. Schmiedmayer, "Quantum technologies with hybrid systems," *Proceedings of the National Academy of Science of the United States of Amerca*, vol. 112, pp. 3866–3873, 2015. 4.6

[130] R. Wiegner, J. Von Zanthier, and G. S. Agarwal, "Quantum interference and non-locality of independent photons from disparate sources," *Journal of Physics B: Atomic, Molecular and Optical Physics*, vol. 44, p. 055501, 2011. 4.6

[131] I. V. Inlek, *Multi-species trapped atomic ion mudules for quantum networks*. PhD thesis, University of Maryland and National Institute of Standards and Technology, 2016. Available at http://iontrap.umd.edu/publications/theses/. 4.6

[132] R. DeVoe and R. Brewer, "Observation of superradiant and subradiant spontaneous emission of two trapped ions," *Physical Review Letters*, vol. 76, no. 12, p. 2049, 1996. 4.6, 6.1

[133] C. Navarrete-Benlloch, I. de Vega, D. Porras, and J. I. Cirac, "Simulating quantum-optical phenomena with cold atoms in optical lattices," *New Journal of Physics*, vol. 13, p. 023024, 2011. 4.6

[134] V. Giovannetti, S. Lloyd, and L. Maccone, "Advances in quantum metrology," *Nature Photonics*, vol. 5, pp. 222–229, 2011. 4.6

[135] K. Predehl, G. Grosche, S. M. F. Raupach, S. Droste, O. Terra, J. Alnis, T. Legero, T. W. Hänsch, T. Udem, R. Holzwarth, and H. Schnatz, "A 920-kilometer optical fiber link for frequency metrology at the 19th decimal place," *Science*, vol. 336, pp. 441–444, 2012. 4.6

[136] U. Yurtsever, D. Strekalov, and J. P. Dowling, "Interferometry with entangled atoms," *European Physical Journal D*, vol. 22, pp. 365–371, 2003. 4.6

[137] K. Y. Bliokh, F. J. .Rodríguez-Fortuño, F. Nori, and A. V. Zayats, "spin - orbit interactions of light," *Nature Photonics*, vol. 9, p. 796, 2015. 5.1, 5.2.2

[138] R. A. Beth, "Mechanical detection and measurement of the angular momentum of light," *Physical Review*, vol. 50, p. 115, 1936. 5.1

[139] L. Allen, M. W. Beijersbergen, R. J. C. Spreeuw, and W. J. P., "Orbital angular momentum of light and the transformation of laguerre-gaussian laser modes," *Physical Review A*, vol. 48, p. 8185, 1992. 5.1

[140] M. Onoda, S. Murakami, and N. Nagaosa, "Hall effect of light," *Physical Review Letters*, vol. 93, p. 083901, 2004. 5.1

[141] O. Hosten and P. Kwiat, "Observation of the spin hall effect of light via weak measurements," *Science*, vol. 319, p. 787, 2008. 5.1

[142] D. Haefner, S. Sukhov, and A. A. Dogariu, "Spin hall effect of light in spherical geometry," *Physical Review Letters*, vol. 102, p. 123903, 2009. 5.1

[143] P. Lodahl, S. Mahmoodian, S. Stobbe, P. Schneeweiss, J. Volz, A. Rauschenbeutel, H. Pichler, and P. Zoller, "Chiral quantum optics," *Nature*, no. 541, p. 473, 2017. 5.1, 5.8.3

[144] R. Mitsch, C. Sayrin, B. Albrecht, P. Schneeweiss, and A. Rauschenbeutel, "Quantum state-controlled directional spontaneous emission of photons into a nanophotonic waveguide," *Nature Communications*, vol. 5, p. 5713, 2014. 5.1

[145] M. Scheucher, A. Hilico, E. Will, J. Volz, and A. Rauschenbeutel, "Quantum optical circulator controlled by a single chirally coupled atom," *Science*, p. aaj2118, 2016. 5.1

[146] C. G. Darwin, "Notes on the theory of radiation," *Proceeding of the Royal Society of London A*, vol. 136, no. 829, pp. 36–52, 1932. 5.1

[147] G. Araneda, S. Walser, Y. Colombe, D. B. Higginbottom, Y. Volz, R. Blatt, and A. Rauschenbeute, "Wavelength-scale errors in optical precision localization due to spin-orbit coupling of light," *Nature Physics*, vol. 15, no. 1, p. 17, 2019. 5.1, 5.6, 5.8.1

[148] A. Aiello, P. Banzer, M. Neugebauer, and G. Leuchs, "From transverse angular momentum to photonic wheels," *Nature Photonics*, vol. 9, no. 12, p. 789, 2015. 5.2.2

[149] M. V. Berry, "Optical currents," *Journal of Optics A: Pure and Applied Optics*, vol. 11, no. 9, p. 094001, 2009. 5.2.2, 5.2.2, 5.4, 5.4.2

[150] K. Y. Bliokh, A. Y. Bekshaev, and F. Nori, "Dual electromagnetism: helicity, spin, momentum and angular momentum," *New Journal of Physics*, vol. 15, no. 3, p. 033026, 2013. 5.2.2

[151] S. M. Barnett, "Optical angular-momentum flux," *Journal of Optics B: Quantum and Semiclassical Optics*, vol. 4, no. 2, p. S7, 2002. 5.2.2

[152] G. Moe and G. Happer, "Conservation of angular momentum for light propagating in a transparent anisotropic medium," *Journal of Physics B: Atomic, Molecular and Optical Physics*, vol. 10, no. 7, p. 1191, 1977. 5.3.1

[153] H. Arnoldus, X. Li, and J. Shu, "Subwavelength displacement of the far-field image of a radiating dipole," *Optics Letters*, vol. 33, p. 1446, 2008. 5.3.2

[154] J. Dressel, M. Malik, F. M. Miatto, A. N. Jordan, and R. W. Boyd, "Colloquium: Understanding quantum weak values: Basics and applications," *Reviews of Modern Physics*, vol. 86, no. 1, p. 307, 2014. 5.4

[155] A. Y. Bekshaev, K. Y. Bliokh, and F. Nori, "Transverse spin and momentum in two-wave interference," *Physical Review X*, vol. 5, p. 011039, Mar 2015. 5.4.2

[156] G. C. Knee, J. Combes, C. Ferrie, and E. M. Gauger, "Weak-value amplification: state of play," *Quantum Measurements and Quantum Metrology*, vol. 3, no. 1, pp. 32–37, 2016. 5.4.2

[157] J. Goodman, "Introduction to fourier optics," 2008. 5.4.3

[158] L. Novotny and B. Hecht, *Principles of nano-optics*. Cambridge University press, 2012. 5.4.4

[159] K. I. Mortensen, L. S. Churchman, J. A. Spudich, and H. Flyvbjerg, "Optimized localization analysis for single-molecule tracking and super-resolution microscopy," *Nature Methods*, vol. 7, no. 5, pp. 377–381, 2010. 5.5.2, 5.8.1, 5.9

[160] S. Stallinga and B. Rieger, "Accuracy of the Gaussian point spread function model in 2D localization microscopy," *Optics Express*, vol. 18, pp. 24461–24476, 2010. 5.5.2

[161] N. Bobroff, "Position measurement with a resolution and noise-limited instrument," *Review of Scientific Instruments*, vol. 57, p. 1152, 1986. 5.5.2, 5.5.3

[162] R. E. Thompson, D. R. Larson, and W. W. Webb, "Precise nanometer localization analysis for individual fluorescent probes," *Biophysical Journal*, vol. 82, no. 5, p. 2775, 2002. 5.5.2

[163] J. D. Wong-Campos, K. G. Johnson, B. Neyenhuis, J. Mizrahi, and C. Monroe, "High-resolution adaptive imaging of a single atom," *Nature Photonics*, vol. 10, p. 606, 2016. 5.5.2

[164] P. D. Howes, R. Chandrawati, and M. M. Stevens, "Colloidal nanoparticles as advanced biological sensors," *Science*, vol. 346, no. 6205, p. 1247390, 2014. 5.6

[165] P. Zhang, S. Lee, H. Yu, N. Fang, and S. H. Kang, "Super-resolution of fluorescence-free plasmonic nanoparticles using enhanced dark-field illumination based on wavelength-modulation," *Scientific Reports*, vol. 5, p. 11447, 2015. 5.6

[166] J. Petersen, J. Volz, and A. Rauschenbeutel, "Chiral nanophotonic waveguide interface based on spin-orbit interaction of light," *Science*, vol. 346, no. 6205, pp. 67–71, 2014. 5.6

[167] S. Walser, *To be published.* PhD thesis. 5.6

[168] M. V. Berry, "Lateral and transverse shifts in reflected dipole radiation," *Proceedings of the Royal Society of London A*, vol. 467, no. 2133, pp. 2500–2519, 2011. 5.7

[169] S. M. Barnett and M. V. Berry, "Superweak momentum transfer near optical vortices," *Journal of Optics*, vol. 15, no. 12, p. 125701, 2013. 5.7

[170] J. Arlt, "Handedness and azimuthal energy flow of optical vortex beams," *Journal of Modern Optics*, vol. 50, no. 10, pp. 1573–1580, 2003. 5.7

[171] J.-S. Lee and E. Pottier, *Polarimetric radar imaging: from basics to applications.* CRC press, 2009. 5.8.1

[172] M. P. Hayes and P. T. Gough, "Synthetic aperture sonar: A review of current status," *IEEE Journal of Oceanic Engineering*, vol. 34, p. 207, 2009. 5.8.1

[173] B. P. Abbott, R. Abbott, T. D. Abbott, F. Acernese, K. Ackley, C. Adams, T. Adams, P. Addesso, R. X. Adhikari, V. B. Adya, *et al.*, "Search for post-merger gravitational waves from the remnant of the binary neutron star merger GW170817," *Astrophysiscal Journal Letters*, vol. 851, no. 1, p. L16, 2017. 5.8.1

[174] I. Bialynicki-Birula and Z. Bialynicka-Birula, "Gravitational waves carrying orbital angular momentum," *New Journal of Physica*, vol. 18, no. 2, p. 023022, 2016. 5.8.1

[175] A. Yildiz, J. N. Forkey, S. A. McKinney, T. Ha, Y. E. Goldman, and P. R. Selvin, "Myosin V walks hand-over-hand: single fluorophore imaging with 1.5-nm localization," *Science*, vol. 300, no. 5628, pp. 2061–2065, 2003. 5.8.1

[176] A. R. Small and R. Parthasarathy, "Superresolution localization methods," *Annual Review of Physical Chemistry*, vol. 65, pp. 107–125, 2014. 5.8.1

[177] K. Y. Bliokh and F. Nori, "Transverse and longitudinal angular momenta of light," *Physics Reports*, vol. 592, pp. 1 – 38, 2015. 5.8.1

[178] N. G. Khlebtsov and B. N. Khlebtsov, "Optical polarizability of metal nanoparticles and their biospheric conjugates," in *Saratov Fall Meeting 2005: Coherent Optics of Ordered and Random Media VI*, vol. 6164, p. 616405, 2006. 5.8.1

[179] M. Krenn and A. Zeilinger, "On small beams with large topological charge ii: photons, electrons and gravitational waves," *New Journal of Physics*, 2018. 5.9

[180] N. Skribanowitz, I. Herman, J. MacGillivray, and M. Feld, "Observation of Dicke superradiance in optically pumped HF gas," *Physical Review Letters*, vol. 30, no. 8, p. 309, 1973. 6.1

[181] E. M. Purcell, H. C. Torrey, and R. V. Pound, "Resonance absorption by nuclear magnetic moments in a solid," *Physical Review*, vol. 69, no. 1-2, p. 37, 1946. 6.1

[182] M. Kiffner, M. Macovei, J. Evers, and C. Keitel, "Chapter 3 - vacuum-induced processes in multilevel atoms," vol. 55 of *Progress in Optics*, pp. 85 – 197, Elsevier, 2010. 6.1

[183] K. Drexhage, "Influence of a dielectric interface on fluorescence decay time," *Journal of Luminescence*, vol. 1, pp. 693–701, 1970. 6.1

[184] S. Haroche and D. Kleppner, "Cavity quantum electrodynamics," *Physics Today*, vol. 42, no. 1, pp. 24–30, 1989. 6.1

[185] G.-i. Kweon and N. Lawandy, "Quantum electrodynamics in photonic crystals," *Optics Communications*, vol. 118, no. 3-4, pp. 388–411, 1995. 6.1

[186] M. Brune, P. Nussenzveig, F. Schmidt-Kaler, F. Bernardot, A. Maali, J. Raimond, and S. Haroche, "From lamb shift to light shifts: Vacuum and subphoton cavity fields measured by atomic phase sensitive detection," *Physical Review Letters*, vol. 72, no. 21, p. 3339, 1994. 6.1

[187] D. Heinzen and M. Feld, "Vacuum radiative level shift and spontaneous-emission linewidth of an atom in an optical resonator," *Physical Review Letters*, vol. 59, no. 23, p. 2623, 1987. 6.1

[188] C. Hood, T. Lynn, A. Doherty, A. Parkins, and H. Kimble, "The atom-cavity microscope: Single atoms bound in orbit by single photons," *Science*, vol. 287, no. 5457, pp. 1447–1453, 2000. 6.1

[189] A. Kreuter, C. Becher, G. Lancaster, A. Mundt, C. Russo, H. Häffner, C. Roos, J. Eschner, F. Schmidt-Kaler, and R. Blatt, "Spontaneous emission lifetime of a single trapped ca+ ion in a high finesse cavity," *Physical Review Letters*, vol. 92, no. 20, p. 203002, 2004. 6.1

[190] J. Gallego, W. Alt, T. Macha, M. Martinez-Dorantes, D. Pandey, and D. Meschede, "Strong Purcell effect on a neutral atom trapped in an open fiber cavity," *arXiv preprint arXiv:1804.08526*, 2018. 6.1

[191] K. J. Vahala, "Optical microcavities," *Nature*, vol. 424, no. 6950, p. 839, 2003. 6.1

[192] R. G. Hulet, E. S. Hilfer, and D. Kleppner, "Inhibited spontaneous emission by a Rydberg atom," *Physical Review Letters*, vol. 55, no. 20, p. 2137, 1985. 6.1

[193] M. Bayer, T. Reinecke, F. Weidner, A. Larionov, A. McDonald, and A. Forchel, "Inhibition and enhancement of the spontaneous emission of quantum dots in structured microresonators," *Physical Review Letters*, vol. 86, no. 14, p. 3168, 2001. 6.1

[194] D. Kleppner, "Inhibited spontaneous emission," *Physical Review Letters*, vol. 47, no. 4, p. 233, 1981. 6.1

[195] G. Hétet, L. Slodička, A. Glätzle, M. Hennrich, and R. Blatt, "QED with a spherical mirror," *Physical Review A*, vol. 82, no. 6, p. 063812, 2010. 6.1, 6.1

[196] G. Alber, J. Bernád, M. Stobińska, L. Sánchez-Soto, and G. Leuchs, "QED with a parabolic mirror," *Physical Review A*, vol. 88, no. 2, p. 023825, 2013. 6.1

[197] J. Eschner, C. Raab, F. Schmidt-Kaler, and R. Blatt, "Light interference from single atoms and their mirror images," *Nature*, vol. 413, no. 6855, p. 495, 2001. 6.1

[198] J. Bentham, *Panopticon or the inspection house (1791)*. Kessinger Publishing, WhiteFish MT, 2009. 1

[199] J. Turneaure, C. Everitt, B. Parkinson, D. Bardas, J. Breakwell, S. Buchman, W. Cheung, D. Davidson, D. DeBra, W. Fairbank, *et al.*, "The gravity-probe-b relativity gyroscope experiment: Development of the prototype flight instrument," *Advances in Space Research*, vol. 9, no. 9, pp. 29–38, 1989. 6.2.1

[200] D. B. Higginbottom, G. T. Campbell, G. Araneda, F. Fang, Y. Colombe, B. C. Buchler, and P. K. Lam, "Fabrication of ultrahigh-precision hemispherical mirrors for quantum-optics applications," *Scientific Reports*, vol. 8, no. 1, p. 221, 2018. 6.2.1

[201] D. B. Higginbottom, *Atom-light couplers with one, two and ten billion atoms*. PhD thesis, Australian National University, 2018. 6.2.1

[202] J. D. Siverns and Q. Quraishi, "Ion trap architectures and new directions," *Quantum Information Processing*, vol. 16, no. 12, p. 314, 2017. 6.2.3, 6.2.3

[203] M. Brownnutt, M. Kumph, P. Rabl, and R. Blatt, "Ion-trap measurements of electric-field noise near surfaces," *Reviews of Modern Physics*, vol. 87, no. 4, p. 1419, 2015. 6.2.3

[204] D. R. Leibrandt, R. J. Clark, J. Labaziewicz, P. Antohi, W. Bakr, K. R. Brown, and I. L. Chuang, "Laser ablation loading of a surface-electrode ion trap," *Physical Review A*, vol. 76, no. 5, p. 055403, 2007. 6.3.1

[205] S. Olmschenk and P. Becker, "Laser ablation production of Ba, Ca, Dy, Er, La, Lu, and Yb ions," *Applied Physics B*, vol. 123, no. 4, p. 99, 2017. 6.3.1

[206] M. Steiner, H. M. Meyer, C. Deutsch, J. Reichel, and M. Köhl, "Single ion coupled to an optical fiber cavity," *Physical Review Letters*, vol. 110, no. 4, p. 043003, 2013. 6.5

[207] B. Brandstätter, A. McClung, K. Schüppert, B. Casabone, K. Friebe, A. Stute, P. O. Schmidt, C. Deutsch, J. Reichel, R. Blatt, and T. Northup, "Integrated fiber-mirror ion trap for strong ion-cavity coupling," *Review of Scientific Instruments*, vol. 84, no. 12, p. 123104, 2013. 6.5

[208] P. Lodahl, "Quantum-dot based photonic quantum networks," *Quantum Science and Technology*, vol. 3, no. 1, p. 013001, 2017. 6.5

[209] P. C. Humphreys, N. Kalb, J. P. Morits, R. N. Schouten, R. F. Vermeulen, D. J. Twitchen, M. Markham, and R. Hanson, "Deterministic delivery of remote entanglement on a quantum network," *Nature*, vol. 558, no. 7709, p. 268, 2018. 6.5, 7